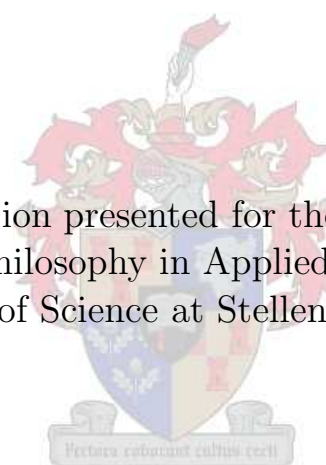# Comparative analysis of predictive equations for transfer processes in different porous structures

by

Sonia Woudberg

Dissertation presented for the degree of
Doctor of Philosophy in Applied Mathematics
in the Faculty of Science at Stellenbosch University

Promoter: Prof. Jean Prieur du Plessis [1]

December 2012

[1]Prof. J.P. Du Plessis acted as promoter from January 2007 until 3 December 2010, the day on which he unexpectedly passed away. Proff. G.J.F. Smit and I.M. Rewitzky acted as promoters thereafter.

Declaration

By submitting this dissertation electronically, I declare that the entirety of the work contained therein is my own, original work, that I am the sole author thereof (save to the extent explicitly otherwise stated), that reproduction and publication thereof by Stellenbosch University will not infringe any third party rights and that I have not previously in its entirety or in part submitted it for obtaining any qualification.

December 2012

i

Abstract

Research on transfer processes in various types of porous media has become important for the optimization of high technology engineering devices and processes. In this study the micro-structural parameters of different types of porous media, namely granular media, foamlike media and fibre beds, are characterized and quantified. Existing analytical modelling procedures for the three different types of porous media have been unified and refined to improve their predictive capabilities. Deterministic equations are proposed for predicting the streamwise pressure gradient, permeability and inertial coefficient of each type of porous medium. The equations are applicable over the entire porosity range and steady laminar flow regime and well suited as drag models in numerical computations.

It is shown that the improved granular model can be regarded as qualitative and quantitative proof of the extensively used semi-empirical Ergun equation. The proposed model is used to provide physical meaning to the empirical coefficients. An Ergun-type equation is also proposed for foamlike media by remodelling the interstitial geometric configuration and accompanying flow conditions.

The range of applicability of the existing foam model has been extended by incorporating the effect of developing flow in the pressure drop prediction. An equation is proposed in which the variation in the cross-sectional shape of the fibres can be incorporated into the interstitial form drag coefficient used in the foam model. This serves as an improvement on the constant value previously used. The existing foam model is also adapted to account for anisotropy resulting from compression. Two case studies are considered, namely compression of a non-woven glass fibre filter and compression of a soft polyester fibre material. The significant effect of compression on permeability is illustrated. In each case study the permeability values range over more than an order of magnitude for the narrow porosity ranges involved. The pressure drop prediction of the foam model is furthermore adapted to account for the combined effects of compression and developing flow. The newly proposed model diminishes the significant over-prediction of the existing foam model.

An equation is furthermore proposed for predicting the permeability of Fontainebleau sandstones in which the effect of blocked throats is accounted for. Lastly, equations are proposed for predicting diffusivity ratios of unconsolidated arrays of squares and cubes. The prediction of the diffusivity ratio proposed in the present study, as opposed to model predictions from the literature, takes into account diffusion that may take place in stagnant fluid volumes. It is shown that a specific weighted average model proposed in the literature is not adequate to predict the diffusivity ratio of fully staggered arrays of squares, since it is shown not to be applicable to rectangular unit cells. Instead a new weighted average model is proposed which is applicable over the entire porosity range and for both staggered and non-staggered arrays of solid squares and cubes. The proposed weighted average model provides satisfactory agreement with experimental data from the literature and numerical data generated in the present study.

Opsomming

Navorsing op oordragsprosesse in verskeie tipes poreuse media het belangrik geword vir die optimisering van hoë-tegnologie ingenieurstoestelle- en prosesse. In hierdie studie word die mikro-struktuur parameters van verskillende tipes poreuse media, naamklik korrelagtige media, sponsatige media en veselbeddens gekarakteriseer en gekwantifiseer. Bestaande analitiese modelleringsprosedures vir die drie verskillende tipes poreuse media is verenig en verfyn om die voorspelbare bekwaamheid daarvan te verbeter. Deterministiese vergelykings is voorgestel vir die voorspelling van die stroomsgewyse gradiënt, permeabiliteit en inersiële koëffisiënt van elke tipe poreuse medium. Die vergelykings is geldig oor die hele porositeitsgrens en gestadigde laminêre vloeigrens en goed geskik as weerstandsmodelle in numeriese berekeninge.

Dit is aangetoon dat die verbeterde korrelmodel beskou kan word as kwalitatiewe en kwantitatiewe bewys van die ekstensiewe gebruikte semi-empiriese Ergun vergelyking. Die voorgestelde model is gebruik om fisiese betekenis aan die empiriese koëffisiënte te gee. 'n Ergun-tipe vergelyking is ook voorgestel vir sponsagtige media deur hermodellering van die tussenruimtelike geometriese konfigurasie en gepaardgaande vloeikondisies.

Die grense van toepaslikheid van die bestaande sponsmodel is uitgebrei deur die inkorporering van die effek van ontwikkelende vloei in die voorspelling van die drukval. 'n Vergelyking is voorgestel waarin die variasie in die deursnit vorm van die vesels ingesluit is in die sponsmodel. Dit dien as verbetering op die konstante waarde wat voorheen gebruik is. Die bestaande sponsmodel is ook aangepas om voorsiening te maak vir anisotropie as gevolg van kompressie. Twee gevallestudies is oorweeg, naamlik kompressie van 'n nie-geweefde glasvesel filter en kompressie van 'n sagte polyester veselmateriaal. Die beduidende effek van kompressie op permeabiliteit is aangetoon. In elke gevallestudie strek die permeabiliteit waardes oor meer as 'n grootte orde vir die skrale porositeitgrense betrokke. Die drukvalvoorspelling van die sponsmodel is verder aangepas om voorsiening te maak vir die gekombineerde effekte van kompressie en ontwikkelende vloei. Die nuwe voorgestelde model verminder die beduidende oor-voorspelling van die bestaande sponsmodel.

'n Vergelyking is verder voorgestel vir die voorspelling van die permeabiliteit van Fontaine-bleau sandsteen waarin die effek van geblokte porieë in ag geneem is. Laastens is vergelykings voorgestel vir die voorspelling van die diffusiwiteitsverhoudings van nie-konsoliderende rangskikkings van vierkante en kubusse. Die diffusiwiteitsverhouding voorspel in die huidige studie, teenoor modelvoorspellings vanaf die literatuur, neem diffusie in ag wat plaasvind in die stagnante vloeistofvolumes. Dit is aangetoon dat 'n geweegde gemiddelde model, voorgestel in die literatuur, nie in staat is om die diffusiwiteitsverhouding van ten volle verspringende rangskikkings van vierkante te voorspel nie, aangesien dit nie toepaslik is vir reghoekige eenheidselle nie. 'n Nuwe geweegde model is in plaas daarvan voorgestel wat toepaslik is oor die hele porositeitsgrens en vir beide verspringende en nie-verspringende rangskikkings van soliede vierkante en kubusse. Die voorgestelde geweegde

gemiddelde model bied bevredigende ooreenstemming met eksperimentele data uit die literatuur en numeriese data gegenereer in die huidige studie.

Vir professor Jean Prieur du Plessis

... lank lewe die RUC model!

Acknowledgements

I wish to express my sincere gratitude towards the following people who supported me in their own special way:

- God, for an amazing grace that eclipses all human knowledge and understanding. Thank you for showing me Your Master plan.
  … laat U gees deur my VLOEI soos 'n rivier van lewende WATER!

- My parents, Johann and Linda Woudberg for their unconditional love and support. Thank you for giving me the opportunities to spread my wings.

- Herman Fidder for turning my world upside down.

- My sister and brother in law, Tania and André Heunis, for their love and support when I needed it most.

- Kristin, André, Van Heerden and Johann Heunis for showing me how important family is.

- Professor Prieur du Plessis for believing in me. It was an incredible journey with memories that will last forever.

- Emeritus professor Narisscia Botha, my official mentor, for sharing expert advice and for setting the example of living life at its fullest each day, irrespective of what life throws at you.

- Anna Kotzé, my unofficial mentor, and the team at Anna Kotzé Consult for giving me a supporting system that one can only dream of.

- The Kotzé family for great times on Evaskraal.

- Professors Francois Smit and Ingrid Rewitzky for being willing to take over the reigns during the final stages of completing this dissertation.

- Van Heerden Heunis for superb assistance with the media interaction during the time of the L'Oréal-UNESCO award.

- The authorities involved in the L'Oréal-UNESCO-ANSTI For Women in Science Partnership for having confidence in me and for acknowledging my hard work.

- Wilhelm Frank for the prestigious scholarship.

- The National Research Foundation for Thuthuka (Researchers In Training) funding.

- Stellenbosch University for several research grants and the privilege to be an employee.

- All the people who hosted me during research visits abroad.

- All the people who contributed to the development of the RUC model.

- All the rest, for making life interesting.

... ek het rykdom in my hart!

Preface

In 1988 professor Jean Prieur du Plessis introduced a geometric pore-scale model for predicting pressure drops over metallic foams. After the success of this model, he developed similar models for predicting flow through granular porous media and fibre beds. Over the past three decades, the mathematical modelling procedures accompanying the geometric models have been refined to improve their predictive capabilities and scientific correctness, with considerable success. Many post-graduate students and researchers have worked with professor Du Plessis and contributed to the development of the models. Several masters and doctoral theses have been delivered, accompanied by numerous publications in international journals. A post-graduate course on Porous Media was established by professor Du Plessis in the former Department of Applied Mathematics, nowadays a division of the Department of Mathematical Sciences. This led to the establishment of the Flow Modelling group at Stellenbosch University.

This dissertation is dedicated to professor Du Plessis, my supervisor and inspiring mentor since 2004, who unexpectedly passed away on 3 December 2010. Professor Matiur Rahman from Dalhousie University in Halifax, Canada, shared the following words (with which his students and the rest of his fellow research collaborators will agree to):

"He was a fantastic applied mathematician with excellent mathematical knowledge. His work on porous media brings considerable accolades among scientists and engineers around the world. He was a person with a beautiful mind."

In this dissertation are captured the most important characteristics and major contributions made to the models over the years, including my contribution. My wish is that this work will form the basis for the next three decades of research on the models and that this dissertation will serve as a complete guide to the models for future research.

All the work and results presented in this dissertation were obtained solely under the supervision of professor Du Plessis. Many thanks to emeritus professor Narisscia Botha for taking over the role as my mentor. Sincere thanks to professors Francois Smit and Ingrid Rewitzky who were willing to act as supervisors during the final stages of completion of this dissertation. Their support during a crucial time is truly appreciated.

Contents

6   Short duct foam RUC model   163

7   Geometrically adapted foam RUC model   196

CONTENTS

Nomenclature

Standard characters

Notation:	Units:	Description:
a	[m]	radius of cylinder or sphere
a'	[m]	cell size of dodecahedron used by Bhattacharya et al. (2002)
A	[ ]	empirical coefficient in Ergun equation
A'	[ ]	coefficient in Ergun-type equation for foamlike media
A_e	[m^2]	uniform cross-sectional duct area
$\mathcal{A}_p$	[m^2]	projected cross-sectional area of solid body
$A_{p_\parallel}$	[m^2]	streamwise cross-sectional flow area in RUC
$A_{p_\perp}$	[m^2]	transverse cross-sectional flow area in RUC
A_s	[m^2]	total solid surface area of porous medium
A_{sp}	[m^2]	total spherical solid surface area
A_{vd}	[m^{-1}]	dynamic specific surface
A_{vp}	[m^{-1}]	specific surface with respect to total pore space
A_{vs}	[m^{-1}]	static specific surface
b	[m]	radius of cylinder or sphere
B	[ ]	empirical coefficient in Ergun equation
B'	[ ]	coefficient in Ergun-type equation for foamlike media
c	[m]	diagonal cell size
c_d	[ ]	interstitial form drag coefficient
C_d	[ ]	form drag coefficient
C_f	[ ]	Forchheimer coefficient
C_1	[ ]	coefficient
C_2	[ ]	coefficient
d	[m]	cell size of RUC

Notation:	Units:	Description:
d'	[m]	cubic cell size used by Bhattacharya et al. (2002)
d_e	[m]	average length of tortuous flow path in RUC
d'_f	[m]	cylindrical fibre diameter used by Bhattacharya et al. (2002)
d_g	[m]	grain diameter used for sandstones
d_p	[m]	pore diameter in foam RUC
d'_p	[m]	pore diameter used by Bhattacharya et al. (2002)
d_s	[m]	solid width in RUC
$d_{s_\parallel}$	[m]	streamwise solid width in RUC
$d_{s_\perp}$	[m]	transverse solid width in RUC
d_{strut}	[m]	foam strut diameter
d_{window}	[m]	foam window diameter
$d_\parallel$	[m]	RUC dimension in streamwise direction
$d_{\parallel o}$	[m]	RUC thickness in streamwise direction in uncompressed state
$d_\perp$	[m]	RUC dimension in transverse direction
D	$[\text{m}^2.\text{s}^{-1}]$	diffusion coefficient in Fick's law
D_a	[m]	diameter of cylinder with radius a
D_{AB}	$[\text{m}^2.\text{s}^{-1}]$	diffusion coefficient of a binary mixture
D_{eff}	$[\text{m}^2.\text{s}^{-1}]$	effective diffusion coefficient
D_h	[m]	hydraulic diameter
D_p	$[\text{N}.\text{m}^{-2}]$	pressure drag on particle
D_{PS}	$[\text{m}^2.\text{s}^{-1}]$	effective diffusion coefficient for PS model
D_s	[m]	equivalent particle diameter
D_{sp}	[m]	diameter of sphere
D_{SP}	$[\text{m}^2.\text{s}^{-1}]$	effective diffusion coefficient for SP model
e	[ ]	analytical sample thickness relative to its uncompressed state
e_{exp}	[ ]	experimental sample thickness relative to its uncompressed state
$e_{\parallel o}$	[ ]	sample thickness in streamwise direction in uncompressed state
f	$[\text{m}^{-2}]$	total drag factor

Notation:	Units:	Description:
f_{app}	[ ]	apparent friction factor
$\underline{f}_b$	[N.kg^{-1}]	body force per unit mass
$f_{B_{an}}$	[ ]	analytical inertial coefficient of Du Plessis et al. (1994) used by Bhattacharya et al. (2002)
$f_{B_{exp}}$	[ ]	empirical inertial coefficient of Bhattacharya et al. (2002)
f_{BK}	[ ]	friction factor used in the Blake-Kozeny equation
f_{CK}	[ ]	friction factor used in the Carman-Kozeny equation
f_d	[m^{-2}]	total drag factor in terms of d
f_{dds}	[m^{-2}]	total drag factor in terms of $d - d_s$
f_{ds}	[m^{-2}]	total drag factor in terms of d_s
f_f	[ ]	Darcy-Weisbach friction factor
f_{fd}	[ ]	friction factor for fully developed flow
f_0	[m^{-2}]	drag factor in low Reynolds number limit
f_{0_d}	[m^{-2}]	drag factor in low Reynolds number limit in terms of d
$f_{0_{dds}}$	[m^{-2}]	drag factor in low Reynolds number limit in terms of $d - d_s$
$f_{0_{ds}}$	[m^{-2}]	drag factor in low Reynolds number limit in terms of d_s
f_∞	[m^{-2}]	drag factor in steady laminar limit of inertial flow regime
f_{∞_d}	[m^{-2}]	drag factor in steady laminar limit of inertial flow regime in terms of d
$f_{\infty_{ds}}$	[m^{-2}]	drag factor in steady laminar limit of inertial flow regime in terms of d_s
$f_{\infty_{dds}}$	[m^{-2}]	drag factor in steady laminar limit of inertial flow regime in terms of $d - d_s$
F	[ ]	dimensionless total drag factor
F_d	[ ]	dimensionless total drag factor in terms of d
F_{dds}	[ ]	dimensionless total drag factor in terms of $d - d_s$
F_{ds}	[ ]	dimensionless total drag factor in terms of d_s
F_o	[ ]	Forchheimer number
F_0	[ ]	dimensionless drag factor in low Reynolds number limit

Notation:	Units:	Description:
F_{0_d}	[ ]	dimensionless drag factor in low Reynolds number limit in terms of d
$F_{0_{dds}}$	[ ]	dimensionless drag factor in low Reynolds number limit in terms of $d - d_s$
$F_{0_{ds}}$	[ ]	dimensionless drag factor in low Reynolds number limit in terms of d_s
F_∞	[ ]	dimensionless drag factor in steady laminar limit of inertial flow regime
F_{∞_d}	[ ]	dimensionless drag factor in steady laminar limit of inertial flow regime in terms of d
$F_{\infty_{dds}}$	[ ]	dimensionless drag factor in steady laminar limit of inertial flow regime in terms of $d - d_s$
$F_{\infty_{ds}}$	[ ]	dimensionless drag factor in steady laminar limit of inertial flow regime in terms of d_s
$\mathcal{F}$	[N]	total drag force
$\mathcal{F}_k$	[N]	drag force on solid(s) due to kinetic energy of fluid
$\mathcal{F}_p$	[N]	pressure drag force
$\mathcal{F}_s$	[N]	drag force on solid(s) due to stationary fluid
$\mathcal{F}_v$	[N]	viscous drag force
g	[m.s^{-2}]	magnitude of gravitational acceleration
G	[ ]	empirical shape function used by Bhattacharya et al. (2002)
$\mathcal{G}_0$	[ ]	function value for $x \to 0$
$\mathcal{G}_\infty$	[ ]	function value for $x \to \infty$
h	[m]	sample thickness in streamwise direction (Akaydin et al. (2011))
h_A	[m]	height at point A
h_C	[m]	height at point C
Hg	[ ]	Hagen number
$\underline{j}_c$	[kg.m^{-2}.s^{-1}]	mass flux of diffusing species
$\underline{j}_{c_\parallel}$	[kg.m^{-2}.s^{-1}]	average streamwise diffusive pore flux
$\underline{J}_c$	[kg.m^{-2}.s^{-1}]	average total diffusive flux

Notation:	Units:	Description:
k, k_1	[m^2]	hydrodynamic or Darcy permeability
k_2	[m^{-1}]	non-Darcy flow coefficient
$k_{B_{an}}$	[m^2]	analytical permeability of Du Plessis et al. (1994) used by Bhattacharya et al. (2002)
$k_{B_{exp}}$	[m^2]	empirical permeability of Bhattacharya et al. (2002)
k_{BK}	[m^2]	permeability of the Blake-Kozeny equation
k_{CK}	[m^2]	permeability of the Carman-Kozeny equation
k_d	[m^2]	permeability in terms of d
k_{dds}	[m^2]	permeability in terms of $d - d_s$
k_{ds}	[m^2]	permeability in terms of d_s
k_{exp}	[m^2]	experimental permeability values
k_{koz}	[ ]	Kozeny constant
k_o	[ ]	shape factor in Carman-Kozeny equation
K_d	[ ]	dimensionless permeability in terms of d
K_{dp}	[ ]	dimensionless permeability in terms of d_p
K_{dds}	[ ]	dimensionless permeability in terms of $d - d_s$
K_{ds}	[ ]	dimensionless permeability in terms of d_s
l	[m]	microscopic length
l_m	[m]	molecular mean free path
L	[m]	dimension along fibre axis
L_m	[m]	macroscopic length
L_e	[m]	effective average path length
$\mathcal{L}$	[ ]	lineality
M	[ ]	coefficient in Forchheimer equation
n	[ ]	exponent/coefficient in binomial series expansion
$\underline{n}$	[ ]	normal unit vector directed into solid
$\widehat{\underline{n}}$	[ ]	unit vector in streamwise direction
$\widetilde{\underline{n}}$	[ ]	unit vector of interstitial velocity field
$\underline{n}_D$	[ ]	inwardly directed normal vector on $S_{\perp_D}$
$\underline{n}_U$	[ ]	inwardly directed normal vector on $S_{\perp_U}$
N	[ ]	coefficient in Forchheimer equation
p	[Pa]	interstitial static pressure

Notation:	Units:	Description:
p_A	[Pa]	interstitial static pressure at point A
p_C	[Pa]	interstitial static pressure at point C
$\overline{p}_w$	[Pa]	average pressure over two transverse or stagnant surfaces of solid
$\widetilde{p}_w$	[Pa]	difference between actual pressure and average wall pressure
$\underline{q}$	[m.s^{-1}]	superficial velocity, Darcy velocity or specific discharge
q_{exp}	[m.s^{-1}]	experimental values for magnitude of superficial velocity
$\underline{r}_o$	[m]	position vector of REV centroid
R_h	[m]	hydraulic radius
Re	[]	Reynolds number (general definition)
Re_{BK}	[]	Reynolds number used in the Blake-Kozeny equation
Re_c	[]	critical Reynolds number at which developing flow and the inertial flow regime weigh equally
$Re_{c_{qds}}$	[]	critical Reynolds number for Re_{qds}
Re_{CK}	[]	Reynolds number used in the Carman-Kozeny equation
Re_D	[]	Reynolds number used by Dietrich et al. (2009)
Re_{Dh_c}	[]	critical Reynolds number at which developing flow and fully developed flow weigh equally
Re_h	[]	Reynolds number in terms of the hydraulic diameter
Re_p	[]	particle Reynolds number
Re_k	[]	Reynolds number in terms of permeability k
Re_{qd}	[]	cell Reynolds number, defined in terms of q and d
Re_{qdds}	[]	pore Reynolds number, defined in terms of q and $d - d_s$
Re_{qds}	[]	particle Reynolds number, defined in terms of q and d_s
s	[ ]	shifting exponent
$\widetilde{S}_{face}$	[m^2]	cross-sectional area of solid "facing" upstream
$\mathcal{S}_{ff}$	[m^2]	total fluid-fluid interfaces on REV boundary
S_{fs}	[m^2]	total fluid-solid interfaces in RUC
$\mathcal{S}_{fs}$	[m^2]	total fluid-solid interfaces in REV
S_g	[m^2]	total stagnant surface areas in RUC
$S_{||}$	[m^2]	total streamwise surface areas in RUC
$S_\perp$	[m^2]	total transverse surface areas in RUC

Notation:	Units:	Description:
$S_{\perp_D}$	[m^2]	total downstream transverse surface areas in RUC
$S_{\perp_U}$	[m^2]	total upstream transverse surface areas in RUC
t	[ ]	shifting exponent
$t_\parallel$	[m]	sample thickness in streamwise direction (Le Coq (2008))
T	[ ]	kinematical tortuosity
$\underline{u}$	[m.s^{-1}]	intrinsic phase average fluid velocity
u_m	[m.s^{-1}]	magnitude of mean axial velocity
U_f	[m^3]	total fluid volume in RUC
U_f'	[m^3]	total fluid volume in RUC excluding stagnant volumes
$\mathcal{U}_f$	[m^3]	total fluid volume in REV
$U_{f_\mathcal{L}}$	[m^3]	total effective streamwise fluid volume in RUC
U_g	[m^3]	total stagnant fluid volume in RUC
U_o	[m^3]	total (fluid and solid) volume of RUC
$\mathcal{U}_o$	[m^3]	total (fluid and solid) volume of REV
U_s	[m^3]	total solid volume in RUC
$\mathcal{U}_s$	[m^3]	total solid volume in REV
U_t	[m^3]	total transfer fluid volume in RUC
$U_\parallel$	[m^3]	total streamwise fluid volume in RUC
$U_\perp$	[m^3]	total transverse fluid volume in RUC
$\underline{v}$	[m.s^{-1}]	interstitial fluid velocity
$\underline{v}_A$	[m.s^{-1}]	interstitial fluid velocity at point A
$\underline{v}_C$	[m.s^{-1}]	interstitial fluid velocity at point C
$\underline{v}_\infty$	[m.s^{-1}]	free stream velocity
$\underline{w}_\parallel$	[m.s^{-1}]	streamwise average channel velocity
$\underline{w}_\perp$	[m.s^{-1}]	transverse average channel velocity
V_o	[m^3]	total volume of porous medium
V_s	[m^3]	total solid volume of porous medium
V_p	[m^3]	total pore volume of porous medium
x, y, z	[m]	distance along rectangular Cartesian coordinate
x^+	[ ]	dimensionless axial distance

Greek symbols

Notation:	Units:	Description:
α	[ ]	exponent
β	[ ]	average channel velocity ratio
ϵ	[ ]	porosity
ϵ_B	[ ]	effective or backbone porosity
ϵ_c	[ ]	percolation threshold porosity
ϵ_o	[ ]	porosity in uncompressed state
η	[m]	passability
η_d	[m]	passability in terms of d
η_{dd_s}	[m]	passability in terms of $d - d_s$
η_{d_s}	[m]	passability in terms of d_s
μ	[kg.m^{-1}.s^{-1}]	fluid dynamic viscosity
ν	[ ]	exponent
ξ	[ ]	geometric coefficient
ρ	[kg.m^{-3}]	fluid density
σ	[ ]	volumetric ratio
$\underline{\underline{\tau}}$	[N.m^{-2}]	local shear stress tensor
τ_w	[N.m^{-2}]	magnitude of local wall shear stress
$\tau_{w_\parallel}$	[N.m^{-2}]	magnitude of wall shear stress on streamwise surfaces
$\tau_{w_\perp}$	[N.m^{-2}]	magnitude of wall shear stress on transverse surfaces
ϕ	[ ]	solid volume fraction
ϕ_s	[ ]	sphericity
ϕ_c	[kg.m^{-3}]	concentration of diffusing species
χ	[ ]	tortuosity
χ_{geo}	[ ]	geometrical tortuosity used in RUC model
χ_{kin}	[ ]	kinematical tortuosity used in RUC model
ψ	[ ]	geometric factor
ψ_o	[ ]	geometric factor of uncompressed state
ψ_B	[ ]	geometric factor as a function of the backbone porosity
Ψ	[ ]	tensorial fluid phase quantity
ω_A	[ ]	mass fraction of species A

Miscellaneous

Notation:	Description:
Δ, δ	operator indicating a change
Δs	transverse displacement of centroid of fluid
Δp	streamwise pressure drop
$\Delta \bar{x}$	displacement of centroid of fluid in x-direction
$\Delta \bar{y}$	displacement of centroid of fluid in y-direction
δp	transverse pressure drop
∇	del operator
$\underline{}$	vector (underlined)
$\underline{\underline{}}$	diadic (doubly underlined)
$\equiv$	definition
$\langle\ \rangle$	phase average operator
$\langle\ \rangle_f$	intrinsic phase average operator
$\{\ \}$	deviation operator

Acronyms

Notation:	Description:
PPI	<u>P</u>ores <u>P</u>er <u>I</u>nch
REV	<u>R</u>epresentative <u>E</u>lementary <u>V</u>olume
RUC	<u>R</u>epresentative <u>U</u>nit <u>C</u>ell
SVF	<u>S</u>olid <u>V</u>olume <u>F</u>raction
UC	<u>U</u>nit <u>C</u>ell

Subscripts

Notation:	Description:
AA	RUC with corner points AAAA
BB	RUC with corner points BBBB
c	critical
D	downstream
f	fluid phase
fs	fluid-solid interface
o	total solid- and fluid volume
s	solid phase
U	upstream
w	wall
$\|\|$	parallel to streamwise direction
$\perp$	perpendicular to streamwise direction
0	lower Reynolds number limit
∞	upper Reynolds number limit

List of Figures

List of Tables

Chapter 1

Introduction

Transport in porous media occurs naturally, is used in daily life and is encountered in many science and engineering disciplines, e.g. the medical and soil sciences, civil engineering, chemical engineering, petroleum engineering, reservoir engineering and agricultural engineering (e.g. Scheidegger (1957), Dullien (1979), Bear & Bachmat (1991), Kaviany (1995)). Examples of porous media occurring naturally are sand, sandstones, coal and plant tissue. In the human body the liver, lungs, blood vessels and bones are all porous. Everyday use of porous media include textiles, leathers, paper and various building materials such as bricks and concrete. Examples of transport in porous media in the various engineering disciplines are the flow of water and solutes in the root zone in soil, the transport of moisture through and under engineering structures, coal gasification for the production of synthetic gases and flow through chemical packed bed reactors and filters.

In South Africa, as well as internationally, research on transfer phenomena in various types of porous media has become important for the optimization of high technology engineering processes, since the transport phenomena affect planning, productivity and design. In respect thereof, knowledge and understanding of the basic underlying physical flow processes in porous media, especially metallic foams, are crucial (Hwang et al. (2002), Topin et al. (2006)). The parameters that govern fluid flow in these materials are the pressure drop (Dukhan (2006), Lacroix et al. (2007), Dukhan & Patel (2008)), permeability and inertial coefficient (Antohe et al. (1997)) as well as the dynamic specific surface (Huu et al. (2009)). The pressure drop, for example, is proportional to the fluid pumping power. An excess in pressure drop requires additional energy for fluid flow and therefore needs to be minimized. Innocentini et al. (1999a), Innocentini et al. (1999b) and Xu et al. (2008) mention that permeability is the most important parameter for the optimization of filtration devices. Bhattacharya et al. (2002), in turn, emphasize the need for the characterization of porous materials for fluid flow and the need for accurate evaluation of their transport properties.

Solutions to management decisions in the various engineering environments can be provided with the aid of a tool that enables one to predict the response of a system under certain physical conditions. Nowadays, both commercial and dedicated computational

1

codes used as tools are in abundance. Significant contributions have been made in computer simulations over the past few years, and although it may be time-consuming, costly and subject to errors/uncertainties it still is an ever growing field. The same applies to the execution of experiments to obtain experimental data (Chen & Papathanasiou (2006)). An equally important issue is the scarcity of analytical work on the micro-structural properties of porous materials and the lack of simple and efficient predictive equations for various transport processes to be used independently for analysis as well as for large scale computational efforts. Therefore, a great deal of effort has been devoted to the development of theoretical models as tools for formulating predictive equations.

The proposed study is, firstly, aimed at the characterization of different porous materials for the mathematical quantification of the pore-scale geometry and, secondly, to provide equations that can accurately predict the pressure drop and/or permeability and inertial coefficient experienced by passage of fluid through different types of porous media. Such a mathematical description can only be obtained with knowledge and understanding of the underlying physical flow processes involved.

1.1 Objectives

The objective throughout this study is to provide mathematical models that contain no empirical coefficients and that are based on sound physical principles. The following statement of Dana Mackenzie is acknowledged and serves as motivation for this study to try and prove the contrary:

"Every model has parameters that are 'tuned' to make the output match observations more closely. In some cases, the tuning causes the models to violate the very physics that has been so painstakingly included."

- Dana Mackenzie, *Mathematicians confront climate change*, SIAM News 40(5), June 2007.

Below is a list of the major objectives for this study:

1. Refining and improving existing predictive equations for the pressure drop, permeability and inertial coefficient for granular media, foamlike media and fibre beds.

2. Capturing and presenting the major contributions made to the existing models over the past three decades: The analytical modelling procedure for the different porous medium geometries have been presented *independently* in the past. The present study is aimed at the *unification* of the modelling procedures. This implies that the existing analytical modelling procedures need to be refined to ensure that all steps and parameters in the modelling procedure are applicable to all three pore-scale model geometries.

3. Proposing a much shorter and direct analytical modelling procedure in the Darcy flow regime that is applicable to all three porous medium geometries: In the past the direct modelling procedure was only applied to the fibre model. In this study it will also be applied to the granular and foam model geometries and unified into one modelling procedure.

4. Illustrating that the geometric pore-scale model for granular media can be regarded as a theoretical derivation of the semi-empirical Ergun equation. Another related objective is to quantify the Ergun coefficients as a function of porosity.

5. Illustrating that the geometric pore-scale model for foamlike media can serve as an Ergun-type equation for the latter media. Also in this case, the coefficients of the Ergun-type equation for foamlike media are to be quantified as a function of porosity.

6. Adapting the analytical modelling procedure for foamlike media to account for developing flow.

7. Adapting the geometric pore-scale model for foamlike media from an isotropic structure to an anisotropic one to account for the effect of compression on pressure drop and permeability.

8. Using the models for granular and foamlike media to predict the permeability of sandstones in which the effect of pore blockage at very low porosities is accounted for.

9. Using the models for granular media and fibre beds to predict the effective diffusivity of unconsolidated porous media: This involves mass transport as opposed to all the other objectives, mentioned above, involving momentum transport.

1.2   Overview

This dissertation will be presented in the following manner: The first and present chapter, gives a general introduction towards the occurrence and usefulness of porous media, followed by a motivation and the objectives for the present study.

Chapter 2 gives a general overview of some important characteristics of porous media. (A reader acquainted with the field of porous media may prefer to omit reading this chapter and proceed to Chapter 3.) A classification is given of the different types of porous media to be considered in the present study. An outline of the various transfer processes and flow regimes is also presented. The difficulties involved in solving the Navier-Stokes and continuity equations in a porous medium are addressed and the method of volume averaging is introduced to circumvent these difficulties. The volume averaged equation for the streamwise pressure gradient is simplified up to the point where the introduction of a conceptual geometric pore-scale model is necessary for closure modelling. An overview of

analytical modelling procedures and some conceptual geometric models from the literature are also presented.

In **Chapter 3** a brief outline of the three geometric pore-scale models, resembling granular media, foamlike media and fibre beds, is given, since they form the basis of this study. Different arrays of solid material are introduced for the granular and fibre models and volume partitioning is applied to the fluid domain of all three models. The porous medium parameters that influence the pressure drop, as defined in Chapter 2, are quantified for each model in terms of the respective pore-scale linear dimensions. Relations between the pore-scale linear dimensions of each geometric model and those of models based on cylindrical and spherical geometry are provided through application of the hydraulic diameter. This is necessary to compare the models to others from the literature. A brief discussion is then provided on the controversy about which pore scale linear dimension to use when dealing with foamlike media. Emphasis is also placed on accurately relating the linear dimensions used in the foam model to actual measured values.

Chapter 4 presents a unified analytical closure modelling procedure for the three geometric pore-scale models. Previously, the closure modelling procedures of the three models were presented independently. The streamwise pressure gradient is quantified in two asymptotic limits. In the lower limit two analytical modelling procedures are presented. The first one comprises of minor adaptations to the existing modelling procedures in order to obtain unification whereas the second one is a much shorter and direct modelling procedure. Equations for the streamwise pressure gradient are obtained for each of the three models in each of the two asymptotic limits. A power addition technique is then applied to the equations obtained for the streamwise pressure gradient in the two asymptotic limits in order to obtain a unified equation for each model that is applicable over the entire steady laminar flow regime. Sets of predictive equations for the permeability and passability are also presented. Each set of equations is expressed in terms of the three pore-scale linear dimensions introduced.

In **Chapter 5** a historical overview of the development of the geometric pore-scale models is presented. The granular model is validated against the extensively used semi-empirical Ergun equation and its empirical coefficients are expressed as a function of porosity. In this manner it is illustrated that the granular model serves as a theoretical derivation of the Ergun equation. The predictive equations proposed by the granular model are simplified by application of series expansion and a throwback method. Model predictions are presented for the dynamic specific surface area of ceramic foams, by application of the foam model, and compared to model predictions from the literature. It is shown that the pressure drop prediction, provided by the foam model, serves as a theoretical Ergun-type equation for foamlike media. As in the case of the granular model, the empirical coefficients of an Ergun-type equation for foamlike media are expressed as a function of porosity. The foam model is furthermore used to predict the passability of Aluminium and Mullite foams. A comparison of the pressure drop predictions of the granular and foam models is provided and the discrepancies discussed from a physical point of view. The fibre model is then validated against a number of analytical models and numerical and experimental data from the literature. Model predictions for the Kozeny constant,

provided by the granular and fibre models, are compared with model predictions from the literature based on cylindrical and spherical geometry. The latter models are furthermore used to predict the critical Reynolds number.

In **Chapter 6** the foam model is adapted to account for the effect of developing flow on the pressure drop and permeability through the incorporation of the friction factor-Reynolds number product. It is illustrated that the over-prediction in permeability, observed by previous authors who have worked on the foam model, may be attributed to the effect of developing flow and is not necessarily solely due to lumps of solid material at the intersection of struts. A method is proposed in which the variation in the cross-sectional shape of the fibres is incorporated into the foam model. As a result, a unified semi-empirical equation is proposed for the interstitial form drag coefficient used in the foam model.

Chapter 7 presents an adaptation of the transversely isotropic foam model to an anisotropic structure by the shortening of the strut in the streamwise direction. The anisotropic pore-scale model is used to determine the effect of compression on permeability by adapting the analytical modelling procedure accordingly. Two case studies are considered: In the first case study the foam model is applied to airflow through a non-woven glass fibre filter and in the second case study to a soft polyester fibrous material found in pillows. In the second study the combined effects of compression and developing flow on the pressure drop are investigated.

In **Chapter 8** the permeability predictions of the granular and foam models are adapted to predict the permeability of Fontainebleau sandstone by accounting for the effect of blocked throats at very low porosities. Equations are proposed for determining the percolation threshold porosity of a sandstone sample if the average grain diameter of the sample is known as well as the percolation threshold porosity and grain diameter of another sample. The fibre and granular models are furthermore used to predict the diffusivity ratio of unconsolidated arrays of squares and cubes, respectively, both in which the diffusion process may be regarded as transversely isotropic and in the absence of fluid flow. Numerical results are presented for the diffusivity ratio of two-dimensional staggered and non-staggered arrays of solid rectangles and compared to a weighted average model proposed in the literature. A specific case of a staggered array of solid squares (or cubes), for which this weighted average model is no longer adequate, is outlined and a weighted average model is proposed instead to predict the diffusivity ratio. Lastly, a summary is given of contributions made to the existing geometric pore-scale models by previous authors over the past three decades, with emphasis on the involvement of the author of this dissertation in some of the applications.

In **Chapter 9** the overall contributions of the author of this dissertation to the particular field of study are given as well as future work that may result from this study.

1.3 Publications

Table 1.1 presents the publications accompanying this dissertation in chronological order as the work appears in the subsequent chapters. In all the papers below, the author of this dissertation is the main contributor, irrespective of the order in which the authors' names appear in each publication.

Table 1.1: Published papers resulting from this dissertation.

Relevant chapter	Reference of publication
Chapter 5	Du Plessis, J.P. and **Woudberg, S.** (2008), *Pore-scale derivation of the Ergun equation to enhance its adaptability and generalization*, Chemical Engineering Science, vol. 63, no. 9, pp. 2576-2586.
Chapter 6	**Woudberg, S.** and Du Plessis, J.P. (2010), *An adaptable analytical Ergun-type equation for high porosity spongelike porous media*, in Porous Media and its Applications in Science, Engineering and Industry (Editor: K. Vafai), Proceedings of the Third International Conference on Porous Media and its Applications in Science, Engineering and Industry, Montecatini, Italy, 20-25 June 2010, AIP, New York, pp. 3-8.
Chapter 7	Du Plessis, J.P., **Woudberg, S.** and Le Coq, L. (2010), *Modelling and analysis of permeability of anisotropic compressed non-woven filters*, in Porous Media and its Applications in Science, Engineering and Industry (Editor: K. Vafai), Proceedings of the Third International Conference on Porous Media and its Applications in Science, Engineering and Industry, Montecatini, Italy, 20-25 June 2010, AIP, New York, pp. 272-277.
Chapter 8	**Woudberg, S.** and Du Plessis, J.P., (2008), *Predicting the permeability of very low porosity sandstones*, Transport in Porous Media, vol. 73, pp. 39-55.
	Du Plessis, E., **Woudberg, S.** and Du Plessis, J.P. (2010). *Pore-scale modelling of diffusion in unconsolidated porous structures*, Chemical Engineering Science, vol. 65, no.8, pp. 2541-2551.
	Du Plessis, E. and **Woudberg, S.** (2009), *Modelling of Diffusion in Porous Structures*, in Computational Methods in Multiphase Flow V (Editors: A.A. Mammoli and C.A. Brebbia), Proceedings of the Fifth International Conference on Computational and Experimental Methods in Multiphase and Complex Flow (Multiphase Flow V), New Forest, UK, 15-17 June 2009, WIT Press, UK, pp. 399-408.

Chapter 2

Porous media

2.1 Introduction

In this chapter a general overview of some important characteristics of porous media are presented as well as a classification of the different types of porous media. The different flow regimes, associated with flow in porous media are discussed, after which the flow regimes of relevance to the present study, are specified. The assumptions made are stated, when relevant, throughout this chapter. In this way, the focus of the present study is narrowed down to where it fits into the bigger picture of flow through porous media.

Special attention is given to the pore space since the mathematical description thereof plays an important role in pressure drop and permeability predictions. The hydraulic diameter, as representative average diameter for porous media, is also defined. The microscopic and macroscopic levels are furthermore defined due to their underlying importance in the definition of the average velocities associated with flow through porous media.

The first step in the analytical modelling procedure to obtain model predictions for the pressure drop, permeability and inertial coefficient, is addressed, followed by the difficulties encountered. Thereafter the method to be employed in the present study, to address these difficulties, is described. The equation for the pressure drop prediction is simplified up to the point where the introduction of a conceptual geometric pore-scale model is necessary for closure modelling. An overview of analytical modelling procedures and some conceptual geometric models from the literature are also presented, for comparison in subsequent chapters.

2.2 Classification

Three types of porous media will be considered, namely granular media, foamlike media and fibre beds.

Granular porous media consist of assemblages of "loose" and relatively closely spaced granules. Such an assemblage of closely spaced granules, is referred to as a packed bed. In a packed bed the granules are usually held immobile by contact with each other. The granules need not be spherical and uniform. An example of a granular porous medium is a bed of sand particles or rocks of arbitrary shapes and sizes, as shown in Figure 2.1.

Figure 2.1: Example of a granular porous medium.

A packed bed can also have, for example, pellets or raschig rings as packing material. Granular porous media find application in several separation and filtration processes in which contaminated water or air is filtered through porous beds of sand whilst the impure solid particles are retained. Granular porous media also find application in chemical packed bed reactors and in thermal energy storage devices (Peak et al. (2000)).

Foamlike media consist of a network of connected struts (Giani et al. (2005b)). What makes these porous materials so attractive, and superior to granular packed beds, are their high porosity, their low flow resistance yielding a low pressure drop (Moreira & Coury (2004), Lacroix et al. (2007), Edouard et al. (2008)), and their high ratio of solid surfaces with respect to their total volume (Giani et al. (2005a)). Examples of foamlike porous media are metallic foams and ceramic foams. A picture of a metallic foam is shown in Figure 2.2 (p 9).

Foamlike media are often used as fluid distributors in fuel cells (Depois & Mortensen (2005), Crosnier et al. (2006), Gerbaux et al. (2009)) and in filtration devices (Philipse & Schram (1991)). They also serve as catalytic supports (Richardson et al. (2000), Lacroix et al. (2007), Gerbaux et al. (2010)), as heat sinks in several heat exchanger devices (Lu et al. (1998), Bhattacharya et al. (2002), Dietrich et al. (2009)) and for the cooling of high-power electronic components, such as computer chips (Antohe et al. (1997), Giani et al. (2005a), Liu et al. (2006)). They are also placed between the combustor and turbine sections of jet engines to lower the operating temperature in the turbine (Azzi et al. (2007)). The thermal efficiency of the heat transfer device depends on the hydraulic
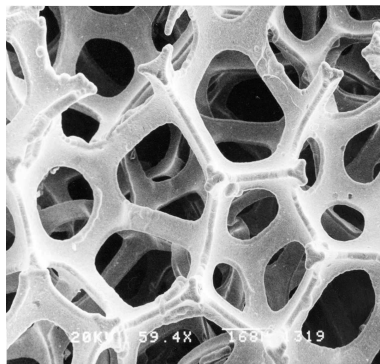
Figure 2.2: Example of a foamlike porous medium. (Picture supplied by prof. G.J.F. Smit.)

properties of the porous material (Antohe et al. (1997)).

Fibre beds consist of assemblages of long, straight, "loose" and relatively closely spaced fibres. The fibres can be parallel with respect to one another or randomly orientated. The former configuration, is also referred to as an unidirectional fibre bed. The flow through the unidirectional fibres is, in turn, classified as flow parallel and flow perpendicular to the fibre axes. In the present study, only flow perpendicular to unidirectional fibre beds is considered. An example of a unidirectional fibre bed is a timber drying stack in a timber drying kiln (Smit et al. (2007)) and banks of heat exchanger tubes (Bergelin et al. (1950), Happel (1959)). Parallel flow through unidirectional fibre beds find application in, for example, cigarette filters, plant stems and in heat exchanger tube banks. Flow perpendicular to unidirectional fibre beds find application in, for example, filters for cleansing liquids and gases, and for regulating their flow (Drummond & Tahir (1984)).

Porous media are also classified as consolidated or unconsolidated (e.g. Adler et al. (1990), Bear & Bachmat (1991)). *Unconsolidated* (or dispersed) porous media have unconnected solid matrices. Granular porous media and fibre beds fall in this category. The granular porous medium shown in Figure 2.1 (p 8) is thus an unconsolidated porous medium. *Consolidated* (or non-dispersed) porous media, on the other hand, have connected solid matrices, and hence, foamlike media fall in this category. The metallic foam shown in Figure 2.2 is therefore a consolidated porous medium.

Randomly orientated fibres may connect at certain points in the microscopic flow domain. These fibres may be curved, and consequently entangled, and are regarded as "without loose ends". Due to the latter characteristics, these types of fibres are classified as consolidated and are referred to as *fibrous media*. Hence, some authors in the literature (e.g. Higdon & Ford (1996)), divide porous media into only two categories, namely granular media and fibrous media. In their classification, foamlike media fall under fibrous media, without any reference made to fibre beds. The same notion is used in the present study, i.e. there will be distinguished between granular media, foamlike media and fibre beds, but the term fibrous media will include both foamlike media and randomly orientated

fibres.

Examples of fibrous media include non-woven fabrics (e.g. Le Coq (2008)), as shown in Figure 2.3, and many materials produced in the pulp and paper industry, e.g. filtration paper (Spielman & Goren (1968), Higdon & Ford (1996)). The properties of fibrous media are also closely related to long entangled polymer chains in solution (Jackson & James (1986), Higdon & Ford (1996)).
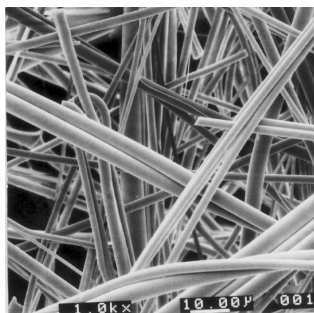
Figure 2.3: Example of a fibrous porous medium. (Picture supplied by prof. L. Le Coq.)

Fibrous porous media find, for example, application in heat exchanger devices, fuel cells and filtration processes (e.g. Kirsch & Fuchs (1967), Le Coq (2008)). A fibrous filter is a device used to remove impure particles present in air or water, which is filtered through filter paper while the impure solid particles are retained. Filtration efficiency of fibrous filters is of major concern for indoor air filtration since high levels of pollutants may have a bad effect on the health of humans. The filtration efficiency is determined by the permeability of the fibrous filters which, in turn, depends on the micro-structural characterization of these porous materials.

2.3 Pore space

The continuous fluid phase within the pore space, which contributes to flow, is known as the inter-connected or *effective pore space* of the porous medium (Scheidegger (1957), Collins (1961)). The pore space that does not contribute to any fluid flow through the porous medium is referred to as the *isolated pore space* and may be considered as part of the solid matrix (Bear (1972)).

Pores that are connected only from one side, are called *dead-end pores* (also "blind" pores or stagnant "pockets"). Although these pores can be penetrated, their contribution to the overall transport through the porous medium is negligible. In sandstone or sintered glass, for example, experiments have indicated that the volume of dead-end pores is less than 1% of the total pore volume (Dullien (1979)). Since the dead-end pores contribute so little to the total pore volume, the effect of their inclusion in the effective pore volume is negligible. Although the dead-end pores are included in experimental measurements of

the pore space, the model to be presented in the present study will not take any dead-end pores into account. It will, however, take inter-connected stagnant pores into account, i.e. pores connected from more than one side and in which no fluid flow occurs. Thus, whenever reference is made in this study to the pore space, it is understood to be the effective pore space, excluding the dead-end pores and isolated pore space but including the inter-connected stagnant pores.

Generally, unconsolidated porous media are composed of granules of different sizes, also called poly-dispersed media (Kaviany (1995)). In consolidated media, on the other hand, the pore space vary in cross-section. Several authors (e.g. Pettijohn et al. (1972), Dullien (1979)) emphasize the complexity of porous micro-structures and the difficulty to characterize the pore-scale geometry by means of an average grain or pore dimension. The pore (or grain) size distribution is defined as the probability density function giving the distribution of pore (or grain) volume by a characteristic pore (or grain) size (Dullien (1979)). By performing a statistical average over the pore size distribution (usually Gaussian (Miwa & Revankar (2011))), the average pore size can be obtained (Kaviany (1995)). Scheidegger (1957) states that it is easier to determine grain size, average grain size and grain size distribution, than pore size, average pore size and pore size distribution. Hence, for granular media the former properties are usually specified to characterize the pore-scale geometry, rather than quantities related to the pores.

Sieve analysis is a common procedure used to determine grain size distributions (e.g. Bear (1972), Pettijohn et al. (1972)). The sieve apparatus consists of a column of layered sieves of different size openings. Each lower sieve in the column has smaller sieve openings than the one above it. A mechanical shaker is used to shake the column and each sieve collects the particles of its specified size of openings. The weight of the particles on each sieve is then recorded and expressed as a fraction of the total weight of particles.

For consolidated media, information regarding the pore size is required to characterize the pore-scale geometry. As opposed to the relatively simple experimentally measured grain size distribution in the case of granular media, estimation of the pore size distribution rely on more advanced measuring techniques and, in addition, depend on both the experimental method and the use of a pore-scale model (Dullien (1979)).

Several methods have been proposed in the literature for measuring pore size and pore size distributions. These methods are classified as direct and indirect methods. The older direct methods include the methods of mercury intrusion porosimetry, gas expansion and liquid displacement (e.g. Nakao (1994), Sakai (1994), Lee et al. (1997), Safinia et al. (2006)).

In mercury porosimetry the pore volume of the sample is measured by intrusion of mercury at high pressures into the porous medium through the use of a porosimeter. Due to the non-wetting properties of mercury, a porous sample can be immersed in it without entry of mercury into the sample at atmospheric pressure. The pore volume is determined by measuring the volume of mercury injected through the sample as the hydrostatic pressure of mercury is increased. The pore-size distribution can be determined from the intrusion volume-pressure curve together with a geometric model. According to Innocentini et al.

(1999), mercury porosimetry is not suitable for highly porous materials such as metallic foams, i.e. of pores with radii $\geq 100\,\mu\mathrm{m}$ (Montillet et al. (1992)).

In the gas expansion method a sample of known bulk volume is enclosed in a container of known volume. This container is connected to an evacuated container of known volume. The pressure is increased and the pressure difference is measured from which the pore volume can be determined by application of the ideal gas law.

In the method of liquid displacement, the pores of the porous medium are initially filled with a liquid after which the liquid is displaced by a gas or another immiscible liquid.

Due to the high pressures involved in the latter methods, the samples are subject to destruction (Safinia et al. (2006)). Nowadays, more advanced techniques are available to determine pore size and pore size distributions, such as image analysis (Philipse & Schram (1991), Richardson et al. (2000), Incera Garrido et al. (2008)). Such non-destructive direct methods include scanning electron and/or light microscopy (e.g. Buciuman & Kraushaar-Czarnetzki (2003), Lacroix et al. (2007)), X-ray computed tomography (e.g. Farber et al. (2003), Taud et al. (2005)) and Magnetic Resonance Imaging (Philipse & Schram (1991)).

In Scanning Electron Microscopy (abbreviated SEM) a scanning electron microscope is used to obtain a two-dimensional image of a cross-section of the porous medium. An electron beam is used to visualize the sample by extracting information of the interactions of the electrons with the specimen. The area of an individual pore is converted into that of an equivalent circle. The diameter of the equivalent circle then serves as the pore diameter (Miwa & Revankar (2011)).

In light microscopy light is used instead of electrons. A much larger magnification can however be obtained from electron microscopy. Image processing and analysis together with the use of a pore-scale model yields a reconstructed three-dimensional structure.

In X-ray computed tomography, X-ray images are used to reconstruct a three-dimensional pore structure by making use of electromagnetic radiation attenuation by matter (Innocentini et al. (1999)) and a mathematical algorithm.

In Magnetic Resonance Imaging (abbreviated MRI) a magnetic field and radio waves are used to create detailed images of internal structures. It, however, has a limited resolution compared to X-ray computed tomography (Philipse & Schram (1991)) due to large signal to noise ratios.

Indirect methods, on the other hand, involve the use of empirical equations, such as Darcy's law, which can be used to obtain average pore sizes, from experimental permeability data (Sakai (1994)). The latter method is referred to as permeametry (Montillet et al. (1992)). Such indirect methods are not desirable, if the objective is to determine the permeability or pressure drop by using an independently determined value for the relevant pore-scale linear dimension. Hence, for validation of the pore-scale models, to be presented in this study, the pore-scale linear dimensions, whether it is the grain size or pore size, should be inferred from one of the direct experimental methods.

2.4   Microscopic versus macroscopic media

The term, *microscopic*, refers to parameters and equations applicable at the pore-level. These parameters will also be referred to as interstitial parameters, since they describe the interstitial properties within the porous domain. The term, *macroscopic*, refers to parameters obtained by averaging the microscopic parameters over a statistically representative portion of the porous domain.

Although the present study is aimed at understanding the fluid-solid interaction at pore level, knowledge and measurements of microscopic parameters are impractical for scientists and engineers in industry whose primary focus is the optimization of large scale production processes, such as chemical reactors. The first step in the analytical modelling procedure is thus to relate the microscopic parameters to measurable macroscopic parameters. The macroscopic parameters allow for the transformation of microscopic equations into macroscopic equations.

The continuum approach will be adopted in which the discontinuous nature of the fluid molecules at the molecular level can be disregarded. This implies that the length scales at the pore level, are assumed to be much larger than the size of the molecules and their mean free path (Dagan (1989)).

2.5   Homogeneous versus inhomogeneous media

Whitaker (1969) and Kim et al. (1987) state that there exist no real homogeneous and isotropic porous media. The latter two assumptions, however, help to make the physical flow processes amenable to mathematical analysis.

A porous medium is described as homogeneous with respect to a macroscopic parameter if that property is invariant under coordinate translation (e.g. Whitaker (1969), Dullien (1979), Kim et al. (1987), Adler et al. (1990), Bear & Bachmat (1991)). It is important to note that the macroscopic parameter should be measured over a statistically representative portion of the porous domain. If the size of this measuring volume remains unchanged and the volume is translated across the porous medium in an arbitrary direction along a straight line and the value of the macroscopic parameter remains constant, then the porous medium is said to be homogeneous. The direction of translation is not fixed and the measuring volume may contain non-uniform particles. If a porous medium is not homogeneous, it is inhomogeneous or heterogeneous.

For the present study the following assumption is made:

Assumption 2-1 : The porosity of the porous medium is uniform.

2.6   Isotropic versus anisotropic media

A porous medium is described as isotropic at a point with respect to a macroscopic parameter, if that property is invariant under coordinate rotation (e.g. Dullien (1979), Kim et al. (1987), Bear & Bachmat (1991)). This simply means that if the flow, with respect to any given point in the porous medium, is the same in all directions then the porous medium is isotropic. If the porous medium is not isotropic, it is anisotropic.

The term *randomness* or *disordered packing* is often associated with isotropy. The contrary is also true, i.e. an *ordered packing* refers to anisotropy (Collins (1961), Dullien (1979)). When particles are placed in an ordered array and staggered in a certain direction, then there will be at least one direction in which no staggering occurs, resulting in anisotropy. This will be illustrated in the present study for an array of cubic particles.

Periodicity relates to an ordered array, rather than randomness, and is therefore associated with anisotropy. Some authors in the literature (e.g. Kaviany (1995)), however, tend to disagree and associate periodicity with isotropy.

For the present study the following assumption is made regarding isotropy:

Assumption 2-2 : The porous medium is isotropic.

2.7   Transfer processes

The transfer processes common to transport in porous media, and fluid flow in general, include momentum transfer, mass transfer and energy transfer. Momentum transfer occurs due to a velocity gradient, mass transfer due to a concentration gradient and energy transfer due to a temperature gradient. The conservation of the three entities, i.e. momentum, mass and energy, can be described by the respective conservation equations and corresponding physical laws, also known as constitutive equations (Kaviany (1995)). The constitutive equations of relevance to the present study are formulated in Appendix A.1 (p 279).

The mechanisms of flow in porous media include hydrodynamic dispersion, which is a result of both mechanical (or convective) dispersion and molecular diffusion (e.g. Whitaker (1969)). Hydrodynamic dispersion is also referred to as miscible displacement or the mixing of fluids (Dullien (1979)). Mechanical dispersion leads to the spreading of any initially close group of tracer particles through the porous medium as a direct result of the movement of the fluid (Bear & Bachmat (1991)). Tracer particles do not interact among themselves (Dagan (1989)) and do not affect the physical flow properties or the kinetic behaviour of the fluid. Molecular diffusion may be regarded as hydrodynamic dispersion in the absence of convection and results from variations in tracer concentration within the fluid phase (Bear (1972), Dullien (1979)).

14

Other thermodynamic flow mechanisms occurring in porous media are electrical conduction and adsorption. The latter occurs at the fluid-solid interfaces because of a lack of thermodynamic equilibrium between a gas or vapor and the solid surfaces in contact with it. As a result, the gas molecules accumulate at the fluid-solid interfaces until equilibrium is reached (Scheidegger (1957), Dullien (1979)). The surface absorption is called adsorption (Kaviany (1995)).

Fluid flow in porous media can involve single or two-phase flow (e.g. the fluid phase consists of both liquid and gas). In two-phase flow in porous media interfacial tension and capillary pressure between the immiscible fluids have to be taken into consideration (Collins (1961), Happel & Brenner (1965), Bear (1972), Kaviany (1995)).

Given the above-mentioned transfer processes and flow mechanisms in porous media, the following assumption refines the scope of the present study:

Assumption 2-3 : Only isothermal, single phase flow of a chemically and electrically inactive viscous fluid is considered.

Since two-phase flow will not be considered, the affects of interfacial tension and capillary pressure need not be accounted for. Adsorption and chemical reaction at the fluid-solid interfaces are also disregarded.

In addition to the assumption of viscous flow, Assumption 2-4 holds, unless stated otherwise:

Assumption 2-4 : The viscosity of the fluid is uniform.

In order to ensure that all pores are completely filled with fluid, Assumption 2-5 is made:

Assumption 2-5 : The flow domain is fully saturated with fluid.

Only momentum transfer and mass transfer in the form of molecular diffusion will be considered in the present study, but treated independently, i.e. when diffusion is considered the pressure is assumed to be uniform throughout the porous medium. Mass transfer will be limited to the fluid phase itself, i.e. inter-phacial mass transfer will be disregarded. Heat transfer will also be disregarded, which complies with the assumption of isothermal flow conditions.

2.7.1   Secondary effects

Secondary effects in porous media that may influence the physical flow behaviour inside a porous medium, include wall effects (also known as channeling), flow development within

the pores and slip flow. The wall effect, mainly of significance in granular media (Seguin et al. (1998)), is caused by an external surface, i.e. the walls of a container, that create a relatively high porosity near the wall due to the discrepancy between the radii of curvature of the wall and those of the particles (Dullien (1979), Winterberg & Tsotsas (2000)). The larger local porosities near the wall yield a reduction in the flow resistance and consequently result in an increase in local flow velocities in these regions. The wall effect is therefore also referred to as channeling (Jackson & James (1986), Kaviany (1995)). The wall effect is locally negligible if the ratio of the diameter of the container to the average particle diameter is greater than 10 (Dullien (1979)).

Hydrodynamically developing flow occurs in the entrance region of pores and results from the development of the velocity boundary layer from its initial profile at the pore entrance to the invariant form downstream. The developing velocity boundary layer is a direct result of the viscous behaviour of the fluid and the geometry of the pore structure (Shah & London (1978)).

Slip flow occurs at low gas pressures and small pore sizes and results in a non-zero velocity at the pore walls. Under these conditions the mean free path of the gas molecules are of the same order as the pore size (Kaviany (1995)). This may lead to higher gas permeabilities than liquid permeabilities.

For wall effects to be neglected in the present study Assumption 2-6 is introduced, i.e.

Assumption 2-6 : The porous medium is unbounded.

Regarding flow development, Assumption 2-7 is made:

Assumption 2-7 : The flow is fully developed.

Assumption 2-7 will be applicable in Chapters 4 and 5 after which the assumption will be relaxed in Chapters 6 and 7 when hydrodynamically developing flow is considered.

The boundary condition at the pore walls is given by Assumption 2-8:

Assumption 2-8 : A no-slip boundary condition applies.

Slip flow will therefore be disregarded.

2.8 Parameters

The pressure drop prediction, for example, over a porous medium is influenced by macroscopic parameters such as the porosity, permeability, specific surface area (or pore-scale

linear dimension, e.g. particle size distribution) and the flow regime. It is also influenced (although to a lesser degree) by particle shape, particle roughness and manner of packing (Happel & Brenner (1965)).

2.8.1 Porosity

The *porosity*, ϵ, of a porous medium (also known as the void fraction, or simply voidage (Dullien (1979))), is defined as the volume fraction of the porous sample that is occupied by the effective pore space (Section 2.3, p 10). The porosity is thus a macroscopic parameter and is also referred to in the literature as the effective porosity. The porosity may be expressed either as a fraction between 0 and 1 or as a percentage. The former notation will be used in the present study. Sandstones, for example, may have porosities as low as 0.1, whereas fibrous media, at the other extreme, may have porosities above 0.9.

The porosity of a porous medium may depend on the mode of packing, particle shape, the grain size distribution in the case of unconsolidated media, but also on the ratio of particle to container diameter (Collins (1961)). For granular media of non-uniform grain size, the smaller particles tend to fill the pores formed between the larger particles, thus reducing the porosity. For packed beds of uniform spheres, on the other hand, the porosity depends on the mode of packing, but is independent of the radius of the spheres (Scheidegger (1957)). The porosity ranges reported for packed beds of uniform spheres vary considerably. The loosest packing yields a porosity of 0.476, while the most compact packing yields a porosity of 0.2595 (e.g. Collins (1961), Happel & Brenner (1965), Bear (1972), Kaviany (1995)). All other arrangements of beds of uniform spheres have porosities falling between these two limits. Dullien (1979), however, reports the range as $0.36 \leq \epsilon \leq 0.44$ and Kaviany (1995) gives the range as $0.37 \leq \epsilon \leq 0.43$. Kaviany (1995) provides a table with porosity values of a wide variety of porous materials.

If the porosity of a porous medium is uniform, then the porous medium is homogeneous (Bear & Bachmat (1991)).

The porosity of fibrous media, and specifically metallic foams fall in the range $0.6 - 0.95$ (Edouard et al. (2008)). Giani et al. (2005b) gives the range as $0.8 - 0.97$. These highly porous materials are therefore characterized by the Solid Volume Fraction (abbreviated SVF) rather than by porosity. The SVF, ϕ, is defined as

$$\phi \equiv 1 - \epsilon \,. \tag{2.1}$$

Porosity can be determined experimentally by simply weighing a known volume of the porous medium, then saturating it with water and re-weighing it (Kim et al. (1987)). Otherwise the same techniques as used to measure pore-size distributions (Section 2.3) are utilized. According to the results of Farber et al. (2003), the method of mercury intrusion porosimetry yields more accurate estimates for porosity, than X-ray computed tomography. An advantage of the latter technique, however, is that it provides a more detailed description of the actual material regarding pore shape, pore size, pore inter-connectivity

as well as the internal layout of the porous medium. This information cannot be obtained through mercury porosimetry and the gas expansion method (Farber et al. (2003)). Safinia et al. (2006) describes the method of X-ray tomography as the "most superior technique" for measuring porosities. The porosity estimates obtained from the X-ray computed tomography method is at least as accurate as the resolution of the instrument (i.e. several micrometers).

2.8.2 Permeability

The *hydrodynamic permeability* (also hydraulic conductivity (Pettijohn et al. (1972)) or intrinsic conductivity (Dagan (1989)) is a measure of the ability of a porous medium to transmit fluid through it (Bear (1972)). It is a macroscopic parameter which, for a Newtonian fluid (Appendix A.1, p 279), is dependent solely on the pore-scale geometry (Collins (1961), Dullien (1979), Dagan (1989)). It is thus independent of both fluid properties and flow mechanisms. The hydrodynamic permeability, or simply permeability, k (for isotropic media), is defined by Darcy's law (e.g. Adler et al. (1990)), which may be expressed in vector form, as

$$\underline{q} = -\frac{k}{\mu}\nabla P \; , \tag{2.2}$$

where $\underline{q} = (Q/A)\,\widehat{\underline{n}}$ is known as the superficial velocity, Darcy velocity, filter velocity (e.g. Scheidegger (1957)) or specific discharge (e.g. Bear (1972)). The parameter, Q, denotes the volumetric flow rate, i.e. the discharge through the cross-sectional area A, normal to the macroscopic flow direction, $\widehat{\underline{n}}$. The dynamic viscosity of the traversing Newtonian fluid is denoted by μ and P is defined as

$$P = p + \rho\,g\,z \; , \tag{2.3}$$

with p the static pressure and the term, $\rho\,g\,z$, the hydrostatic pressure (Shaughnessy Jr. et al. (2005)). The elevation head, z, is the distance measured vertically from an arbitrarily chosen reference level, ρ is the fluid density and g is the magnitude of the gravitational acceleration, which is assumed to remain constant with variations in z. For horizontal flow and relatively small values of z, the gravitational term may be neglected (Collins (1961)).

Since the effect of gravitation will be assumed to be negligible in the present study, Darcy's law in scalar form may be expressed as

$$q = \frac{k}{\mu}\frac{\Delta p}{L} \; , \tag{2.4}$$

where q denotes the magnitude of the superficial velocity and Δp is the pressure drop over a bed length L in the macroscopic flow direction of the porous medium. For discharge in

the x-direction of a rectangular Cartesian coordinate system, Darcy's law can be expressed as

$$q = -\frac{k}{\mu}\frac{\mathrm{d}p}{\mathrm{d}x} \ , \tag{2.5}$$

with $\mathrm{d}p/\mathrm{d}x$ the pressure drop in the macroscopic flow (x-) direction.

For an isotropic porous medium, as described in Section 2.6 (p 14), the permeability is the same in all directions.

2.8.3 Passability

Similarly to the permeability at low Reynolds numbers, the passability (Gerbaux et al. (2009)), η, is defined for higher Reynolds numbers as

$$\eta \equiv \frac{\rho \, q^2}{-\frac{\mathrm{d}p}{\mathrm{d}x}\Big|_{Re\gg1}} \ . \tag{2.6}$$

The passability is thus a type of inertial coefficient.

2.8.4 Tortuosity

Tortuosity is a measure of the tortuousness of flow provided by the pore structure. Dullien (1979) states that the tortuosity measures the deviation from the macroscopic flow direction of the fluid at every point. The concept of tortuosity was introduced by Carman (1937) as a correction to his calculated permeability in order to obtain agreement with experimental permeability values. The tortuosity, T, for isotropic media, may be defined as

$$T \equiv \left(\frac{L_e}{L}\right)^2 \ , \tag{2.7}$$

where L is the displacement in the average flow direction and L_e is the effective average path length (e.g. Adler et al. (1990)). The tortuosity is thus (according to equation (2.7)) a dimensionless quantity greater than unity.

Various other definitions have been used in the literature for tortuosity (e.g. Bear (1972), Clennel (1997)). Bear (1972) defines the tortuosity as the inverse of equation (2.7) in which he defines L_e as the average length of the steamlines in the pore space. According to the definition of Bear (1972), the tortuosity is a scalar quantity less than unity. Diedericks (1999) and Cloete (2006) provided brief discussions on the fair amount of ambiguity accompanying the phrase "effective average path length" associated by some authors with the length L_e. If the average of the pathlines is determined, then the tortuosity is

a purely geometrical concept but if the average of the streamlines is determined, then it becomes a kinematical concept.

Another definition used in the literature for tortuosity, is L_e/L (Scheidegger (1957), Epstein (1989)). According to Bear (1972), the latter definition is a mistake since the effect of tortuosity was introduced by Carman (1937) in two ways, hence leading to the square in equation (2.7): Firstly, the winding flow path, as a result of the geometry of the porous medium, is accounted for and secondly the effect of the tortuous flow path on the superficial velocity. If a suitable geometric model is used to determine the effective average path length, L_e, then L_e/L (i.e. without the square) is referred to as a *geometrical tortuosity* (Bear (1972)). The geometrical tortuosity is, however, independent of the fluid and fluid mechanical properties. Bear (1972) states that L_e/L fails to take into account the effect of tortuosity on the average velocity. The square in equation (2.7) thus accounts for both the structural and fluid mechanical properties and is therefore referred to as a *kinematical tortuosity* (Scheidegger (1957)).

The tortuosity, as it will be defined in the present study, will be introduced in Chapter 3, when the pore-scale models are introduced.

Besides predicting hydrodynamic fluid flow behaviour, such as pressure drop and permeability, the tortuosity may be used to predict the effective diffusivity. This will be addressed in Chapter 8. Diedericks & Du Plessis (1996) have furthermore used the tortuosity to predict the formation factor, of relevance in electrical conduction.

2.8.5   Pore-scale linear dimensions

The relation between different pore-scale linear dimensions used in different geometric pore-scale models and their relation to experimentally measured values of the actual material is important as it affects the accuracy of pressure drop and permeability predictions. Due to the large variations in particle and pore diameters usually observed, average diameters such as the hydraulic diameter are often used. The *hydraulic diameter*, D_h, was initially introduced for conduit flow and defined as four times the hydraulic radius, R_h, i.e. (Happel & Brenner (1965))

$$
\begin{aligned}
D_h &\equiv 4\,R_h \\
&= \frac{4 \times \text{cross-sectional area available for flow}}{\text{wetted perimeter}}.
\end{aligned}
\tag{2.8}
$$

For flow through a porous medium the hydraulic diameter can be expressed as (Whitaker (1969))

$$
\begin{aligned}
D_h &= \frac{4 \times \text{volume available for flow}}{\text{wetted surface}} \\
&= \frac{4 \times \text{volume of pores/volume of porous medium}}{\text{wetted surface/volume of porous medium}}
\end{aligned}
$$

20

$$= \frac{4\,\epsilon\,V_o}{A_s} \tag{2.9}$$

$$= \frac{4\,\epsilon\,V_s}{A_s\,(1-\epsilon)}\,, \tag{2.10}$$

where V_o denotes the volume of the porous medium, and V_s and A_s, respectively denotes the total volume and total surface area of the solid phase. Equation (2.10) thus represents an average diameter for the exceedingly complicated pore-scale geometry of a porous medium (Bear (1972)).

For granular porous media consisting of non-uniform particles an average particle diameter, also known as the effective or *equivalent particle diameter*, D_s, is defined as (Whitaker (1969), Dullien (1979))

$$D_s \;\equiv\; \frac{6\,V_s}{A_s}\,. \tag{2.11}$$

The numerical value in the numerator of equation (2.11) was chosen such that for a bed of uniform spheres D_s will be equal to the spherical diameter. Let $D_s = D_h = 4R_h$. It then follows from equations (2.10) and (2.11) that the hydraulic radius for porous media can be expressed as

$$R_h \;=\; \frac{\epsilon\,D_h}{6\,(1-\epsilon)}\,, \tag{2.12}$$

or

$$D_h \;=\; \frac{6\,(1-\epsilon)\,R_h}{\epsilon}\,. \tag{2.13}$$

The hydraulic diameter and radius become important in the comparison of different geometric models from the literature. The equations have to be expressed in terms of the same pore-scale linear dimension to make direct comparison possible.

2.8.6 Specific surface areas

The specific surface is a measure of the adsorption capacity of the porous medium from the fluid flowing through it. It is related to the permeability of porous media (Collins (1961), Dullien (1979)). The specific surface is of special interest in foamlike porous media due to its high surface area that enhances heat and mass transfer. The specific surface plays an important role in a variety of porous media applications, e.g. in the design of filter columns and reactor columns, as the surfaces contribute to the momentum, heat and mass transfer in the porous medium (Montillet et al. (1992)).

The most general definition of the specific surface of a porous medium is the average interface area per unit volume (Adler et al. (1990)). The unit volume can either be the total volume of the porous medium, V_o, the total volume of the solid phase, V_s, or the total volume of the pore space, V_p (Bear (1972)). The *dynamic specific surface*, A_{vd}, i.e.

the specific surface measured with respect to the total volume of the porous medium, was originally defined for unconsolidated media as (e.g. Sabiri & Comiti (1995))

$$A_{vd} \equiv \frac{A_s}{V_o} \; . \tag{2.14}$$

Comiti & Renaud (1989) defined the dynamic specific surface in terms of the *area presented by the particles to the flow* whereas in equation (2.14) the *total solid surface area* is considered. The *static specific surface* measured with respect to the total volume of the solid phase, A_{vs}, is defined as

$$A_{vs} \equiv \frac{A_s}{V_s} \; . \tag{2.15}$$

The equivalent particle diameter, D_s, (equation (2.11)) can be expressed in terms of the static specific surface, i.e.

$$D_s = \frac{6}{A_{vs}} \; . \tag{2.16}$$

The specific surface with respect to the total volume of the pore space, A_{vp}, is defined as

$$A_{vp} \equiv \frac{A_s}{V_p} \; , \tag{2.17}$$

with V_p the total volume of the pore space.

Mercury porosimetry, gas adsorption methods (referred to as BET methods), X-ray computed tomography, SEM, MRI and permeametry are commonly used to determine specific surface areas (e.g. Joy (1953), Philipse & Schram (1991), Montillet et al. (1992), Santamarina et al. (2002), Buciuman & Kraushaar-Czarnetzki (2003), Große et al. (2008), Incera Garrido et al. (2008), Dietrich et al. (2009)). (The abbreviation "BET" refers to the first initials of the family names of the three people who introduced the theory (Dukhan & Patel (2008)).) The surface area is obtained from the relationship between the applied pressure and volume of gas (or liquid) absorbed.

Philipse & Schram (1991) and Montillet et al. (1992) state that the BET method is much more accurate than the method of mercury porosimtery, since the former method, as opposed to the latter, takes surface roughness into account. Permeametry measurements, on the other hand, has the advantage of being much simpler to carry out.

Bear (1972) and Montillet et al. (1992) emphasize the fact that the values obtained for specific surface areas, depend on the measuring technique used, as each method has its own margin of uncertainty. Bear (1972) recommends that the definition of surface area and the method of measurement should be chosen according to the particular problem at hand.

2.9 Flow regimes

Flow is mainly classified as either *laminar* or *turbulent*. In laminar flow the local velocities are free from macroscopic fluctuations. In laminar flow the streamlines are separate from one another (Pettijohn et al. (1972)). In steady (i.e. time-independent) laminar flow the velocities at fixed points within the flow domain remain constant, but velocities may be different at different points. In steady fully developed laminar flow the velocity distribution at a pore cross-section remains invariant along the axial pore distance with no velocity components in the normal direction (i.e. for two-dimensional flow) (Bear (1972)). Turbulent flow is associated with time-dependent random fluid motion. In turbulent flow the streamlines are intertwined and continuously changing with time (Pettijohn et al. (1972)).

The different flow regimes are often classified with aid of the Reynolds number. The Reynolds number is defined as the ratio of inertial forces to viscous forces (Bear (1972)). The sum of the viscous and inertial forces yields the total flow resistance (Kaviany (1995)). The *inertial forces* are associated with acceleration or deceleration of fluid particles and the *viscous forces* result from the shearing motions of the fluid (Happel & Brenner (1965)). The *Reynolds number*, Re, is thus a dimensionless quantity and was originally introduced for the classification of flow regimes in conduit flow. By analogy, the Reynolds number for flow through porous media may be defined as (Bear (1972))

$$Re \equiv \frac{\rho \, q \, l}{\mu} \, , \tag{2.18}$$

with l being a pore-scale linear dimension. In this definition, both ρ and μ are assumed to be uniform. For flow in conduits the length l will be a channel diameter. For flow through granular porous media an average granular diameter is usually employed whereas for foamlike media an average pore diameter is used (Bear (1972), Philipse & Schram (1991), Xu et al. (2008)). Due to difficulties in measuring an average pore diameter, Collins (1961) proposed $\sqrt{k/\epsilon}$ as a measure of pore diameter, whereas Boomsma & Poulikakos (2002), Depois & Mortensen (2005) and Xu et al. (2008), amongst others, used $\sqrt{k}$. Dukhan & Patel (2008), on the other hand, used the inverse of the specific surface area as a measure of pore diameter. They argue that the use of $\sqrt{k}$ in the Reynolds number is problematic, since the permeability of a specific sample depends on the velocity range over which it is calculated and permeability is often calculated indirectly from empirical curve fitting of pressure drop data. The specific surface area is, as opposed to $\sqrt{k}$, a purely geometrical parameter.

Darcy's law (Section 2.8.2, p 18) is valid for steady single phase flow of an incompressible (i.e. constant density) Newtonian fluid at low flow rates. A few years after the formulation of Darcy's law in 1856, it was modified by Forchheimer (1901) to account for the non-linear flow behaviour at higher Reynolds numbers (i.e. higher values of q for constant l and μ/ρ). This empirical relation is given by (e.g. Scheidegger (1957), Collins (1961))

$$-\frac{\mathrm{d}p}{\mathrm{d}x} = N \, q + M \, q^2 \, , \tag{2.19}$$

where the coefficients N and M depend on both the fluid and porous medium properties. An alternative form of the Forchheimer equation is given by (e.g. Garrouch & Ali (2001), Moreira & Coury (2004), Edouard et al. (2008))

$$-\frac{\mathrm{d}p}{\mathrm{d}x} \;=\; \frac{\mu}{k_1}\,q \;+\; k_2\,\rho\,q^2 \;, \tag{2.20}$$

where k_1 is the Darcy permeability and k_2 is the non-Darcy flow coefficient (or inertial coefficient). The non-Darcy coefficient is sometimes expressed in terms of the form drag coefficient (Appendix A.3.1, p 281).

An alternative dimensionless number, other than the Reynolds number, is the Forchheimer number (Innocentini et al. (1999b), Garrouch & Ali (2001)), denoted by F_o. The Forchheimer number is also defined as the ratio of inertial forces to viscous forces and can alternatively be used to classify different flow regimes in porous media. The Forchheimer number is expressed in terms of the permeability and is obtained by taking the ratio of the inertial and viscous terms in equation (2.20), i.e.

$$F_o \;=\; \frac{k_2\,\rho\,q^2}{\mu\,q}\,k_1 \;=\; \frac{\rho\,q\,k_1 k_2}{\mu}\;. \tag{2.21}$$

Philipse & Schram (1991) used the product $k_1 k_2$ as an alternative for the characteristic length l in the Reynolds number, which can be obtained from the experimental pressure drop data by application of equation (2.20). They thus worked with the Forchheimer number instead of the Reynolds number.

It is known that the failure of Darcy's law cannot be attributed to turbulence (e.g. Happel & Brenner (1965), Bear (1972), Garrouch & Ali (2001)), since laminar inertial effects precedes turbulence. Experimental evidence shows that actual turbulence occurs at Reynolds numbers of at least one order of magnitude higher than those indicating the onset of inertial effects. (According to Bear (1972), these are also the findings of several other authors in the literature.) Bear (1972) states that the square in equation (2.19) should be attributed to inertial effects rather than to turbulence. He argues that although the pressure drop for turbulence in pipe flow is proportional to the square of the superficial velocity, it is not necessarily the case in porous media. For porous media a quadratic behaviour is also observed for high Reynolds number flow, but cannot necessarily be attributed to turbulence. In addition, the Reynolds number at which the transition takes place between laminar and turbulent flow in pipes is several orders of magnitude higher than in flow through porous media (Philipse & Schram (1991)).

The addition of a third cubic term to equation (2.19) has been suggested in the literature to account for the effect of turbulence in porous media. Experimental data is, however, correlated within experimental error over the entire flow regime by equation (2.19) (Dullien (1979)).

Four different flow regimes have been proposed for flow through porous media (Dybbs & Edwards (1984), Montillet et al. (1992), Bird et al. (2007)):

(1) The *Darcy or creeping flow regime*. This is the steady laminar flow regime where Darcy's law is valid. This regime is also referred to as the low Reynolds number flow regime. The viscous forces are thus predominant over the inertial forces. Low velocity flow occurs for a constant l and μ/ρ.

(2) The *inertial flow regime*. This is the steady laminar flow regime where inertial effects govern the flow. In this regime Darcy's law is no longer valid. Hence, this regime is also referred to as the non-linear steady laminar flow regime. The inertial forces are predominant over the viscous forces. Flow separation occurs, boundary layers become more pronounced and flow recirculation is present on the lee side of solids. High velocity flow occurs for a constant l and μ/ρ.

(3) The *unsteady laminar flow regime* (e.g. Kaviany (1995)). Laminar wake oscillations occur in the pores and vortices form (Dybbs & Edwards (1984)).

(4) The *turbulent flow regime* (e.g. Lage et al. (1997)). In this flow regime the flow is highly unsteady, random and chaotic (Dybbs & Edwards (1984)). According to Montillet et al. (1992) this flow regime is seldom reached in fluid flow experiments involving porous media. Seguin et al. (1998) have observed turbulence in packed beds, but not in synthetic foams.

The classification of the different flow regimes, presented above, leads to Assumption 2-9:

Assumption 2-9 : The flow is steady and laminar.

Consequently, only flow regimes (1) and (2) will be considered in the present study.

The transition between the different flow regimes is continuous and gradual (Bear (1972), Dullien (1979), Seguin et al. (1998)). Collins (1961) owes these gradual transitions to the distribution of pore sizes in porous media. Two critical Reynolds numbers can be defined that indicate the Reynolds number at which the viscous and inertial effects weigh equally. The first critical Reynolds number indicates the transition between the Darcy and inertial flow regimes, and the second indicates the transition between the inertial and turbulent flow regimes.

A direct comparison of proposed values from the literature for the two critical Reynolds numbers is hampered due to the fact that the classification of the flow regimes is by no means exact. An uncertainty factor of 750 is associated with the Reynolds number indicating the transitions (Scheidegger (1957), Dullien (1979)). This large margin of uncertainty may be attributed partly to the nature of the porous medium (Seguin et al. (1998), Philipse & Schram (1991), Depois & Mortensen (2005)), i.e. the difference in pore structure (including the curvature of the pores), surface roughness, particle diameter, porosity, the measuring technique used as well as the criteria used to describe the critical

point of transition between the regimes. However, despite these difficulties, Seguin et al. (1998), present a comparison between proposed values/ranges from various authors for particle and pore Reynolds numbers indicating the onset of fluctuations in packed beds (i.e. the end of the steady laminar flow regime). (Note that the latter definition for the critical point of transition between flow regimes differs from the one presented in this study in which the critical Reynolds number is defined as that Reynolds number at which the two flow regimes contribute equally to the pressure drop.) Seguin et al. (1998) also give an average value of 180 for the pore Reynolds number indicating the end of the steady laminar flow regime in packed beds. At this Reynolds number the inertial effects contribute almost 70% to the pressure drop. Higher pore Reynolds number values indicating the end of the steady laminar flow regime in synthetic foams have also been reported by Seguin et al. (1998). Seguin et al. (1998) (in their second paper) give an average value of 900 for the pore Reynolds number indicating the onset of the turbulent flow regime in packed beds. At this Reynolds number the inertial effects contribute 91% to the pressure drop.

2.10 Analytical modelling procedures from the literature

In most analytical modelling procedures presented in the literature, the common goal throughout is to predict either the pressure drop, permeability, non-Darcy coefficient or the total drag force of the assemblage of particles. In earlier years, only unconsolidated media were considered because of the mathematical complexity created by consolidated porous micro-structures.

Most modelling procedures in the literature attempt to solve the microscopic Navier-Stokes and continuity equations (e.g. Happel & Brenner (1965)), either analytically or numerically. The Navier-Stokes equation is a microscopic equation describing momentum transport in fluid flow. It is obtained by substituting the shear stress, described by a Newtonian fluid, into the momentum transport equation (Appendix A.2, p 280). For incompressible flow the Navier-Stokes and continuity equations are respectively given by

$$\rho \frac{\partial \underline{v}}{\partial t} \,+\, \nabla \cdot (\rho \, \underline{v} \, \underline{v}) \;=\; -\nabla p \,+\, \mu \nabla^2 \underline{v} \,, \tag{2.22}$$

and

$$\nabla \cdot \underline{v} \;=\; 0 \,, \tag{2.23}$$

where $\underline{v}$ denotes the interstitial fluid velocity and p is the interstitial static pressure. The only active forces that are taken into consideration in equation (2.22) are those due to pressure and shear resulting from the fluid's viscosity. The gravitational force is thus assumed negligible.

Solutions to the differential Navier-Stokes equation are subject to the specification of boundary conditions. Boundary conditions for flow in porous media are extremely difficult to specify due to the complex pore-scale geometry. To obtain the pressure drop from the Navier-Stokes equation (i.e. equation (2.22)), requires, in addition, knowledge of the interstitial velocity field. Although the interstitial velocity field can nowadays be measured by the method of particle image velocimetry (Wang & Khalili (2003)), observation and measurement of parameters at the microscopic level, however, remain impractical and undesirable.

In the literature both stochastic and deterministic mathematical techniques, mostly of statistical nature, have been employed to address these difficulties. The stochastic models are associated with random phenomena and space-dependent variables (Dagan (1989)). In the present study only deterministic methods based on the continuum approach will be considered. One such commonly used deterministic method is the modification of the Stokes equations to account for the hydrodynamic resistance imposed by the presence of neighbouring particles. Stokes flow concerns the steady motion of an unbounded incompressible Newtonian fluid with a uniform approaching velocity of magnitude, U, past an isolated stationary sphere of radius a in the creeping flow regime. Based on these assumptions, the Navier-Stokes equation, simplifies by omitting the inertial terms (i.e. the terms on the left hand side of equation (2.22)). The resulting equation is given by

$$\nabla p = \mu \nabla^2 \underline{v} . \tag{2.24}$$

Together with the continuity equation for incompressible flow (i.e. equation (2.23)), these two equations are known as the creeping motion or Stokes equations (Happel & Brenner (1965)). By solving the creeping motion equations, Stokes' law is obtained which gives the drag or flow resistance of a single sphere of radius a in an infinite stream in the creeping flow regime, i.e.

$$\mathcal{F} = 6 \pi \mu a v_\infty , \tag{2.25}$$

where $\mathcal{F}$ is the Stokes drag force and v_∞ is the magnitude of the free stream velocity. Stokes' law was modified by several authors in the literature to account for the hydrodynamic resistance imposed by the presence of neighbouring particles (Dullien (1979)).

Another commonly used deterministic approach, aimed at deriving the laws governing macroscopic variables, is the method of volume averaging, which will be employed in the present study.

2.10.1   Method of volume averaging

In the method of volume averaging, macroscopic variables are obtained by averaging over a statistically representative portion of the porous domain, known as a Representative Elementary Volume (abbreviated REV). An REV is defined as an averaging volume, $\mathcal{U}_o$, of finite extent within the porous domain, consisting of both fluid and solid phases,
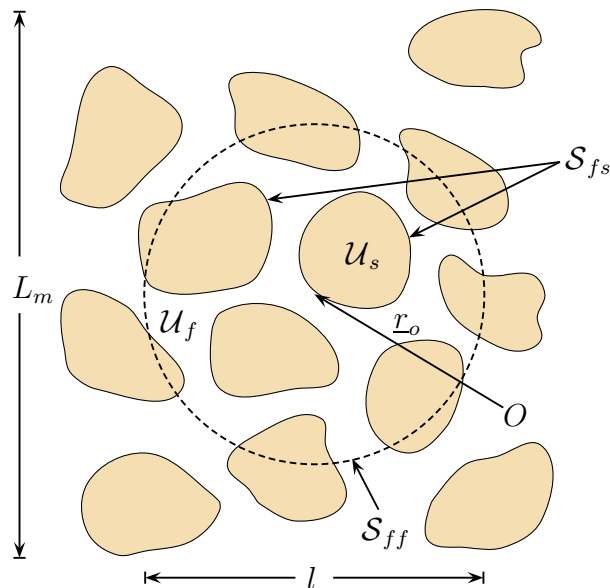
Figure 2.4: A two-dimensional schematic representation of a spherical REV. The dashed circle indicates the REV boundary.

respectively denoted by $\mathcal{U}_f$ and $\mathcal{U}_s$. A two-dimensional schematic representation of a spherical REV is shown in Figure 2.4 for an unconsolidated porous medium. The fluid-solid interfaces within the REV are denoted by $\mathcal{S}_{fs}$ and $\mathcal{S}_{ff}$ represents the fluid-fluid interfaces on the REV boundary.

An REV is defined at every point within the unbounded porous medium. The centroid of each REV is indicated by a position vector, $\underline{r}_o$, relative to some arbitrary origin O, as illustrated in Figure 2.4 for a single REV. Spatial averages can be assigned to every point (within the REV) with respect to the REV centroid. In this manner, fields of macroscopic variables can be obtained as continuously differentiable functions of the space coordinates.

The method of volume averaging is based on the continuum approach and in addition to the continuous fluid phase, the porous medium is considered as being composed of a spatial network of inter-connected pores (Bear (1972)).

Although the shape of the REV is not prescribed, it should remain constant in size and orientation. The size of the REV should be such that small variations in the local volume will not change the values of the local average properties. Any addition of extra surrounding pores and/or solid material should not cause the macroscopic pore structure parameter under consideration, such as the porosity, to fluctuate (Dullien (1979), Kaviany (1995)). The REV should be large with respect to any molecular scale, i.e. the size of the molecules and the mean free path of the molecules, l_m. It should also be small with respect to the macroscopic dimension, L_m, of the porous medium, i.e. $l_m \ll l \ll L_m$.

The porosity, ϵ, of the REV is defined as

$$\epsilon \equiv \frac{\mathcal{U}_f}{\mathcal{U}_o} \ . \tag{2.26}$$

The porosity relates the superficial and intrinsic phase average velocities, as discussed in the next section.

2.10.2   Average velocities

Macroscopic variables, such as average velocities, can be obtained by volume averaging of the interstitial velocity field over an REV. The mathematical formulation of the average velocities presented in this section results from application of the volume averaging theory and identities presented in Appendix B (p 283).

The *superficial velocity*, $\underline{q}$, is defined as the phase average of the interstitial fluid velocity field $\underline{v}$, i.e.

$$\underline{q} \equiv \langle \underline{v} \rangle = \frac{1}{\mathcal{U}_o} \iiint\limits_{\mathcal{U}_f} \underline{v}\,\mathrm{d}\mathcal{U} \,. \tag{2.27}$$

The *intrinsic phase average velocity*, $\underline{u}$, is defined as

$$\underline{u} \equiv \langle \underline{v} \rangle_f = \frac{1}{\mathcal{U}_f} \iiint\limits_{\mathcal{U}_f} \underline{v}\,\mathrm{d}\mathcal{U} \,. \tag{2.28}$$

The relation between the superficial velocity and the intrinsic phase average velocity is given by

$$\underline{q} = \epsilon\,\underline{u} \,. \tag{2.29}$$

Equation (2.29) is known as the Dupuit-Forchheimer relation (Scheidegger (1957), Bear (1972)).

2.10.3   Macroscopic equations

The average velocities, defined in Section 2.10.2, will be used to obtain the macroscopic Navier-Stokes and continuity equations. In addition to the assumption of uniform viscosity, the following assumption is made regarding the fluid properties:

Assumption 2-10 : The flow is incompressible.

The mathematical procedure for volume averaging of the microscopic Navier-Stokes and continuity equations for incompressible flow is presented in Appendix B (p 283). The macroscopic volume averaged continuity and Navier-Stokes equations for incompressible flow is respectively given by

$$\nabla \cdot \underline{q} = 0 \,, \tag{2.30}$$

and

$$-\nabla \langle p \rangle \;=\; \rho \frac{\partial \underline{q}}{\partial t} \;+\; \rho \nabla \cdot \left(\underline{q}\,\underline{q}/\epsilon \right) \;+\; \rho \nabla \cdot \langle \{\underline{v}\}\,\{\underline{v}\} \rangle \;-\; \mu \nabla^2 \underline{q}$$
$$+\; \frac{1}{\mathcal{U}_o} \iint\limits_{\mathcal{S}_{fs}} \left(\underline{n}\,p - \underline{n} \cdot \underline{\underline{\tau}} \right) \mathrm{d}\mathcal{S} \,. \qquad (2.31)$$

In the surface integral of equation (2.31), $\underline{n}$ denotes the inwardly directed (with respect to the solid) unit vector normal to the fluid-solid interfaces and $\underline{\underline{\tau}}$ is the local shear stress tensor. All the terms in equation (2.31) are expressed in terms of macroscopic parameters, except for the momentum dispersion term, i.e. $\rho \nabla \cdot \langle \{\underline{v}\}\,\{\underline{v}\} \rangle$, and the surface integral term. According to Assumption 2-9, the time-dependent term (i.e. the first term) on the right hand side of equation (2.31) falls away.

All the terms containing derivatives of the superficial velocity field as well as the momentum dispersion term, may also be neglected, subject to Assumption 2-11 (Du Plessis & Diedericks (1997)):

Assumption 2-11 : The superficial velocity field and porosity are uniform.

Experimental justification of Assumption 2-11 has been provided by Dybbs & Edwards (1984), provided that wall effects (Section 2.7.1, p 15) are negligible. Since all the macroscopic terms resulting from the interstitial rate of change of momentum, i.e. the terms on the left hand side of equation (2.22), fall away after application of the method of volume averaging and the accompanying assumptions, macroscopic conservation of momentum applies. The streamwise pressure gradient, subject to Assumption 2-11, thus simplifies to

$$-\nabla \langle p \rangle \;=\; \frac{1}{\mathcal{U}_o} \iint\limits_{\mathcal{S}_{fs}} \left(\underline{n}\,p - \underline{n} \cdot \underline{\underline{\tau}} \right) \mathrm{d}\mathcal{S} \,. \qquad (2.32)$$

The surface integral of equation (2.32) still contains microscopic parameters, i.e. the interstitial static pressure, p, and the shear stress dyadic, $\underline{\underline{\tau}}$, of which the latter is a function of the interstitial velocity field, $\underline{v}$. Closure modelling of the interstitial fluid-solid interaction is necessary to express the streamwise pressure gradient in terms of measurable macroscopic parameters. The scientific challenge is thus to quantify the physical interaction between the traversing fluid and the solids in view of the interstitial velocity and pressure differences at the interfacial boundaries. Since this requires knowledge of the pore-scale geometry, a conceptual model is needed to obtain closure. The introduction of a conceptual model makes transport processes in porous media amenable to mathematical analysis.

2.11 Conceptual models from the literature

A conceptual model represents a simplification of the actual complex porous medium geometry. With the aid of a conceptual model the physical transport processes in porous media can be described mathematically. No unique conceptual model exists for a given porous medium (Bear & Bachmat (1991)). The criteria set by Bear (1972) for a conceptual model are the following: The model should be a simplified version but should still incorporate as much as possible of the characteristics of the actual porous medium, without becoming too complicated. The tendency is thus to try and maintain a balance between accuracy and simplicity. Dagan (1989) adds that the model should lead to predicted values of the right order of magnitude.

The conceptual models used in the deterministic modelling procedures available in the literature can broadly be categorized into the *capillary* (or hydraulic radius) *models* and the *drag* (or cell, also submerged object) *models* (e.g. Happel & Brenner (1965), Adler et al. (1990), Kaviany (1995), Bird et al. (2007)).

The models mentioned above are mostly applicable to unconsolidated media because of its relatively simple porous micro-structure compared to consolidated media for which a priori knowledge of the complex pore structure is usually impossible (Dullien (1979)). This is nowadays still substantiated by the numerous theoretical models available in the literature for unconsolidated porous media as opposed to the very few models available for consolidated media.

In addition to capillary and drag models, advanced computerized models are also available that involve three-dimensional numerical reconstruction of real porous samples (Adler et al. (1990), Nabovati et al. (2009)). The three-dimensional fictitious porous media are generated in a random manner, based on statistical approaches, of which the statistical properties are assumed to be the same as the real samples. The method of numerical reconstruction may be more exact than the conceptual models and less expensive compared to experimental imaging techniques (Nabovati et al. (2009)), but requires extensive computational resources.

2.11.1 Capillary models

In the capillary models flow inside conduits is considered. They are therefore also referred to as models based on conduit flow. A packed column, with spherical particles as packing material, is regarded as a bundle or network of tortuous capillary tubes. The capillary tubes may be arbitrarily shaped but are assumed to have a uniform diameter along its entire length. It is furthermore assumed that the random packing of spheres is statistically uniform.

The capillary tube geometry results in the solid phase being regarded as continuous. The hydraulic radius concept is employed in which the hydraulic diameter for tube flow

is adjusted towards an average particle diameter for porous media. The porosity range under consideration is typically that associated with a packed bed, i.e. in the approximate range of $0.3 \leq \epsilon \leq 0.5$.

Most capillary models are semi-empirical. One such model is the extensively used Ergun equation (e.g. Happel & Brenner (1965), Bird et al. (2007)), relating the pressure drop Δp over the column of length L to the magnitude of the superficial velocity, q. A derivation of the Ergun equation is presented in Appendix C (p 286) and is given by

$$\frac{\Delta p}{L} \; = \; 150 \, \frac{(1-\epsilon)^2}{\epsilon^3} \frac{\mu \, q}{D_h^2} \; + \; 1.75 \, \frac{(1-\epsilon)}{\epsilon^3} \frac{\rho \, q^2}{D_h} \; , \qquad (2.33)$$

where D_h is the hydraulic diameter for porous media, as defined by equation (2.13).

The Ergun equation is a direct superposition of two asymptotic limits: a lower laminar limit for modelling flow in the Darcy regime, described by the Blake-Kozeny equation, and an upper limit for modelling, presumably, turbulent flow described by the Burke-Plummer equation. As mentioned in Section 2.9 (p 23), it is well agreed upon in the literature that the failure of Darcy's law cannot be attributed to turbulence. The Blake-Kozeny equation is given by the first term on the right hand side of equation (2.33) and the Burke-Plummer equation by the second term.

Macdonald et al. (1979) performed numerous experiments on flow through packed beds to verify the validity of the Ergun equation. Based on their empirical verification for smooth particles, they proposed coefficient values of 180 and 1.8 for the Ergun equation, instead of the values of 150 and 1.75, as presented in equation (2.33). The empirical verification of Macdonald et al. (1979) is given by

$$\frac{\Delta p}{L} \; = \; 180 \, \frac{(1-\epsilon)^2}{\epsilon^3} \frac{\mu \, q}{D_h^2} \; + \; 1.8 \, \frac{(1-\epsilon)}{\epsilon^3} \frac{\rho \, q^2}{D_h} \; , \qquad (2.34)$$

and is accepted in the literature as an improvement on the Ergun equation.

2.11.2 Drag models

In the drag models a packed column is regarded as a collection of submerged solids acting as obstacles to the fluid flow around them. The porous domain is constructed with the translation of an elementary unit cell, yielding a spatially periodic arrangement of solids immersed in a fluid. The solid obstacles may include geometries other than the spherical shape, i.e. cylinders. The identical unit cells each consist of a single solid surrounded by fluid. The porosity of the cell is assumed to be the same as that of the entire assemblage.

The drag models are much more complex than the capillary models. This is due to the discontinuous nature of the solid matrix used to solve the partial differential transport equations. In most cases these models involve extensions or generalizations of the Stokes

drag (equation (2.25)) to account for the affect of neighbouring solids. The total drag of the system is determined by summing the resistances of the submerged obstacles under the assumption of no solid interaction. For concentrated systems the pressure drop is obtained by dividing the total drag force by the total cell volume. Since creeping flow is usually considered the results are expressed in terms of the permeability rather than the pressure drop.

Happel (1958) proposed a concentric spherical cell model in which the unit cell consists of a single solid sphere surrounded by a fluid envelope. The outside surface of the fluid envelope is assumed to be frictionless, i.e. the tangential stresses are zero. Two adjacent cells will thus have the same velocity at the point where they touch. Hence, the model is also referred to as the free surface cell model. The closer two spherical particles are with respect to each other, the smaller its surrounding fluid envelope becomes and the larger the resistance to its motion. The fluid envelope thus represents the extent of the interaction of the solid with its surroundings. The wall effect is neglected in the modelling procedure and a no-slip boundary condition is assumed at the surface of the solid spheres. The creeping motion equations are solved and the following extension of the Stokes drag (equation (2.25)) is proposed for a dilute suspension (Happel & Brenner (1965)):

$$\mathcal{F} \;=\; 6\,\pi\,\mu\,a\,v_\infty\left[1 + 1.5\,(1-\epsilon)^{1/3}\right]\;, \tag{2.35}$$

where $\mathcal{F}$ denotes the total drag force of the suspension and a is the spherical radius. For concentrated systems the permeability is given by (Happel & Brenner (1965))

$$k \;=\; \frac{2\,a^2}{9\,(1-\epsilon)}\left[\frac{3 - (9/2)(1-\epsilon)^{1/3} + (9/2)(1-\epsilon)^{5/3} - 3\,(1-\epsilon)^2}{3 + 2\,(1-\epsilon)^{5/3}}\right]\;. \tag{2.36}$$

Happel (1959) extended his theory of concentrated assemblages of spheres to arrays of cylinders. In this case, a unit cell is composed of two concentric cylinders. The inner cylinder represents one of the rods in the assemblage and the outer cylinder represents a fluid envelope with a free surface, i.e. with zero shear stress at the boundary. The same assumptions hold as in the case of the concentric spherical cell model. The permeability for unidirectional flow perpendicular to the cylinder axes is given by

$$k \;=\; \frac{a^2}{8\,(1-\epsilon)}\left[-\ln(1-\epsilon) + \frac{(1-\epsilon)^2 - 1}{(1-\epsilon)^2 + 1}\right]\;. \tag{2.37}$$

Hasimoto (1959) also considered flow through periodic arrays of spheres. The unit cell is defined by three linearly independent vectors acting at a corner of the cell. A dilute suspension of spheres is obtained in the form of simple, body-centered and face-centered cubic arrays. Each particle in the array is replaced with a point force retarding the motion of the fluid. The Stokes equations were then modified to include the discontinuous force field by making use of the Dirac delta function. Owing to the periodic arrangement of the particles, he assumed that the velocity fields and pressure gradients are also periodic. The periodicity allowed for the introduction of Fourier series. He assumed furthermore

that the mean velocity over the surface of each spherical particle vanishes and that the wall effect is negligible. The following extension of the Stokes drag (equation (2.25)) was proposed for a dilute system of spheres in a simple cubic array:

$$\mathcal{F} \;=\; 6\,\pi\,\mu\,a\,v_\infty\,\left[1 + 1.7601(1-\epsilon)^{1/3}\right]\;. \tag{2.38}$$

For body-centered and face-centered cubic arrays the coefficient of 1.7601 should be replaced with 1.791. Hasimoto also extended his theory to unidirectional flow perpendicular to square arrays of cylinders. The resulting expression for the permeability is given by

$$k \;=\; \frac{a^2}{8\,(1-\epsilon)}\left[-\ln(1-\epsilon) - 1.476 + 2\,(1-\epsilon) + \mathcal{O}((1-\epsilon)^2)\right]\;. \tag{2.39}$$

Kuwabara (1959) considered the same concentric cylindrical cell model as Happel (1959), but instead of the zero shear stress at the boundary, assumed zero vorticity at the boundary of the fluid envelope. The equation obtained for the permeability is given by

$$k \;=\; \frac{a^2}{8\,(1-\epsilon)}\left[-\ln(1-\epsilon) - \frac{3}{2} + 2\,(1-\epsilon)\right]\;. \tag{2.40}$$

The models and corresponding equations from the literature, presented above, will be used to validate the predictive equations for the pressure drop and permeability to be proposed in Chapter 4.

2.12   Summary

Flow through granular media, foamlike media and fibre beds are considered in the present study. Assumptions made include isothermal, single phase flow of a chemically and electrically inactive viscous fluid. Granular media and fibre beds are referred to as unconsolidated media whereas foamlike media are referred to as consolidated.

The porous medium under consideration is assumed to be homogeneous and isotropic, unless otherwise stated. It is furthermore assumed that the porous medium is unbounded. As a result, wall effects may be neglected. Fully developed flow and a no-slip boundary condition are assumed, unless otherwise stated. The flow is assumed to be steady, laminar, fully saturated, incompressible and Newtonian.

The first step in the analytical modelling procedure is to solve the transport equations, i.e. the Navier-Stokes and continuity equations, for flow through a porous medium. Difficulties involved in specifying the complex boundaries and interstitial velocity field, hampers solutions for the pressure drop prediction. The method of volume averaging is proposed to address this problem by relating the microscopic parameters to measurable macroscopic parameters. By application of the volume averaging procedure the average velocities of

relevance in a porous medium are obtained. It is assumed that the superficial velocity field and porosity are uniform which simplifies the expression for the streamwise pressure gradient to a surface integral representing the fluid-solid interaction. The quantification of the fluid-solid interaction relies on the introduction of a conceptual geometric pore-scale model, which is the subject of the next chapter.

Chapter 3

Representative Unit Cell models

"The first, and, perhaps the most important step in the modelling process is the construction of a conceptual model of the system and of its behaviour."

- Bear & Bachmat (1991)

3.1 Introduction

The conceptual drag model to be used in the present study is the rectangular Representative Unit Cell (abbreviated RUC) model. In this chapter the three RUC models are introduced, i.e. the granular RUC model, the RUC model for foamlike media (or simply the foam RUC model) and the RUC model for unidirectional fibre beds (or simply the fibre RUC model). Different arrays are introduced for the unconsolidated models. The total fluid domain of each RUC model is partitioned into different sub-volumes, depending on the orientation of the particular fluid channel with respect to the streamwise direction.

The porous medium parameters that influence the pressure drop, permeability and inertial coefficient, as defined in Chapter 2, are quantified in terms of the pore-scale linear dimensions of the respective RUC models. Special attention is given to the estimation of the relation between the pore-scale linear dimensions of the respective models as well as their relation to the actual measured values as input parameters. This is important since the permeability, for instance, has a dimension of length squared. For the unconsolidated models, special attention is given to the relation between the pore-scale linear dimensions of the RUC models and the linear dimensions of models based on cylindrical and spherical geometries. These relations will be useful in Chapter 5 when the granular and fibre models are compared to models from the literature based on spherical and cylindrical geometry, respectively. For the foam RUC model a three-dimensional pore diameter is introduced as opposed to the existing two-dimensional cross-sectional pore width. Which one to use in order to obtain model predictions, depends on how the pore diameter is defined and measured experimentally.

3.2 RUC model

The rectangular RUC is defined as the smallest rectangular volume, U_o, into which the average geometrical and physical properties of the REV (as introduced in Section 2.10.1, p 27) can be embedded, e.g. the porosity of the RUC is equal to the porosity of the REV. The geometric pore-scale model is generic in the sense that it takes on three distinct rectangular geometries, namely one for granular media, one for foamlike media and one for fibre beds. The respective RUC models are shown in Figure 3.1. The granular RUC model was initially introduced by Du Plessis & Masliyah (1991), the foam RUC model by Du Plessis & Masliyah (1988) and the fibre RUC model by Du Plessis (1991). In each RUC, the total fluid volume is denoted by U_f and the total volume of the solid phase is denoted by U_s. (The manner in which there will be distinguished between parameters associated with an REV and those of the RUC, is by writing all the parameters associated with an REV in calligraphic font.)

Characteristics shared by two or all three RUC models will be discussed in the first part of this chapter. In subsequent sections the models will be regarded separately and the respective model parameters will be quantified in terms of the linear dimensions of the respective models.

In the granular and fibre RUC models, presented in Figure 3.1, the respective shaded volumes represent the solid phase, whereas in the foam RUC model, the shaded volume represents the fluid phase. Since both the granular and fibre RUC models represent unconsolidated porous media (Section 2.2, p 8), these two RUC models will also be referred to as the unconsolidated models. For the fibre RUC model, only flow perpendicular to the axes of unidirectional fibres will be considered. This type of flow will also be referred to as cross-flow. As a result, the velocity will have no components in the direction parallel to the fibre axis. Hence, flow through the fibre RUC may be regarded as two-dimensional and, consequently, the fibre RUC model may be regarded as the two-dimensional equivalent of the granular model.

The *streamwise direction*, indicated by $\widehat{\underline{n}}$ in Figure 3.1, is defined as the direction of the superficial velocity, i.e.
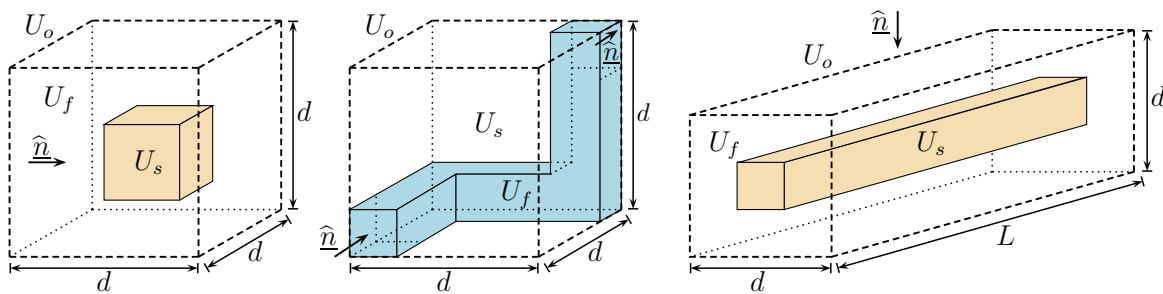
Figure 3.1: RUC model for granular media (*left*), foamlike media (*middle*) and fibre beds (*right*).

37

$$\widehat{\underline{n}} \equiv \frac{\underline{q}}{q} \ . \tag{3.1}$$

The RUCs for granular and foamlike media are cubic with linear dimension d, as shown in Figure 3.1 (p 37). In the case of the fibre RUC model, the cross-section of the RUC, parallel to the streamwise direction is square with linear dimension d. The linear dimension d will be referred to as the *cell size* and may be defined as the average length scale over which similar changes in geometrical and physical properties take place. It typically represents the average solid to solid or pore to pore distance.

The RUCs of the unconsolidated models contain only one solid. The solid resembles the average solid geometry of the corresponding REV. In the granular RUC model the solid is cubic and in the fibre RUC model the solid fibre is rectangular, with a square cross-sectional area parallel to the streamwise direction. In the foam RUC model the three mutually perpendicular square duct sections resemble the average pore geometry of the corresponding REV.

Regarding the solid phase, the following assumption is made:

Assumption 3-1 : The solid material is rigid, smooth, impermeable and stationary.

Deformation of the solid material as well as surface roughness and sedimentary flows, in which the solid phase has a non-zero velocity, may thus be disregarded.

The porosity, ϵ, is defined in RUC notation as

$$\epsilon \equiv \frac{U_f}{U_o} \ . \tag{3.2}$$

In the next section staggering of the solid material in the unconsolidated models with respect to that of neighbouring RUCs will be addressed, which leads to the introduction of different arrays.

3.3 Arrays for unconsolidated models

For the unconsolidated RUC models two arrays are introduced, depending on the relative positioning of the solids in neighbouring RUCs with respect to the streamwise direction. A two-dimensional schematic representation of the arrays, referred to as a *fully staggered array* and a *regular array*, are respectively shown in Figure 3.2(a) and (b) (p 39). The third dimension of the RUCs is assumed to extend into the plane of the paper. The boundaries of a typical RUC are indicated by the bold dashed lines.

(a) Fully staggered array   (b) Regular array
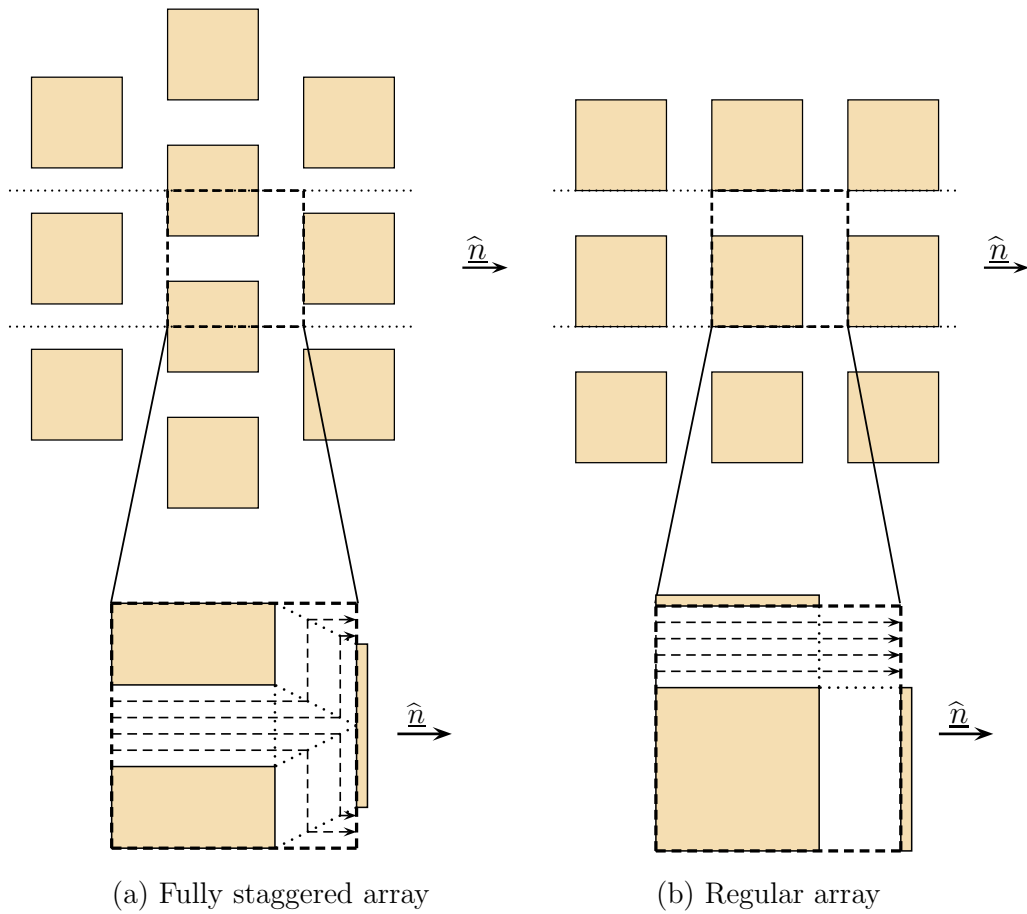
Figure 3.2: A two-dimensional schematic representation of (a) a fully staggered and (b) a regular array.

In a fully staggered array, maximum possible staggering occurs in the streamwise direction, as illustrated schematically in the upper part of Figure 3.2(a). In a regular array no staggering occurs in any of the three principal directions. The condition of no staggering is illustrated two-dimensionally in Figure 3.2(b).

The pair of dotted lines shown for each array in the upper part of Figure 3.2 represent the boundaries of a streamtube, with respect to which the following assumption is made:

Assumption 3-2 : The fluid flows through a streamtube bounding the RUC in the streamwise direction.

As a result of Assumption 3-2 the fluid particles, directly adjacent to the streamtube, have the same streamwise velocity. No fluid exchange thus occurs over the fluid-fluid interfaces of the streamtube in the direction perpendicular to the streamwise direction. Consequently, there will be no fluid flow between adjacent RUCs in the direction perpendicular to the streamwise direction. Assumption 3-2 serves the same role as the frictionless

39

surface of the unit cell models of Happel (1958) and Happel (1959). A shift in position of the streamtube in the direction perpendicular to the streamwise direction will have no effect on the flow, since it does not alter the solid configuration.

The rectangular geometry of the adjacent solid surfaces in the RUC models yields pair-wise sets of equal parallel plates. In respect thereof, the following assumption is made:

Assumption 3-3 : The channel width is uniform.

The uniform channel width yields a parallel plate configuration where two adjacent plates are a uniform distance apart. The parallel alignment of the solid surfaces with that of the streamtube ensures that one of the fluid channels will always be aligned with the streamwise direction, leaving the remaining channel(s) oriented in transverse directions. In the foam RUC model, shown in Figure 3.1 (p 37), flow between double pairs of parallel plates is assumed, whereas in the unconsolidated models flow between a single pair of parallel plates is assumed. The parallel plate geometry allows for the assumption of plane-Poiseuille (or Hagen-Poiseuille) flow in the analytical modelling procedure with the RUC model. The mathematical description thereof will be given in Chapter 4.

In a rectangular Cartesian coordinate system, in which one of the axes corresponds to the streamwise direction, the one (or two) principal directions perpendicular to the streamwise direction will be referred to as the transverse direction(s). Any property referring to the streamwise direction will henceforth be denoted by a subscript $\parallel$ and any property relating to the transverse direction(s) by $\perp$.

The next assumption deals with the fluid flow behaviour through the RUC:

Assumption 3-4 : The fluid enters and exits the RUC in the streamwise direction.

The fluid thus enters the RUC through the upstream normal face (which extends into the paper in Figure 3.2, p 39), and exits the RUC through the corresponding downstream normal face.

Since the two arrays are defined based on staggering of solids with respect to the stream-wise direction, Assumption 3-5 addresses the condition of staggering in the transverse direction(s):

Assumption 3-5 : The solid surfaces parallel to the streamwise direction are aligned in the transverse direction(s).

According to Assumption 3-5 there will thus be no staggering in the transverse direc-tion(s). Assumption 3-5 differs from the model characteristics specified by Diedericks (1999) in which the solids are allowed to have some lateral displacement with respect

to each other in the transverse direction(s). The disadvantage of this model characteristic proposed by Diedericks (1999), although lesser restrictive, is that the assumption of flow between parallel plates is only strictly valid at very low porosities where the lateral displacement is negligible.

3.3.1 Fully staggered array

The following assumption is peculiar to a fully staggered array:

Assumption 3-6 : All pore sections are traversed by the fluid.

According to Assumption 3-6, a fully staggered array contains no stagnant fluid domains. For the RUC shown in Figure 3.2(a) (p 39), the fluid enters the RUC in the streamwise direction, after which the streamwise flux is deviated into pair-wise opposite transverse directions on the lee side of the solid to circumvent the neighbouring downstream solid obstacle providing the maximum possible staggering. According to Assumption 3-4, the fluid exits the RUC and enters the neighbouring RUC in the streamwise direction. After circumventing the downstream solid obstacle the streamwise flux reunites on the lee side of the solid after which the fluid again flows in the streamwise direction and the flow pattern repeats itself.

3.3.2 Regular array

The following assumption is peculiar to a regular array:

Assumption 3-7 : The solids are aligned in all three principal directions.

The fluid thus enters the RUC in the streamwise direction and continues to flow in the streamwise direction without being deviated into a transverse direction. The fluid volumes in the transverse channels between solids of neighbouring RUCs are thus stagnant, which leads to the following assumption:

Assumption 3-8 : The stagnant fluid volumes exclude isolated and dead-end pores, as described in Section 2.3 (p 10).

These stagnant fluid volumes form part of the inter-connected pore space but do not contribute to the momentum transport through the porous medium. The stagnant volumes differ from the dead-end pores in the sense that the stagnant fluid volumes are inter-connected, i.e. connected from more than one side.

Staggering in the consolidated foam model will be addressed in Section 3.15 (p 58).

3.4 Isotropy

Since no random unconsolidated structure will be free from some degree of staggering, a staggered array, as opposed to a non-staggered array, can be associated with isotropy (Section 2.6, p 14), provided that staggering occurs in every direction. As soon as an ordered structure is introduced, as in the case of any array, some degree of periodicity is created. This is the case in a fully staggered array, which is periodic over of a displacement of $2d$, with d being the RUC length as indicated in Figure 3.1 (p 37). This is because the RUC shown in Figure 3.2(a) (p 39) will be reproduced after every second consecutive RUC in the streamwise direction. The RUC has therefore been referred to, by some previous authors who have used the model, as "quasi-periodic". However, the characteristic length associated with the size of the RUC is d and not $2d$.

Whitaker (1969) introduced the term *transversely isotropic* with respect to a given macroscopic property of a square array that is not invariant to arbitrary coordinate rotations about any point, but, indeed invariant to 90° rotations about certain points. The term "transversely isotropic" was also used by Kim et al. (1987). The fully staggered array would thus adhere to Whitaker's definition of transverse isotropy over the cell size d of the RUC, should the same degree of staggering be provided in the other principal direction(s), as in the streamwise direction. This is however not the case, since no staggering occurs in the transverse direction(s), as can be visualized from Figure 3.2(a).

The regular array, as it appears in Figure 3.2(b) (p 39), cannot be regarded as transversely isotropic because it is periodic over the cell size d of the RUC and because no staggering occurs in any of the three principal directions.

The above discussion explains why both the fully staggered and regular arrays of the unconsolidated RUC models cannot be isotropic or even transversely isotropic. In all previous studies regarding the unconsolidated RUC models, the models were assumed to be isotropic with respect to its average geometrical and physical properties. The assumption of alignment of solid surfaces in the transverse direction(s) (i.e. Assumption 3-5) was not made by these authors. The solid surfaces were allowed to overlap in all the principal direction(s), thus providing staggering in all the principal directions, but such an array can, however, not be physically constructed.

It is thus clear that isotropy and even transverse isotropy cannot be justified in the unconsolidated RUC models. As a result thereof, the RUC model cannot be regarded as a building block. It will be illustrated in Chapter 4 that the only manner in which transverse isotropy can be justified in the unconsolidated RUC models is by performing a mathematical weighted average over the equations obtained for a fully staggered and regular array. Although the fibre RUC model is three-dimensionally transversely anisotropic, two-dimensional transverse isotropy will be assumed due to the cross-flow considered.

The foam RUC model, on the other hand, may be regarded as transversely isotropic which may be justified by the presence of a fluid-fluid interface, equal to the channel cross-sectional flow area, on each of the six faces of the RUC. The fluid-fluid interfaces

are assumed to be connected to the square duct sections of neighbouring RUCs to yield the same macroscopic flow properties in each of the three principal flow directions.

3.5   Piece-wise straight streamlines

The parallel plate configuration gives rise to the following assumption:

Assumption 3-9 : Piece-wise straight streamlines are applicable between and parallel to the solid surfaces.

The piece-wise straight streamlines are illustrated two-dimensionally in the enlarged RUCs shown in Figure 3.2 (p 39). The piece-wise straight streamlines illustrate the partitioning of the streamwise flux into pair-wise opposite transverse directions in a fully staggered array as well as the presence of a stagnant fluid domain in a regular array. The stagnant fluid volume in the regular array is characterized by the absence of streamlines in that particular fluid domain since these volumes do not contribute to momentum transport.

3.6   Volume partitioning

The piece-wise straight streamlines allow for the fluid domain within an RUC to be partitioned into different sub-volumes, depending on the orientation of the pairs of parallel solid surfaces, adjacent to the specific sub-volume, with respect to the streamwise direction. A two-dimensional representation of the volume partitioning of the two-dimensional RUCs in Figure 3.2, is shown in Figure 3.3 (p 44).

Although the volume partitioning of the RUC model for foamlike media is not shown, the same definitions for the respective fluid volumes, as given below, are applicable to this model.

The total solid surfaces parallel to the streamwise direction are denoted by $S_\parallel$ and are referred to as the *streamwise surfaces*. The sum of fluid domains between any pair(s) of streamwise surfaces is denoted by $U_\parallel$ and will be referred to as the *streamwise volume*. The total solid surfaces oriented perpendicular to the streamwise direction are denoted by $S_\perp$ and are referred to as the *transverse surfaces*. The sum of fluid domains between any pair(s) of transverse surfaces is denoted by $U_\perp$ and will be referred to as the *transverse volume*. The fluid volume between the pair(s) of solid surfaces oriented perpendicular to the streamwise direction and in which the fluid remains stationary is denoted by U_g and is referred to as the *stagnant volume*. The total solid surfaces adjacent to U_g are denoted by S_g and are referred to as the *stagnant surfaces*. The total fluid volume not subject to any wall shear stresses is denoted by U_t and is referred to as the *transfer volume*. There will thus be no streamwise pressure drop over a transfer volume. As a result, the same

(a) Fully staggered array   (b) Regular array
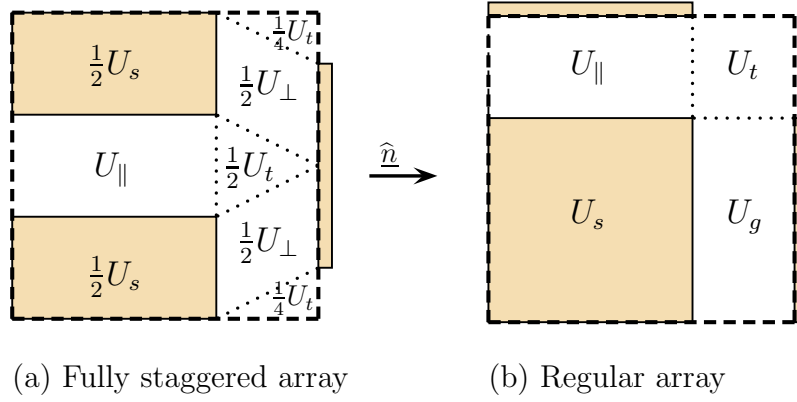
Figure 3.3: A two-dimensional representation of the volume partitioning of the fluid domain within an RUC in (a) a fully staggered and (b) a regular array.

pressure value may be assigned to all points within U_t. A transfer volume simply serves as a transition region between any two of the volumes $U_\parallel$, $U_\perp$ and U_g. The total solid surfaces "facing" the streamwise flux and with normal vector parallel to the streamwise direction are denoted by S_{face}.

The total fluid volume, U_f, within an RUC, may thus be expressed as the sum of the respective sub-volumes, i.e. (Lloyd et al. (2004))

$$U_f = U_\parallel + U_\perp + U_g + U_t . \tag{3.3}$$

For a fully staggered array $U_g = 0$ and for a regular array $U_\perp = 0$. The total fluid-solid interfaces, S_{fs}, within an RUC may similarly be expressed as (Lloyd et al. (2004))

$$S_{fs} = S_\parallel + S_\perp + S_g . \tag{3.4}$$

(Equation (3.4) does not contain a parameter with a subscript t, since the transfer volumes are not bounded by solid surfaces.)

3.7 Streamwise average channel velocity

The *streamwise average channel velocity*, $\underline{w}_\parallel$, was originally introduced by Du Plessis & Masliyah (1988) as a more accurate representation of the average pore velocity than the intrinsic phase average velocity, $\underline{u}$. Diedericks (1999) presented a formal derivation of the streamwise average channel velocity, of which the final result may be expressed as,

$$\underline{w}_\parallel \equiv \frac{1}{U_{f\mathcal{L}}} \iiint\limits_{U_f} \underline{v} \, dU . \tag{3.5}$$

The streamwise average channel velocity determines the average over the effective stream-wise fluid volume, $U_{f\mathcal{L}} = U_{\parallel} + U_t$, in the RUC. In the intrinsic phase average velocity the average was determined over the total fluid volume, U_f.

Let $A_{p_{\parallel}}$ denote the total streamwise cross-sectional flow area available for fluid discharge through the RUC. The relation between the streamwise average channel velocity and the superficial velocity may then be expressed as

$$\underline{w}_{\parallel} \;=\; \frac{\underline{q}\,d^2}{A_{p_{\parallel}}} \,, \tag{3.6}$$

for the granular and foam RUC models and as

$$\underline{w}_{\parallel} \;=\; \frac{\underline{q}\,d\,L}{A_{p_{\parallel}}} \,, \tag{3.7}$$

for the fibre RUC model.

3.8   Coefficient β

The magnitudes of the total cross-sectional areas available for fluid discharge in the streamwise and transverse channels of the RUC may differ. As a result, the magnitude of the streamwise average channel velocity, $w_{\parallel}$, may be different from the magnitude of the transverse average channel velocity, $w_{\perp}$. This difference was accounted for by Lloyd et al. (2004) through the introduction of the coefficient β, defined from flux conservation as

$$\beta \equiv \frac{w_{\perp}}{w_{\parallel}} \;=\; \frac{A_{p_{\parallel}}}{A_{p_{\perp}}} \,, \tag{3.8}$$

where $A_{p_{\perp}}$ denotes the total transverse cross-sectional flow area and $A_{p_{\parallel}}$ is as defined in Section 3.7 (p 44). The value of β will be determined separately for the three RUC models in subsequent sections.

3.9   Geometrical tortuosity χ_{geo}

Du Plessis (1994) defined the *geometrical tortuosity* χ_{geo} (Section 2.8.4, p 19) as the ratio of the average length of the tortuous flow path, d_e, to the streamwise cell size, d, of the RUC, i.e.

$$\chi_{geo} \;\equiv\; \frac{d_e}{d} \,, \qquad \chi_{geo} \geq 1 \tag{3.9}$$

where d_e may be defined as

$$d_e \equiv \frac{U_f'}{A_{p_\parallel}} \; . \tag{3.10}$$

The total fluid volume, U_f', in equation (3.10) excludes any stagnant fluid volumes, since the RUC model, proposed at that time, did not take the presence of any stagnant fluid volumes into account, i.e.

$$\chi_{geo} = \frac{U_f'}{A_{p_\parallel} d} = \frac{U_f}{U_\parallel + U_t} = \frac{U_\parallel + U_t + U_\perp}{U_\parallel + U_t} \; . \tag{3.11}$$

The tortuosity was used to obtain the relation between the streamwise average channel velocity and the superficial velocity, i.e.

$$\underline{w}_\parallel = \frac{\underline{q}\, \chi_{geo}}{\epsilon} \; . \tag{3.12}$$

According to Bear (1972), the definition of the tortuosity, presented in equation (3.9) is erroneous, since it only takes the geometrical aspect into account and not the effect which the tortuous flaw path has on the velocity. In the present study the latter effect is incorporated into the coefficient β.

Du Plessis & Masliyah (1988) defined the tortuosity as the inverse of equation (3.9). The latter ratio, i.e.

$$\mathcal{L} \equiv \frac{d}{d_e} \; , \qquad \mathcal{L} \leq 1 \; . \tag{3.13}$$

was named the *lineality*, $\mathcal{L}$, by Diedericks & Du Plessis (1995). The lineality describes the "straightness" of flow through the porous medium, as opposed to the tortuosity which describes the "non-straightness" of the streamlines.

For each of the three RUC models the geometrical tortuosity, χ_{geo}, will be quantified in terms of porosity. In a subsequent section the tortuosity (i.e. described by equation (3.11)) will be extended to include stagnant fluid volumes, and will be referred to as the geometric factor.

3.10 Coefficient ξ

The coefficient ξ was originally introduced by Lloyd et al. (2004) for flow through two-dimensional prismatic porous domains. The intention was to account for the reduction in the tortuosity due to the splitting of the streamwise flux into two equal but directionally opposite transverse fluxes in a fully staggered array. The coefficient ξ was introduced into

the equation for the tortuosity which then classifies it as a kinematical tortuosity χ_{kin}, i.e.

$$\chi_{kin} \;=\; \frac{U_f'}{A_{p_\parallel} d} \;=\; \frac{U_\parallel + U_t + \xi U_\perp}{U_\parallel + U_t} \;,\tag{3.14}$$

where the total fluid volume, U_f', excludes any stagnant fluid volumes. In the present study the definition of the coefficient ξ will be generalized to be applicable for all three RUC models. The word "splitting" only applies to the two-dimensional fibre model.

The coefficient ξ will, in the present study, be introduced into the models for essentially the same reason as stated above, i.e. to account for the reduced *area* of the transverse surfaces subject to shear stresses due to the division of the streamwise flux into directionally opposite transverse fluxes in the transverse channels of a fully staggered array. The coefficient ξ is formally defined for the present study as:

$$\xi \;=\; \begin{cases} 1 & \text{if the streamwise flux is not divided into pair-wise opposite transverse} \\ & \text{directions in } U_\perp, \\ 2^{-i} & \text{if the streamwise flux is divided into pair-wise opposite transverse} \\ & \text{directions in } U_\perp, \\ 0 & \text{if } U_\perp = 0, \end{cases}$$

where i is the number of symmetry planes normal to the streamwise direction that can be assigned to the RUC. The coefficient ξ is a geometric coefficient since the division of the flux depends on the pore-scale geometry as well as the degree of staggering of the neighbouring solid material. Its introduction into the analytical modelling procedure will be shown in Chapter 4.

3.11 Geometric factor ψ

The *geometric factor*, ψ, was introduced by Lloyd et al. (2004) as an extension of the tortuosity concept to capture the effect of stagnant fluid domains. The geometric factor is defined by the following volumetric ratio:

$$\psi \;\equiv\; \frac{U_f}{U_\parallel + U_t} \;=\; \frac{U_f}{A_{p_\parallel} d} \;=\; \frac{U_\parallel + U_t + U_\perp + U_g}{U_\parallel + U_t} \;,\tag{3.15}$$

where the total fluid volume, U_f, includes the total stagnant fluid volume. The geometric factor is equal to the geometrical tortuosity (equation (3.11)) in the absence of the stagnant fluid volume, U_g. The geometric factor is used to obtain a relation between the streamwise average channel velocity and the superficial velocity. This relation follows from equations (3.6), (3.7) and (3.15) and is given by

$$\underline{w}_\parallel \;=\; \frac{q\,\psi}{\epsilon} \;.\tag{3.16}$$

Equation (3.16) will replace equation (3.12) in the present study. The geometric factor ψ together with the coefficient β yields the same effect as the kinematical tortuosity introduced by Carman (1937).

For each of the three RUC models the geometric factor, ψ, will be expressed as a function of porosity. (Note that in Woudberg et al. (2006) the geometric factor was denoted by χ, but is equivalent to the parameter ψ in the present study.)

3.12 Interstitial form drag coefficient c_d

For flow in porous media the form drag coefficient may be different from those for flow past a single object in an infinite stream (Appendix A.3.1, p 281), due to the influence of neighbouring solid material. The form drag coefficients for porous media will be referred to as the interstitial form drag coefficients, denoted by c_d, instead of simply the form drag coefficient, denoted by C_D.

3.13 Specific surface areas

In this section, the specific surface areas, as described in Section 2.8.6 (p 21), will be expressed in RUC notation. The dynamic specific surface, A_{vd}, is given by (Fourie & Du Plessis (2002))

$$A_{vd} = \frac{S_{fs}}{U_o} \ . \tag{3.17}$$

In equation (3.17), S_{fs} represents the total solid surface area and not only the area presented by the particles to the fluid (as defined by Sabiri & Comiti (1995)). The static specific surface, A_{vs}, is defined in RUC notation as (Diedericks (1999))

$$A_{vs} = \frac{S_{fs}}{U_s} \ , \tag{3.18}$$

and the specific surface with respect to the total volume of the pore space, A_{vp}, is given by

$$A_{vp} = \frac{S_{fs}}{U_f} \ . \tag{3.19}$$

In the next three sections the RUC characteristics and parameters, discussed above, will be discussed separately for the three RUC models.

3.14 Granular RUC model

The granular RUC model was initially introduced by Du Plessis & Masliyah (1991). A schematic representation of the RUC is shown in Figure 3.4, which is an enlargement of the model on the left hand side in Figure 3.1 (p 37), except that in Figure 3.4 the linear dimension d_s is also indicated.
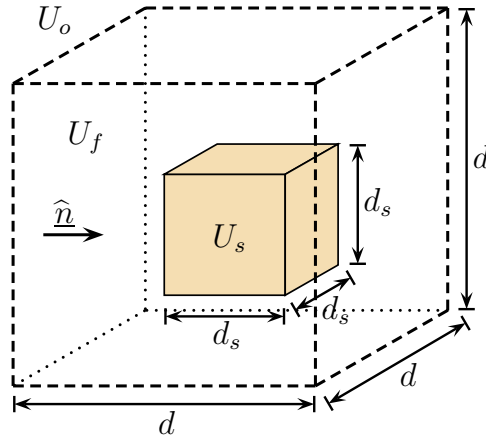
Figure 3.4: Granular RUC model.

The particle size or *solid width*, d_s, can be expressed as

$$d_s = (1 - \epsilon)^{\frac{1}{3}} d .$$
(3.20)

The linear dimension of the RUC or *cell size*, d, is given by

$$d = \frac{d_s}{(1 - \epsilon)^{\frac{1}{3}}} ,$$
(3.21)

and the uniform *pore width*, $d - d_s$, which is a measure of the pore size, leads to

$$d - d_s = \left[1 - (1 - \epsilon)^{\frac{1}{3}}\right] d .$$
(3.22)

The different arrays associated with the granular RUC model are discussed in the following subsections.

3.14.1 Fully staggered array

A three-dimensional schematic representation of an RUC associated with a fully staggered array (Woudberg (2006)) is shown in Figure 3.5(a). The downstream solid surfaces in Figure 3.5 are those of neighbouring solids adjacent to a typical RUC in a fully staggered array. The three-dimensional schematic representation in Figure 3.5(a) is shown for easier visualization of the reunion of the divided streamwise flux on the lee side of the solid cube.
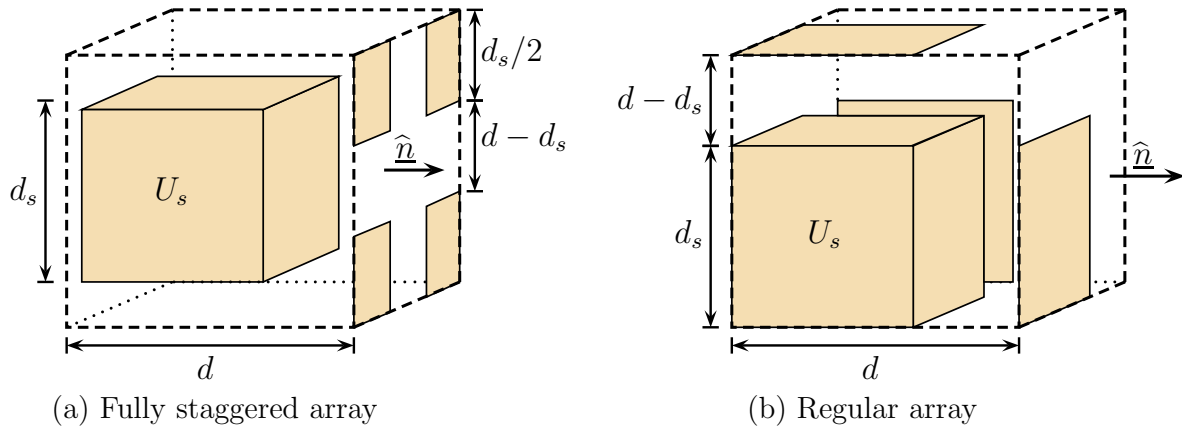
Figure 3.5: A three-dimensional schematic representation of an RUC associated with a granular (a) fully staggered array and a (b) regular array.

3.14.2 Regular array

A three-dimensional schematic representation of an RUC associated with a regular array (Woudberg (2006)) is shown in Figure 3.5(b). The solid surfaces adjacent to the RUC in Figure 3.5(b) are those of neighbouring solids in a regular array. A stagnant fluid domain is present between the two neighbouring solids in the streamwise direction.

3.14.3 Volume partitioning

The quantification of the respective surfaces and volumes of the granular fully staggered and regular arrays, as illustrated two-dimensionally in Figure 3.3 (p 44), are listed in Table 3.1 (p 51) as a function of the linear dimensions d and d_s.

The expressions in Table 3.1 are obtained directly from visualization of the three-dimensional rectangular RUC model geometry. The volume and surface partitioning table of the granular RUC model in terms of d and ϵ is presented in Appendix D (i.e. Table D.1, p 290).

Table 3.1: Volume and surface partitioning table of the granular RUC model in terms of d and d_s.

Parameters	Granular RUC model	
U_o	d^3	
U_s	d_s^3	
U_f	$d^3 - d_s^3$	
U_t	$(d - d_s)^2 (d + 2d_s)$	
$U_\parallel$	$2 d_s^2 (d - d_s)$	
S_{fs}	$6 d_s^2$	
$S_\parallel$	$4 d_s^2$	
	Fully staggered array	Regular array
$U_\perp$	$d_s^2 (d - d_s)$	0
$S_\perp$	$2 d_s^2$	0
U_g	0	$d_s^2 (d - d_s)$
S_g	0	$2 d_s^2$
S_{face}	d_s^2	0

3.14.4   Model parameters

The values (or expressions) for the model parameters of the granular RUC are presented in Table 3.2.

Coefficient β

The value of the coefficient β, as defined by equation (3.8) in Section 3.8 (p 45), can be obtained as follows for the granular fully staggered array (Woudberg (2006)): Consider Figure 3.6 (p 53) which represents an upstream view of the fully staggered array of Figure 3.5(a) (p 50). The RUC domain in Figure 3.6 is partitioned into two symmetry planes with the aid of the two mutually perpendicular dotted lines.

In order to calculate the value of β from equation (3.8), the transverse cross-sectional flow area, $A_{p_\perp}$, is expressed as

$$A_{p_\perp} = \frac{U_\perp}{\Delta s},$$
(3.23)

where Δs denotes the transverse displacement of the centroid of the fluid in any one of the

Table 3.2: Granular RUC model parameters.

Parameters	Fully staggered Array	Regular Array
β	$\sqrt{2}$	0
ξ	$1/4$	0
χ_{geo}	$\dfrac{\epsilon}{1 - (1 - \epsilon)^{2/3}}$	1
χ_{kin}	$\dfrac{1 + (\xi - 1)(1 - \epsilon)^{2/3} - \xi(1 - \epsilon)}{1 - (1 - \epsilon)^{2/3}}$	1
c_d	1.9	
$A_{p_\parallel}$	$d^2 - d_s^2$	
ψ	$\dfrac{\epsilon}{1 - (1 - \epsilon)^{2/3}}$	

four square domains of the RUC, indicated in Figure 3.6 (p 53). The displacement of the centroid of the fluid results from the fluid circumventing the downstream solid obstacle for streamwise discharge through the RUC. The coefficient β may thus be expressed as

$$\beta = \frac{A_{p_\parallel}\Delta s}{U_\perp} \ .$$

(3.24)

The transverse displacement, Δs, can be calculated from any one of the four square domains of the RUC shown in Figure 3.6 by determining the coordinates of the position of the centroid before and after the transverse shift. In Figure 3.7 (p 54) the transverse displacement of the centroid in the bottom left hand square of the RUC in Figure 3.6 is shown schematically.

Let the coordinates of the position of the centroid before the transverse shift be denoted by $(\bar{x}, \bar{y})$, as indicated in Figure 3.7(a). The latter coordinates may be expressed in terms
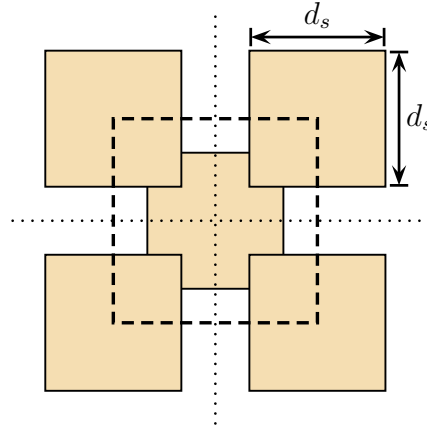
Figure 3.6: A two-dimensional upstream view of a granular fully staggered array.

of the linear dimensions d and d_s as follows :

$$\bar{x} \;=\; \frac{\sum A_i x_i}{\sum A_i} \;=\; \frac{\frac{1}{2}d^3 - dd_s^2 + \frac{1}{2}d_s^3}{d^2 - d_s^2} \;, \tag{3.25}$$

$$\bar{y} \;=\; \frac{\sum A_i y_i}{\sum A_i} \;=\; \frac{\frac{1}{2}d^3 - dd_s^2 + \frac{1}{2}d_s^3}{d^2 - d_s^2} \;, \tag{3.26}$$

where A_i denotes the areas of the composite fluid area, as illustrated in Figure 3.7 (p 54), with $i = 1, 2$, and (x_i, y_i) are the rectangular Cartesian coordinates of the position of the centroid of the respective fluid areas.

Let the coordinates of the position of the centroid after the transverse shift be denoted by $(\bar{x}', \bar{y}')$, as indicated in Figure 3.7(b). Similarly, the coordinates of the position of the centroid after the transverse shift may be expressed as

$$\bar{x}' \;=\; \frac{\frac{1}{2}d^3 - \frac{1}{2}d_s^3}{d^2 - d_s^2} \;, \tag{3.27}$$

$$\bar{y}' \;=\; \frac{\frac{1}{2}d^3 - \frac{1}{2}d_s^3}{d^2 - d_s^2} \;. \tag{3.28}$$

Let $\Delta\bar{x}$ and $\Delta\bar{y}$ respectively denote the displacement of the centroid of the fluid in the x- and y-directions of a rectangular Cartesian coordinate system, as indicated in Figure 3.7(b). It thus follows from equations (3.25) to (3.28) that

$$\Delta\bar{x} \;=\; \bar{x}' - \bar{x} \;=\; \frac{d_s^2}{d + d_s} \;,$$

$$\Delta\bar{y} \;=\; \bar{y}' - \bar{y} \;=\; \frac{d_s^2}{d + d_s} \;. \tag{3.29}$$

The transverse displacement Δs of the centroid of the fluid may then be expressed as

$$\Delta s = \sqrt{(\Delta \bar{x})^2 + (\Delta \bar{y})^2} = \frac{\sqrt{2}\, d_s^2}{d + d_s} \,. \tag{3.30}$$

Substituting equation (3.30) into equation (3.24) and using the expressions for $U_\perp$ and $A_{p_\parallel}$ in Tables 3.1 (p 51) and 3.2 (p 52), respectively, yields $\beta = \sqrt{2}$. Since each of the four square domains of the RUC shown in Figure 3.6 (p 53) will yield the same value for β and assuming that each of them contribute equally to the nett effect of the flow field, the value of $\beta = \sqrt{2}$ may be taken as the average representative value for the granular fully staggered array.

The value of the coefficient β for the granular regular array is zero, since this array does not contain any transverse fluid volumes, thus yielding $w_\perp = \beta\, w_\parallel = 0$.

Coefficient ξ

According to the definition of the coefficient ξ, as given in Section 3.10 (p 46), it follows that $\xi = 0$ for the granular regular array, since $U_\perp = 0$.

As already mentioned and indicated in Figure 3.6, the granular fully staggered array has two symmetry planes. According to the definition for ξ in Section 3.10, it follows that for this array, $\xi = 1/4$.

Note that the value of ξ for the granular fully staggered array was incorrectly given by Woudberg (2006) and Woudberg et al. (2006) as $1/2$. The latter value is the same as the value that will be assigned to the fully staggered array of the fibre RUC model. This cannot be the case according to the definition for the geometric factor ξ given in

(a) Before shift
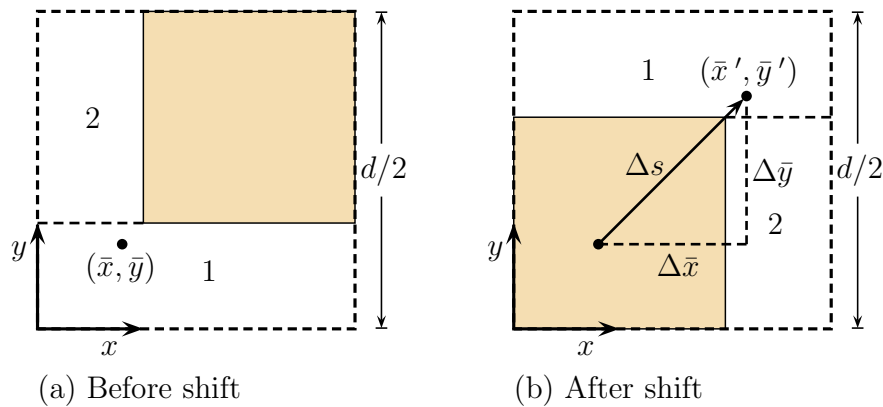
(b) After shift

Figure 3.7: A two-dimensional representation of the position of the centroid (a) before and (b) after the transverse shift.

Section 3.10 (p 46). The number of symmetry planes normal to the streamwise direction is different for the granular and fibre RUC models. As a result, the coefficient of the permeability predicted by the granular RUC model in the present study will be different from the coefficient of the model proposed by Woudberg (2006) and Woudberg et al. (2006). The value of $\xi = 1/4$ was, however, correctly reported by Du Plessis & Woudberg (2008).

Tortuosity

The values of both the geometrical and kinematical tortuosities for the granular regular array, based on the definitions presented by equations (3.11) and (3.14), respectively, are unity. This can be attributed to the fact that a regular array contains no transverse channels and the fluid can flow freely through the RUC, without being deviated into a transverse direction.

The expressions for the geometrical and kinematical tortuosities, presented in Table 3.2 (p 52) for the granular fully staggered array, result from substitution of the respective equations for the different fluid volumes given in Table 3.1 (p 51) and the linear dimensions of the granular RUC model, given by equations (3.20) and (3.21). Figure 3.8 shows both tortuosities as a function of porosity.
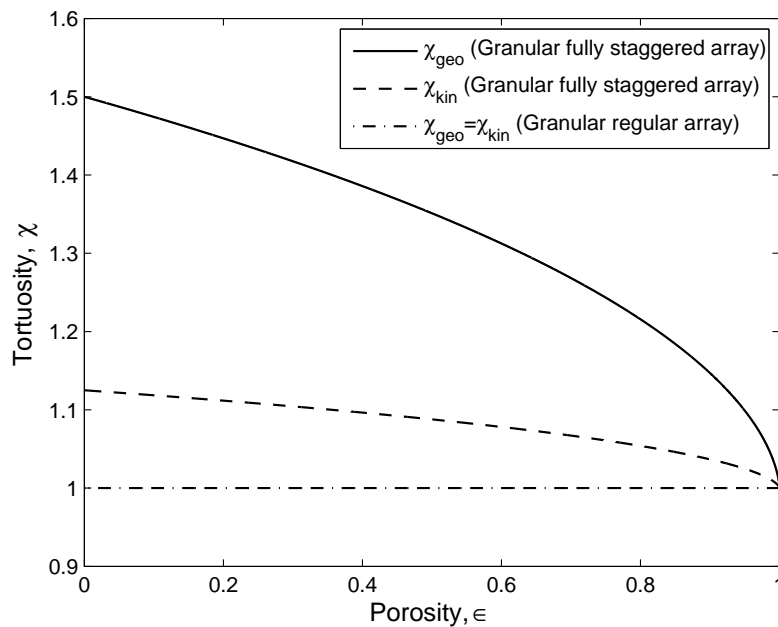
Figure 3.8: Tortuosity of the granular RUC model as a function of porosity.

Although model predictions for χ at $\epsilon = 0$ (i.e. only solid) carries no physical meaning, it is included in Figure 3.8 to show the trend of the curve over the entire porosity range.

It is evident from Figure 3.8 (p 55) that the tortuosity decreases with increasing porosity. This may be attributed to the fact that the flow domain becomes less restrictive as the porosity increases due to the larger fluid domain available for flow.

The reduction in tortuosity provided by the incorporation of the coefficient ξ into the kinematical tortuosity is clear from Figure 3.8. The geometrical tortuosity ranges between $1 \leq \chi_{geo} \leq 1.5$ and the kinematical tortuosity between $1 \leq \chi_{kin} \leq 1.125$. Dullien (1979) states that, provided that the geometric model incorporates the most important features of the pore structure, $1 \leq \chi_{geo} \leq 1.732$. The tortuosity ranges proposed by the granular RUC model thus lie within the range proposed by Dullien (1979).

Geometric factor ψ

The porosity dependence of the geometric factor, presented in Table 3.2 (p 52), is the same for both the fully staggered and regular arrays. Although the RUC model differentiates between the transverse and stagnant fluid volumes, the quantification of $U_\perp$ and U_g in terms of d and d_s is the same (Table 3.1, p 51). For a fully staggered array $U_g = 0$ and for a regular array $U_\perp = 0$, thus yielding the same expressions for ψ according to equation (3.15).

It is furthermore evident from Table 3.2 that the porosity dependence of the geometric factor is the same as that of the geometric tortuosity for a fully staggered array. This is the case, since in the expression for the geometric factor for a fully staggered array $U_g = 0$ and this is also true for the tortuosity (i.e. equation (3.11)) which does not take the presence of stagnant fluid volumes into account.

The fact that the geometric factor yields the same expression for both arrays, whereas those of the tortuosity are different, is an advantage of the geometric factor over the tortuosity.

Interstitial form drag coefficient c_d

The values given in Table A.1 (p 282) for flow past a cube are 1.1 and 1.05. According to Helsør & Svendsen (2007), the form drag coefficient increases with decreasing porosity. Based on these findings and since $c_d = 1.9$ yields the best correspondence with the coefficient value proposed by Macdonald et al. (1979) for flow in the higher Reynolds number flow regime, the latter value will be used for the granular RUC model. Previous authors (e.g. Du Plessis (1994)) have used a value of $c_d = 2$ for the granular RUC model.

The assignment of the value of $c_d = 1.9$ to the interstitial form drag coefficient presents the most empirical aspect of the modelling procedure to be presented in Chapter 4. Experiments and/or numerical computations need to be performed to obtain c_d as a function of porosity, but this falls beyond the scope of the present study.

Table 3.3: Specific surface areas of the granular RUC model.

Parameter	Specific surface areas
A_{vd}	$\dfrac{6\,(1-\epsilon)}{d_s}$
A_{vs}	$\dfrac{6}{d_s}$
A_{vp}	$\dfrac{6\,(1-\epsilon)}{\epsilon\,d_s}$

Specific surface areas

The expressions for the respective specific surface areas, as described in Section 3.13 (p 48), are presented in Table 3.3. These results are obtained from the corresponding expressions in Table 3.1 (p 51) together with equation (3.21).

3.14.5 Pore-scale linear dimensions

The physical flow properties of the granular RUC model to be predicted, i.e. the pressure gradient, permeability and inertial coefficient can be expressed in terms of either of the three pore-scale linear dimensions of the granular RUC model, i.e. the solid width, d_s, the cell size, d, or the pore width, $d - d_s$.

For actual granular porous media some average particle diameter is usually specified as characteristic pore-scale linear dimension. To apply the granular RUC model to flow through an actual granular porous medium, the width d_s of the solid cube in the RUC model needs to be related to the average particle diameter.

The hydraulic radius can be obtained for the granular RUC model from equations (2.8) and (2.10), i.e.

$$R_h \;=\; \frac{\epsilon\,U_s}{S_{fs}\,(1-\epsilon)} \;=\; \frac{\epsilon\,d_s^3}{6\,d_s^2\,(1-\epsilon)} \;=\; \frac{\epsilon\,d_s}{6\,(1-\epsilon)}\;. \tag{3.31}$$

Similarly, for the spherical cell model of Happel (1958) it follows that

$$R_h \;=\; \frac{\epsilon\,V_s}{A_s\,(1-\epsilon)} \;=\; \frac{\epsilon\,\frac{4}{3}\,\pi\,a^3}{4\,\pi\,a^2\,(1-\epsilon)} \;=\; \frac{\epsilon\,a}{3\,(1-\epsilon)}\;. \tag{3.32}$$

Setting equations (3.31) and (3.32) equal, leads to the following relation between the granular solid width, d_s, and the spherical radius, a:

$$d_s \; = \; 2\,a \; = \; D_{sp} \,, \tag{3.33}$$

with D_{sp} being the spherical diameter.

The physical flow properties of the granular RUC model, may, as in the case of the Ergun equation (Appendix C.4, p 289) be expressed in terms of any of the three specific surface areas, i.e. in terms of A_{vd}, A_{vs} or A_{vp}. From Table 3.3 (p 57) it follows that

$$d_s \; = \; \frac{6\,(1-\epsilon)}{A_{vd}} \,, \tag{3.34}$$

$$d_s \; = \; \frac{6}{A_{vs}} \,, \tag{3.35}$$

$$d_s \; = \; \frac{6\,(1-\epsilon)}{\epsilon\,A_{vp}} \,. \tag{3.36}$$

With the aid of equations (3.20) to (3.22), the relations between the specific surface areas and the cell size, d, or pore width, $d - d_s$, can also be obtained.

3.15   Foam RUC model

A schematic representation of the low porosity foam RUC model is shown in Figure 3.9(a) (p 59) and the high porosity model is shown in Figure 3.9(b) (p 59). The low porosity model was originally introduced by Du Plessis & Masliyah (1988) and the high porosity model by Du Plessis et al. (1994). In the low porosity model the pore space of the complex network of inter-connected struts in actual foamlike media is approximated by three mutually perpendicular square duct sections. The only difference between the low and high porosity models is that the fluid and solid volumes are interchanged. In the low porosity model the shaded volume represents the fluid phase whereas in the high porosity model the shaded volume represents the solid phase. Although metallic foams are very high porosity materials, the low porosity model is shown purely for easier visualization of the fluid flow.

In the high porosity model in Figure 3.9(b) the fluid enters the RUC from below into the channel flanked by surfaces A. In line with keeping the model as simple as possible, the fluid is then assumed to move to the left experiencing shear from the flanks annotated B and then backwards along flanks C, before exiting through the square opening at the top. In the high porosity model in Figure 3.9(b) the streamwise direction indicated is different from that in the low porosity model in Figure 3.9(a). The reason being solely for easier explanatory purposes of the flow through the high porosity model, as presented above. Three mutually perpendicular channel sections can be identified in both low and high porosity foam RUC models, each of which consists of double pairs of parallel plates.

(a) Low porosity model   (b) High porosity model
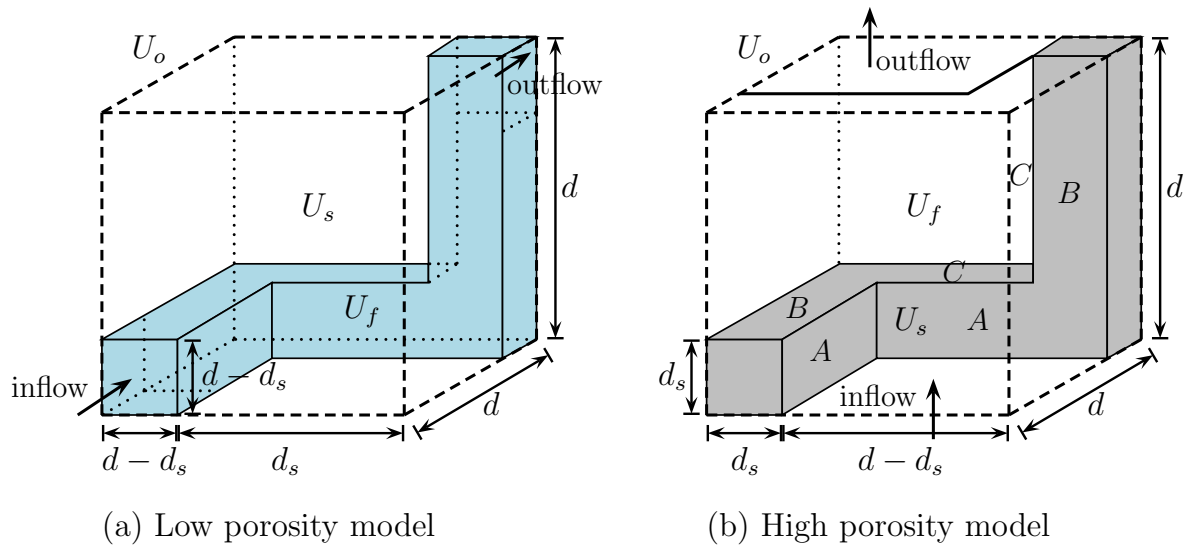
Figure 3.9: The (a) low and (b) high porosity foam RUC models.

These conditions are then assumed to approximate piece-wise plane-Poiseuille flow between each pair of parallel surfaces. The assumption of flow through a streamtube, in which the RUC is allocated, similarly as was assumed for the unconsolidated models, also holds here for the high porosity model.

The linear dimensions of the foam RUC model are shown in Figure 3.9. The linear dimension of the square strut, or rather the *solid width* is denoted by d_s. The uniform *channel width* is expressed as $d - d_s$, with d the *cell size* of the RUC.

For the foam RUC model, three low porosity sub-models were introduced (Smit et al. (2005), Crosnier et al. (2006)), depending on the number of stagnant duct sections present within the RUC. The number of stagnant duct sections determines the extent of deviation of the fluid into the transverse directions and is thus related to the degree of staggering within the RUC. The three low porosity RUC sub-models are the doubly staggered, singly staggered and non-staggered models. The models are classified according to the ratio σ, defined as the total stagnant fluid volume over the total streamwise fluid volume in the RUC (Crosnier et al. (2006)), i.e.

$$\sigma \equiv \frac{U_g}{U_{\|}} \, . \tag{3.37}$$

The three foam RUC sub-models will be introduced in the following sections.

3.15.1 Doubly staggered model

The doubly staggered foam RUC model is shown in Figure 3.10 (p 60) and is the same model as the one presented in Figure 3.9(a).
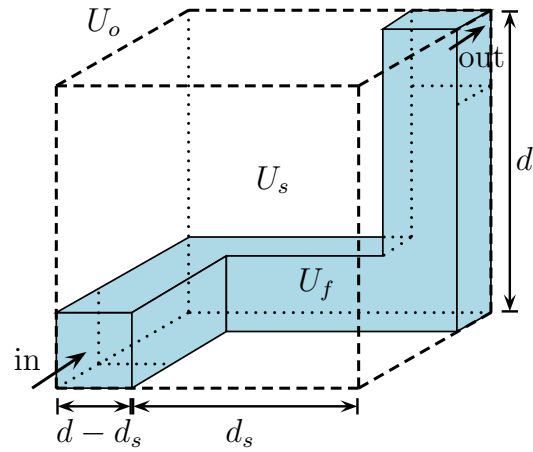
Figure 3.10: Doubly staggered foam RUC model ($\sigma = 0$).

In this model the fluid is forced to flow through all three mutually perpendicular square duct sections. It may thus be regarded as if the fluid is subject to maximum possible staggering. The fluid enters the first square duct section perpendicular to the face of the RUC, after which it is deviated consecutively into the two transverse directions before exiting the RUC again in the streamwise direction. The doubly staggered foam RUC model contains no stagnant duct sections, i.e. $\sigma = 0$ for this model.

3.15.2 Singly staggered model

The singly staggered foam RUC model, shown in Figure 3.11, contains one stagnant duct section, and hence, for this model $\sigma = 1$.
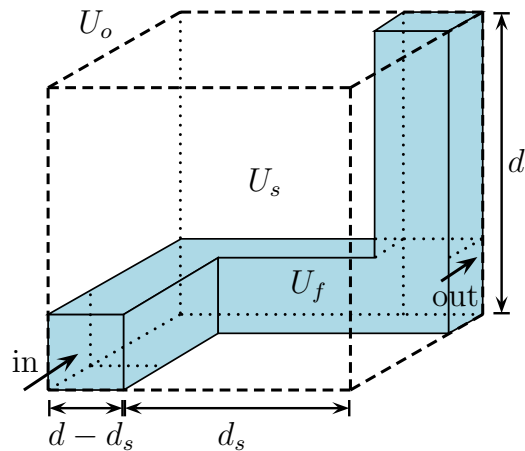
Figure 3.11: Singly staggered foam RUC model ($\sigma = 1$).

The fluid enters the RUC in the streamwise direction after which it is deviated into a transverse direction before leaving the RUC again in the streamwise direction.

3.15.3   Non-staggered model

In the non-staggered foam RUC model, shown in Figure 3.12, two of the three mutually perpendicular square duct sections are stagnant fluid domains. Hence, for this model $\sigma = 2$.
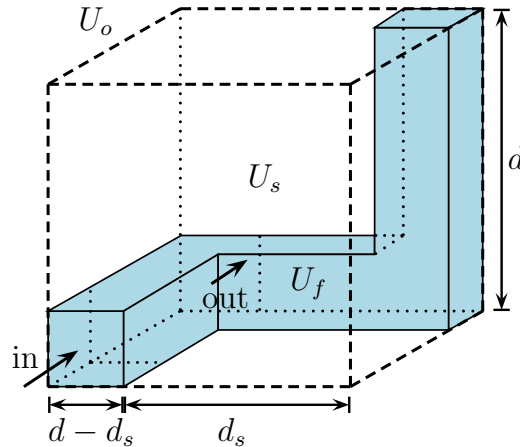
Figure 3.12: Non-staggered foam RUC model ($\sigma = 2$).

After entering the RUC, the fluid continues to flow in the streamwise direction without being deviated into a transverse direction.

3.15.4   Alternative foam RUC models

An alternative RUC configuration for foamlike media was introduced by Du Plessis (1992). These models are described in Appendix E (p 308). Diedericks (1992) and Fourie & Du Plessis (2002) also made use of these alternative foam RUC models. Crosnier et al. (2006) made use of the doubly staggered model shown in Figure 3.10 (p 60), but for the inclusion of stagnant fluid domains the alternative singly and non-staggered RUC models, respectively shown in Figures E.2 and E.3 (p 309), were used.

In the alternative doubly staggered foam RUC model, presented in Figure E.1 (p 308), the streamwise average channel velocity will be different from the transverse average channel velocity due to the splitting of the streamwise flux. This implies that the value of β will be different for the alternative doubly and singly staggered models. This is, however, not the case in the foam RUC models shown in Figures 3.10 to 3.12 (pp 60-61).

Table 3.4: Volume and surface partitioning table of the foam RUC model in terms of d, d_s and σ.

Parameter	Foam RUC sub-models
U_o	d^3
U_s	$3\,d\,d_s^2 - 2\,d_s^3$
U_f	$3\,(d - d_s)^2\,d - 2\,(d - d_s)^3$
U_t	$(d - d_s)^3$
$U_\parallel$	$(d - d_s)^2\,d_s$
S_{fs}	$12\,(d - d_s)\,d_s$
$S_\parallel$	$4\,(d - d_s)\,d_s$
$U_\perp$	$(2 - \sigma)(d - d_s)^2\,d_s$
$S_\perp$	$(8 - 4\,\sigma)\,(d - d_s)\,d_s$
U_g	$\sigma\,(d - d_s)^2\,d_s$
S_g	$4\,\sigma\,(d - d_s)\,d_s$
S_{face}	$(2 - \sigma)\,(d - d_s)\,d_s$

3.15.5 Volume partitioning

The quantification of the respective surfaces and volumes of the foam RUC models is presented in Table 3.4 as a function of the parameters d, d_s and σ. For the doubly staggered model $\sigma = 0$, for the singly staggered model $\sigma = 1$ and for the non-staggered model $\sigma = 2$. A three-dimensional schematic representation of the volume partitioning of the foam RUC models were omitted because of the difficulty indicating the exact fluid-fluid boundaries.

From Table 3.4 it follows that

$$U_\perp \;+\; U_g \;=\; 2\,U_\parallel\,. \tag{3.38}$$

The porosity of the foam RUC model may then be expressed as

$$
\begin{aligned}
\epsilon \;&=\; \frac{U_\parallel \;+\; U_t \;+\; U_\perp \;+\; U_g}{U_\parallel \;+\; U_t \;+\; U_\perp \;+\; U_g \;+\; U_s} \\[2mm]
&=\; \frac{3\,U_\parallel + U_t}{3\,U_\parallel \;+\; U_t \;+\; U_s} \\[2mm]
&=\; \left(\frac{d - d_s}{d}\right)^2 \left(3 - 2\,\frac{d - d_s}{d}\right)\,.
\end{aligned} \tag{3.39}
$$

Equation (3.39) will be used to express the geometric factor of the foam RUC model as a function of porosity alone.

3.15.6   Model parameters

The values (or expressions) for the parameters of the foam RUC model are presented in Table 3.5.

Table 3.5: Model parameters of the foam RUC model.

Parameters	Doubly staggered	Singly staggered	Non-staggered
β	1	1	0
ξ	1	1	0
$\chi = \chi_{geo} =$ χ_{kin}	$2 + 2\cos\left[\dfrac{4\pi}{3} + \dfrac{1}{3}\cos^{-1}(2\,\epsilon - 1)\right]$	$\dfrac{3}{2} + \cos\left[\dfrac{4\pi}{3} + \dfrac{1}{3}\cos^{-1}(2\,\epsilon - 1)\right]$	1
c_d	2		
$A_{p_\parallel}$	$(d - d_s)^2$		
ψ	$2 + 2\cos\left[\dfrac{4\pi}{3} + \dfrac{1}{3}\cos^{-1}(2\,\epsilon - 1)\right]$		

Coefficient β

For the doubly and singly staggered models $\beta = 1$ since the magnitudes of the streamwise and transverse average channel velocities are equal, as described in Section 3.8 (p 45). For the non-staggered model $\beta = 0$ since $w_\perp = 0$ for this model.

Coefficient ξ

According to the definition of the coefficient ξ, as given in Section 3.10 (p 46), $\xi = 1$ for the doubly and singly staggered models, since the streamwise flux is not deviated into pair-wise opposite transverse directions in $U_\perp$. For the non-staggered model $\xi = 0$ since $U_\perp = 0$.

Tortuosity

Since $\xi = 1$ for the doubly and singly staggered foam RUC models it follows that $\chi_{geo} = \chi_{kin} = \chi$ (equations (3.11) and (3.14)). From equation (3.11) and Table 3.4 (p 62) the following expressions are obtained for the tortuosity of the doubly staggered and singly staggered models, respectively:

$$\chi = 3 - 2\frac{d - d_s}{d} \tag{3.40}$$

and

$$\chi = 2 - \frac{d - d_s}{d} \ . \tag{3.41}$$

For the doubly staggered model it follows from equations (3.40) and (3.39) that

$$\frac{\chi}{\epsilon} = \frac{4}{(3 - \chi)^2} \ . \tag{3.42}$$

Similarly, for the singly staggered model it follows from equations (3.41) and (3.39) that

$$\epsilon = 3(2 - \chi)^2 - 2(2 - \chi)^3 \ . \tag{3.43}$$

The third degree polynomials of equations (3.42) and (3.43) may be solved, subject to the constraint that $\chi = 1$ if $\epsilon = 1$. This leads to the respective expressions for the tortuosity as a function of porosity, as presented in Table 3.5 (p 63) (Du Plessis & Diedericks (1997), Smit & Du Plessis (1999), Wilms (2006)).

For the non-staggered model, $\chi = 1$, since in this model the fluid is not deviated into a transverse direction.

Figure 3.13 (p 65) shows the tortuosity, χ, as a function of porosity for the three foam RUC models. The tortuosity decreases with increasing porosity due to the same reason of a less restrictive fluid domain available for flow as was given for the granular model in Section 3.14.4 (p 51). At any given porosity value, the tortuosity predicted by the doubly staggered model is larger than the value predicted by the singly staggered model because of the same reason. In the doubly staggered model the streamwise flux is deviated consecutively into two transverse directions, whereas in the singly staggered model the streamwise flux is deviated into only one transverse direction which makes the flow less restrictive, yielding lower values for the tortuosity.
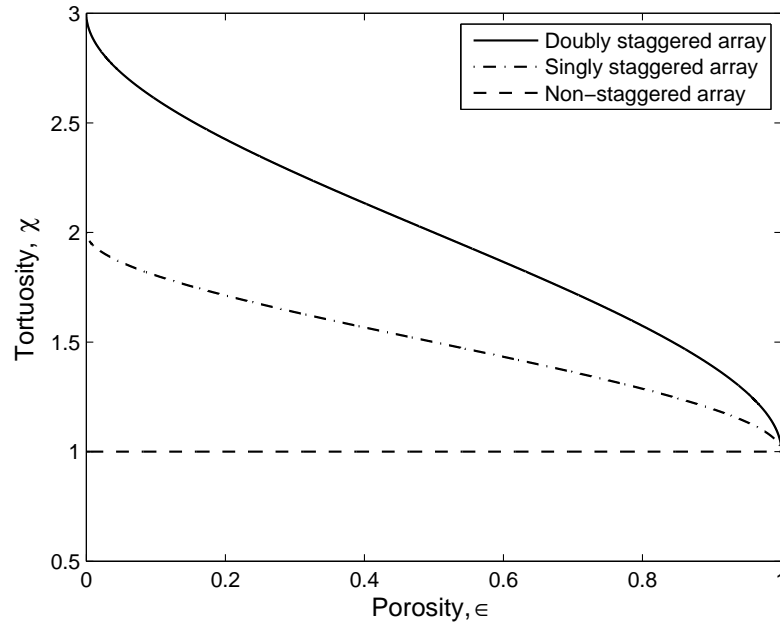
Figure 3.13: Tortuosity of the foam RUC models as a function of porosity.

Geometric factor ψ

From Table 3.4 (p 62) it follows that the geometric factor ψ may be expressed as

$$\psi \; = \; \frac{U_{||} + U_t + U_{\perp} + U_g}{U_{||} + U_t} \; = \; 3 - 2\frac{d - d_s}{d} \; . \tag{3.44}$$

From equation (3.44) it then follows that the ratio of the channel width to cell size may be expressed as

$$\frac{d - d_s}{d} \; = \; \frac{3 - \psi}{2} \; , \tag{3.45}$$

and the ratio of the solid width to cell size is given by

$$\frac{d_s}{d} \; = \; \frac{\psi - 1}{2} \; . \tag{3.46}$$

The cell size may in turn be expressed as

$$d \;\; = \;\; \frac{2\,d_s}{(\psi - 1)} \tag{3.47}$$

$$= \;\; \frac{2\,(d - d_s)}{(3 - \psi)} \; . \tag{3.48}$$

From equations (3.39) and (3.44) it thus follows that

$$\frac{\psi}{\epsilon} \;=\; \frac{4}{(3-\psi)^2} \;.$$
(3.49)

Equation (3.49) also leads to a third degree polynomial, which, subject to the constraint that $\psi = 1$ if $\epsilon = 1$, yields the following expression for the geometric factor as a function of porosity (Smit et al. (2005)):

$$\psi \;=\; 2 + 2\cos\left[\frac{4\pi}{3} + \frac{1}{3}\cos^{-1}(2\epsilon - 1)\right] \;.$$
(3.50)

Similarly as in the case of the granular RUC model, the expression for the geometric factor is the same for all three foam RUC sub-models, whereas the expressions for the tortuosity differ for the three models. For the doubly staggered model the geometric factor is equal to the tortuosity, since the doubly staggered model does not contain stagnant fluid domains.

The volume and surface partitioning table of the foam RUC model in terms of d, ψ and σ is presented in Appendix D (i.e. Table D.2, p 291).

Interstitial form drag coefficient c_d

The interstitial form drag coefficient, c_d, for the foam RUC model is expected to be comparable in magnitude to the empirical value for flow past a single square rod (Du Plessis & Diedericks (1997)). The latter value is presented in Table A.1 (p 282) as $c_d = 2$ and, since no information regarding the interstitial form drag coefficient is available in the literature, the value of 2 will henceforth be used as the drag coefficient for the foam RUC model, unless otherwise stated. A value of $c_d = 2.05$ has been used in the past by several authors who have used the foam RUC model (e.g. Du Plessis et al. (1994), Du Plessis (1996), Diedericks & Du Plessis (1997), Diedericks et al. (1998)).

In Section 3.15.7 (p 67) an empirical method will be proposed in which the interstitial form drag coefficient can be obtained from experimental pressure drop data.

Specific surface areas

The expressions for the respective specific surface areas, as discussed in Section 3.13 (p 48), are presented in Table 3.6 (p 67). These results are obtained from the relevant expressions in Table 3.4 (p 62), together with equations (3.45) and (3.46).

66

Table 3.6: Specific surface areas of the foam RUC model.

Parameter	Specific surface areas
A_{vd}	$\dfrac{3}{d}\,(3-\psi)(\psi-1)$
A_{vs}	$\dfrac{12\,(3-\psi)}{d\,(4-\psi)(\psi-1)}$
A_{vp}	$\dfrac{12\,(\psi-1)}{d\,(3-\psi)\psi}$

3.15.7 Pore-scale linear dimensions

The physical flow properties of the foam RUC model to be predicted can be expressed in terms of either of the three pore-scale linear dimensions of the foam RUC model, i.e. the solid width, d_s, the cell size, d, or the channel width, $d - d_s$.

In predicting flow through consolidated porous media the main difficulty lies in finding a reasonable relationship between the linear dimension defined in the conceptual model and that of the actual structure (e.g. Dukhan (2006), Dukhan & Patel (2008)). The complex consolidated pore-structure of foamlike media makes it extremely difficult to measure accurately the average pore-scale linear dimensions. Some authors (e.g. Innocentini et al. (1999), Lacroix et al. (2007), Edouard et al. (2008)) have expressed the difficulty in relating the effective particle diameter of a bed of uniform spheres (which has been clearly quantified) to the pore diameter of foams. According to Liu et al. (2006), there is no consensus on how to determine the 'equivalent spherical diameter for foams'. Edouard et al. (2008) report that, as a result, the majority of authors empirically adjust the permeability and inertial coefficients to agree with the experimental values.

Some authors in the literature (e.g. Depois & Mortensen (2005), Krishnan et al. (2006), Miwa & Revankar (2011)) regard the pores of foamlike media to be spherical. The unit cell is obtained by subtracting spheres placed at certain positions of a cubic unit cell, from a solid cubic unit cell. As a result, the pore diameter of the foam is equivalent to the granular diameter of a packed bed of uniform spheres. Giani et al. (2005b) states that, simply based on the appearance of metallic foams, the analogy between the interconnected network of struts and a packed bed, which forms the basis of the sphere-like model, is not clear.

The linear dimensions often specified in the literature for foamlike media are the number

of pores per inch (abbreviated PPI), the solid width (also strut or ligament diameter (e.g. Topin et al. (2006), Dukhan & Patel (2008), Mancin et al. (2010), Miwa & Revankar (2011)), the pore diameter (also inner or window diameter (e.g. Incera Garrido et al. (2008), Mancin et al. (2010)) and the cell size (also face diameter or average solid to solid distance) (Buciuman & Kraushaar-Czarnetzki (2003)). According to Dukhan & Patel (2008), all the latter linear dimensions show variations throughout a foam sample. The measurement of these linear dimensions is not an easy task and there is much controversy in the literature about which one of the dimensions is the most reliable and how it should be measured.

The PPI number (or pore count), specified by the manufacturer, is the average number of holes per unit length (measured in inches) in a plane cut through the foam (Buciuman & Kraushaar-Czarnetzki (2003)). A high PPI number corresponds to a small pore size and vica verca. Buciuman & Kraushaar-Czarnetzki (2003) states that the reciprocal of the PPI number can be used as a rough estimate for the pore size. Montillet et al. (1992) refers to the PPI number as the grade of a foam.

Dietrich et al. (2009) provided an empirical relation between the pore size, given by the hydraulic diameter, and the PPI number for ceramic foams (of average porosity $\epsilon = 0.8$), i.e.

$$D_h \;=\; 0.028\,\mathrm{PPI}^{-0.721} \;. \tag{3.51}$$

Dietrich et al. (2009) however stress the fact that equation (3.51) should be regarded as a first order approximation subject to a 40% error. This is due to the large amount of uncertainty associated with the PPI number. Mancin et al. (2010) proposed the following empirical relation:

$$D_h \;=\; 0.0122\,\mathrm{PPI}^{-0.849} \;. \tag{3.52}$$

To the knowledge of the author of this dissertation no *analytical* equation have been proposed that relates the hydraulic diameter to the PPI number.

Giani et al. (2005a) and Miwa & Revankar (2011) emphasized the difference in their correlation of the pore size and that supplied by the manufacturer. Crosnier et al. (2006) and Richardson et al. (2000) also mentioned that the PPI number should not be regarded as exact since each manufacturer has its own method of determining it. Huu et al. (2009) also state that the PPI number is a projection of the three-dimensional pore volume onto some plane which depends on the projection angle. Boomsma & Poulikakos (2002) refer to the pore count supplied by manufacturers as a subjective process. They preferred to perform their own experiments to determine an objective measure of the pore diameter.

Huu et al. (2009) and Miwa & Revankar (2011) state that the definition of the PPI number as the pore count is confusing since a "pore" of foamlike media has not been clearly defined and, consequently, present large uncertainties in the associated values. In the literature a "pore" generally ranges between the window diameter and the cell diameter (Edouard et al. (2008)). Buciuman & Kraushaar-Czarnetzki (2003), for example, specified the cell diameter as representative of the pore diameter. Miwa & Revankar (2011) state that

68

a clear distinction should be made between the cell diameter and the pore diameter. They recommend that for average unidirectional flow a pore diameter measured from a projected area perpendicular to the flow direction should be used, as this measured value is more accurate than the actual pore size. Philipse & Schram (1991) prefer to work with the cell size as they say that the uncertainty accompanying the pore diameter is too high. Incera Garrido et al. (2008) defined a pore as the "communicating window between cells". When measuring the pore diameter two orthogonal lengths were measured for each pore window of which the average is taken.

Measuring the strut diameter is also not an easy task since the thickness of the strut varies along it length. Dukhan & Patel (2008) state that the "particle" diameter of metallic foams is "not trivial". He also refers to the use of the average strut diameter as "problematic" because the strut diameter varies and is triangular with rounded corners, rather than circular. Incera Garrido et al. (2008), for example, measured the strut diameter in the middle of the length of the strut.

Previous authors who have used the foam RUC model (e.g. Du Plessis et al. (1994), Fourie & Du Plessis (2002), Crosnier et al. (2006)) have used different methods of determining the relation between the various pore-scale linear dimensions of the foam RUC model as well as to relate them to experimentally measured values.

Du Plessis et al. (1994), for example, proposed a manner in which the cell size, d, and the interstitial form drag coefficient, c_d, can be obtained from experimental pressure drop data. From a linear plot of $-(1/q)(\mathrm{d}p/\mathrm{d}x)$ versus the magnitude of the superficial velocity, q, a linear curve is obtained from the experimental data. The RUC model prediction is expressed in the same form and the y-intercept and gradient are equated with the corresponding expressions proposed by the RUC model. The equation for the y-intercept is linearly dependent on the cell size, d, whereas the equation for the gradient is linearly dependent on both d and the form drag coefficient, c_d. The value of d can thus be obtained from the former equation and, by knowing the value of d, c_d can be obtained from the equation for the gradient. Crosnier et al. (2006) also used this empirical method to determine the values of d and c_d. The method is, however, not optimal since the values obtained for d and c_d cannot be used to determine the streamwise pressure gradient because it was used to determine d and c_d. What is needed is an independent method to determine the values of d and c_d.

Fourie & Du Plessis (2002) attempted to do this and improve on the empirical approach of Du Plessis et al. (1994) for determining the value of d by excluding the necessity to obtain information regarding the flow behaviour beforehand. A geometrical model was introduced which approximates the consolidated solid micro-structure as a tetrakaidecahedron with struts of uniform triangular cross-section on the edges. The accumulation of solid material at the intersection of struts was accounted for by placing a truncated tetrahedron at the end of each strut. A diagonal cell size, c, was introduced to approximate the measured average cross-sectional pore diameter of the actual foamlike structure. The relation obtained between the diagonal cell size, c, and the cell size, d, is given by

$$d \approx 0.57\,c\,.\qquad(3.53)$$

69
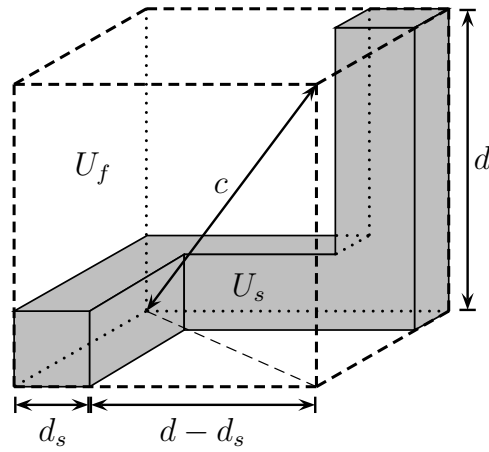
Figure 3.14: Illustration of the diagonal cell size, c, in the high porosity foam RUC model.

The diagonal cell size, c, can, however, be obtained directly from the RUC model, as illustrated graphically by the diagonal length in the high porosity foam RUC model in Figure 3.14, from which it directly follows that

$$c = \sqrt{3}\,d \approx \frac{d}{0.58}\,. \tag{3.54}$$

The latter result is thus the same as equation (3.53), obtained by Fourie & Du Plessis (2002). The effort in trying to reconstruct a more complex solid micro-structure, as was done by Fourie & Du Plessis (2002), did not yield a more accurate characterization of the solid structure, since the same information could be retrieved from the RUC model by defining the three-dimensional cell size.

Du Plessis et al. (1994) mentioned that the channel width, $d-d_s$, of the foam RUC model may not be a direct measure of the visible or experimentally observed pore diameter and that this dimension is only *quasi*-three-dimensional. In order to address this issue and to relate $d-d_s$ to a measurable dimension of the actual foam (without a priori knowledge of the flow behaviour through the porous medium) the three-dimensional pore diameter, d_p, was introduced, as shown in Figure 3.15 (p 71). The following relation between the quasi-three-dimensional pore diameter, $d-d_s$, and the three-dimensional pore diameter, d_p, follows directly from the geometric features shown in Figure 3.15 for the high porosity foam RUC model and is given by

$$d - d_s = \frac{d_p}{\sqrt{3}} \approx 0.58\,d_p\,. \tag{3.55}$$

The relation given by equation (3.55) was proposed by Du Plessis et al. (1994) as "a better observable pore diameter", but not incorporated into their pressure drop prediction.

By application of equation (3.45), the relation between the cell size, d, and the pore diameter, d_p, is obtained as

$$d = \frac{2\,d_p}{\sqrt{3}\,(3-\psi)}\,. \tag{3.56}$$

70
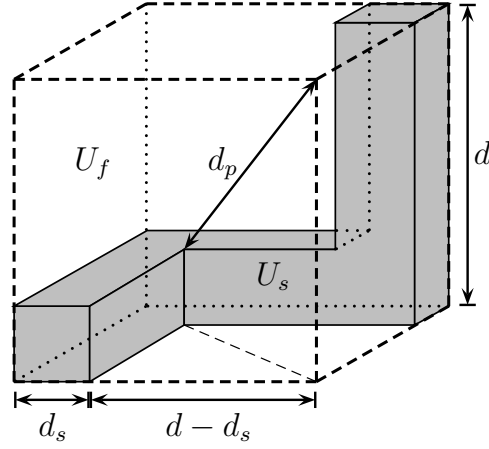
Figure 3.15: Illustration of the pore diameter, d_p, in the high porosity foam RUC model.

With the aid of equation (3.56), the pore diameter can also be expressed in terms of the respective specific surface areas, i.e.

$$
\begin{aligned}
d_p &= \frac{3\sqrt{3}\,(3-\psi)^2(\psi-1)}{2A_{vd}} \,, \\
d_p &= \frac{6\sqrt{3}\,(3-\psi)^2}{A_{vs}\,(\psi-1)(4-\psi)} \,, \\
d_p &= \frac{6\sqrt{3}\,(\psi-1)}{\psi\,A_{vp}} \,.
\end{aligned}
\tag{3.57}
$$

The pressure gradient and permeability predicted by the foam RUC model, may thus, in addition to the three pore-scale linear dimensions mentioned at the beginning of this section, be expressed in terms of the pore diameter, d_p, and any of the three specific surface areas.

For comparison between the pressure drop predicted by the foam RUC model and that of an empirical Ergun-type equation for foamlike media, it is necessary to relate the hydraulic diameter (Section 2.8.5, p 20) to the linear dimensions of the foam RUC model. The hydraulic diameter as a function of d results from equations (2.9), (3.17) and the expression for A_{vd} in Table 3.6 (p 67) and is given by

$$
D_h = \frac{4\,\epsilon\,d}{3\,(3-\psi)(\psi-1)} \,.
\tag{3.58}
$$

The hydraulic diameter as a function of d_s is given by

$$
D_h = \frac{8\,\epsilon\,d_s}{3\,(3-\psi)^2(\psi-1)} \,,
\tag{3.59}
$$

and as a function of $d - d_s$,

$$
D_h = \frac{8\,\epsilon\,(d-d_s)}{3\,(3-\psi)(\psi-1)^2} \,.
\tag{3.60}
$$

If only the PPI number is provided, equations (3.51) and (3.52) may be used as a last alternative, to calculate the values of d_s and $d - d_s$ from equations (3.59) and (3.60), respectively.

3.16 Fibre RUC model

The fibre RUC model was initially introduced by Du Plessis (1991). A schematic representation of the model is shown in Figure 3.16. The linear dimensions of the fibre RUC model are also indicated in Figure 3.16. The length of the fibre and RUC is denoted by L.
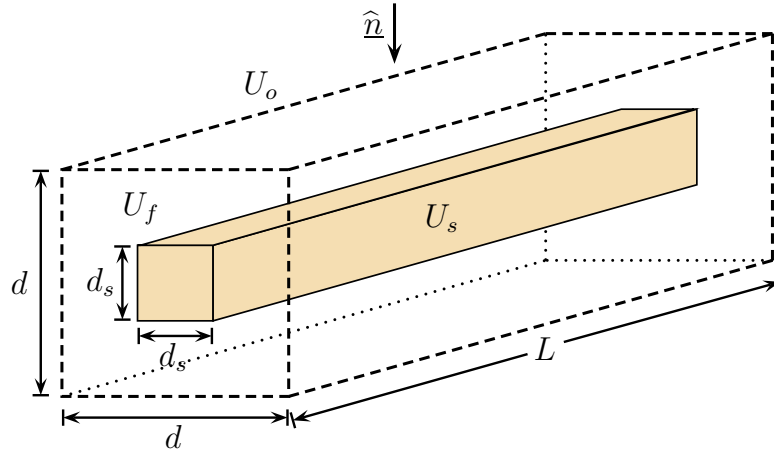
Figure 3.16: Fibre RUC model.

As mentioned in Section 3.2 (p 37), only cross-flow is considered in the fibre RUC model, as indicated by the streamwise direction, $\widehat{n}$, in Figure 3.16. In cross-flow through a bundle of unidirectional fibres, the velocity has no component in the direction parallel to the fibre axis. Flow through the RUC for fibre beds may therefore be regarded as two-dimensional flow, although the pore-scale geometry is three-dimensional.

The *solid width*, d_s, can be expressed as

$$d_s = d\sqrt{1 - \epsilon} \, . \tag{3.61}$$

The linear dimension of the RUC or *cell size*, d, is given by

$$d = \frac{d_s}{\sqrt{1 - \epsilon}} \, , \tag{3.62}$$

and the uniform *pore width*, $d - d_s$, which serves as a measure of the pore size, leads to

$$d - d_s = d\left(1 - \sqrt{1 - \epsilon}\right) \, . \tag{3.63}$$

The different arrays associated with the fibre RUC model are discussed in the following sections.

3.16.1 Fully staggered array

A three-dimensional schematic representation of an RUC associated with a fully staggered array is shown in Figure 3.17. The upstream and downstream solid surfaces in Figure 3.17 are those of neighbouring solids adjacent to a typical RUC in a fully staggered array.
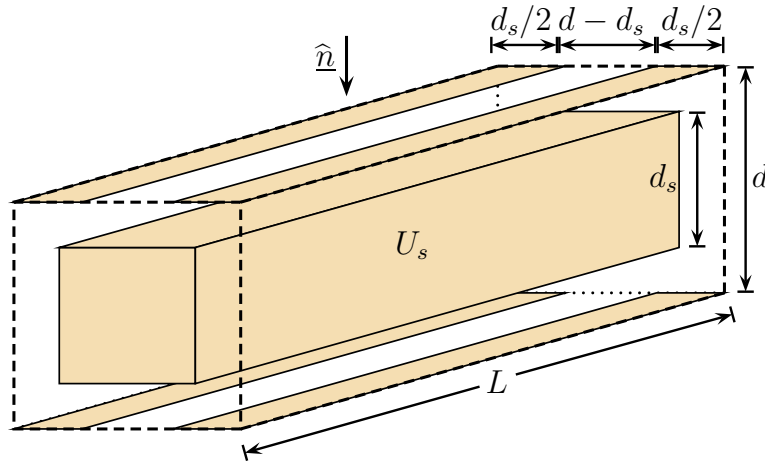
Figure 3.17: A three-dimensional schematic representation of an RUC associated with a fully staggered array for fibre beds.

3.16.2 Regular array

A three-dimensional schematic representation of an RUC associated with a regular array is shown in Figure 3.18 (p 74). The solid surfaces adjacent to the RUC in Figure 3.18 are those of neighbouring solids in a regular array. A stagnant fluid domain is present between the two neighbouring solids in the streamwise direction shown in Figure 3.18.

3.16.3 Volume partitioning

The quantification of the respective surfaces and volumes of the fully staggered and regular arrays for fibre beds, as illustrated two-dimensionally in Figure 3.3 (p 44), are given in Table 3.7 (p 74) as a function of the linear dimensions d, d_s and L.

Table D.3 (p 292) in Appendix D gives expressions for the respective volume and surface parameters in terms of d, ϵ and L.
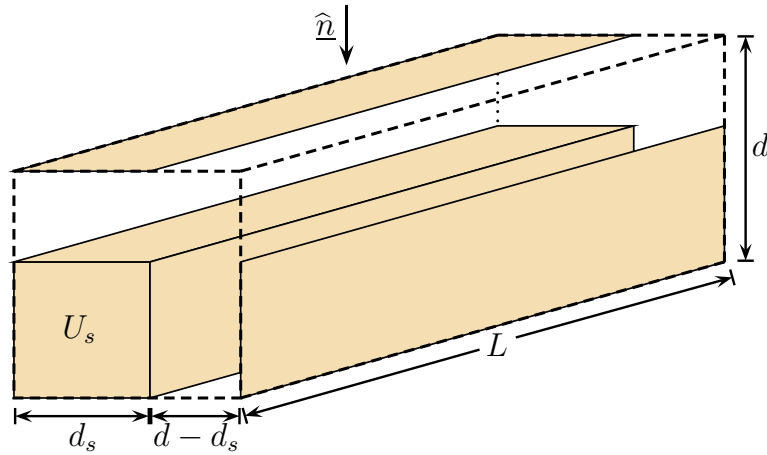
Figure 3.18: A three-dimensional schematic representation of an RUC associated with a regular array for fibre beds.

Table 3.7: Volume and surface partitioning table of the fibre RUC model in terms of d, d_s and L.

Parameter	Fibre RUC model	
U_o	$d^2 L$	
U_s	$d_s^2 L$	
U_f	$(d^2 - d_s^2) L$	
U_t	$(d - d_s)^2 L$	
$U_\parallel$	$d_s (d - d_s) L$	
S_{fs}	$4 d_s L$	
$S_\parallel$	$2 d_s L$	
	Fully staggered array	Regular array
$U_\perp$	$d_s (d - d_s) L$	0
$S_\perp$	$2 d_s L$	0
U_g	0	$d_s (d - d_s) L$
S_g	0	$2 d_s L$
S_{face}	$d_s L$	0

Cloete (2006) redefined the transfer fluid volume in the fully staggered array of the fibre RUC model as a rectangular volume bounded on one side by a fluid-solid interface on which the wall shear stresses are neglected. The other sides of the transfer fluid volume are fluid-fluid interfaces. In parts of the transfer fluid volume defined by Cloete (2006) the fluid flows perpendicular to the streamwise direction and in another part it flows parallel to the streamwise direction. In the transfer fluid volume of the present study the fluid only flows in the streamwise direction. The nett effect of the pressure gradient over the transfer fluid volume defined by Cloete (2006) is, however, shown to be zero so that it still serves as a transfer fluid volume. This newly defined transfer fluid volume of Cloete (2006) leads to a different permeability prediction of increasing complexity, which is not necessarily more accurate, than the permeability prediction that will be proposed in the present study.

3.16.4 Model parameters

The values (or expressions) for the model parameters of the fibre RUC model are presented in Table 3.8 (p 76).

Coefficient β

In the fully staggered array of the fibre RUC model it is assumed that the streamwise flux is split into two equal, but directionally opposite, transverse parts. As a result, the magnitude of the streamwise average channel velocity, $w_\parallel$, will be twice the magnitude of the transverse average channel velocity, $w_\perp$. According to equation (3.8) in Section 3.8 (p 45), it follows that $\beta = 1/2$.

The value of the coefficient β is zero for the regular array, since $w_\perp = \beta\, w_\parallel = 0$.

Coefficient ξ

The fully staggered array associated with the fibre RUC model has one symmetry plane perpendicular to the streamwise direction, as illustrated in Figure 3.19 (p 76). According to the definition given in Section 3.10 (p 46) for ξ, it follows that $\xi = 1/2$.

For the regular array of the fibre RUC model, $\xi = 0$, since $U_\perp = 0$.

Tortuosity

As in the case of the granular regular array, both the geometrical and kinematical tortuosities yield values of unity, for the regular array of the fibre RUC model.

Table 3.8: Fibre RUC model parameters.

Parameters	Fully staggered Array	Regular Array
β	$1/2$	0
ξ	$1/2$	0
χ_{geo}	$\dfrac{\epsilon}{1 - \sqrt{1 - \epsilon}}$	1
χ_{kin}	$1 + \xi\sqrt{1 - \epsilon}$	1
c_d	2.0	
$A_{p_\parallel}$	$(d - d_s)L$	
ψ	$\dfrac{\epsilon}{1 - \sqrt{1 - \epsilon}}$	

Figure 3.19: A two-dimensional upstream view of a fully staggered array associated with a fibre bed. The bold dashed line indicates a symmetry plane.

The expressions for the geometrical and kinematical tortuosities, presented in Table 3.8 (p 76) for the fully staggered array of the fibre RUC model, result from substitution of the respective equations for the different fluid volumes given in Table 3.7 (p 74) and the linear dimensions of the fibre RUC model, given by equations (3.61) and (3.62). Figure 3.20 shows both tortuosities as a function of porosity.
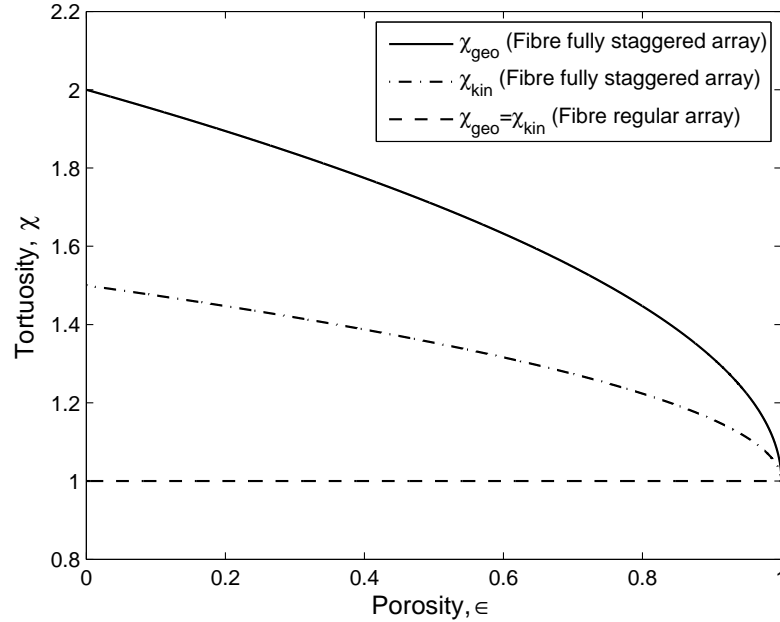
Figure 3.20: Tortuosity of the fibre RUC model as a function of porosity.

The reduction in tortuosity provided by the incorporation of the coefficient ξ into the kinematical tortuosity is again evident.

Geometric factor ψ

Similarly as in the case of the granular RUC model, the expression for the geometric factor, presented in Table 3.8 (p 76), is the same for both the fully staggered and regular arrays. It is also the same as the tortuosity of the fully staggered array, due to the same reasons as given in Section 3.14.4 (p 51).

Interstitial form drag coefficient c_d

The value of the form drag coefficient of 2, presented in Table A.1 (p 282), is for flow past a single square rod in an infinite stream. The value of $c_d = 2$ will also be used in the present study for the fibre RUC model.

Specific surface areas

The expressions for the respective specific surface areas (Section 3.13, p 48) are presented in Table 3.9.

Table 3.9: Specific surface areas of the fibre RUC model.

Parameter	Specific surface areas
A_{vd}	$\dfrac{4\,(1-\epsilon)}{d_s}$
A_{vs}	$\dfrac{4}{d_s}$
A_{vp}	$\dfrac{4\,(1-\epsilon)}{\epsilon\,d_s}$

These results are obtained from the corresponding expressions in Table 3.7 (p 74) together with equation (3.62).

3.16.5   Pore-scale linear dimensions

The physical flow properties of the fibre RUC model to be predicted, can be expressed in terms of either of the three pore-scale linear dimensions of the fibre RUC model, i.e. the solid width, d_s, the cell size, d, or the pore width, $d - d_s$. From a practical point of view, the experimentally measured pore-scale linear dimension usually specified for fibrous porous media is the cross-sectional size of the fibres.

The hydraulic radius, as discussed in Section 2.8.5 (p 20), may be expressed in terms of the solid width of the fibre RUC model as follows:

$$R_h \;=\; \frac{D_h}{4} \;=\; \frac{\epsilon\,U_s}{S_{fs}\,(1-\epsilon)} \;=\; \frac{\epsilon\,d_s^2\,L}{4\,d_s\,L\,(1-\epsilon)} \;=\; \frac{\epsilon\,d_s}{4\,(1-\epsilon)}\,. \tag{3.64}$$

Similarly, the hydraulic radius of the cylindrical cell model of Happel (1959), can be expressed as

$$R_h \;=\; \frac{D_h}{4} \;=\; \frac{\epsilon\,V_s}{A_s\,(1-\epsilon)} \;=\; \frac{\epsilon\,\pi\,a^2\,L}{2\,\pi\,a\,L\,(1-\epsilon)} \;=\; \frac{a\,\epsilon}{2\,(1-\epsilon)}\,. \tag{3.65}$$

Setting equations (3.64) and (3.65) equal, leads to the following relation between the fibre solid width, d_s, and the cylindrical radius, a:

$$d_s \;=\; 2\,a \;=\; D_a \;, \tag{3.66}$$

where D_a denotes the diameter of the inner solid cylinder.

The pressure gradient to be predicted by the fibre RUC model, may in addition to the three pore-scale linear dimensions mentioned above, also be expressed in terms of any of the three specific surface areas. From Table 3.9 (p 78) it thus follows that

$$d_s \;=\; \frac{4\,(1-\epsilon)}{A_{vd}} \;, \tag{3.67}$$

$$d_s \;=\; \frac{4}{A_{vs}} \;, \tag{3.68}$$

$$d_s \;=\; \frac{4\,(1-\epsilon)}{\epsilon\,A_{vp}} \;. \tag{3.69}$$

With the aid of equations (3.61) to (3.63), the relations between the specific surface areas and the cell size, d, or pore width, $d - d_s$ can also be obtained.

3.17   Summary

Three geometric pore-scale models are introduced in this chapter. In each model the solid material represents the average solid geometry of the actual porous medium under consideration. It is assumed that the solid phase is rigid, smooth, impermeable and stationary. The porosity of each RUC is assumed to be equal to the porosity of the corresponding REV. In each RUC model the channel width is assumed to be uniform. It is furthermore assumed that the fluid enters and exits each RUC in the streamwise direction.

For the granular and fibre RUC models two arrays are introduced, namely a fully staggered and a regular array. The solid surfaces parallel to the streamwise direction in each array are assumed to be aligned in the transverse direction(s), thus yielding no staggering in the transverse direction(s). In a fully staggered array maximum possible staggering occurs in the streamwise direction whereas in a regular array no staggering occurs in any of the three principal flow directions. A regular array contains stagnant fluid volumes between neighbouring solids in the streamwise direction.

All three models are assumed to be homogeneous. The RUC model for foamlike media is assumed to be transversely isotropic which may be justified by the presence of a fluid-fluid interface, equal to the channel cross-sectional flow area, on each of the six faces of the RUC. A justification of the assumption of transverse isotropy will be given in Chapter 4 for the granular and fibre RUC models.

The rectangular geometry of the RUC models allows for the assumption of piece-wise straight streamlines between and parallel to the plates. The piece-wise straight streamlines allows for the fluid domain inside each RUC model and array to be partitioned into different sub-volumes.

Stagnant fluid domains are accounted for through the introduction of the geometric factor, ψ. This factor replaces the tortuosity in the equations relating the superficial velocity and the streamwise average channel velocity. For the unconsolidated models the expression for the geometric factor, ψ, is the same as the expression obtained for the tortuosity of the fully staggered array. In the case of the foam RUC model, the expression for the geometric factor is the same as the expression obtained for the tortuosity of the doubly staggered model.

The coefficient β is furthermore introduced, which, together with the geometrical tortuosity, have the same effect as the kinematical tortuosity of Carman (1937). The coefficient ξ was originally introduced for the two-dimensional fibre model and no formal mathematical definition existed for this parameter. Such a definition is provided in this chapter and at the same time its meaning is generalized to be applicable to all three RUC models.

The porous medium parameters presented in Chapter 2 are quantified for each RUC model in terms of the respective pore-scale linear dimensions. The hydraulic diameter is used to facilitate comparison between the linear dimensions of the respective pore-scale models and their spherical and cylindrical counterparts. From the definition of the hydraulic diameter the solid width in the granular RUC model is set equal to the average spherical granular diameter. Similarly, for the fibre RUC model the solid width is set equal to the average cylindrical diameter.

In addition to the channel width, a three-dimensional pore diameter is introduced for the foam RUC model. Which pore-scale linear dimension to use in the foam RUC model when the model prediction is compared to experimental pressure drop data, for example, will depend on how the actual foam dimension was defined and measured. This information should be specified.

Chapter 4

Unified closure modelling with the RUC model

"The next step, often referred to as mathematical modelling of the problem, involves the representation of the conceptual model in the form of mathematical relationships."

- Bear & Bachmat (1991)

4.1 Introduction

In this chapter a unified analytical closure modelling procedure is presented for the three conceptual RUC models. Previously, the closure modelling procedures of the three RUC models were presented independently. The resulting unified equation for the streamwise pressure gradient is applicable to all three models up to the point where the geometric parameters, contained within the unified equation, are quantified for each of the three RUC models. A unified modelling procedure is useful since the geometrical and kinematical properties of the three RUC models can be quantified in terms of the same parameters, as they share the same geometrical features.

Three Reynolds numbers are defined, i.e. one in terms of each of the three pore-scale linear dimensions introduced. The closure modelling procedure of the surface integral of equation (2.32) is performed within two asymptotic limits, i.e. the limit of low Reynolds number flow and the steady laminar limit of the inertial flow regime. In the lower limit two analytical modelling procedures are proposed. The first one still involves the volume averaging theory and the second one comprises of a much shorter and direct modelling procedure.

Equations for the streamwise pressure gradient are obtained for each of the three RUC models in each of the two asymptotic limits. A power addition technique is then applied to the equations obtained for the streamwise pressure gradient in the two asymptotic

81

limits in order to obtain a unified equation for each model that is applicable over the entire steady laminar flow regime. Sets of predictive equations for the permeability and passability (i.e. a variation of the inertial coefficient) are also presented. Each set of equations is expressed in terms of each of the three pore-scale linear dimensions of the RUC models.

4.2   Unified analytical closure modelling procedure

The following assumption is made regarding the transition from the REV to the RUC:

Assumption 4-1 : All the properties of the REV may be embedded into the RUC.

Assumption 4-1 allows for equation (2.32) to be expressed in RUC notation, i.e.

$$-\nabla \langle p \rangle \;=\; \frac{1}{U_o} \iint_{S_{fs}} \left(\underline{n}\, p - \underline{n} \cdot \underline{\underline{\tau}} \right) \mathrm{d}S \;. \tag{4.1}$$

(The difference between equations (4.1) and (2.32) is the calligraphic font, associated with the REV parameters.) Equation (4.1) represents the total resistance to motion of the fluid due to the presence of solid material in the RUC.

The first step in the analytical closure modelling procedure is to decompose equation (4.1) into its streamwise and transverse components. By evaluating the surface integral over the different solid sub-surfaces according to the volume partitioning theory of the RUC (Section 3.6, p 43), yields the following expression for the streamwise component of equation (4.1):

$$-\nabla \langle p \rangle \;=\; \frac{1}{U_o} \iint_{S_\perp + S_g} \underline{n}\, p\, \mathrm{d}S \;-\; \frac{1}{U_o} \iint_{S_\parallel} \underline{n} \cdot \underline{\underline{\tau}}\, \mathrm{d}S \;. \tag{4.2}$$

The transverse component of equation (4.1) is given by

$$\underline{0} \;=\; \frac{1}{U_o} \iint_{S_\parallel} \underline{n}\, p\, \mathrm{d}S \;-\; \frac{1}{U_o} \iint_{S_\perp} \underline{n} \cdot \underline{\underline{\tau}}\, \mathrm{d}S \;-\; \frac{1}{U_o} \iint_{S_g} \underline{n} \cdot \underline{\underline{\tau}}\, \mathrm{d}S \;. \tag{4.3}$$

Note, once again, that in equations (4.2) and (4.3), $\underline{n}$ denotes the inwardly directed (with respect to the solid) unit vector normal to the fluid-solid interfaces. The terms on the right hand side of equation (4.3) add up to zero because there is no nett external pressure

gradient in the transverse direction. The first integral on the right hand side of equation (4.3) is zero due to Assumption 3-5 in which it is assumed that the solid surfaces parallel to the streamwise direction are aligned in the transverse direction. Consequently, the pressure on these surfaces cancel vectorially.

Recall that U_g was defined in Section 3.6 (p 43) as a fluid volume with a zero velocity field. Lloyd (2003), however, showed numerically (for the fibre RUC model) that wall shear stresses are created by those parts of the stagnant surfaces close to the streamwise channel, but these wall shear stresses are negligible, even for higher porosities. (This complies with the definition of U_g presented in Section 3.6.) Consequently, the following assumption is made:

Assumption 4-2 : The contribution of the wall shear stresses to the streamwise pressure gradient by stagnant surfaces is negligible.

Assumption 4-2 applies to all three RUC models. According to this assumption, the third integral on the right hand side of equation (4.3) may be neglected.

Since the first and third terms on the right hand side of equation (4.3) are zero, the second term should also be zero. The physical reason for this is that the flow in the transverse channels of a fully staggered array cancels vectorially due to directionally opposite flow in these channels.

The external streamwise pressure drop times unit area for fluid transport through the RUC is balanced by the sum of the pressure and viscous forces exerted by the solid material on the traversing fluid. The first surface integral of equation (4.2) denotes the inertial pressure forces exerted by the solid material on the traversing fluid due to a pressure variation over the upstream and downstream facing surfaces of the solid material. This pressure variation is analogous to the form drag condition described in Appendix A.3 (p 280). These interstitial inertial pressure forces contribute to the external pressure gradient, as opposed to the macroscopic inertial forces that vanished due to the assumption of a uniform superficial velocity field. Interstitially changes in momentum occur, which become significant at higher Reynolds numbers, but macroscopically momentum is conserved. The second surface integral of equation (4.2) denotes the viscous forces exerted by the solid material on the traversing fluid due to shear stresses at the fluid-solid interfaces. This viscous resistance is analogous to the viscous drag described in Appendix A.3.

Since the Reynolds number is defined as the ratio of inertial forces to viscous forces (Section 2.9, p 23), the contribution of the interstitial pressure and viscous forces to the streamwise pressure gradient depends on the magnitude of the Reynolds number.

4.3 Reynolds number

The Reynolds number will be defined for the RUC models in terms of the magnitude of the superficial velocity, q, and a pore-scale linear dimension (i.e. either d, d_s or $d - d_s$).

The *cell Reynolds number*, Re_{qd}, expressed in terms of the cell size, d, is given by

$$Re_{qd} \equiv \frac{\rho \, q \, d}{\mu} \, . \tag{4.4}$$

The *particle Reynolds number*, Re_{qds}, expressed in terms of the particle size, d_s, is given by

$$Re_{qds} \equiv \frac{\rho \, q \, d_s}{\mu} \, , \tag{4.5}$$

and the *pore Reynolds number*, Re_{qdds}, expressed in terms of the pore size, $d - d_s$, is given by

$$Re_{qdds} \equiv \frac{\rho \, q \, (d - d_s)}{\mu} \, . \tag{4.6}$$

The streamwise pressure gradient predicted by the RUC models will be expressed in terms of each of the latter three Reynolds numbers.

4.4 Lower Reynolds number limit

In the limit of low Reynolds number flow, i.e. when $Re_{qd} \to 0$, for example, viscous drag predominates over form drag. The effect of form drag may thus be neglected, with the shear stresses at the fluid-solid interfaces being the only contribution towards the streamwise pressure gradient.

Two analytical modelling procedures will be presented in this limit, i.e. closure modelling with pressure decomposition and inclusion of the Lloyd correction (Lloyd et al. (2004)) and secondly, a direct modelling procedure. The modelling procedure involving the pressure decomposition (to be presented below) differs from those presented previously in that the modelling procedure below is a unification of the modelling procedures presented independently in the past for the three RUC models. This requires that a weighting procedure should also be performed over the foam RUC model (which has not been done previously) and a mathematical definition had to be presented for the coefficient ξ (as was done in Section 3.10, p 46) that is applicable to all three RUC models. (A mathematical formulation has been presented in the past for the coefficient β only.) The coefficient ξ will be introduced in the present chapter into the two analytical closure modelling procedures. Both modelling procedures will be applicable to all three RUC models up to the point where the fluid-solid interfaces and the different fluid volumes are quantified for

each model. The direct modelling procedure to be presented thereafter serves as a much shorter approach for obtaining the same result.

4.4.1 Closure modelling with pressure decomposition and inclusion of the Lloyd correction

In the volume averaging procedure over an REV the boundaries of the REV intersect the solid and fluid volumes of the porous medium in a random manner. It should therefore also be possible for the walls of the RUC to randomly intersect either solid or fluid volumes. Two types of RUCs can be distinguished according to its particular location over a streamwise displacement of d. The two types of RUCs for the unconsolidated porous structures are illustrated two-dimensionally in Figures 4.1 (p 86) and 4.3 (p 87) for a fully staggered- and regular array (Lloyd et al. (2004)), respectively. The two types of RUCs for the consolidated porous structure are illustrated two-dimensionally for the doubly staggered foam model in Figure 4.2 (p 87). Figures 4.3 also serves as a two-dimensional representation of the two types of RUCs for the singly staggered and non-staggered foam models.

In Figures 4.1 to 4.3 the upstream and downstream facing surfaces of the RUC with corner points AAAA intersect two adjacent solids and the upstream and downstream facing surfaces of the RUC with corner points BBBB do not intersect any solid parts. A single solid volume, U_s, lies completely within the RUC with corner points BBBB and $U_\perp$ (or U_g) and U_t lie completely within the RUC with corner points AAAA. The RUC with corner points AAAA is thus applicable over a streamwise displacement of d_s and the RUC with corner points BBBB is applicable over a streamwise displacement of $d - d_s$. Let $S_{\perp_{AA}}$ denote the transverse surfaces of the RUC with corner points AAAA and let $S_{g_{AA}}$ denote the stagnant surfaces of the RUC with corner points AAAA. The same notation applies to the RUC with corner points BBBB.

To account for the relative frequency of occurrence of the two different types of RUCs over the cell size, d (Lloyd et al. (2004)), the surface integrals of equation (4.2) need to be weighed over a streamwise displacement, d. The weighting factor of the RUC with corner points AAAA in the streamwise direction is d_s/d and the weighting factor of the RUC with corner points BBBB is $(d - d_s)/d$. The streamwise pressure gradient may then be expressed as

$$-\nabla \langle p \rangle = \frac{d_s}{d} \frac{1}{U_o} \iint\limits_{S_{\perp_{AA}} + S_{g_{AA}}} \underline{n}\, p\, \mathrm{d}S + \frac{d - d_s}{d} \frac{1}{U_o} \iint\limits_{S_{\perp_{BB}} + S_{g_{BB}}} \underline{n}\, p\, \mathrm{d}S$$

$$- \frac{1}{U_o} \iint\limits_{S_\parallel} \underline{n} \cdot \underline{\underline{\tau}}\, \mathrm{d}S . \quad (4.7)$$

Regarding the RUC with corner points AAAA, the following assumption is made:
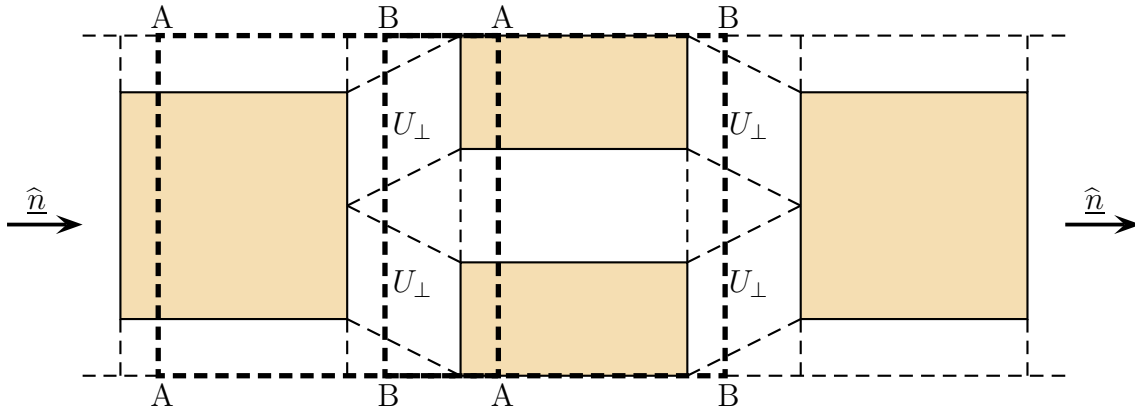
Figure 4.1: Two-dimensional representation of the two types of RUCs associated with a fully staggered array for unconsolidated porous structures.

Assumption 4-3 : There are no streamwise pressure drops over the transverse and stagnant surfaces of the RUC with corner points AAAA.

As a result of Assumption 4-3, the pressure distribution over the two transverse (and stagnant facing surfaces) of the RUC with corner points AAAA cancel vectorially, since the normal vectors on the opposing surfaces have opposite signs. Equation (4.7) then simplifies to

$$-\nabla \langle p \rangle \;=\; \frac{d - d_s}{d}\frac{1}{U_o} \iint\limits_{S_{\perp_{BB}} + S_{g_{BB}}} \underline{n}\, p\, \mathrm{d}S \;-\; \frac{1}{U_o}\iint\limits_{S_\parallel} \underline{n}\cdot\underline{\underline{\tau}}\,\mathrm{d}S \;. \tag{4.8}$$

Although the second integral on the right hand side of equation (4.3) cancel vectorially, it will be shown here that the transverse shear stresses contribute indirectly to the streamwise pressure gradient through the transverse pressure integral term of equation (4.8). To incorporate the contribution of these transverse shear stresses to the streamwise pressure gradient, the pressure on the transverse surfaces (and stagnant surfaces) of the RUC with corner points BBBB is decomposed into the average wall pressure, $\overline{p}_w$, and the wall pressure deviation, $\widetilde{p}_w$, i.e.

$$p \;=\; \overline{p}_w \;+\; \widetilde{p}_w \;. \tag{4.9}$$

The average wall pressure, $\overline{p}_w$, represents the average pressure over the transverse (or stagnant) surfaces and the wall pressure deviation, $\widetilde{p}_w$, is the difference between the actual pressure on these transverse (or stagnant) surfaces and the average wall pressure, $\overline{p}_w$. The contribution of the transverse shear stresses to the streamwise pressure gradient will be incorporated into the wall pressure deviation, $\widetilde{p}_w$. Substituting the pressure decomposition
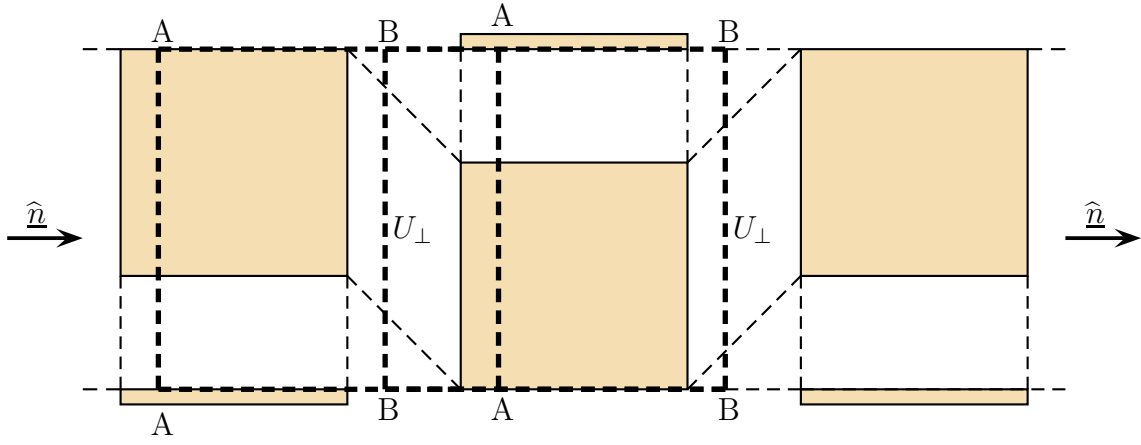
Figure 4.2: Two-dimensional representation of the two types of RUCs associated with a doubly staggered array for consolidated porous structures.
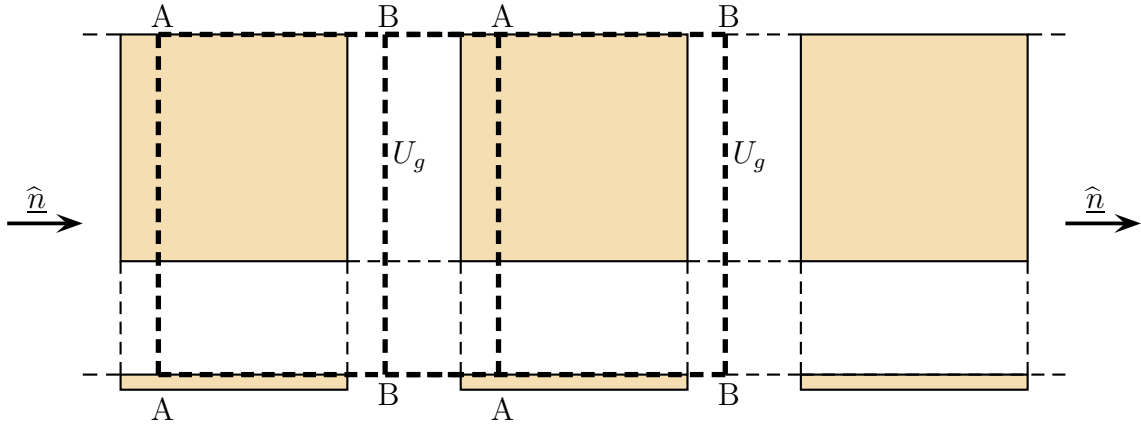
Figure 4.3: Two-dimensional representation of the two types of RUCs associated with a non-staggered array for consolidated and unconsolidated porous structures and a singly staggered array for consolidated porous structures.

of equation (4.9) into the pressure integral term of equation (4.8), leads to

$$-\nabla \langle p \rangle \; = \; \frac{d - d_s}{d} \frac{1}{U_o} \iint\limits_{S_{\perp_{BB}} + S_{g_{BB}}} \underline{n}\,\overline{p}_w\,\mathrm{d}S \; + \; \frac{d - d_s}{d} \frac{1}{U_o} \iint\limits_{S_{\perp_{BB}} + S_{g_{BB}}} \underline{n}\,\widetilde{p}_w\,\mathrm{d}S$$

$$- \frac{1}{U_o} \iint\limits_{S_{\parallel}} \underline{n} \cdot \underline{\underline{\tau}}\,\mathrm{d}S \; . \qquad (4.10)$$

The following assumption is made regarding the pressure deviations on the transverse surfaces of the RUC with corner points BBBB:

87

Assumption 4-4 : The pressure deviations on the transverse surfaces of the RUC with corner points BBBB contribute to the streamwise pressure gradient by an amount equal to the magnitude of the transverse wall shear stresses.

The streamwise pressure gradient may then be expressed as

$$-\nabla \langle p \rangle = \frac{d - d_s}{d} \frac{1}{U_o} \iint\limits_{S_{\perp_{BB}} + S_{g_{BB}}} \underline{n} \, \overline{p}_w \, \mathrm{d}S - \widehat{\underline{n}} \frac{1}{U_o} \iint\limits_{S_\perp} \underline{n} \cdot \underline{\underline{\tau}} \cdot \widetilde{\underline{n}} \, \mathrm{d}S - \frac{1}{U_o} \iint\limits_{S_\parallel} \underline{n} \cdot \underline{\underline{\tau}} \, \mathrm{d}S ,$$

(4.11)

where $\widetilde{\underline{n}}$ denotes the direction of the interstitial velocity field, such that $\underline{v} = v \, \widetilde{\underline{n}}$. Defining τ_w as the magnitude of the local wall shear stress, leads to

$$-\nabla \langle p \rangle = \frac{d - d_s}{d} \frac{1}{U_o} \iint\limits_{S_{\perp_{BB}} + S_{g_{BB}}} \underline{n} \, \overline{p}_w \, \mathrm{d}S + \frac{1}{U_o} \iint\limits_{S_\perp + S_\parallel} \tau_w \, \mathrm{d}S \, \widehat{\underline{n}} .$$

(4.12)

Let $\tau_{w_\parallel}$ denote the magnitude of the wall shear stresses on the streamwise surfaces, $S_\parallel$. Similarly, let $\tau_{w_\perp}$ denote the magnitude of the wall shear stresses on the transverse surfaces, $S_\perp$. The last integral on the right hand side of equation (4.12) will be simplified by making the following assumption:

Assumption 4-5 : The wall shear stresses are uniform.

In addition, the coefficient ξ will be introduced to account for the reduced area of the transverse surfaces subject to shear stresses in a fully staggered array containing $U_\perp-$volumes. Introducing the coefficient ξ then yields the following expression for the streamwise pressure gradient:

$$-\nabla \langle p \rangle = \frac{d - d_s}{d} \frac{1}{U_o} \iint\limits_{S_{\perp_{BB}} + S_{g_{BB}}} \underline{n} \, \overline{p}_w \, \mathrm{d}S + \frac{\tau_{w_\parallel} S_\parallel + \xi \, \tau_{w_\perp} S_\perp}{U_o} \widehat{\underline{n}} .$$

(4.13)

Lloyd (2003) showed for arrays of squares that the remaining surface integral may be expressed in terms of the gradient of the average pressure, i.e.

$$\frac{d - d_s}{d} \frac{1}{U_o} \iint\limits_{S_{\perp_{BB}} + S_{g_{BB}}} \underline{n} \, \overline{p}_w \, \mathrm{d}S = \left(\frac{U_\parallel + U_t}{U_f} - 1 \right) \nabla \langle p \rangle .$$

(4.14)

The surface integral of equation (4.14) was not evaluated by Lloyd (2003) for a fully staggered array. It was evaluated for a staggered array that provides less staggering than

88

the fully staggered array, referred to as an over-staggered array. In Appendix F (p 310) it is shown that equation (4.14) holds for the *fully staggered array* of the fibre RUC model as well as for the regular array. Due to the complexity of the three-dimensional geometric models, equation (4.14) is not evaluated in Appendix F for the arrays of the granular model and for the foam sub-models, but is assumed to be equally applicable to these models. Equation (4.14) will henceforth be referred to as the Lloyd correction. Inclusion of the Lloyd correction in the total streamwise pressure gradient leads to

$$-\nabla \langle p \rangle \;=\; \left(\frac{U_\| + U_t}{U_f} - 1 \right) \nabla \langle p \rangle \;+\; \frac{\tau_{w_\|} S_\| + \xi\, \tau_{w_\perp} S_\perp}{U_o} \, \widehat{n} \,, \tag{4.15}$$

and after simplification, it follows that

$$-\nabla \langle p \rangle \;=\; \frac{\tau_{w_\|} S_\| + \xi\, \tau_{w_\perp} S_\perp}{U_o} \, \psi \, \widehat{n} \,. \tag{4.16}$$

Introducing the coefficient β (Section 3.8, p 45) through the wall shear stress, i.e. $\tau_{w_\|} = (1/\beta)\tau_{w_\perp}$, leads to

$$-\nabla \langle p \rangle \;=\; \frac{S_\| + \beta\, \xi S_\perp}{U_o} \, \tau_{w_\|} \, \psi \, \widehat{n} \,. \tag{4.17}$$

According to equation (B.3) in Appendix B (p 283), the phase average pressure can be expressed in terms of the intrinsic phase average pressure, i.e.

$$-\nabla \left(\epsilon \, \langle p \rangle_f \right) \;=\; \frac{S_\| + \beta\, \xi \, S_\perp}{U_o} \, \tau_{w_\|} \psi \, \widehat{n} \,. \tag{4.18}$$

For a porous medium of uniform porosity, the streamwise pressure gradient may be expressed as

$$-\nabla \langle p \rangle_f \;=\; -\frac{\mathrm{d}p}{\mathrm{d}x} \, \widehat{n} \;=\; \frac{S_\| + \beta\, \xi \, S_\perp}{\epsilon\, U_o} \, \tau_{w_\|} \psi \, \widehat{n} \,. \tag{4.19}$$

The wall shear stresses may be quantfied by making use of the following assumption:

Assumption 4-6 : The flow in the channels of the RUC is described as plane-Poiseuille flow.

Based on Assumption 4-6, the modelling procedure in this limit will be applicable for low to moderate porosities. In plane-Poiseuille flow fully developed flow and a no-slip boundary condition are assumed. The wall shear stresses on the streamwise surfaces for flow of a Newtonian fluid (Appendix A.1, p 279) between parallel plates a uniform distance $d - d_s$ apart, may thus be described as

$$\tau_{w_\|} \;=\; \frac{6\, \mu\, w_\|}{d - d_s} \;=\; \frac{6\, \mu\, q}{d - d_s} \frac{\psi}{\epsilon} \,. \tag{4.20}$$

In equation (4.20) the total streamwise wall shear stress was expressed in terms of the superficial velocity by making use of equation (3.16). Substituting equation (4.20) into equation (4.19) yields

$$-\nabla \langle p \rangle_f \;=\; \frac{S_\parallel + \beta\, \xi S_\perp}{U_o}\, \frac{6\, \psi^2}{\epsilon^2\, (d - d_s)}\, \mu\, q\, \widehat{\underline{n}}\, . \tag{4.21}$$

Application of Darcy's law (Section (2.8.2), p 18) leads to the following expression for the permeability, k:

$$k \;=\; \frac{\mu q}{-\frac{\mathrm{d}p}{\mathrm{d}x}} \;=\; \frac{U_o}{S_\parallel + \beta\, \xi\, S_\perp}\, \frac{\epsilon^2\, (d - d_s)}{6\, \psi^2}\, . \tag{4.22}$$

Equation (4.22) is applicable to all three RUC models. The permeability and streamwise pressure drop may now be quantified for each of the three RUC geometries by making use of the respective volume and surfaces partitioning tables presented in Chapter 3 (i.e Tables 3.1 (p 51), 3.4 (p 62) and 3.7 (p 74)).

Transversely isotropic RUC models

As mentioned in Section 3.4 (p 42), the fully staggered array cannot be regarded as transversely isotropic. A mathematical average will be performed in this section to classify the granular and fibre RUC models as transversely isotropic.

The assumption of alignment of solid surfaces in the transverse direction(s) of the granular and fibre model arrays (i.e. Assumption 3-5, p 40) was made deliberately so that in the fully staggered array staggering occurs only in the streamwise direction whereas in the other two principal directions no staggering occurs. Flow in the transverse direction(s) then corresponds to flow in the streamwise direction of a regular array. Transverse isotropy is obtained for the granular RUC model by giving twice the weight to the coefficient in the resulting equation of the granular regular array and a weight of unity to the coefficient of the granular fully staggered array. After substituting the expressions for the corresponding surfaces and volumes into equation (4.22), the resulting coefficient can be expressed as $12\,(2 + \beta\, \xi)$. The coefficients of the respective models/arrays are presented in Table 4.1 (p 91) and the corresponding values of $\beta\, \xi$ are presented in Table 4.2 (p 92).

As already mentioned in Section 3.14.4 (p 51), the value of the coefficient of the transversely isotropic granular RUC model, as given in Table 4.1, differs from the coefficient value given by Woudberg & Du Plessis (2008) and Woudberg (2006). In Woudberg & Du Plessis (2008) and Woudberg (2006) the value of the coefficient ξ was reported as 1/2. The correct value of $\xi = 1/4$ and the corresponding coefficient value of 25.4 is, however, presented in Du Plessis & Woudberg (2008).

For the fibre RUC model two-dimensional transverse isotropy is obtained by weighing the coefficients of the fibre fully staggered and regular arrays equally. This weighting procedure has not previously been applied to the fibre model.

Table 4.1: Expressions for the respective coefficients of the three RUC models.

Model/Array	Coefficient
Granular	$12\left(2 + \beta\,\xi\right)$
Fully staggered	28.2
Regular	24
Transversely isotropic model	25.4
Foam	$6\left(1 + \beta\,\xi\,\dfrac{(8 - 4\sigma)}{4}\right)$
Doubly staggered	36
Singly staggered	24
Non-staggered	12
Fibre	$12\left(1 + \beta\,\xi\right)$
Fully staggered	15
Regular	12
Transversely isotropic model	13.5

Expressions for the permeability, k, as a function of the cell size, d, i.e. k_d, in terms of the solid width, d_s, i.e. k_{ds}, and in terms of the pore width, $d - d_s$, i.e. k_{dds}, are presented in Tables 4.3 (p 93), 4.4 (p 94) and 4.5 (p 95), respectively, for the various RUC models.

The corresponding expressions for the streamwise pressure gradient are presented in Tables 4.6 to 4.8 (pp 97-99).

4.4.2   Direct modelling procedure

In this section it will be shown that the result of equation (4.19), which is applicable to all three RUC models, can be obtained by following a shorter direct modelling procedure.

Table 4.2: Expressions for $\beta\xi$ for the respective RUC models.

Model/Array	$\beta\xi$
Granular model:	
Fully staggered array	$\sqrt{2}/4$
Regular array	0
Foam model:	
Doubly staggered model	1
Singly staggered model	1
Non-staggered model	0
Fibre model:	
Fully staggered array	$1/4$
Regular array	0

The present work follows the direct modelling procedure of Firdaouss & Du Plessis (2004), who studied the prediction of the permeability for cross-flow through anisotropic periodic unidirectional fibre beds. The authors have distinguished between staggered and non-staggered arrays. A shape factor was introduced in which the unit cell aspect ratio is assumed to be the same as the particle aspect ratio. The aspect ratio was used to determine the permeability coefficient *separately* for each of the five configurations considered by them. In the present study the coefficient ξ was introduced to determine the coefficient value of different arrays in a more general and compact manner. The paper of Firdaouss & Du Plessis (2004) includes errors in some of the equations. (The final result is, however, correct.) The errors were outlined and corrected upon by the author of this dissertation in conjunction with co-authors. An erratum to the paper of Firdaouss & Du Plessis (2004) appears as Firdaouss et al. (2009).

In the present study, it will be shown that the direct modelling procedure can be applied to all three RUC models and the result is the same as that of equation (4.19).

For the purpose of the direct modelling procedure, the Representative Unit Cell (abbreviated RUC), may be referred to as only a Unit Cell (abbreviated UC). The term, "Representative", is associated with the volume averaging procedure. The only manner in which the volume averaging procedure enters the direct modelling procedure is through the superficial velocity, $\underline{q}$, and the streamwise and transverse average channel velocities, $\underline{w}_{\parallel}$ and $\underline{w}_{\perp}$, respectively. Whereas the REV, and consequently the RUC, represents a statistically representative volume of the porous medium over which volumetric averages are determined, the unit cell can be regarded as an elementary building block that can be used to reconstruct the porous medium through duplication and stacking of the unit cell.

Table 4.3: Expressions for the permeability, k_d.

Model/Array	Permeability, k_d
Granular model:	$\dfrac{d^2 \left(1 - (1-\epsilon)^{1/3}\right) \left(1 - (1-\epsilon)^{2/3}\right)^2}{25.4 \,(1-\epsilon)^{2/3}}$
Foam model (Crosnier et al. (2006)):	
Doubly staggered model	$\dfrac{\epsilon^2 \, d^2}{36 \, \psi^2 \, (\psi - 1)}$
Singly staggered model	$\dfrac{\epsilon^2 \, d^2}{24 \, \psi^2 \, (\psi - 1)}$
Non-staggered model	$\dfrac{\epsilon^2 \, d^2}{12 \, \psi^2 \, (\psi - 1)}$
Fibre model:	$\dfrac{d^2 \,(1 - \sqrt{1-\epsilon})^3}{13.5 \,\sqrt{1-\epsilon}}$

When considering the cell in the fully staggered array of Figure 3.2 (p 39) as a unit cell, it is regarded as a building block, as opposed to the RUC which cannot be regarded as a building block because it is based on averages. The unit cell should extend over a streamwise displacement of $2d$, as was done by Firdaouss & Du Plessis (2004), since that is the distance over which periodicity is obtained. This will however, lead to the same result should the unit cell extend over a distance d, since, in addition to the steamwise displacement that doubles, all the volumes and surfaces inside the extended unit cell also doubles. The fact that the same permeability prediction is obtained by Firdaouss & Du Plessis (2004) for a fully staggered array as to be proposed in the present study, serves as proof. To avoid the factor of 2 to be 'carried along', the pressure drop will be evaluated over a streamwise displacement of d. Another difference when dealing with a UC as opposed to an RUC is that when measuring over an REV, uniformly sized solids is not a prerequisite for homogeneity, but when measuring over a unit cell it becomes a prerequisite. Uniformly sized solids will thus be assumed for the purpose of the unit cell to justify the assumption of homogeneity.

The magnitude of the total force over the UC can be expressed as the product of the total pressure drop over the UC and the streamwise cross-sectional flow area, i.e. $\Delta p \, A_{p_\parallel}$. The

Table 4.4: Expressions for the permeability, k_{ds}.

Model/Array	Permeability, k_{ds}
Granular model:	$\dfrac{d_s^2 \left(1 - (1-\epsilon)^{1/3}\right) \left(1 - (1-\epsilon)^{2/3}\right)^2}{25.4\,(1-\epsilon)^{4/3}}$
Foam model (Crosnier et al. (2006)):	
Doubly staggered model	$\dfrac{\epsilon^2\,d_s^2}{9\,\psi^2\,(\psi-1)^3}$
Singly staggered model	$\dfrac{\epsilon^2\,d_s^2}{6\,\psi^2\,(\psi-1)^3}$
Non-staggered model	$\dfrac{\epsilon^2\,d_s^2}{3\,\psi^2\,(\psi-1)^3}$
Fibre model:	$\dfrac{d_s^2\,(1-\sqrt{1-\epsilon})^3}{13.5\,(1-\epsilon)^{3/2}}$

magnitude of this force may also be expressed as the sum of the magnitude of the forces exerted by the solid(s) on the fluid in the streamwise and transverse channels, i.e.

$$\Delta p\, A_{p_\parallel} \;=\; S_\parallel \tau_{w_\parallel} \;+\; \xi S_\perp \tau_{w_\perp}\,. \tag{4.23}$$

The total pressure drop over the UC may thus be expressed as

$$\Delta p \;=\; \frac{S_\parallel \tau_{w_\parallel} \;+\; \xi S_\perp \tau_{w_\perp}}{A_{p_\parallel}}, \tag{4.24}$$

leading to

$$\Delta p \;=\; \frac{S_\parallel + \beta\,\xi\,S_\perp}{A_{p_\parallel}}\,\tau_{w_\parallel} \;=\; \frac{S_\parallel + \beta\,\xi\,S_\perp}{A_{p_\parallel}\,d}\,\tau_{w_\parallel} d\,. \tag{4.25}$$

From equation (3.15) it then follows that

$$\frac{\Delta p}{d} \;=\; \frac{S_\parallel + \beta\,\xi\,S_\perp}{U_f}\,\tau_{w_\parallel}\psi\,. \tag{4.26}$$

Table 4.5: Expressions for the permeability, k_{dds}.

Model/Array	Permeability, k_{dds}
Granular model:	$\dfrac{(d-d_s)^2 \left(1-(1-\epsilon)^{2/3}\right)^2}{25.4\,(1-\epsilon)^{2/3}\left(1-(1-\epsilon)^{1/3}\right)}$
Foam model (Crosnier et al. (2006)):	
Doubly staggered model	$\dfrac{\epsilon^2\,(d-d_s)^2}{9\,\psi^2\,(\psi-1)(3-\psi)^2}$
Singly staggered model	$\dfrac{\epsilon^2\,(d-d_s)^2}{6\,\psi^2\,(\psi-1)(3-\psi)^2}$
Non-staggered model	$\dfrac{\epsilon^2\,(d-d_s)^2}{3\,\psi^2\,(\psi-1)(3-\psi)^2}$
Fibre model:	$\dfrac{(d-d_s)^2(1-\sqrt{1-\epsilon})}{13.5\,\sqrt{1-\epsilon}}$

Equation (4.26) is equivalent to equation (4.19). The direct method is therefore a significantly simpler modelling procedure than the former one involving the method of volume averaging. The pressure decomposition and the Lloyd correction are therefore, in principle, not necessary, but the direct modelling procedure may not be so simple should non-spherical and/or a non-uniform distribution of solids be considered. The direct modelling procedure is therefore more restricted than the modelling procedure involving the method of volume averaging.

Dimensionless parameters

The dimensionless permeability, K_d, expressed in terms of the RUC cell size, d, is defined as

$$K_d \;\equiv\; \frac{k_d}{d^2}\;, \tag{4.27}$$

where k_d is the permeability in terms of the cell size, d. The dimensionless permeability,

K_{ds}, as a function of the solid width, d_s, is similarly defined as

$$K_{ds} \equiv \frac{k_{ds}}{d_s^2} , \tag{4.28}$$

where k_{ds} is the permeability in terms of the solid width, d_s. Lastly, the dimensionless permeability, K_{dds}, expressed in terms of the pore width, $d - d_s$, is defined as

$$K_{dds} \equiv \frac{k_{dds}}{(d - d_s)^2} , \tag{4.29}$$

where k_{dds} is the permeability in terms of the pore width, $d - d_s$. Expressions for the respective dimensionless permeabilities are presented in Tables D.4 to D.6 (pp 293-295) in Appendix D.

For unidirectional flow in the positive x-direction of a rectangular Cartesian coordinate system, the streamwise pressure gradient of a Newtonian fluid in the limit of low Reynolds number flow may, analogously to Darcy's law (Section 2.8.2, p 18), be expressed as

$$-\left.\frac{\mathrm{d}p}{\mathrm{d}x}\right|_{Re \to 0} = \mu\, f_0\, q , \tag{4.30}$$

where f_0 is the drag (or shear) factor in the asymptotic limit of low Reynolds number flow. The relation between f_0 and the permeability is given by

$$f_0 = \frac{1}{k} . \tag{4.31}$$

The dimensionless drag factor in the limit of low Reynolds number flow, defined in terms of the RUC cell size, d, is given by

$$F_{0_d} \equiv f_{0_d}\, d^2 , \tag{4.32}$$

where f_{0_d} is the drag factor in the limit of low Reynolds number flow in terms of the cell size, d. The dimensionless drag factor in the limit of low Reynolds number flow, defined in terms of the solid width, d_s, is given by

$$F_{0_{ds}} \equiv f_{0_{ds}}\, d_s^2 , \tag{4.33}$$

where $f_{0_{ds}}$ is the drag factor in the limit of low Reynolds number flow in terms of the solid width, d_s. Lastly, the dimensionless drag factor in the limit of low Reynolds number flow, defined in terms of the pore width, $d - d_s$, is given by

$$F_{0_{dds}} \equiv f_{0_{dds}}\, (d - d_s)^2 , \tag{4.34}$$

where $f_{0_{dds}}$ is the drag factor in the limit of low Reynolds number flow in terms of the pore width, $d - d_s$. Expressions for the respective dimensionless drag factors are presented in Tables D.7 to D.9 (pp 296-298) in Appendix D.

Table 4.6: Expressions for the streamwise pressure gradient, $-\mathrm{d}p/\mathrm{d}x$, in the limit of low Reynolds number flow as a function of d.

Model/Array	Streamwise pressure gradient, $-\mathrm{d}p/\mathrm{d}x$
Granular model:	$\dfrac{25.4\,(1-\epsilon)^{2/3}\,\mu\,q}{d^2\,\left(1-(1-\epsilon)^{1/3}\right)\left(1-(1-\epsilon)^{2/3}\right)^2}$
Foam model (Crosnier et al. (2006)):	
Doubly staggered model	$\dfrac{36\,\psi^2\,(\psi-1)\,\mu\,q}{\epsilon^2 d^2}$
Singly staggered model	$\dfrac{24\,\psi^2\,(\psi-1)\,\mu\,q}{\epsilon^2 d^2}$
Non-staggered model	$\dfrac{12\,\psi^2\,(\psi-1)\,\mu\,q}{\epsilon^2 d^2}$
Fibre model:	$\dfrac{13.5\,\sqrt{1-\epsilon}\,\mu\,q}{d^2\,(1-\sqrt{1-\epsilon})^3}$

4.5 Steady laminar limit of the inertial flow regime

In the steady laminar limit of the inertial flow regime, form drag (Appendix A.3, p 280) predominates over viscous drag. The shear stress integral term of equation (4.2) is therefore negligible, yielding

$$-\nabla\,\langle p\rangle \;=\; \frac{1}{U_o}\iint\limits_{S_\perp + S_g} \underline{n}\,p\,\mathrm{d}S\,. \tag{4.35}$$

The pressure variation over the solid surfaces normal to the streamwise direction is largely due to separation of the boundary layer (Roberson & Crowe (1985)). As a result, a recirculation pattern is generated on the lee side of the solid. The microscopic inertial effects in this limit will be modelled through consideration of interstitial flow recirculation within the separation zone on the lee side of the solid material, as illustrated schematically in Figure 4.4 (p 99) for a fully staggered array. A similar configuration is assumed to be applicable to the doubly and singly staggered foam RUC models. (Molale (2007) confirmed

Table 4.7: Expressions for the streamwise pressure gradient, $-\mathrm{d}p/\mathrm{d}x$, in the limit of low Reynolds number flow as a function of d_s.

Model/Array	Streamwise pressure gradient, $-\mathrm{d}p/\mathrm{d}x$
Granular model:	$\dfrac{25.4\,(1-\epsilon)^{4/3}\,\mu\,q}{d_s^2\,\left(1-(1-\epsilon)^{1/3}\right)\left(1-(1-\epsilon)^{2/3}\right)^2}$
Foam model (Crosnier et al. (2006)):	
Doubly staggered model	$\dfrac{9\,\psi^2\,(\psi-1)^3\,\mu\,q}{\epsilon^2\,d_s^2}$
Singly staggered model	$\dfrac{6\,\psi^2\,(\psi-1)^3\,\mu\,q}{\epsilon^2\,d_s^2}$
Non-staggered model	$\dfrac{3\,\psi^2\,(\psi-1)^3\,\mu\,q}{\epsilon^2\,d_s^2}$
Fibre model:	$\dfrac{13.5\,(1-\epsilon)^{3/2}\,\mu\,q}{d_s^2\,(1-\sqrt{1-\epsilon})^3}$

numerically for the fibre RUC model the presence of interstitial recirculation on the lee side of solids in the steady laminar inertial flow regime.)

A form drag condition (Appendix A.3.1, p 281) for flow past a single obstacle in an infinite stream will be adopted through the introduction of the interstitial form drag coefficient for granular media, foamlike media and fibre beds (Sections 3.14.4 (p 51), 3.15.6 (p 63) and 3.16.4 (p 75), respectively). The modelling procedure in this limit will thus be applicable at moderate to high porosities.

The stagnant surfaces may be neglected from the surface integral in equation (4.35) since interstitial flow recirculation will not occur in the stagnant fluid volumes. Another reason for neglecting the stagnant surfaces from the surface integral is because stagnant fluid domains are unlikely to occur at high porosities. Furthermore, splitting the surface integral over the transverse surfaces into upstream and downstream transverse surfaces, denoted respectively by $S_{\perp_U}$ and $S_{\perp_D}$, yields

Table 4.8: Expressions for the streamwise pressure gradient, $-\mathrm{d}p/\mathrm{d}x$, in the limit of low Reynolds number flow as a function of $d - d_s$.

Model/Array	Streamwise pressure gradient, $-\mathrm{d}p/\mathrm{d}x$
Granular model:	$\dfrac{25.4\,(1-\epsilon)^{2/3}\left(1-(1-\epsilon)^{1/3}\right)\mu\,q}{(d-d_s)^2\,\left(1-(1-\epsilon)^{2/3}\right)^2}$
Foam model (Crosnier et al. (2006)):	
Doubly staggered model	$\dfrac{9\,\psi^2\,(\psi-1)(3-\psi)^2\,\mu\,q}{\epsilon^2\,(d-d_s)^2}$
Singly staggered model	$\dfrac{6\,\psi^2\,(\psi-1)(3-\psi)^2\,\mu\,q}{\epsilon^2\,(d-d_s)^2}$
Non-staggered model	$\dfrac{3\,\psi^2\,(\psi-1)(3-\psi)^2\,\mu\,q}{\epsilon^2\,(d-d_s)^2}$
Fibre model:	$\dfrac{13.5\,\sqrt{1-\epsilon}\,\mu\,q}{(d-d_s)^2\,(1-\sqrt{1-\epsilon})}$
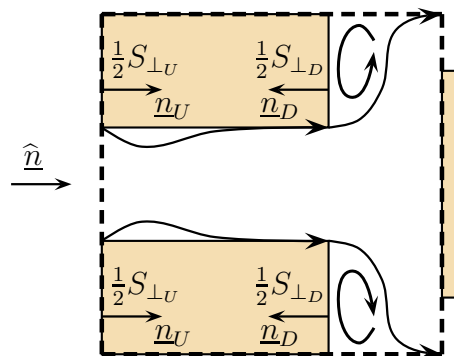
Figure 4.4: Schematic illustration of the interstitial recirculation on the lee side of the solids in an RUC associated with a fully staggered array.

$$-\nabla \langle p \rangle \;=\; \frac{1}{U_o} \iint\limits_{S_{\perp_U}} \underline{n}\, p \, \mathrm{d}S \;+\; \frac{1}{U_o} \iint\limits_{S_{\perp_D}} \underline{n}\, p \, \mathrm{d}S \, . \tag{4.36}$$

Let $\underline{n}_U$ denote the inwardly directed normal vector on $S_{\perp_U}$ and similarly, let $\underline{n}_D$ be the inwardly directed normal vector on $S_{\perp_D}$, as indicated in Figure 4.4 (p 99).

It then follows that $-\underline{n}_D = \underline{n}_U = \widehat{n}$, yielding

$$-\nabla \langle p \rangle \;=\; \frac{\widehat{n}}{U_o} \left[\iint\limits_{S_{\perp_U}} p \, \mathrm{d}S \;-\; \iint\limits_{S_{\perp_D}} p \, \mathrm{d}S \right] . \tag{4.37}$$

Equation (4.37) can be simplified with the aid of the following assumption:

Assumption 4-7 : The pressure on the upstream and downstream transverse surfaces is uniform.

Since $S_{\perp_U} = S_{\perp_D} = S_{face}$, it follows that

$$-\nabla \langle p \rangle \;=\; \frac{S_{face}}{U_o} \Delta p \, \widehat{n} \, . \tag{4.38}$$

The streamwise pressure drop Δp is then approximated by

$$\Delta p \;=\; \frac{\mathcal{F}_p}{\mathcal{A}_p} \;=\; C_d \frac{\rho \, v_\infty^2}{2} \, , \tag{4.39}$$

where $\mathcal{F}_p$ is the total pressure drag force on a single submerged body, $\mathcal{A}_p$ is the projected cross-sectional area of the body, which, in this case is equal to S_{face}, C_d is the form drag coefficient (Appendix A.3.1, p 281) and v_∞ is the magnitude of the velocity, far upstream, with which the fluid approaches the body. Thus, in adopting the form drag condition from equation (4.39) for flow past a single body in an infinite stream to flow past a body in a porous medium, the form drag coefficient, C_d, becomes the interstitial form drag coefficient, c_d, and the following assumption is made:

Assumption 4-8 : The approaching (or free stream) velocity is equal to the streamwise average channel velocity.

With the aid of Assumption 4-8 and the transition from C_d to c_d, the effect of the porous medium is incorporated into the total pressure drag. The streamwise pressure gradient may accordingly be expressed as

$$-\nabla \langle p \rangle \;=\; \frac{S_{face}}{2\,U_o} \, c_d \, \rho \, w_\parallel^2 \, \widehat{n} \, . \tag{4.40}$$

For a porous medium of uniform porosity, equation (B.3) (p 284) in Appendix B can be employed to yield

$$-\nabla \langle p \rangle_f \;=\; \frac{S_{face}}{2 \, \epsilon \, U_o} \, c_d \, \rho \, w_{\parallel}^2 \, \widehat{\underline{n}} \,. \tag{4.41}$$

By making use of equation (3.16) the streamwise pressure gradient may be expressed in terms of the magnitude of the superficial velocity as follows:

$$-\nabla \langle p \rangle_f \;=\; -\frac{\mathrm{d}p}{\mathrm{d}x} \widehat{\underline{n}} \;=\; \frac{S_{face} \, \psi^2}{2 \, \epsilon^3 \, U_o} \, c_d \, \rho \, q^2 \, \widehat{\underline{n}} \,. \tag{4.42}$$

Equation (4.42) is applicable to all three RUC models. Expressions for the streamwise pressure gradient, $-\mathrm{d}p/\mathrm{d}x$, in terms of the cell size, d, the solid width, d_s, and the pore width, $d - d_s$, are presented in Tables 4.9 (p 102), 4.10 (p 103) and 4.11 (p 104), respectively, for the various RUC models. For the non-staggered foam model the streamwise pressure gradient in the steady laminar limit of the inertial flow regime is zero simply because the presence of stagnant fluid volumes were disregarded in this regime due to the reasons previously mentioned.

The closure modelling procedure presented in this section was similarly followed by Du Plessis & Van der Westhuizen (1993) for the 2D fibre model and by Du Plessis et al. (1994) for the foam RUC model. It was shown in this section that the same closure modelling procedure may be used for all three RUC models. The result of equation (4.42) is different from the result obtained by Crosnier et al. (2006) for foamlike media. The latter authors have also incorporated the Lloyd correction in the closure modelling procedure at higher Reynolds numbers. There is, however, no evidence for the scientific correctness for such an approach, since Lloyd et al. (2004) have verified numerically the validity of the Lloyd correction only in the Darcy regime.

An alternative closure modelling procedure for the steady laminar limit of the inertial flow regime was followed by Du Plessis (1994), Du Plessis (2002), Wilms (2006) and Woudberg (2006). This modelling approach, in which Bernoulli's equation is employed, is presented in Appendix G (p 315). Both methods, however, lead to the same result. The one method cannot be regarded as inferior to the other, since in both methods over-simplifying assumptions are made: In the modelling approach presented above, the form drag condition for flow past a *single* solid in an infinite stream is adopted and in the modelling procedure presented in Appendix G Bernoulli's equation for ideal flow, i.e. non-viscous flow, is used.

The passability (Section 2.8.3, p 19), η, can be expressed in RUC notation as (Crosnier et al. (2006))

$$\eta \;=\; \frac{2 \, \epsilon^3 \, U_o}{c_d \, S_{face} \, \psi^2} \,. \tag{4.43}$$

Expressions for the passability as a function of the cell size, d, i.e. η_d, in terms of the solid width, d_s, i.e. η_{ds}, and in terms of the pore width, $d - d_s$, i.e. η_{dds}, are presented in

Table 4.9: Expressions for the streamwise pressure gradient, $-\mathrm{d}p/\mathrm{d}x$, in the steady laminar limit of the inertial flow regime as a function of d.

Model/Array	Streamwise pressure gradient, $-\mathrm{d}p/\mathrm{d}x$
Granular model:	$\dfrac{(1-\epsilon)^{2/3}}{2\,\epsilon\,d\,\left(1-(1-\epsilon)^{2/3}\right)^2}\,c_d\,\rho\,q^2$
Foam model Doubly staggered model	$\dfrac{(\psi-1)(3-\psi)\,\psi^2}{4\,\epsilon^3 d}\,c_d\,\rho\,q^2$
Singly staggered model	$\dfrac{(\psi-1)(3-\psi)\,\psi^2}{8\,\epsilon^3 d}\,c_d\,\rho\,q^2$
Non-staggered model	0
Fibre model:	$\dfrac{\sqrt{1-\epsilon}}{2\,\epsilon\,d\,(1-\sqrt{1-\epsilon})^2}\,c_d\,\rho\,q^2$

Tables 4.12, 4.13 and 4.14 (pp 105-107), respectively, for the various RUC models. No expressions are given for the non-staggered foam models since the pressure gradient is zero for this model because, as already mentioned, interstitial flow recirculation is assumed not to occur in the stagnant fluid domains.

Dimensionless parameters

The streamwise pressure gradient for flow in the steady laminar limit of the inertial flow regime may, analogously to equation (4.30), be expressed as

$$-\left.\frac{\mathrm{d}p}{\mathrm{d}x}\right|_{Re\gg1} = \mu f_\infty\, q\,, \tag{4.44}$$

where f_∞ denotes the drag (or shear) factor in the steady laminar limit of the inertial flow regime. The relation between f_∞ and the passability, η, is given by

$$f_\infty = \frac{\rho\,q}{\mu\,\eta}\,. \tag{4.45}$$

102

Table 4.10: Expressions for the streamwise pressure gradient, $-\mathrm{d}p/\mathrm{d}x$, in the steady laminar limit of the inertial flow regime as a function of d_s.

Model/Array	Streamwise pressure gradient, $-\mathrm{d}p/\mathrm{d}x$
Granular model:	$\dfrac{(1-\epsilon)}{2\,\epsilon\,d_s\,(1-(1-\epsilon)^{2/3})^2}\,c_d\,\rho\,q^2$
Foam model	
Doubly staggered model	$\dfrac{(\psi-1)^2(3-\psi)\,\psi^2}{8\,\epsilon^3 d_s}\,c_d\,\rho\,q^2$
Singly staggered model	$\dfrac{(\psi-1)^2(3-\psi)\,\psi^2}{16\,\epsilon^3 d_s}\,c_d\,\rho\,q^2$
Non-staggered model	0
Fibre model:	$\dfrac{(1-\epsilon)}{2\,\epsilon\,d_s\,(1-\sqrt{1-\epsilon})^2}\,c_d\,\rho\,q^2$

The dimensionless drag factor in the steady laminar limit of the inertial flow regime, defined in terms of the RUC cell size, d, is given by

$$F_{\infty_d} \;\equiv\; f_{\infty_d}\,d\;, \tag{4.46}$$

where f_{∞_d} is the drag factor in the steady laminar limit of the inertial flow regime in terms of the cell size, d. The dimensionless drag factor in the steady laminar limit of the inertial flow regime, defined in terms of the solid width, d_s, is given by

$$F_{\infty_{ds}} \;\equiv\; f_{\infty_{ds}}\,d_s\;, \tag{4.47}$$

where $f_{\infty_{ds}}$ is the drag factor in the steady laminar limit of the inertial flow regime in terms of the solid width, d_s. Lastly, the dimensionless drag factor in the steady laminar limit of the inertial flow regime, defined in terms of the pore width, $d - d_s$, is given by

$$F_{\infty_{dds}} \;\equiv\; f_{\infty_{dds}}\,(d - d_s)\;, \tag{4.48}$$

where $f_{\infty_{dds}}$ is the drag factor in the steady laminar limit of the inertial flow regime in

Table 4.11: Expressions for the streamwise pressure gradient, $-\mathrm{d}p/\mathrm{d}x$, in the steady laminar limit of the inertial flow regime as a function of $d - d_s$.

Model/Array	Streamwise pressure gradient, $-\mathrm{d}p/\mathrm{d}x$
Granular model:	$\dfrac{(1-\epsilon)^{2/3}\left(1-(1-\epsilon)^{1/3}\right)}{2\,\epsilon\,(d-d_s)\left(1-(1-\epsilon)^{2/3}\right)^2}\,c_d\,\rho\,q^2$
Foam model	
Doubly staggered model	$\dfrac{(\psi-1)(3-\psi)^2\,\psi^2}{8\,\epsilon^3(d-d_s)}\,c_d\,\rho\,q^2$
Singly staggered model	$\dfrac{(\psi-1)(3-\psi)^2\,\psi^2}{16\,\epsilon^3(d-d_s)}\,c_d\,\rho\,q^2$
Non-staggered model	0
Fibre model:	$\dfrac{\sqrt{1-\epsilon}}{2\,\epsilon\,(d-d_s)\left(1-\sqrt{1-\epsilon}\right)}\,c_d\,\rho\,q^2$

terms of the pore width, $d - d_s$. Expressions for the respective dimensionless drag factors are presented in Tables D.10 to D.12 (pp 299-301) in Appendix D.

4.6 Powered addition of laminar limits

The power addition technique of Churchill & Usagi (1972) (Appendix H, p 318) allows for two asymptotic limits, each of which dominates in its own region of applicability, to be 'added' in order to obtain a unified expression. The unified equation is applicable over the entire range of the independent variable. Application of the power addition technique to the drag factors in the two steady laminar limits, i.e. f_0 and f_∞, yields

$$f = \left(f_0^s + f_\infty^s\right)^{1/s} , \qquad (4.49)$$

where s is a shifting exponent and f is the total drag factor, defined as

$$f = -\frac{\mathrm{d}p}{\mathrm{d}x}\frac{1}{\mu\,q} . \qquad (4.50)$$

104

Table 4.12: Expressions for the passability, η_d.

Model/Array	Passability, η_d
Granular model:	$\dfrac{2\,\epsilon\,d\,\left(1-(1-\epsilon)^{2/3}\right)^2}{c_d\,(1-\epsilon)^{2/3}}$
Foam model:	
Doubly staggered model	$\dfrac{4\,\epsilon^3\,d}{c_d\,\psi^2\,(\psi-1)(3-\psi)}$
Singly staggered model	$\dfrac{8\,\epsilon^3\,d}{c_d\,\psi^2\,(\psi-1)(3-\psi)}$
Fibre model:	$\dfrac{2\,\epsilon\,d\,(1-\sqrt{1-\epsilon})^2}{c_d\,\sqrt{1-\epsilon}}$

The dimensionless total drag factor will be denoted by, F, and is given by

$$F \;=\; (F_0^s + F_\infty^s)^{1/s} \;, \tag{4.51}$$

where F_0 is the dimensionless drag factor in the low Reynolds number limit and F_∞ is the dimensionless drag factor in the steady laminar limit of the inertial flow regime. The shifting exponent is an empirical parameter of which the value is determined by the physical process under consideration. To the knowledge of the author of this dissertation, no analytical expression has been proposed to determine the value of s. It should be noted that the influence of the shifting exponent, s, is predominantly in the vicinity of the independent variable at which the asymptotes intersect. The shifting exponent determines the rate at which the transition takes place between the two asymptotic limits in the transition region. The asymptotic conditions are not influenced by the numerical value of s. A major advantage of the power addition technique is that the flow behaviour in the transition region is implicitly accounted for in the unified expression and need not be modelled analytically.

A value of $s = 1$ has mostly been used by previous authors who have used the RUC model (e.g. Du Plessis & Masliyah (1988), Du Plessis & Masliyah (1991), Du Plessis & Van der Westhuizen (1993)). The reason for using a value of unity is firstly, because of simplicity, and secondly because it leads to the following Forchheimer type equation, which is simply

Table 4.13: Expressions for the passability, η_{ds}.

Model/Array	Passability, η_{ds}
Granular model:	$\dfrac{2\,\epsilon\,d_s\left(1-(1-\epsilon)^{2/3}\right)^2}{c_d\,(1-\epsilon)}$
Foam model:	
Doubly staggered model	$\dfrac{8\,\epsilon^3\,d_s}{c_d\,\psi^2\,(\psi-1)^2(3-\psi)}$
Singly staggered model	$\dfrac{16\,\epsilon^3\,d_s}{c_d\,\psi^2\,(\psi-1)^2(3-\psi)}$
Fibre model:	$\dfrac{2\,\epsilon\,d_s\,(1-\sqrt{1-\epsilon})^2}{c_d\,(1-\epsilon)}$

a superposition of the streamwise pressure gradients in the two asymptotic limits:

$$-\frac{\mathrm{d}p}{\mathrm{d}x} \;=\; \frac{\mu\,q}{k} \;+\; \frac{\rho\,q^2}{\eta} \;=\; f_0\,\mu\,q \;+\; f_\infty\,\mu\,q \;=\; f\mu\,q\,. \tag{4.52}$$

Although a value of $s=1$ will be used (unless otherwise stated), a more accurate predictive equation may, however, be obtained by closer inspection of the influence of the shifting effect of s, a matter that will not be attempted in the present study. For $s=1$ the dimensionless total drag factor applicable over the entire steady laminar flow regime may be expressed as

$$F \;=\; \frac{S_\parallel + \beta\,\xi S_\perp}{U_o}\,\frac{6\,\psi^2}{\epsilon^2\,(d-d_s)} \;+\; \frac{S_{face}\,\psi^2}{2\,\mu\,\epsilon^3\,U_o}\,c_d\,\rho\,q\,, \tag{4.53}$$

and the streamwise pressure gradient is given by

$$-\frac{\mathrm{d}p}{\mathrm{d}x} \;=\; \frac{S_\parallel + \beta\,\xi S_\perp}{U_o}\,\frac{6\,\psi^2}{\epsilon^2\,(d-d_s)}\,\mu\,q \;+\; \frac{S_{face}\,\psi^2}{2\,\epsilon^3\,U_o}\,c_d\,\rho\,q^2\,. \tag{4.54}$$

The unified equations for the streamwise pressure gradient and the dimensionless drag factor are presented in Tables 4.15 to 4.17 (pp 108-110) and 4.18 to 4.20 (pp 111-113), respectively, as a function of the Reynolds numbers, Re_{qd}, Re_{qds} and Re_{qdds}, respectively.

Table 4.14: Expressions for the passability, η_{dds}.

Model/Array	Passability, η_{dds}
Granular model:	$\dfrac{2\,\epsilon\,(d-d_s)\left(1-(1-\epsilon)^{2/3}\right)^2}{c_d\,(1-\epsilon)^{2/3}\left(1-(1-\epsilon)^{1/3}\right)}$
Foam model: Doubly staggered model	$\dfrac{8\,\epsilon^3\,(d-d_s)}{c_d\,\psi^2\,(\psi-1)(3-\psi)^2}$
Singly staggered model	$\dfrac{16\,\epsilon^3\,(d-d_s)}{c_d\,\psi^2\,(\psi-1)(3-\psi)^2}$
Fibre model:	$\dfrac{2\,\epsilon\,(d-d_s)\left(1-\sqrt{1-\epsilon}\right)}{c_d\,\sqrt{1-\epsilon}}$

4.7 Summary

In this chapter the closure modelling procedures of the three RUC models are unified up to the point where the geometric parameters of the three RUC models are quantified in terms of the respective pore-scale linear dimensions. The fluid-solid interaction is quantified in two asymptotic limits, namely the limit of low Reynolds number flow and the steady laminar limit of the inertial flow regime.

Two closure modelling procedures are presented for the lower asymptotic limit, i.e. one in which pressure decomposition is used together with the Lloyd correction and another based on a direct method. In the former modelling procedure it is assumed that there are no transverse pressure drops over the stagnant surfaces. It is also assumed that the pressure deviation on the transverse surfaces contributes to the streamwise pressure gradient by an amount equal to the magnitude of the transverse wall shear stresses. The wall shear stresses are furthermore assumed to be uniform. It is illustrated that the Lloyd correction, which was originally evaluated only for the two-dimensional over-staggered and regular arrays of the fibre RUC model, is also applicable to the fully staggered array. The flow in the pores is described as plane-Poiseuille flow.

The direct modelling procedure of Firdaouss & Du Plessis (2004) for the two-dimensional fibre model is adapted (i.e. a different degree of staggering is introduced as well as the

Table 4.15: Expressions for the streamwise pressure gradient, $-\mathrm{d}p/\mathrm{d}x$, as a function of Re_{qd}.

Model/Array	Streamwise pressure gradient, $-\mathrm{d}p/\mathrm{d}x$
Granular model:	$$\dfrac{25.4\,(1-\epsilon)^{2/3}\,\mu\,q}{d^2\,(1-(1-\epsilon)^{1/3})\,\left(1-(1-\epsilon)^{2/3}\right)^2} +$$ $$\dfrac{(1-\epsilon)^{2/3}\,c_d\,\mu\,q}{2\,\epsilon\,d^2\,\left(1-(1-\epsilon)^{2/3}\right)^2}\,Re_{qd}$$
Foam model: Doubly staggered	$$\dfrac{36\,\psi^2(\psi-1)\,\mu\,q}{\epsilon^2 d^2} + \dfrac{(\psi-1)(3-\psi)\,\psi^2\,c_d\,\mu\,q}{4\,\epsilon^3\,d^2}\,Re_{qd}$$
Singly staggered	$$\dfrac{24\,\psi^2(\psi-1)\,\mu\,q}{\epsilon^2 d^2} + \dfrac{(\psi-1)(3-\psi)\,\psi^2\,c_d\,\mu\,q}{8\,\epsilon^3\,d^2}\,Re_{qd}$$
Fibre model:	$$\dfrac{13.5\sqrt{1-\epsilon}\,\mu\,q}{d^2\,(1-\sqrt{1-\epsilon})^3} + \dfrac{\sqrt{1-\epsilon}\,c_d\,\mu\,q}{2\,\epsilon\,d^2(1-\sqrt{1-\epsilon})^2}\,Re_{qd}$$

coefficient ξ) and unified to also be applicable to the granular and foam RUC models. This modelling procedure yields the same result as the modelling procedure involving pressure decomposition and the Lloyd correction. It is therefore illustrated that the Lloyd correction is not necessary and that the direct modelling procedure yields a much simpler approach to the same result, but only for uniformly sized solids.

Transverse isotropy is introduced for the granular and fibre RUC models by performing a weighted average over the staggered and non-staggered arrays. For the lower Reynolds number limit sets of equations for the granular, foam and fibre RUC models are provided in terms of each of the three pore-scale linear dimensions for the following parameters: the permeability, pressure gradient and drag factor. The predictive equations for the granular model presented in this chapter are published in Du Plessis & Woudberg (2008).

In the steady laminar limit of the inertial flow regime the microscopic inertial effects are modelled through consideration of interstitial flow recirculation together with a form drag condition, from which an interstitial form drag coefficient is inferred. It is assumed that the approaching velocity is equal to the streamwise average channel velocity. The final

Table 4.16: Expressions for the streamwise pressure gradient, $-\mathrm{d}p/\mathrm{d}x$, as a function of Re_{qds}.

Model/Array	Streamwise pressure gradient, $-\mathrm{d}p/\mathrm{d}x$
Granular model:	$\dfrac{25.4\,(1-\epsilon)^{4/3}\,\mu\,q}{d_s^2\,(1-(1-\epsilon)^{1/3})\,(1-(1-\epsilon)^{2/3})^2}\,+$ $\dfrac{(1-\epsilon)\,c_d\,\mu\,q}{2\,\epsilon\,d_s^2\,(1-(1-\epsilon)^{2/3})^2}\,Re_{qds}$
Foam model: Doubly staggered	$\dfrac{9\,\psi^2(\psi-1)^3\,\mu\,q}{\epsilon^2 d_s^2}\;+\;\dfrac{(\psi-1)^2(3-\psi)\,\psi^2\,c_d\,\mu\,q}{8\,\epsilon^3\,d_s^2}\,Re_{qds}$
Singly staggered	$\dfrac{6\,\psi^2(\psi-1)^3\,\mu\,q}{\epsilon^2 d_s^2}\;+\;\dfrac{(\psi-1)^2(3-\psi)\,\psi^2\,c_d\,\mu\,q}{16\,\epsilon^3\,d_s^2}\,Re_{qds}$
Fibre model:	$\dfrac{13.5(1-\epsilon)^{3/2}\,\mu\,q}{d_s^2\,(1-\sqrt{1-\epsilon})^3}\;+\;\dfrac{(1-\epsilon)\,c_d\,\mu\,q}{2\,\epsilon\,d_s^2\,(1-\sqrt{1-\epsilon})^2}\,Re_{qds}$

result for the pressure gradient in this limit differs from that of Crosnier et al. (2006) who have also incorporated the Lloyd correction in this limit. The Lloyd correction was derived for flow in the Darcy regime and cannot be assumed to be applicable in the inertial flow regime without justification. For the higher Reynolds number limit sets of equations for the granular, foam and fibre RUC models are provided in terms of each of the three pore-scale linear dimensions for the following parameters: the passability, pressure gradient and drag factor.

A power addition technique is applied to all three RUC models to obtain a single equation for the streamwise pressure gradient applicable over the entire steady laminar flow regime. For simplicity, a value of unity is used for the shifting exponent. Sets of equations for the granular, foam and fibre RUC models are provided in terms of each of the three pore-scale linear dimensions for the pressure gradient, passability and the dimensionless total drag factor.

Table 4.17: Expressions for the streamwise pressure gradient, $-\mathrm{d}p/\mathrm{d}x$, as a function of Re_{qdds}.

Model/Array	Streamwise pressure gradient, $-\mathrm{d}p/\mathrm{d}x$
Granular model:	$\dfrac{25.4\,(1-\epsilon)^{2/3}\left(1-(1-\epsilon)^{1/3}\right)\mu\,q}{(d-d_s)^2\left(1-(1-\epsilon)^{2/3}\right)^2}\; +$ $\dfrac{(1-\epsilon)^{2/3}(1-(1-\epsilon)^{1/3})\,c_d\,\mu\,q}{2\,\epsilon\,(d-d_s)^2\left(1-(1-\epsilon)^{2/3}\right)^2}\,Re_{qdds}$
Foam model:	
Doubly staggered	$\dfrac{9\,\psi^2(\psi-1)(3-\psi)^2\,\mu\,q}{\epsilon^2(d-d_s)^2}\;+\;\dfrac{(\psi-1)(3-\psi)^2\,\psi^2\,c_d\,\mu\,q}{8\,\epsilon^3\,(d-d_s)^2}\,Re_{qdds}$
Singly staggered	$\dfrac{6\,\psi^2(\psi-1)(3-\psi)^2\,\mu\,q}{\epsilon^2(d-d_s)^2}\;+\;\dfrac{(\psi-1)(3-\psi)^2\,\psi^2\,c_d\,\mu\,q}{16\,\epsilon^3\,(d-d_s)^2}\,Re_{qdds}$
Fibre model:	$\dfrac{13.5\sqrt{1-\epsilon}\,\mu\,q}{(d-d_s)^2(1-\sqrt{1-\epsilon})}\;+\;\dfrac{\sqrt{1-\epsilon}\,c_d\,\mu\,q}{2\,\epsilon\,(d-d_s)^2(1-\sqrt{1-\epsilon})}\,Re_{qdds}$

Table 4.18: Expressions for the dimensionless drag factor, F_d, as a function of Re_{qd}.

Model/Array	Dimensionless total drag factor, $F_d = f_d d^2$
Granular model:	$$\dfrac{25.4\,(1-\epsilon)^{2/3}}{\left(1-(1-\epsilon)^{1/3}\right)\left(1-(1-\epsilon)^{2/3}\right)^2} +$$ $$\dfrac{(1-\epsilon)^{2/3}\,c_d}{2\,\epsilon\left(1-(1-\epsilon)^{2/3}\right)^2}\,Re_{qd}$$
Foam model: Doubly staggered	$$\dfrac{36\,\psi^2\,(\psi-1)}{\epsilon^2} \;+\; \dfrac{(\psi-1)(3-\psi)\,\psi^2\,c_d}{4\,\epsilon^3}\,Re_{qd}$$
Singly staggered	$$\dfrac{24\,\psi^2\,(\psi-1)}{\epsilon^2} \;+\; \dfrac{(\psi-1)(3-\psi)\,\psi^2\,c_d}{8\,\epsilon^3}\,Re_{qd}$$
Fibre model:	$$\dfrac{13.5\sqrt{1-\epsilon}}{(1-\sqrt{1-\epsilon})^3} \;+\; \dfrac{\sqrt{1-\epsilon}\,c_d}{2\,\epsilon\,(1-\sqrt{1-\epsilon})^2}\,Re_{qd}$$

Table 4.19: Expressions for the dimensionless drag factor, F_{ds}, as a function of Re_{qds}.

Model/Array	Dimensionless total drag factor, $F_{ds} = f_{ds}d_s^2$
Granular model:	$\dfrac{25.4\,(1-\epsilon)^{4/3}}{\left(1-(1-\epsilon)^{1/3}\right)\left(1-(1-\epsilon)^{2/3}\right)^2} +$ $\dfrac{(1-\epsilon)\,c_d}{2\,\epsilon\left(1-(1-\epsilon)^{2/3}\right)^2}\,Re_{qds}$
Foam model: Doubly staggered	$\dfrac{9\,\psi^2\,(\psi-1)^3}{\epsilon^2} \;+\; \dfrac{(\psi-1)^2(3-\psi)\,\psi^2\,c_d}{8\,\epsilon^3}\,Re_{qds}$
Singly staggered	$\dfrac{6\,\psi^2\,(\psi-1)^3}{\epsilon^2} \;+\; \dfrac{(\psi-1)^2(3-\psi)\,\psi^2\,c_d}{16\,\epsilon^3}\,Re_{qds}$
Fibre model:	$\dfrac{13.5\,(1-\epsilon)^{3/2}}{(1-\sqrt{1-\epsilon})^3} \;+\; \dfrac{(1-\epsilon)\,c_d}{2\,\epsilon\,(1-\sqrt{1-\epsilon})^2}\,Re_{qds}$

Table 4.20: Expressions for the dimensionless drag factor, F_{dds}, as a function of Re_{qdds}.

Model/Array	Dimensionless total drag factor, $F_{dds} = f_{dds}(d - d_s)^2$
Granular model:	$\dfrac{25.4\,(1-\epsilon)^{2/3}\left(1-(1-\epsilon)^{1/3}\right)}{\left(1-(1-\epsilon)^{2/3}\right)^2} +$ $\dfrac{(1-\epsilon)^{2/3}(1-(1-\epsilon)^{1/3})\,c_d}{2\,\epsilon\left(1-(1-\epsilon)^{2/3}\right)^2}\,Re_{qdp}$
Foam model: Doubly staggered	$\dfrac{9\,\psi^2\,(\psi-1)(3-\psi)^2}{\epsilon^2} \;+\; \dfrac{(\psi-1)(3-\psi)^2\,\psi^2\,c_d}{8\,\epsilon^3}\,Re_{qdp}$
Singly staggered	$\dfrac{6\,\psi^2\,(\psi-1)(3-\psi)^2}{\epsilon^2} \;+\; \dfrac{(\psi-1)(3-\psi)^2\,\psi^2\,c_d}{16\,\epsilon^3}\,Re_{qdp}$
Fibre model:	$\dfrac{13.5\sqrt{1-\epsilon}}{(1-\sqrt{1-\epsilon})} \;+\; \dfrac{\sqrt{1-\epsilon}\,c_d}{2\,\epsilon\,(1-\sqrt{1-\epsilon})}\,Re_{qdp}$

Chapter 5

Model validation

5.1   Introduction

A historical overview of the development of the RUC models is presented in this chapter. The granular model is validated against the extensively used semi-empirical Ergun equation (Appendix C, p 286) and its empirical coefficients are expressed as a function of porosity. In this manner it is illustrated that the granular RUC model serves as a theoretical derivation of the Ergun equation. The predictive equations of the granular model are simplified by application of series expansion and a throwback method at a specific porosity.

The foam RUC model is used to predict the dynamic specific surface of ceramic foams. These predictive values are compared to experimental data as well as theoretical models from the literature. It is shown that the foam RUC model serves as a theoretical Ergun-type equation for foamlike media. As in the case of the granular RUC model, the empirical coefficients of the empirical Ergun-type equation for foamlike media are quantified in terms of porosity by application of the foam RUC model. The pressure gradient, permeability and passability predictions, provided by the foam RUC model, are verified against experimental data including the empirical Ergun-type equation. A comparison is furthermore drawn between the pressure drop over granular and foamlike media.

The fibre model is validated against a number of analytical models as well as numerical and experimental data from the literature. Values for the Kozeny constant, predicted by the unconsolidated models, are compared with model predictions based on cylindrical and spherical geometries. The unconsolidated models are furthermore used to predict the critical Reynolds number, i.e. the Reynolds number at which the Darcy and inertial flow regimes contribute equally to the pressure drop.

5.2 Historical overview of the development of the RUC model

This section provides an overview of the development and contributions made to the RUC model over the past three decades. In all the previous analytical modelling procedures with the RUC model, the following assumptions were made, unless otherwise stated:

- The solid phase is rigid, smooth, impermeable and stationary.

- Isothermal, steady, incompressible, laminar, single phase flow of a Newtonian fluid are considered. As a result, turbulence is disregarded.

- The fluid is chemically and electrically inactive and all pores are fully saturated with fluid.

- The porous medium is unbounded, homogeneous and isotropic.

Du Plessis & Masliyah (1988) were the first to introduce the concept of a rectangular RUC model in the form of the foam RUC model. Maximum possible staggering was assumed by default. No distinction was made between staggered and non-staggered arrays. Consequently, stagnant fluid volumes were not accounted for. The average velocities in the streamwise and transverse duct sections were assumed to be equal in magnitude. The analytical modelling procedure was based on flow development within the pores with a uniform velocity profile at the entrance of each pore section. The apparent friction factor for developing flow in a square duct in the limit of very short and very long plates, as presented in Shah & London (1978), were added by application of the power addition technique (Churchill & Usagi (1972)). The result was expressed as a function of the Reynolds number. A shifting parameter of unity was used in the power addition technique. The contribution of the shear stresses in the transverse pore sections to the streamwise pressure gradient was accounted for implicitly through the pressure term in the surface integral. The streamwise pressure gradient according to Du Plessis & Masliyah (1988) is given by

$$-\frac{\mathrm{d}p}{\mathrm{d}x} \;=\; \frac{42.7\,\chi\,(\chi-1)}{\epsilon^2\,d^2}\,\mu q\,\sqrt{1+\frac{0.117}{(\chi-1)}\,Re_{qd}}\;. \tag{5.1}$$

Du Plessis & Masliyah (1991) were the first to introduce the granular RUC model. The same modelling procedure as was used by Du Plessis & Masliyah (1988) was followed in which developing flow between parallel plates was assumed. The streamwise pressure gradient prediction of Du Plessis & Masliyah (1991) is given by

$$-\frac{\mathrm{d}p}{\mathrm{d}x} \;=\; \frac{36\,(1-\epsilon)^{2/3}}{[1-(1-\epsilon)^{1/3}][1-(1-\epsilon)^{2/3}]\,d^2}\,\mu q\,\sqrt{1+\frac{0.0822\,[(1-\epsilon)^{-1/3}-1]}{1+(1-\epsilon)^{1/3}}\,Re_{qd}}\;. \tag{5.2}$$

The assumption of developing flow led to $|\nabla p| \propto |\underline{q}|^{3/2}$ in the inertial flow regime as

opposed to $|\nabla p| \propto |\underline{q}|^2$, as predicted by the empirical Burke-Plummer equation (Appendix C.3, p 288).

Du Plessis (1991) introduced the fibre RUC model for modelling cross-flow through prismatic porous domains. Also for this model the modelling procedure of Du Plessis & Masliyah (1988) for developing flow between parallel plates was assumed. The streamwise pressure gradient prediction of Du Plessis (1991) is given by

$$-\frac{\mathrm{d}p}{\mathrm{d}x} = \frac{24\sqrt{1-\epsilon}}{[1-\sqrt{1-\epsilon}]^2 d^2} \mu q \sqrt{1 + \frac{0.0822\,[1-\sqrt{1-\epsilon}]}{\sqrt{1-\epsilon}} Re_{qd}}\,. \tag{5.3}$$

Du Plessis & Van der Westhuizen (1993) followed a different analytical modelling approach for the fibre RUC model than flow development within the pores. The microscopic inertial effects were modelled through consideration of interstitial flow recirculation on the lee side of the solid material, similarly as presented in Section 4.5 (p 97). The fluid-solid interaction was quantified in the asymptotic limit of low Reynolds number flow and the steady laminar limit of the inertial flow regime. In the lower limit fully developed flow between parallel plates was assumed and in the upper limit the pressure gradient is expressed in terms of an internal form drag coefficient, analogous to the external form drag condition for flow past a single obstacle in an infinite stream. The power addition technique (Churchill & Usagi (1972)), with a shifting parameter of unity, was applied to obtain a unified expression for the streamwise pressure gradient, given by

$$-\frac{\mathrm{d}p}{\mathrm{d}x} = \frac{24\sqrt{1-\epsilon}}{[1-\sqrt{1-\epsilon}]^2 d^2} \mu q + \frac{(1+\sqrt{1-\epsilon})^2 (1-\epsilon)^{3/2})\,c_d}{2\,\epsilon^2} \mu q\, Re_{qd}\,. \tag{5.4}$$

This approach led to $|\nabla p| \propto |\underline{q}|^2$ in the inertial flow regime instead of the dependence of $|\nabla p| \propto |\underline{q}|^{3/2}$ proposed by Du Plessis (1991).

Du Plessis (1994) adapted the modelling procedure of Du Plessis & Van der Westhuizen (1993) in the inertial flow regime for the granular RUC model. The pressure deficit on the lee side of the solid cube was approximated by Bernoulli's equation, as described in Appendix G (p 315). Different streamwise and transverse average channel velocities were assumed. The streamwise pressure gradient prediction of Du Plessis (1994) is given by

$$-\frac{\mathrm{d}p}{\mathrm{d}x} = \frac{41\,(1-\epsilon)^{2/3}\,\mu q}{[1-(1-\epsilon)^{1/3}][1-(1-\epsilon)^{2/3}]\,d^2} + \frac{(1-\epsilon)\,\mu q}{\epsilon\, d^2[1-(1-\epsilon)^{2/3}]^2} Re_{qd}\,. \tag{5.5}$$

Du Plessis et al. (1994) applied the modelling procedure of Du Plessis & Van der Westhuizen (1993) to the foam RUC model. The streamwise pressure gradient prediction is given by

$$-\frac{\mathrm{d}p}{\mathrm{d}x} = \frac{36\,\chi\,(\chi-1)}{\epsilon^2\,d^2} \mu q + \frac{2.05\,\chi\,(\chi-1)}{d^2\,\epsilon^2\,(3-\chi)} \mu q\, Re_{qd}\,. \tag{5.6}$$

Diedericks (1999) adapted the granular RUC model of Du Plessis (1994), the foam RUC model of Du Plessis et al. (1994) and the fibre RUC model of Du Plessis & Van der

Westhuizen (1993) to account for anisotropy. A low and high porosity anisotropic foam RUC model were introduced.

Firdaouss & Du Plessis (2004) used a direct modelling procedure to predict the permeability of arrays of squares and rectangles, thus introducing anisotropy. This work is an extension of the two-dimensional fibre RUC model of Du Plessis & Van der Westhuizen (1993). The authors have distinguished between staggered and non-staggered arrays. A shape factor was introduced in which the unit cell aspect ratio is assumed to be the same as the particle aspect ratio. For a regular array of squares the permeability is given by

$$k \; = \; \frac{(1 - \sqrt{1 - \epsilon})^3 \, d^2}{12 \, \sqrt{1 - \epsilon}} \; , \tag{5.7}$$

and for a fully staggered array of squares,

$$k \; = \; \frac{(1 - \sqrt{1 - \epsilon})^3 \, d^2}{15 \, \sqrt{1 - \epsilon}} \; . \tag{5.8}$$

Lloyd (2003) and Lloyd et al. (2004) extended the work of Firdaouss & Du Plessis (2004) for predicting the permeability of two-dimensional arrays of squares, by application of the fibre RUC model. Volume partitioning was applied to the fluid domain. An over-staggered, fully staggered and regular array were introduced. This led to the introduction of the geometric factor. The pressure on the transverse surfaces was decomposed into the average wall pressure and the wall pressure deviation, similarly as presented in Section 4.4.1 (p 85). The contribution of the transverse shear stresses was manifested into the streamwise pressure gradient through the pressure deviation part of the surface integral over the transverse surfaces. It was assumed that the pressure deviations on the transverse channel walls contribute to the streamwise pressure gradient by an amount equal to the magnitude of the transverse wall shear stresses.

A commercial code, CFX, based on the finite volume method was used to determine the accuracy of the assumptions used in the modelling procedure with the RUC model. Different locations of the RUC model along the streamwise direction were considered. The surface integrals were weighed according to the relative frequency of occurrence of the RUC over a streamwise displacement equal to the streamwise dimension of the RUC. Based on this weighting procedure and its comparison with the simulation results of the CFX code, it was shown that the average wall pressure evaluated over the transverse surfaces is expressible in terms of the gradient of the average pressure. In addition to the difference between the streamwise and transverse average channel velocities, the reduction in the wall shear stresses due to the splitting of the streamwise flux in a fully staggered array was also accounted for. Thus, by following the volume averaging method, instead of the direct method, the same expressions for the permeability, as proposed by Firdaouss & Du Plessis (2004), were obtained for a fully staggered and regular array.

Terblanche (2006) used the commercial CFD package, FLUENT, to verify some of the assumptions made in the closure modelling procedure with the fibre RUC model in both

the lower and upper Reynolds number limits. An alternative closure modelling procedure, based on the application of Bernoulli's equation, is proposed for the steady laminar limit of the inertial flow regime.

Smit et al. (2005) and Wilms (2006) adapted the analytical modelling procedure of Du Plessis et al. (1994) for the foam RUC model by introducing the Lloyd correction into the lower Reynolds number term. Stagnant fluid volumes were introduced which then led to the introduction of the doubly staggered, singly staggered and non-staggered foam sub-models. Wilms (2006) also applied the weighting procedure of Lloyd (2003) to the higher Reynolds number term. The streamwise pressure gradient is given by

$$-\frac{\mathrm{d}p}{\mathrm{d}x} \;=\; \frac{36\,\psi^2\,(\psi-1)}{\epsilon^2\,d^2}\,\mu q \;+\; \frac{c_d\,\psi\,(\psi-1)}{2\,d^2\,\epsilon^3}\,\mu q\,Re_{qd}\;. \tag{5.9}$$

The introduction of stagnant fluid domains led to the replacement of the tortuosity with the geometric factor and the Lloyd correction added an additional geometric factor to the pressure gradient prediction in the limit of low Reynolds number flow (compare equations (5.6) and (5.9)).

Crosnier et al. (2006) also adapted the analytical modelling procedure of Du Plessis et al. (1994) for the foam RUC model by introducing the Lloyd correction into the modelling procedure. The weighting procedure of Lloyd (2003) as well as the Lloyd correction were included in the higher Reynolds number term. The streamwise pressure drop was approximated by the condition of form drag, according to the modelling procedure of Du Plessis & Van der Westhuizen (1993). The doubly staggered, singly staggered and non-staggered models were also introduced. In the Darcy regime the same modelling procedure as Smit et al. (2005) and Wilms (2006) was followed. The streamwise pressure gradient is given by

$$-\frac{\mathrm{d}p}{\mathrm{d}x} \;=\; \frac{36\,\psi^2\,(\psi-1)}{\epsilon^2\,d^2}\,\mu q \;+\; \frac{c_d\,\psi^2\,(\psi-1)(2-\sigma)}{2\,d^2\,\epsilon^2(3-\psi)}\,\mu q\,Re_{qd}\;. \tag{5.10}$$

Woudberg (2006) and Woudberg et al. (2006) adapted the analytical modelling procedure of Du Plessis (1994) for the granular RUC model by including the Lloyd correction into the analytical modelling procedure. Stagnant fluid volumes were introduced which led to the introduction of the regular array. Average geometrical isotropy of the RUC model was justified mathematically (which was not done by Du Plessis (1994)). This weighted average changed the coefficient obtained by Du Plessis (1994) in the lower Reynolds number limit from 41 to 26.8. In the limit of low Reynolds number flow the power addition technique (Churchill & Usagi (1972)) was applied to the pressure drop prediction in the limit of low porosities and the pressure drop prediction in the limit of high porosities, of which the latter is described by the Stokes drag for flow past a single obstacle. It was, however, found that the low porosity granular RUC model alone is adequate, since the accuracy of the model prediction did not improve significantly by addition of the higher porosity term. The streamwise pressure gradient is given by

$$-\frac{\mathrm{d}p}{\mathrm{d}x} \;=\; \frac{26.8\,(1-\epsilon)^{2/3}\,\mu\,q}{[1-(1-\epsilon)^{1/3}][1-(1-\epsilon)^{2/3}]^2\,d^2} \;+\; \frac{(1-\epsilon)\,\mu q}{\epsilon\,d^2[1-(1-\epsilon)^{2/3}]^2}\,Re_{qd}\;. \tag{5.11}$$

The introduction of stagnant fluid domains led to the replacement of the tortuosity in the model of Du Plessis (1994) with the geometric factor. The inclusion of the Lloyd correction added a factor of $(1 - (1 - \epsilon)^{2/3})$ to the streamwise pressure gradient prediction in the limit of low Reynolds number flow (compare equations (5.5) and (5.11)). The coefficient of 26.8 differs from the coefficient of 25.4 proposed for the granular RUC model in the present study. (The reason for the difference in coefficient values is given in Section 3.14.4 (p 51)).

Cloete (2006) redefined the RUC for fibre beds by giving it a streamwise length of twice that of the original RUC so that the basic structure of the RUC is the same as that of a unit cell. The transfer fluid volume was also redefined as a volume bounded on one-side by a fluid-solid interface on which the wall shear stresses are neglected. The nett effect of the pressure gradient over the transfer fluid volume is zero, but the transverse fluid-solid interfaces are reduced which affects the total permeability, given by

$$K_d \;=\; \frac{(1 - \sqrt{1 - \epsilon})^3}{12 \left[\sqrt{1 - \epsilon} + \xi^2(2\sqrt{1 - \epsilon} - 1)\right]} \;. \tag{5.12}$$

Molale (2007) used the commercial CFD package, FLUENT, to verify the assumption of plane-Poiseuille flow in the fibre RUC model. The numerical computations confirm the presence of developing flow at the inlet and outlet of both the streamwise and transverse channels. The assumption of interstitial recirculation on the lee side of solids in the inertial flow regime is also verified numerically.

In Table 5.1 (p 120) a time-line, in authors-year format, is presented of the authors who have contributed to the direct *development* of the various RUC models. The authors are given in chronological order and categorized according to the respective RUC models they have worked on. A table of authors who contributed towards *applications* of the RUC models will be presented in Chapter 8.

5.3   Granular RUC model

The well-known and frequently utilized Ergun equation was originally formulated semi-empirically to predict the pressure drop for Newtonian flow through a packed bed of predominantly spherical granules. (A derivation of the Ergun equation is presented in Appendix C (p 286).) It has served well and is still utilized extensively, especially in the chemical engineering field.

In this section a dimensionless drag factor, fD_h^2, defined as

$$fD_h^2 \;=\; \frac{D_h^2}{k} \;+\; \frac{D_h}{\eta} Re_h \;, \tag{5.13}$$

will be used to facilitate comparison between the granular RUC model and the Ergun

Table 5.1: Time-line of contributions made by various authors to the RUC model.

Reference	RUC model		
	Granular	Foam	Fibre
Du Plessis & Masliyah (1988)		×	
Du Plessis & Masliyah (1991)	×		
Du Plessis (1991)			×
Du Plessis & Van der Westhuizen (1993)			×
Du Plessis (1994)	×		
Du Plessis et al. (1994)		×	
Diedericks (1999)	×	×	×
Firdaouss & Du Plessis (2004)			×
Lloyd (2003) & Lloyd et al. (2004)			×
Terblanche (2006)			×
Smit et al. (2005) & Wilms (2006)		×	
Crosnier et al. (2006)		×	
Woudberg (2006) & Woudberg et al. (2006)	×		
Cloete (2006)			×
Molale (2007)			×

equation and since drag is an additive quantity. The Reynolds number, Re_h, defined in terms of the hydraulic diameter, D_h, is given by

$$Re_h \equiv \frac{\rho \, q D_h}{\mu} \, . \tag{5.14}$$

From equations (4.52) and (C.17) the Ergun equation may be expressed in the following dimensionless form:

$$f D_h^2 = \frac{A \, (1 - \epsilon)^2}{\epsilon^3} + \frac{B \, (1 - \epsilon)}{\epsilon^3} \, Re_h \, , \tag{5.15}$$

with $A = 150$ and $B = 1.75$. The hydraulic diameter for porous media, i.e. $D_h = D_s$, is equal to the spherical granular diameter, D_{sp} for a packed bed of spheres (Section 2.8.5, p 20). The Ergun equation is applicable in the Reynolds number range of $0.4 < Re_h < 1000$ (Comiti & Renaud (1989)).

Despite its extensive use, the Ergun equation has received a lot of criticism regarding its limited applicability and the over-simplification of the capillary model. (Skartsis et al.

120

(1992), for example, give a comprehensive discussion on the limitations of the Carman-Kozeny equation.) Equation (5.15) is strictly applicable only in the range of porosities applicable to packed beds, i.e. for porosities ranging from 0.38 to 0.47 (Happel & Brenner (1965)), and then only for traversing Newtonian fluids. The average porosity of 0.38 to 0.47, i.e. 0.43, will be used henceforth as the average porosity associated with a packed bed. The representation of a packed bed as a bundle of straight capillary tubes is regarded as inadequate in the sense that the cylindrical pores exclude inter-connectedness of the pore space (Dullien (1979)). Also, in the Forchheimer regime, similarity of experimental results with turbulence effects was used to obtain the functional dependence of inertial drag on porosity and the Reynolds number. It is at present fairly commonly accepted that the origin of the Forchheimer regime lies purely in the presence of laminar inertial effects and cannot be attributed to turbulence (e.g. Bear (1972)). In addition, it is pointed out by Scheidegger (1957) that the critical Reynolds number above which "turbulence" initiates, differs for porous media by a factor of 25 in comparison with the critical Reynolds number associated with straight capillary tubes. Furthermore, in the literature (e.g. Dagan (1989) and Bear (1972)) the introduction of the tortuosity factor into the model is regarded as merely a "fudge factor" to obtain correlation with experimental data.

A quantitative improvement on the Ergun equation, yet still empirically based on a comparative analysis of numerous experimental results, was subsequently proposed by Macdonald et al. (1979). It was suggested that $A = 180$ and $B = 1.8$, yielding

$$fD_h^2 = \frac{180\,(1-\epsilon)^2}{\epsilon^3} + \frac{1.8\,(1-\epsilon)}{\epsilon^3}\,Re_h \; . \tag{5.16}$$

Equation (5.16) will also be referred to as the improved Ergun equation. In the next subsections it will be shown that the pressure gradient prediction of the granular RUC model can be regarded as qualitative and quantitative proof of the Ergun equation.

5.3.1   Comparison with the Ergun equation

The motivation for the choice of a shifting exponent of unity in the power addition technique, apart from simplicity, is that the pressure drop prediction of the granular RUC model can be compared directly with the Ergun equation, which is simply a direct superposition of two asymptotic limits.

In Figure 5.1 (p 122) is shown a comparison between the granular RUC model, presented in Table 4.19 (p 112), i.e.

$$F_{ds} = f_{ds}d_s^2 = \frac{25.4\,(1-\epsilon)^{4/3}}{\left(1-(1-\epsilon)^{1/3}\right)\left(1-(1-\epsilon)^{2/3}\right)^2} + \frac{(1-\epsilon)\,c_d}{2\,\epsilon\,\left(1-(1-\epsilon)^{2/3}\right)^2}\,Re_{qds} \;, \tag{5.17}$$

the Ergun equation (i.e. equation (5.15)), the improved Ergun equation (i.e. equation (5.16)) and the former granular RUC models (i.e. equations (5.2) and (5.5)) at $\epsilon = 0.43$. In equation (5.17), f_{ds} denotes the total drag factor in terms of the solid width d_s.
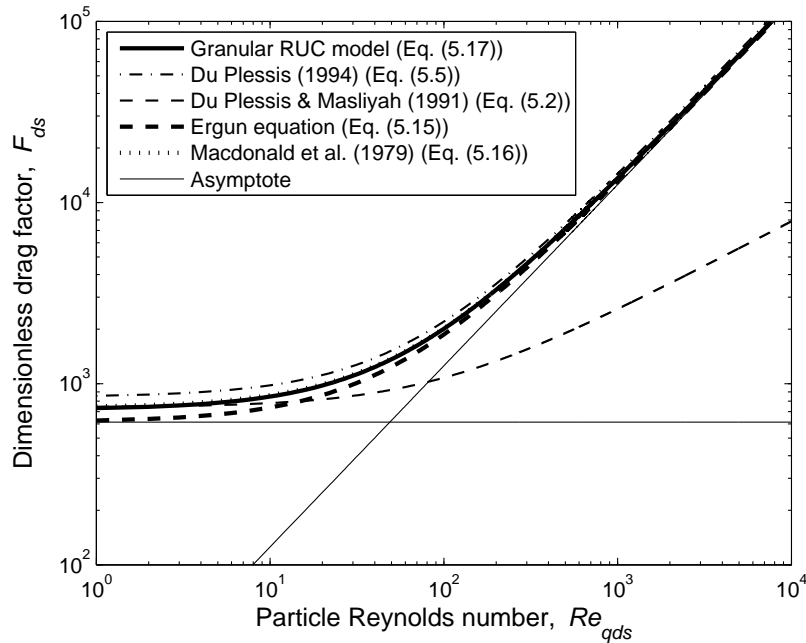
Figure 5.1: Comparison of the granular RUC models with the Ergun equation and the improved Ergun equation of Macdonald et al. (1979) at $\epsilon = 0.43$.

In Section 3.14.5 (p 57) it was shown that the hydraulic diameter for porous media is also equal to the solid width of the granular RUC model, i.e. $D_h = D_s = D_{sp} = d_s$. Consequently, for the granular RUC model, $Re_{qds} = Re_h$ and therefore equation (5.17) is directly comparable to equations (5.15) and (5.16). Furthermore, for the granular RUC model $c_d = 1.9$ (Section 3.14.4, p 51).

In Figure 5.1 all the RUC models, except the one of Du Plessis & Masliyah (1991), approach the asymptotic limits of the Ergun equation at low and high values of the particle Reynolds number. The model of Du Plessis & Masliyah (1991) yields a functional dependency of $q^{3/2}$, whereas all the other RUC models yield functional dependencies of q^2, in correspondence to that of the Ergun and improved Ergun equations. In Figure 5.1 the present granular RUC model (i.e. equation (5.17)) is hardly distinguishable from the improved Ergun equation over the entire Reynolds number range presented. This is not the case for the granular RUC models of Du Plessis & Masliyah (1991) and Du Plessis (1994). The granular RUC model proposed in this study may thus be regarded as an improvement on the former granular RUC models.

The advantages of the RUC model include the following: The RUC model provides interconnectivity of the pore space, which is not the case in the capillary tube model of the Ergun equation. The RUC model is derived from sound physical principles and therefore avoids the introduction of empirical coefficients. The interstitial form drag coefficient, c_d, and the shifting exponent, s, are the most empirical aspects of the model, as these values should be inferred from experimental measurements. The RUC model is applicable over the entire porosity range and also over the entire laminar Reynolds number range.

Another advantage of the RUC model is that it is physically adaptable to account for other physical fluid flow phenomena, i.e. non-Newtonian flow behaviour (Woudberg et al. (2006)), pore-blockage in very low porosity sandstones (Woudberg & Du Plessis (2008)), drag flow behaviour in fluidized beds (Halvorsen et al. (2006)) and diffusive transport (Du Plessis et al. (2010)), as will be discussed in Chapter 8. The Ergun equation, on the other hand, is not physically adaptable as new empirical coefficients need to be obtained for every other application.

Simplification of results and direct comparison between the granular RUC model, given by equation (5.17), and the improved Ergun equation can be achieved by series expansions of the powered terms in equation (5.17), following the work of Du Plessis & Roos (1993).

5.3.2 Series truncation with throwback

If the different power series in equation (5.17) are substituted with the corresponding series expansions presented in Appendix J (p 321), it follows that

$$f_{ds}d_s^2 = \frac{171.45}{\epsilon^3}\left[1 - 2\epsilon + \frac{13}{12}\epsilon^2 + ...\right] + \frac{9\,c_d}{8\,\epsilon^3}\left[1 - \frac{4}{3}\epsilon + \frac{29}{108}\epsilon^2 + ...\right]Re_{qds}\ . \qquad (5.18)$$

The infinite series may be truncated, but should then be locally corrected at a specific porosity value. This is accomplished by the method of throwback in which the effect of the omitted terms is accounted for by adjusting the coefficient of the last retained term in the truncated series. This is done by calculating the difference between the original and approximated equations at a specific porosity, referred to as the throwback porosity.

In the present study the truncations will be affected at the mean porosity value for the range in which the Ergun equation holds, i.e. at $\epsilon = 0.43$. The latter porosity value will thus serve as the throwback porosity. Truncation after two terms, coupled with throwback, of each of the infinite series in equation (5.18), yields

$$f_{ds}d_s^2 = \frac{171.45}{\epsilon^3}\left[1 - 1.55\,\epsilon\right] + \frac{9\,c_d}{8\,\epsilon^3}\left[1 - 1.21\,\epsilon\right]Re_{qds}\ . \qquad (5.19)$$

Equation (5.19) represents a simplified form of equation (5.17) and is valid for a range of porosity values around the throwback porosity of 0.43.

Similarly, simplified equations can be obtained for the dimensionless permeability, k/d_s^2, and the dimensionless passability, η/d_s. Series expansion applied to the dimensionless permeability leads to

$$\frac{k}{d_s^2} = \frac{\left(1 - (1-\epsilon)^{1/3}\right)\left(1 - (1-\epsilon)^{2/3}\right)^2}{25.4\,(1-\epsilon)^{4/3}} = \frac{\epsilon^3}{171.45}\left[1 + 2\,\epsilon + \frac{35}{12}\epsilon^2 + ...\right]\ . \qquad (5.20)$$

Truncation after the first power of the porosity and application of throwback at $\epsilon = 0.43$

yields,

$$\frac{k}{d_s^2} = \frac{\epsilon^3}{171.45}\left[1 + 4.65\,\epsilon\right]\ . \tag{5.21}$$

Series expansion applied to the dimensionless passability, η/d_s, leads to

$$\frac{\eta}{d_s} = \frac{2\,\epsilon\,(1 - (1 - \epsilon)^{2/3})^2}{c_d\,(1 - \epsilon)} = \frac{8\,\epsilon^3}{9\,c_d}\left[1 + \frac{4\,\epsilon}{3} + \frac{163}{108}\,\epsilon^2 + ...\right]\ . \tag{5.22}$$

Truncation after the first power of the porosity together with throwback at $\epsilon = 0.43$ yields,

$$\frac{\eta}{d_s} = \frac{8\,\epsilon^3}{9\,c_d}\left[1 + 2.52\epsilon\right]\ . \tag{5.23}$$

Equation (5.21) can also be obtained by taking the inverse of the first term on the right hand side of equation (5.19), according to equation (5.13). Similarly equation (5.23) can alternatively be obtained by taking the inverse of the second term on the right hand side of equation (5.19)

5.3.3   Severe series truncation with throwback

If more severe truncation is applied, i.e. retaining only the first term of each infinite series in equation (5.18), it follows after throwback at $\epsilon = 0.43$ that

$$f_{ds}d_s^2 = \frac{57.185}{\epsilon^3} + \frac{0.540\,c_d}{\epsilon^3}\,Re_{qds} = 719 + 12.9\,Re_{qds}\ . \tag{5.24}$$

The two coefficients 719 and 12.9 represent the predicted values of $A\,(1-\epsilon)^2/\epsilon^3$ and $B\,(1-\epsilon)/\epsilon^3$, respectively, in equation (5.15) at a porosity of 0.43.

5.3.4   Porosity dependence of the Ergun coefficients

The values of the coefficients A and B at $\epsilon = 0.43$, as calculated from equation (5.24), are given in Table 5.2 (p 125) together with values for these coefficients proposed by Macdonald et al. (1979) and the spherical cell model of Happel (1958) (Section 2.11.2, p 32).

For porosity values other than 0.43 the full expressions for the coefficients A and B, i.e. respectively given by

$$A = \frac{25.4\,\epsilon^3}{(1-\epsilon)^{2/3}\left(1 - (1-\epsilon)^{1/3}\right)\left(1 - (1-\epsilon)^{2/3}\right)^2}\ , \tag{5.25}$$

124

Table 5.2: Model predictions for the Ergun coefficients A and B at $\epsilon = 0.43$.

Model	Coefficient A, $\epsilon = 0.43$
Blake-Kozeny (Bird et al. (2007))	150
Carman-Kozeny-Blake (Bird et al. (2007))	180
Macdonald et al. (1979)	180
Happel (1958)	165
Granular RUC model	176
Model	Coefficient B, $\epsilon = 0.43$
Burke-Plummer (Bird et al. (2007))	1.75
Macdonald et al. (1979)	1.80
Granular RUC model	1.80

and

$$B \;=\; \frac{\epsilon^2 c_d}{2\left(1 - (1-\epsilon)^{2/3}\right)^2} \;, \tag{5.26}$$

should be used.

The spherical cell model of Happel (1958) yields the following porosity dependence of the coefficient A:

$$A \;=\; \frac{18\epsilon^3}{(1-\epsilon)}\left[\frac{3 + 2\left(1-\epsilon\right)^{5/3}}{3 - (9/2)(1-\epsilon)^{1/3} + (9/2)(1-\epsilon)^{5/3} - 3\left(1-\epsilon\right)^2}\right] \;. \tag{5.27}$$

A graphical representation of the porosity dependence of the coefficients A and B are given in Figures 5.2 and 5.3 (p 126), respectively. Both the granular RUC model and the spherical cell model of Happel (1958) predict a more or less constant value for the coefficient A up to a porosity of 0.6. The value of the coefficient B predicted by the granular RUC model varies significantly over the entire porosity range, as shown in Figure 5.3. Although $\epsilon = 0$ and $\epsilon = 1$ corresponds to only solid and no solid, respectively, these values are included in Figures 5.2 and 5.3 to show the porosity dependence over the entire porosity range.

For porosities ranging from $\epsilon = 0.34$ to $\epsilon = 0.48$, reported empirical values for the coefficient A ranging from 157 to 180 have been obtained in the literature, with an average value of $A = 169$ (Macdonald et al. (1979)). According to a survey by Kemblowski &
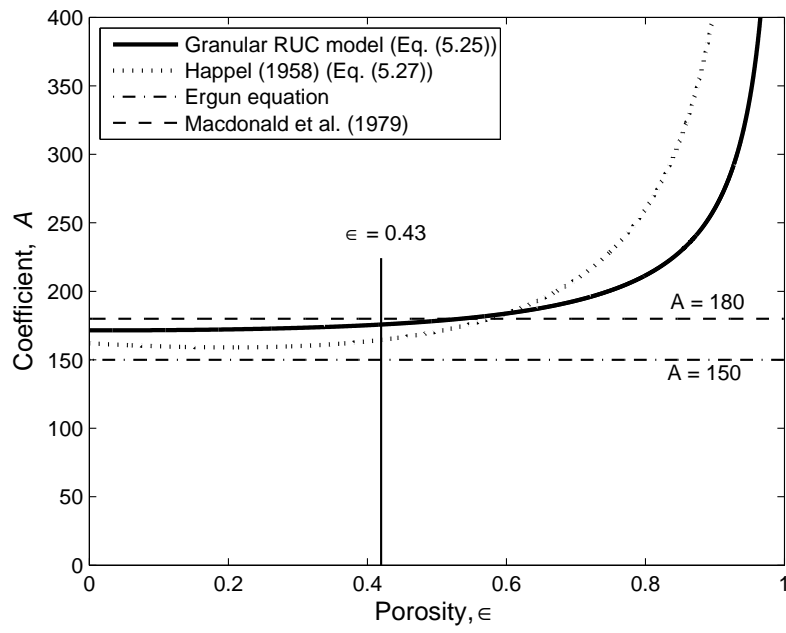
Figure 5.2: Porosity dependence of the coefficient A.
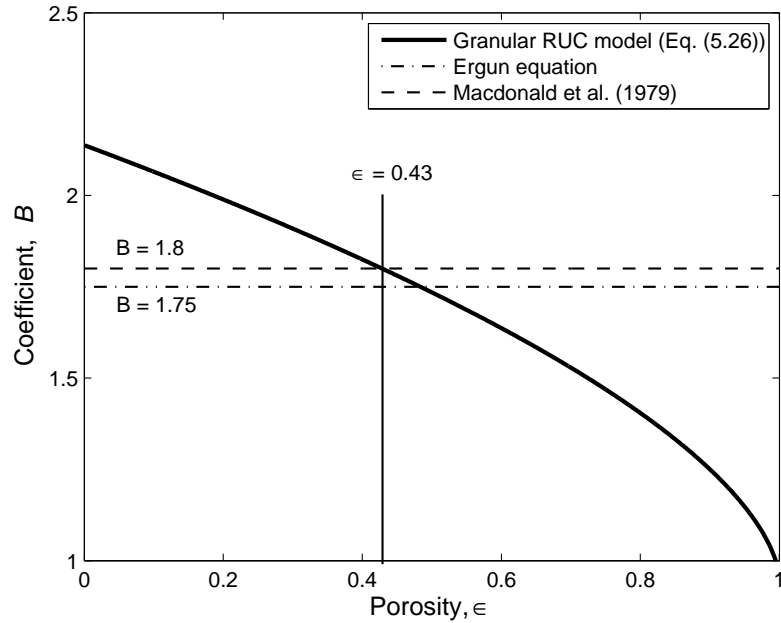
Figure 5.3: Porosity dependence of the coefficient B.

126

Michniewicz (1979), the values suggested for the coefficient A for flow of Newtonian fluids through granular beds, range from $A = 150$ to $A = 200$. The majority of references, however, suggest the value of $A = 180$, corresponding to the improved Ergun equation of Macdonald et al. (1979), rather than the value of $A = 150$ proposed by the Ergun equation. For the same porosity range of $0.34 \leq \epsilon \leq 0.48$, the values for A predicted by the granular RUC model range from 174 to 177.6, with an average value of 176. The range of coefficient values for A, predicted by the granular RUC model, lies well within the above given ranges obtained from experiments.

For the same porosity range as considered for the coefficient A, empirical values for the coefficient B ranging from 1.49 to 1.77 have been obtained in the literature, with an average value of $B = 1.63$ (Macdonald et al. (1979)). Values for the coefficient B predicted by the granular RUC model range from 1.75 to 1.88 with an average value of 1.81. (The values for the coefficient B have been obtained by using $c_d = 1.9$.) The RUC model somewhat over-estimates the average value of the coefficient B, in comparison with the reported experimental values of Macdonald et al. (1979). The discrepancy of the average value of the coefficient B from the empirical data may be attributed to the value used for the form drag coefficient c_d, which may not be a physically representative value. In order to obtain a more accurate value for c_d numerical analysis needs to be performed, but this falls beyond the scope of the present study.

Table 5.2 (p 125) shows that the coefficient values proposed by the granular RUC model for A and B at $\epsilon = 0.43$ are, however, in satisfactory agreement with the values proposed by the improved Ergun equation. The coefficient B, predicted by the granular RUC model at $\epsilon = 0.43$, corresponds 100% with the value proposed by Macdonald et al. (1979) and the coefficient A is within 2% from the empirical value. The granular RUC model may hence be regarded as a theoretical validation of the Ergun equation (or rather the improved Ergun equation).

5.4 Foam RUC model

Many authors in the literature have been concerned with measuring the pressure drop of water or airflow through metallic foams (e.g. Montillet et al. (1992), Antohe et al. (1997), Peak et al. (2000), Richardson et al. (2000), Boomsma & Poulikakos (2002), Hwang et al. (2002), Depois & Mortensen (2005), Dukhan (2006), Liu et al. (2006), Stemmet et al. (2006), Topin et al. (2006), Dukhan & Patel (2008), Gerbaux et al. (2009), Mancin et al. (2010), Miwa & Revankar (2011)) and ceramic foams (e.g. Philipse & Schram (1991), Innocentini et al. (1999a), Richardson et al. (2000), Moreira & Coury (2004), Lacroix et al. (2007), Incera Garrido et al. (2008)). Numerical studies have also been performed to predict the permeability and inertial coefficient of foamlike media (e.g. Xu et al. (2008), Gerbaux et al. (2010)).

It is well emphasized in the literature that foams have a different and much more complicated porous micro-structure than granular media forming a packed bed (e.g. Boomsma

& Poulikakos (2002), Hwang et al. (2002), Dukhan & Patel (2008), Huu et al. (2009)). Liu et al. (2006) have shown that the pressure drop over granular media is eight times higher than that of metallic foams. This is attributed to the larger wetting surface area of granular media resulting in more fluid-solid friction than in the case of foamlike media. Richardson et al. (2000) gives the ratio as ten to one. The lower pressure drop provided by foamlike media is what makes them useful as catalyst supports and heat sinks in heat transfer devices (Lacroix et al. (2007)). Another advantage of foams is that the effect of channeling, as observed in granular packed beds (Section 2.7.1, p 15), is negligible. The porosity and hence the permeability of foamlike media, confined by external boundaries, remains unchanged close to the walls (Boomsma & Poulikakos (2002), Krishnan et al. (2006)).

In addition to the irregular pore geometry of foams, the pores are randomly orientated (Miwa & Revankar (2011)). For certain foams within a certain porosity range irregular lumps of solid material are observed at the intersection of struts (Huu et al. (2009)). Some foams, furthermore, have hollow struts (Incera Garrido et al. (2008)), and the cross-section of the struts of some foams changes from being circular to triangular over a certain porosity range.

The geometrical modelling of foamlike media is therefore much more difficult than its granular counterpart, leading to fever studies in the literature regarding the analytical prediction of pressure drops and permeabilities than the customary procedure of empirical curve fitting. Authors who have used the latter procedure to relate the pressure drop and superficial velocities and/or the permeability and porosity include Philipse & Schram (1991), Peak et al. (2000), Richardson et al. (2000), Hwang et al. (2002), Moreira & Coury (2004), Dukhan (2006), Liu et al. (2006), Dukhan & Patel (2008), Incera Garrido et al. (2008), Gerbaux et al. (2009).

5.4.1 Existing geometric models for foamlike media

Four well recognized geometric pore-scale models used in the literature for approximating the intricate solid geometry of foamlike media, are given by Lacroix et al. (2007) and Huu et al. (2009), namely (i) the RUC model (ii) the cubic unit cell model (iii) the tetrakaidecahedron model and (iv) the dodecahedron model.

The cubic unit cell model was proposed by Lu et al. (1998) and used by Giani et al. (2005b) and Lacroix et al. (2007). It consists of a cubic unit cell with cylindrical fibres on the edges. The construction of the model was based on its analogy with cross-flow through banks of cylinders (Giani et al. (2005b)).

The tetrakaidecahedron model was proposed by Richardson et al. (2000) and also used by Fourie & Du Plessis (2002) (Section 3.15.7, p 67), Buciuman & Kraushaar-Czarnetzki (2003), Incera Garrido et al. (2008) and Xu et al. (2008). Each cell consists of 14 faces (or windows) of which six faces are squares and the remaining eight hexagonal (Buciuman & Kraushaar-Czarnetzki (2003), Mancin et al. (2010)). Triangular fibres are placed on

the edges of each face. Philipse & Schram (1991) found that the structural parameters predicted by the tetrakaidecahedron model lead to higher values than those obtained through image analysis. Although this is the case, Philipse & Schram (1991) state that the geometric model should be used as a first order approach, should it be the case that image analysis cannot be performed.

The dodecahedron model was used by Bhattacharya et al. (2002) and Huu et al. (2009). The dodecahedron and tetrakaidecahedron models have more or less the same number of struts per face (2.6 and 2.5, respectively). Each cell of the dodecahedron model consists of 12 pentagonal faces with triangular fibres on the edges (in the case of high porosity) and cylindrical fibres (at lower porosities). In the latter case the accumulation of solid material at the intersection of fibres is present. Huu et al. (2009) represented the accumulation of solid material at the intersection of fibres as a tetrahedron. Bhattacharya et al. (2002), on the other hand, combined the dodecahedron model with the cubic unit cell model. The dodecahedron model was used to represent the accumulation of solid material at the intersection of fibres.

5.4.2   Predicting dynamic specific surface areas

The dynamic specific surface values can be obtained from experimental pressure drop data (i.e. with the method of permeametry). If one, however, needs to predict the pressure drop, an independent method is required to determine the structural parameters needed for the determination of the pressure drop. In this regard, geometrical models are required to fulfil this need.

Dietrich et al. (2009) performed pressure drop measurements on three different types of foams at different superficial air velocities (up to $9\,\mathrm{m/s}$) under isothermal conditions. The three different types of foams considered, are made of Aluminium, Mullite and Oxide-Bonded Silicon Carbide (abbreviated OBSiC). The porosity, supplied by the manufacturer of the foams, ranges from 0.75 to 0.85 for the different samples.

Buciuman & Kraushaar-Czarnetzki (2003) proposed the following expression to determine the dynamic specific surface area, A_{vd}, of each foam sample:

$$A_{vd} \;=\; C \, \frac{1}{d_{strut} + d_{window}} \, (1 - \epsilon)^n \;, \tag{5.28}$$

where d_{strut} denotes the strut diameter and d_{window} is the window diameter (or pore diameter) of the foam sample. Equation (5.28) was derived from the tetrakaidekahedron model of Richardson et al. (2000) (Section 5.4.1, p 128). From this model the values of $C = 4.82$ and $n = 0.5$ were obtained, so that

$$A_{vd} \;=\; 4.82 \, \frac{1}{d_{strut} + d_{window}} \, (1 - \epsilon)^{1/2} \;. \tag{5.29}$$

Dietrich et al. (2009) obtained experimental data for the dynamic specific surface areas of

Table 5.3: Dynamic specific surface area values of Dietrich et al. (2009).

Foam	ϵ	Dynamic specific surface area, $A_{vd}\,(m^{-1})$			
		Exp.	Eq. (5.29)	Eq. (5.30)	Eq. (5.31)
Aluminium	0.754	1090	1097	927	1204
	0.808	664	656	590	752
	0.802	1204	1369	1222	1562
	0.806	1402	1665	1494	1907
	0.854	1109	917	884	1092
Mullite	0.736	–	1264	1050	1368
	0.785	–	744	650	837
	0.789	1291	1135	998	1282
	0.793	1395	1321	1166	1497
	0.834	–	966	902	1132
OBSiC	0.742	–	1085	906	1180
	0.791	–	664	585	751
	0.791	–	998	879	1129
	0.791	–	1335	1175	1510
	0.845	–	908	862	1074

the foam samples by means of Magnetic Resonance Imaging (Section 2.3, p 10) whereas light microscopy (Section 2.3) was used to measure the strut diameter and pore sizes. The experimental measurements for the dynamic specific surface areas are given in Table 5.3. From this data Dietrich et al. (2009) proposed empirical coefficient values of $C = 2.87$ and $n = 0.25$ by correlating equation (5.28) to the data, thus yielding

$$A_{vd} \; = \; 2.87 \, \frac{1}{d_{strut} + d_{window}} \, (1 - \epsilon)^{1/4} \; . \tag{5.30}$$

According to Dietrich et al. (2009), only the results obtained for the dynamic specific surface areas of the Aluminium foams are reliable. The latter values for C and n were thus obtained only from the Aluminium data. In Table 5.3 the values obtained from equations (5.29) and (5.30) are given for all three foam types.

Since the strut diameter and pore sizes were measured perpendicular to the streamwise direction, it follows that in RUC notation $d_{window} = d - d_s$ and $d_{strut} = d_s$. The dynamic

Table 5.4: Absolute relative percentage errors for the dynamic specific surface area values of Dietrich et al. (2009).

Foam	ϵ	Absolute relative percentage error for A_{vd} (%)		
		Eq. (5.29)	Eq. (5.30)	Eq. (5.31)
Aluminium	0.754	0.6	14.9	10.5
	0.808	1.2	11.1	13.3
	0.802	13.7	1.5	29.7
	0.806	18.8	6.6	36.0
	0.854	17.3	20.3	1.5
Mullite	0.736	–	–	–
	0.785	–	–	–
	0.789	12.1	22.7	0.7
	0.793	5.3	16.4	7.3
	0.834	–	–	–

specific surface predicted by the foam RUC model is given in Table 3.6 (p 67) as

$$A_{vd} \; = \; \frac{3\,(3-\psi)(\psi-1)}{d} \; , \tag{5.31}$$

with

$$\psi \; = \; 2 + 2\cos\left[\frac{4\pi}{3} + \frac{1}{3}\cos^{-1}(2\epsilon-1)\right] \; . \tag{5.32}$$

Values for the dynamic specific surface area predicted by equation (5.31) for the different foam samples are also presented in Table 5.3 (p 130). All these values are of the same order of magnitude as the theoretical model of Buciuman & Kraushaar-Czarnetzki (2003) and the empirical model of Dietrich et al. (2009).

Table 5.4 gives values for the absolute relative percentage error for A_{vd} (calculated with the aid of equation (I.2) in Appendix I, p 320) predicted by the various models measured with respect to the experimental data given in Table 5.3.

The absolute relative percentage errors provided by the RUC model is comparable to the those of the models of Buciuman & Kraushaar-Czarnetzki (2003) and Dietrich et al. (2009). Contrary to the data of the Mullite foam, which is regarded by Dietrich et al. (2009) to be less reliable than that of the Aluminium foams, the absolute relative percentage errors provided by the RUC model for the Mullite foam is less than those provided by the models of Buciuman & Kraushaar-Czarnetzki (2003) and Dietrich et al. (2009). For

the Aluminium foam, however, the contrary is true. (No values are presented in Table 5.4 (p 131) for the OBSiC-foam since no experimental data were provided by Dietrich et al. (2009) for this foam (Table 5.3, p 130).)

Buciuman & Kraushaar-Czarnetzki (2003) stress the fact that the deviations of their theoretical model may be attributed to the difficulty in correctly assessing the average pore-scale linear dimensions (i.e. the strut diameter and the pore width). Another reason reported for the deviations is the imperfections in the morphology of real foams. The imperfections may include hollow struts and pore blockage, which are also not accounted for in any of the models used in the analysis above. Lastly, surface roughness may also have an effect. Given all the latter factors that may influence the accuracy of model predictions, it is satisfactory that the RUC model yields predicted values of the same order of magnitude as the experimental values.

An advantage of the RUC model is that the dynamic specific surface area can be expressed in terms of any of the three pore scale linear dimensions. The dynamic specific surface in terms of the solid width d_s is given by

$$A_{vd} = \frac{3}{2\,d_s}(3 - \psi)(\psi - 1)^2 \,, \tag{5.33}$$

and in terms of the pore width,

$$A_{vd} = \frac{3\,(3 - \psi)^2(\psi - 1)}{2\,(d - d_s)} \,. \tag{5.34}$$

For the model predictions for A_{vd} provided by Buciuman & Kraushaar-Czarnetzki (2003) and Dietrich et al. (2009), both d_{strut} and d_{window} need to be known, whereas for the RUC model either d_{strut} or d_{window} needs to be known to predict the value of A_{vd}.

Other model predictions from the literature

More model predictions from the literature for the dynamic specific surface will be presented below. The structural parameters will be expressed in RUC notation. The strut diameter will be denoted by d_s, the cell size by d and the pore diameter by $d - d_s$.

The dynamic specific surface predicted by the tetrakaidecahedron model of Richardson et al. (2000) (Section 5.4.1, p 128), as a function of the pore diameter, is given by

$$A_{vd} = \frac{12.979\,(1 - \epsilon)^{1/2}[1 - 0.971(1 - \epsilon)^{1/2}]}{(d - d_s)} \,. \tag{5.35}$$

The dynamic specific surface of the cubic unit cell model of Lu et al. (1998), Giani et al. (2005b) and Lacroix et al. (2007) with cylindrical fibres can be obtained as follows: Let U_o and U_s respectively denote the volume of the unit cell and total volume of cylinders.

The volume of the unit cell is then given by $U_o = d^3$ and the total volume of cylinders by $U_s = (1 - \epsilon)U_o = (1 - \epsilon)d^3$. Since each strut is shared amongst four unit cells, it follows that

$$U_s = \frac{12}{4}\pi \left(\frac{d_s}{2}\right)^2 d = 3\pi \left(\frac{d_s^2}{4}\right) d \ . \tag{5.36}$$

Consequently, the strut diameter can be expressed as

$$d_s = d \left(\frac{4}{3\pi}(1 - \epsilon)\right)^{1/2} \ . \tag{5.37}$$

The dynamic specific surface is then given by

$$A_{vd} = \frac{4}{d_s}(1 - \epsilon) \ , \tag{5.38}$$

or in terms of the cell size it follows that

$$A_{vd} = \frac{2 \left(3\pi (1 - \epsilon)\right)^{1/2}}{d} \ . \tag{5.39}$$

Since Giani et al. (2005b) did not specify the pore diameter, Lacroix et al. (2007) determined the relation between the strut diameter and the pore diameter of the cubic unit cell model, which is given by

$$d_s = \frac{\sqrt{\frac{4}{3\pi}(1 - \epsilon)}}{1 - \sqrt{\frac{4}{3\pi}(1 - \epsilon)}} (d - d_s) \ . \tag{5.40}$$

Equation (5.40) results from the fact that the pore diameter is expressed as $d - d_s$ together with equation (5.37). The dynamic specific surface may then be expressed in terms of the pore diameter, as follows

$$A_{vd} = \frac{4 (1 - \epsilon) \left[1 - \sqrt{\frac{4}{3\pi}(1 - \epsilon)}\right]}{\sqrt{\frac{4}{3\pi}(1 - \epsilon)} (d - d_s)} \ . \tag{5.41}$$

For the dodecahedron model (Section 5.4.1, p 128) the dynamic specific surface for high porosities (with triangular fibres) is given by

$$A_{vd} = \frac{60}{\sqrt{5}} \frac{d_s}{d^2} \left(1 - \frac{1}{2}\sqrt{\frac{2}{3}} \frac{d_s}{d} \phi_d^2\right) \ , \tag{5.42}$$

and for low porosities (with cylindrical fibres),

$$A_{vd} = \frac{1}{d} \left[\frac{\frac{12\pi d_s \phi_d^2}{d}\left(1 - \frac{d_s \phi_d^2}{2d}\sqrt{\frac{2}{3}}\right)}{\sqrt{5}\,\phi_d\sqrt{3 - \phi_d}} + \frac{\sqrt{15}\left(1 - \frac{d_s \phi_d^2}{2d}\sqrt{\frac{2}{3}}\right)^2 \sin^2\left(\frac{\pi}{5}\right)}{2 (3 - \phi_d)}\right] \ , \tag{5.43}$$

133
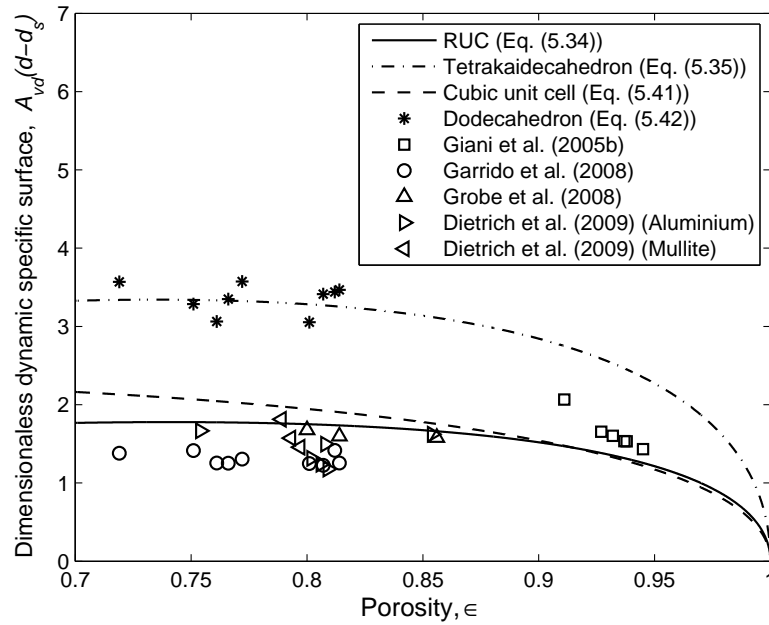
Figure 5.4: Dimensionless dynamic specific surface of foamlike media as a function of porosity.

with $\phi_d = 1.6180$. Equations (5.42) and (5.43) cannot be expressed as an explicit function of porosity.

Figure 5.4 shows the dimensionless dynamic specific surface, i.e. $A_{vd}(d-d_s)$, as a function of porosity. The dodecahedron and tetrakaidecahedron models yield similar predictions. This result was also obtained by Richardson et al. (2000). The RUC model and the cubic unit cell model, on the other hand, yield similar predictions. This result was also reported by Huu et al. (2009), who also stated that the former two models provided more accurate predictions. According to the results of the present study, the opposite is true. Figure 5.4 shows that the RUC model provides the most satisfactory agreement with the experimental data.

Incera Garrido et al. (2008) observed an over-prediction by the cubic unit cell model of equation (5.41), which is also evident in the lower porosity range of Figure 5.4. They attributed the over-prediction to (i) the uniform strut diameter assumed in the model, (ii) the accumulation of solid material at the intersection of struts which is not accounted for in the model and (iii) the influence of closed pores. It is noted here that the dodecahedron model which accounts for the accumulation of solid material at the intersection of struts, did not yield a more accurate prediction than the RUC model. It, in fact, led to less accurate results than the simple cubic unit cell and RUC models. Giani et al. (2005a) argues that the increased complexity of the tetrakaidecahedron model above that of the simple cubic unit cell is not worth the relative inaccuracy of its model predictions for the structural parameters. Based on an acceptable level of accuracy, simplicity and adaptive capabilities towards anisotropy, Giani et al. (2005b) chose to work with the cubic unit

cell model. The same argument applies to the preference of using the RUC model in the present study.

Incera Garrido et al. (2008) furthermore report relative deviations for their measured pore size distribution ranging between 36% and 47%. Miwa & Revankar (2011) reported deviations of up to 40% and that their mean projected pore diameter and cell size measurements deviated significantly from the values supplied by the manufacturer of the foams. As discussed in Section 3.15.7 (p 67), the latter measured values depend on how the pore diameter is defined. The deviations of the model predictions for the dynamic specific surface from the experimental data, may thus also be attributed to the large uncertainties in the measurements of the pore-scale linear dimensions.

5.4.3 Pressure drop predictions

Lacroix et al. (2007) state that although a direct analogy between granular and foamlike media has no physical meaning, due to the large difference in average porosity between these two types of porous media, it is useful to adapt the Ergun equation in order to provide an Ergun-type equation for foamlike media. Dukhan & Patel (2008) admits that the modelling of fluid flow through foamlike media is more challenging than in the case of granular media and that the two media have distinct pore-scale geometries. Still, they claim that the Ergun equation with a suitable pore-scale linear dimension, that can replace the equivalent particle diameter, is appropriate for correlating pressure drop data of foams.

Some authors (e.g. Innocentini et al. (1999b)) have at least expressed the need for a reliable analytical model that relates permeability to the structural parameters of foams. Due to the lack thereof, many authors in the literature (e.g. Innocentini et al. (1999), Richardson et al. (2000), Moreira & Coury (2004), Lacroix et al. (2007), Dietrich et al. (2009)) have used the Ergun equation to obtain pressure drop predictions for foamlike media. In the process, the coefficients of the Ergun equation have been adjusted towards quantitative agreement with experimental pressure drop data for non-granular media such as metallic foams (Edouard et al. (2008)), despite the distinct geometrical micro-structures of granular and foamlike media.

Dietrich et al. (2009), for example, have performed pressure drop measurements on different types of ceramic foams. They have correlated their experimental data with the Ergun equation and proposed values for the coefficients A and B for foamlike media. The same porosity dependence of the pressure drop was used as for granular media. Although new empirical coefficients were proposed in this case, such a practice is not recommendable as it does not provide physical insight into the flow process at hand. It resembles a fudge factor approach for which the coefficients may have to be adjusted for every other application.

Richardson et al. (2000) expressed the Ergun equation in terms of the dynamic specific surface and empirically related the Ergun coefficients to the porosity and pore diameter.

The dynamic specific surface was obtained by application of the tetrakaidecahedron model. Incera Garrido et al. (2008), however, refers to the model of Richardson et al. (2000) as "incorrect", since it does not provide satisfactory agreement with experimental data.

Lacroix et al. (2007) referred to the RUC model, cubic unit cell model, tetrakaidecahedron model and dodecahedron model as "very complex" and therefore reverted back to an empirical cure fitting procedure. A focus of the present study is, however, to illustrate that the RUC model is a relatively simple geometric pore-scale model that can be used to predict the pressure drop over foamlike media. Lacroix et al. (2007) have used the same Ergun coefficients but applied the cubic unit cell model to determine the strut diameter and its relation to the effective particle diameter. The relation between the pore diameter and the effective particle diameter of a granular packed bed of uniform granules is obtained by setting the specific surface areas of the (spherical) granular and (cylindrical) foam model geometries equal. The authors admit that, although the correlation provides good agreement with the experimental data, there is no physical justification for this semi-empirical modelling procedure. Although they claim that they have used no fitted parameters, the Ergun equation coefficients remain such parameters.

Huu et al. (2009) followed the same modelling approach as Lacroix et al. (2007), but instead of using the specific surface area of the cubic unit cell model, they used the corresponding expression of the dodecahedron model.

The models of Richardson et al. (2000) and Lacroix et al. (2007) make use of combined geometries, i.e. the capillary tube model on which the Ergun equation is based and a geometric model representative of the consolidated foam micro-structure. Using two totally different model geometries to form a combined model is physically not justifiable. This is, however, not the case with the RUC model, as its modelling procedure and the estimation of the pore-scale linear dimension used in the model is based on the same geometric model.

Innocentini et al. (1999) used the Ergun equation with an equivalent particle diameter as representative of the pore diameter but admits that the correlation produces errors in the permeability prediction of up to 50%. Dukhan & Patel (2008) also applied the Ergun equation but used the reciprocal of the surface area to replace the equivalent particle diameter, because, as stated by Dukhan (2006), the determination of an equivalent particle diameter for foamlike media is not an easy task.

The problem in applying the Ergun equation to foamlike media is that the coefficients and functional dependence of the pressure drop on porosity and the Reynolds number were obtained empirically for granular media. The Ergun equation is therefore expected to be valid only for granular media and not for other pore geometries as foamlike media and fibre beds. For each new application or flow conditions new empirical coefficients should be proposed together with a different functional dependency of the pressure drop on porosity.

Although the empirical nature of the Ergun equation inhibits straight-forward generalization and adaptation to other physical flow processes, it has, for instance, been used as a drag model in the fluidization state of a fluidized bed (e.g. Gidaspow (1994)) and it has

136

been adapted to predict non-Newtonian flow behaviour (e.g. Christopher & Middleman (1965), Brea et al. (1976), Kemblowski & Michniewicz (1979)).

As illustrated in Chapters 3 and 4, different pore-scale geometries lead to different porosity dependencies for the pressure drop. Therefore, in order to apply to different physical flow conditions, the actual physical differences should be re-modelled (geometrically and mathematically) to provide physical compliance between the model and reality. The concept of remodelling is supported by Boomsma & Poulikakos (2002) and is considered an important aspect, as it is the only meaningful manner in which generalizations could be attempted. In the following section it will be illustrated that the foam RUC model can be regarded as a theoretical Ergun-type equation for foamlike media.

According to Edouard et al. (2008) (and many other authors from the literature) the pressure drop over foamlike media also follows the quadratic relationship in superficial velocity described by the Forchheimer equation (2.20), i.e.

$$-\frac{\mathrm{d}p}{\mathrm{d}x} \; = \; \frac{\mu}{k_1}\,q \; + \; k_2\,\rho\,q^2 \; , \tag{5.44}$$

where k_1 is the Darcy permeability and k_2 is the non-Darcy flow coefficient.

Figure 5.5 (p 138) compares the permeability k_1, dimensionalized with the pore diameter, $d - d_s$, with various empirical values from the literature obtained for foamlike media as a function of porosity. Figure 5.6 (p 138) shows the non-Darcy coefficient k_2, also dimensionalized with the pore diameter, $d - d_s$. Also shown in Figures 5.5 and 5.6 are the model predictions provided by the doubly staggered foam and granular RUC models (obtained from Tables 4.5 (p 95) and 4.14 (p 107), respectively).

The over-prediction and under-prediction of the granular RUC model in Figures 5.5 and 5.6, respectively, confirms that for foamlike media the pore-scale geometry should be re-modelled since it leads to a different porosity dependence than in the case of granular media. As reported by Edouard et al. (2008), and also shown by Figures 5.5 and 5.6, the permeability increases with porosity and the non-Darcy coefficient, on the other hand, decreases with porosity. Overall the RUC model predictions agree well with the wide variety of experimental data provided in the literature.

The model predictions of Huu et al. (2009) are given by

$$k_1 \; = \; \frac{6\,\epsilon^3}{25\,A_{vd}^2} \; , \tag{5.45}$$

and

$$k_2 \; = \; \frac{6\,\epsilon^3}{1.75\,A_{vd}} \; , \tag{5.46}$$

with the dynamic specific surface given by equation (5.42) for high porosities and by equation (5.43) for low porosities. The model predictions provided by equations (5.45)

137
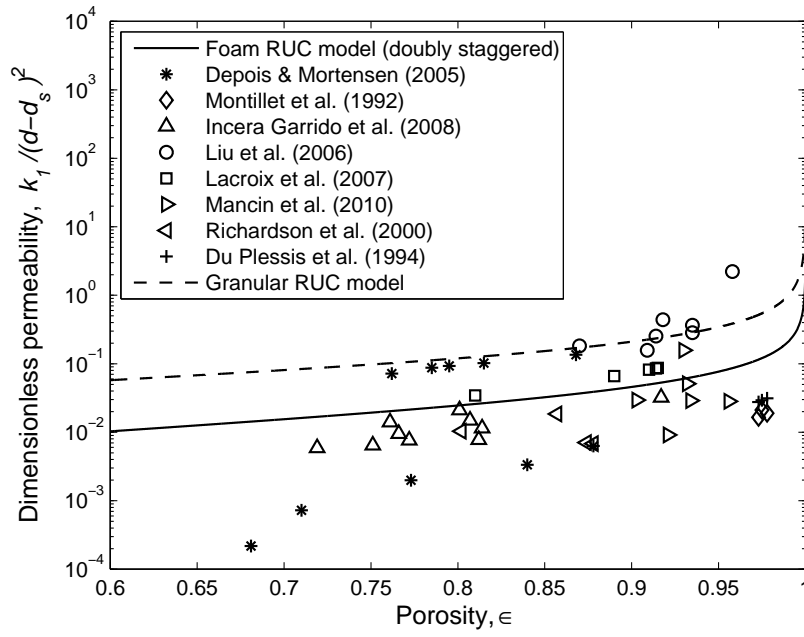
Figure 5.5: Dimensionless permeability of foamlike media as a function of porosity.
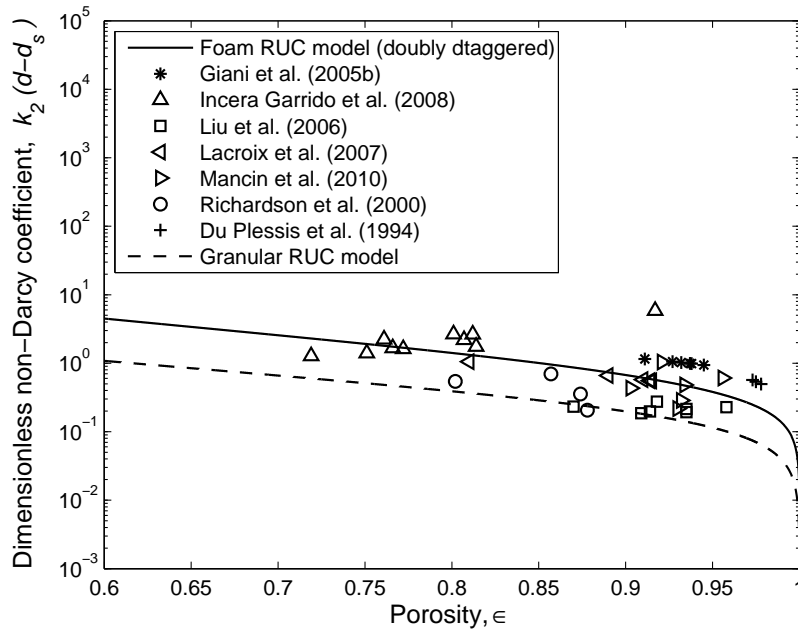
Figure 5.6: Dimensionless non-Darcy coefficient for foamlike media as a function of porosity.

and (5.46) are not shown in Figures 5.5 and 5.6 (p 138), respectively, since equations (5.42) and (5.43) cannot be expressed as an explicit function of porosity. Huu et al. (2009), however, found that the model predictions of their high porosity model were more accurate than that of the low porosity model. This was attributed to the accumulation of solid material at the intersection of struts which is accounted for in the high porosity model but not in the low porosity model.

Concluding remarks from the literature

Various authors in the literature have drawn different conclusions regarding the comparison of the various models described above. Edouard et al. (2008), for instance, found that the empirical model prediction of Richardson et al. (2000) for k_1 agree well with the experimental data but the prediction for k_2 were "out of scale". This is, however, not observed in Figure 5.6 (p 138) where satisfactory agreement is obtained with the other models. They also found the RUC model of Du Plessis et al. (1994) and the semi-empirical model of Lacroix et al. (2007) to give the most accurate predictions. They state that the standard deviation associated with the latter two models for $\epsilon > 0.9$ is below $\pm 30\%$, which is referred to by Edouard et al. (2008) as "low". Edouard et al. (2008) therefore recommend the use of the latter two models for "reliable values" of k_1 and k_2 to be obtained. They state furthermore that the models of Du Plessis et al. (1994) and Lacroix et al. (2007) are applicable to any type of foam and excludes any "fitting method". The author of this dissertation however disagree with the latter statement that the model of Lacroix et al. (2007) does not contain any fitting parameters. Although Lacroix et al. (2007) kept the Ergun coefficients unchanged, those coefficients were originally empirical curve fitting parameters.

Mancin et al. (2010) add the models of Fourie & Du Plessis (2002) and Bhattacharya et al. (2002) to the list of models that do not contain empirical curve fitting parameters. They state that the model of Lacroix et al. (2007) yields satisfactory pressure drop predictions in the vicinity of $\epsilon = 0.93$ and that the model of Fourie & Du Plessis (2002) under-predicts their experimental pressure drop data over the entire porosity range under consideration. They obtained better results with the models of Du Plessis et al. (1994) and Bhattacharya et al. (2002). Since Mancin et al. (2010) found that no model seemed to predict the pressure drop with acceptable accuracy, they proposed a model in which an empirical dependence of the hydraulic diameter on the PPI number is incorporated. The use of the PPI number has, however, been regarded as unfavourable by many authors in the literature (Section 3.15.7, p 67).

Reasons for large variations in pressure drop data

Peak et al. (2000) mentioned that the large variation in pressure drop data of foams (as observed in Figure 5.5 (p 138) for the permeability), as opposed to that of packed beds, is not unusual. Incera Garrido et al. (2008) reports deviations of up to 20% in the pressure

drop of foam samples *having the same morphology*. Depois & Mortensen (2005) regard variations within 25% as "very good". According to Edouard et al. (2008), the deviations of model predictions from experimental data can be as high as 100%. Adjustment of the values of k_1 and k_2 by several authors in the literature to fit experimental pressure drop data led to variations in the value of the Ergun coefficient, A, between 100 and 865 and variations in B between 0.65 and 2.65 (Edouard et al. (2008)).

Reasons for the large deviations of model predictions from experimental data are the following: There are large variations in pore diameter of the same sample from which the average pore diameter is calculated because of different manufacturing processes leading to imperfections within the foam packing (Incera Garrido et al. (2008), Miwa & Revankar (2011)). Incera Garrido et al. (2008) states that, even though the same method of replication is used, the morphology of foams from different manufacturers differ considerably. There are furthermore inconsistency in the definition and measurement of the pore diameter (Edouard et al. (2008), Miwa & Revankar (2011)).

In addition to uncertainties in the measurement of the pore size and strut diameters, the presence of closed pores also have an effect as well as foam compression (Dukhan & Patel (2008)). Closed pores lead to a higher drag coefficient. The number of closed pores of a given foam sample can also differ significantly (Incera Garrido et al. (2008)).

The values of k_1 and k_2 are often measured indirectly by application of the Forchheimer equation (Edouard et al. (2008)) which can affect their accuracy since other parameters, with their own uncertainties, are also involved. Another very important reason for the large variation in the values of k_1 and k_2 are their dependence on the velocity range used, which is usually not specified by authors (Innocentini et al. (1999a)). There is also a large amount of uncertainty in the method of extrapolation in order to determine the values of k_1 and k_2 from the Forchheimer relation (Innocentini et al. (1999a)).

5.4.4 Ergun-type equation for foamlike media

Dietrich et al. (2009) expressed the Ergun equation in the following form:

$$\frac{\Delta p}{L} \;=\; A' \, \frac{\mu \, q}{\epsilon \, D_h^2} \;+\; B' \, \frac{\rho \, q^2}{\epsilon^2 \, D_h} \; . \tag{5.47}$$

If equation (5.47) is compared to the Ergun equation presented in Appendix C.4 (i.e. equation (C.17), p 289), it follows that

$$A' \;=\; \frac{A \, (1-\epsilon)^2}{\epsilon^2} \; , \tag{5.48}$$

and

$$B' \;=\; \frac{B \, (1-\epsilon)}{\epsilon} \; . \tag{5.49}$$

For the Ergun equation $A = 150$ and $B = 1.75$, which yields $A' = 264$ and $B' = 2.32$ for granular packed beds of average porosity $\epsilon = 0.43$. For the granular RUC model it follows from equations (5.25) and (5.26) that

$$A' = \frac{25.4\,\epsilon^3\,(1-\epsilon)^2}{\epsilon^2\,(1-\epsilon)^{2/3}\left(1-(1-\epsilon)^{1/3}\right)\left(1-(1-\epsilon)^{2/3}\right)^2}\,, \tag{5.50}$$

and

$$B' = \frac{\epsilon\,c_d\,(1-\epsilon)}{2\left(1-(1-\epsilon)^{2/3}\right)^2}\,, \tag{5.51}$$

respectively. Equations (5.50) and (5.51) respectively yields coefficient values of $A' = 309$ and $B' = 2.38$ for the same average bed porosity of $\epsilon = 0.43$.

Dietrich et al. (2009) state that equation (5.47) is also suitable to predict the pressure drop of ceramic foams. They expressed the coefficient A' in terms of the permeability, k, i.e.

$$A' = \frac{\epsilon\,D_h^2}{k}\,, \tag{5.52}$$

and the coefficient B' in terms of the passability, η, i.e.

$$B' = \frac{\epsilon^2\,D_h}{\eta}\,. \tag{5.53}$$

Equations (5.52) and (5.53) were obtained by fitting the following Forchheimer-type equation to their experimental pressure drop data:

$$\frac{\Delta p}{L} = \frac{\mu}{k}\,q \;+\; \frac{\rho}{\eta}\,q^2\,, \tag{5.54}$$

and comparing it to equation (5.47). The experimental values for the permeability and passability are given in Table 5.5 (p 142).

Dietrich et al. (2009) found the three types of ceramic foams to be "geometrically similar". They presented the Hagen number, $Hg = (\Delta p/L)(D_h^3\rho/\mu^2)$, graphically as a function of their Reynolds number, $Re_D = (\rho q D_h)/(\epsilon\mu)$. On a log-log plot they fitted a single line through their experimental results and concluded that the pressure drop is roughly independent of the material and porosity (the porosity range considered for the three types of ceramic foams is $0.736 \leq \epsilon \leq 0.854$, as is evident from Table 5.5).

For all three ceramic foams considered Dietrich et al. (2009) proposed mean coefficient values of $A' = 110$ and $B' = 1.45$ (within an experimental error of $\pm 20\%$).

Similarly as was illustrated that the empirical coefficients of the Ergun equation can be expressed as a function of porosity, the empirical coefficients of the Ergun-type equation

141

Table 5.5: Comparison of the permeability and passability values of the ceramic foams of Dietrich et al. (2009) with the RUC model predictions.

Foam	ϵ	Permeability, $k \times 10^{-9}\,(\mathrm{m^2})$		Passability, $\eta \times 10^{-5}\,(\mathrm{m})$		Absolute relative percentage error (%)	
		Exp.	RUC	Exp.	RUC	k	η
Aluminium	0.754	130	52	88	87	60	1
	0.808	77	176	187	195	129	4
	0.802	54	52	114	104	3	9
	0.806	32	39	98	92	23	6
	0.854	144	75	180	153	48	15
Mullite	0.736	90	—	95	—	—	—
	0.785	299	—	186	—	—	—
	0.789	88	43	122	90	51	26
	0.793	45	38	102	85	15	17
	0.834	120	—	190	—	—	—
OBSiC	0.742	65	—	95	—	—	—
	0.791	276	—	135	—	—	—
	0.791	56	—	123	—	—	—
	0.791	46	—	84	—	—	—
	0.845	220	—	150	—	—	—

for foamlike media (i.e. equation (5.47)) can also be expressed as a function of porosity by application of the foam RUC model. By expressing the pressure gradient predicted by the foam RUC model in the same form as equation (5.47), predictions for the coefficients A' and B' can be obtained. The pressure gradient predicted by the doubly staggered foam RUC model is given by (Table 4.15, p 108)

$$\frac{\Delta p}{L} \;=\; \frac{36\,\psi^2(\psi - 1)\,\mu\,q}{\epsilon^2\,d^2} \;+\; \frac{(\psi - 1)(3 - \psi)\,\psi^2\,c_d\,\mu\,q}{4\,\epsilon^3\,d^2}\,Re_{qd}\,, \qquad (5.55)$$

with the Reynolds number, Re_{qd}, defined as (Section 4.3, p 84)

$$Re_{qd} \;=\; \frac{\rho\,q\,d}{\mu}\,. \qquad (5.56)$$

The relationship between the cell size, d, and the hydraulic diameter, D_h, is given by

equation (3.58), i.e.

$$D_h = \frac{4\,\epsilon\,d}{3\,(3-\psi)(\psi-1)}\,. \tag{5.57}$$

Consequently the pressure gradient predicted by the doubly staggered foam RUC model can be expressed in terms of the hydraulic diameter as follows:

$$\frac{\Delta p}{L} = \frac{16\,\psi^3}{(\psi-1)\,\epsilon\,D_h^2}\frac{\mu\,q}{} + \frac{\psi^2\,c_d}{3}\frac{\rho\,q^2}{\epsilon^2\,D_h}\,. \tag{5.58}$$

Equating equations (5.47) and (5.58) yields

$$A' = \frac{16\,\psi^3}{(\psi-1)}\,, \tag{5.59}$$

and

$$B' = \frac{\psi^2\,c_d}{3}\,, \tag{5.60}$$

with the porosity dependence of the geometric factor, ψ, given by

$$\psi = 2 + 2\cos\left[\frac{4\pi}{3} + \frac{1}{3}\cos^{-1}(2\epsilon - 1)\right]\,. \tag{5.61}$$

According to equations (5.59) and (5.60), the coefficients A' and B' depend on the porosity and pore size, since the geometric factor ψ is a function of porosity and the porosity is related to the pore size through equation (3.39). The foam RUC model illustrates through equations (5.59) and (5.60) that the 'constant empirical coefficients' of Dietrich et al. (2009) relate to the pore-scale geometry and therefore have physical meaning, rather than just being constant empirical values. In Figure 5.7 (p 144) the porosity dependence of the coefficient A' predicted by the foam and granular RUC models (i.e. equations (5.59) and (5.50), respectively) are shown graphically. Similarly, Figure 5.8 (p 144) shows the coefficient B' as a function of porosity as predicted by the foam and granular RUC models (i.e. equations (5.51) and (5.60)).

Figure 5.7 shows that in comparison with the values of the coefficient A', predicted by the granular RUC model, the values predicted by the foam RUC model remain more or less constant with change in porosity. Figure 5.8 shows that the coefficient B', predicted by both the foam and granular RUC models, vary significantly with change in porosity.

According to Dietrich et al. (2009), the coefficient values A' and B' for foamlike media are independent of the material and geometrical parameters (i.e. porosity and pore size). This is contrary to the findings of the present study. According to the foam RUC model, this is only true for the coefficient A'. Figure 5.8 shows that the coefficient B' is sensitive to the value of the interstitial form drag coefficient, c_d, and porosity.
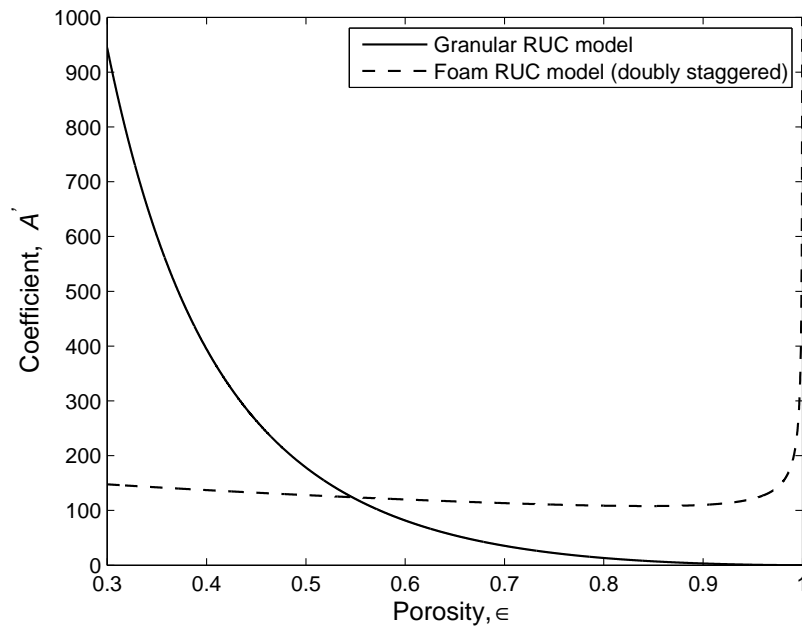
Figure 5.7: Coefficient A' as a function of porosity.
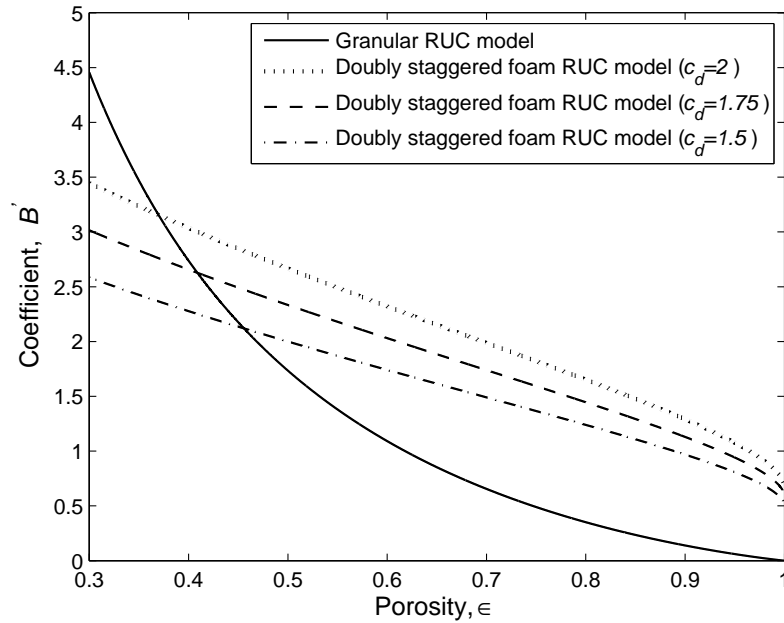
Figure 5.8: Coefficient B' as a function of porosity.

By determining the mean porosity of the three geometrically similar ceramic foams, model predictions for the coefficients A' and B' can be obtained. Using $\epsilon = 0.79$ as the mean porosity (obtained from Table 5.5, p 142) and $c_d = 2$ (Section 3.15.6, p 63) it follows that the coefficient values predicted by the foam RUC model are given by $A' = 109$ and $B' = 1.69$. The latter values are in satisfactory agreement with the values of $A' = 110$ and $B' = 1.45$ proposed by Dietrich et al. (2009). The absolute relative percentage error of the RUC model prediction for A' is less than 1%, measured with respect to the value proposed by Dietrich et al. (2009). For the coefficient B' the absolute relative percentage error is 17%, which is within the experimental error range of $\pm 20\%$ given by Dietrich et al. (2009). Since the coefficient B' is sensitive to the value of the form drag coefficient, c_d, a slightly lower value for c_d may improve the model prediction for the coefficient B', as illustrated in Figure 5.8 (p 144). The sensitivity of the coefficient B' to the porosity may be another reason for the relatively large percentage error.

Another advantage of the RUC model is that because it is based on sound physical principles, it can provide physical meaning to the model predictions (and essentially the empirical coefficients), whereas this cannot be done for the empirical models.

From equations (5.54), (5.58) and the relation

$$A_{vd} = 4\,\frac{\epsilon}{D_h}\,, \tag{5.62}$$

it follows that the permeability predicted by the foam RUC model can be expressed as

$$k = \frac{\epsilon^3\,(\psi - 1)}{A_{vd}^2\,\psi^3}\,. \tag{5.63}$$

Similarly, the passability predicted by the foam RUC model is given by

$$\eta = \frac{12\,\epsilon^3}{c_d\,\psi^2\,A_{vd}}\,. \tag{5.64}$$

The experimental porosity and dynamic specific surface area values, given in Table 5.3 (p 130), were used to predict the permeability and passability with the aid of equations (5.63) and (5.64), respectively. The predicted values are presented in Table 5.5. A value of 2 was used for the interstitial form drag coefficient.

For both the Aluminium and Mullite foams the predicted η-values show satisfactory agreement with the experimental values. For the Aluminium foam the absolute relative percentage error for η (according to equation (I.2) in Appendix I, p 320), ranges between 1% and 15%. For the Mullite foam the maximum error is 26%. Table 5.5 shows that a wide range of absolute relative percentage errors (calculated according to equation (I.2)) are obtained for the k-values. This may be attributed to the fact that the A_{vd}-values are squared in the expression for the permeability (i.e. in equation (5.63)), hence the experimental error in the measurement of A_{vd} is also squared. The passability, on the
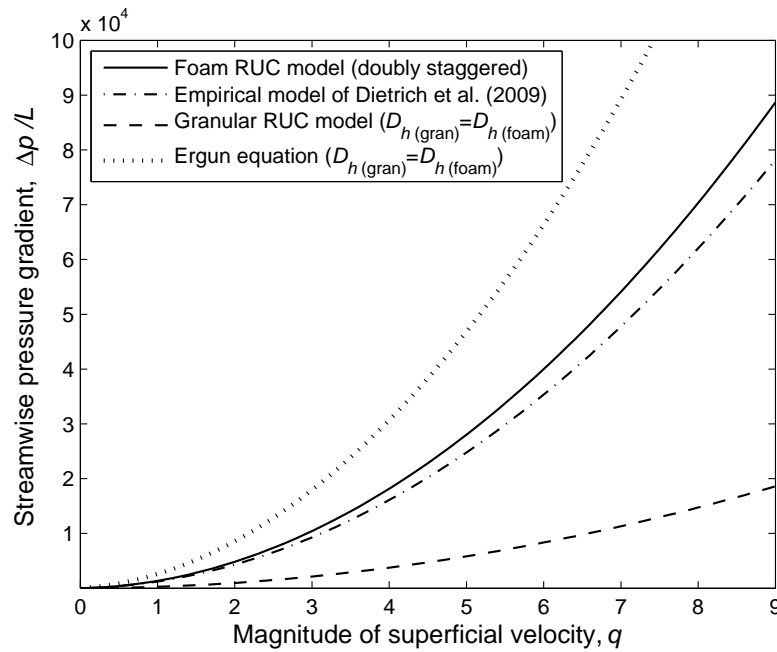
Figure 5.9: Streamwise pressure gradient as a function of the magnitude of the superficial velocity for foamlike and granular media for $\epsilon = 0.80$.

other hand, is a linear function of A_{vd}. Despite the deviations between the predicted and experimental permeability values presented in Table 5.5 (p 142), the average A'-value proposed by Dietrich et al. (2009) to correlate all their experimental data agrees well with the coefficient A' predicted by the foam RUC model.

5.4.5 Comparison between pressure drop predictions of granular and foamlike media

Figure 5.9 shows the streamwise pressure gradient, i.e. equation (5.47), as a function of the magnitude of the superficial velocity for the Aluminium foam. As already mentioned, only the experimental data for the dynamic specific surface areas of the Aluminium foams were reliable (according to Dietrich et al. (2009)). Similar figures for the other two types of foams are therefore omitted. The average of the experimental dynamic specific surface area values given in Table 5.3 (p 130) for the Aluminium foam was calculated as $1\,094\,\mathrm{m}^{-1}$ and the average porosity value as 0.80. From equation (5.62) the average hydraulic diameter was obtained. The streamwise pressure gradient predicted by the granular RUC model (with the aid of equations (5.47), (5.50) and (5.51)), as a function of the magnitude of the superficial velocity, is also shown in Figure 5.9. In Table 5.6 (p 147) the values for the coefficients A' and B' are summarized for the various models under consideration in Figure 5.9.

The pressure drop predicted by the granular RUC model at $\epsilon = 0.8$ is about 79% lower

146

Table 5.6: Values for the coefficients $A^{'}$ and $B^{'}$.

Model	$A^{'}$	$B^{'}$
Foam (RUC)	109	1.65
Foam (Dietrich et al. (2009))	110	1.45
Granular (RUC)	394	2.7
Granular (Ergun equation)	338	2.63

than the pressure drop predicted by the foam RUC model evaluated at the same porosity. The lower pressure drop predicted by the granular RUC model for the same porosity of $\epsilon = 0.80$ can be attributed to the coefficient values $A^{'}$ and $B^{'}$ as well as to the value used for the hydraulic diameter. Table 5.6 and Figures 5.7 and 5.8 (p 144) show that both the coefficients $A^{'}$ and $B^{'}$ have higher values at $\epsilon = 0.80$ for the foam RUC model than for the granular model. The relationship between the hydraulic diameter and the cell size d of the foam RUC model is given by equation (5.57). Similarly, for the granular model it follows from equations (5.62), (3.20) and the equation for A_{vd} in Table 3.3 (p 57) that

$$D_h = \frac{4\,\epsilon\,d}{6\,(1 - \epsilon)^{2/3}} \; . \tag{5.65}$$

Figure 5.10 (p 148) shows that the hydraulic diameter measured with respect to the RUC cell size d is more or less the same at $\epsilon = 0.80$ for both models (i.e 1.5 for the granular model versus 1.3 for the foam model).

The pressure drop calculated with the Ergun equation at $\epsilon = 0.80$ is about 88% higher than the pressure drop predicted by the granular RUC model. In previous studies, the granular RUC model has successfully served as drag model in pressure drop simulations over a fluidized bed of porosity $\epsilon = 0.80$ (Halvorsen et al. (2006)). As mentioned in Section 5.3 (p 119), the Ergun equation is not applicable at $\epsilon = 0.80$. The Ergun coefficients were originally obtained for packed beds of average porosity 0.43. Either new coefficients should be obtained for porosities beyond the packed bed range, in this case at $\epsilon = 0.80$, or an additional term should be added to the Ergun equation to account for the porosity dependence of the coefficients. It was shown by Woudberg (2006) that for $\epsilon > 0.80$ an extra term, provided by Wen & Yu (1966) and Rowe (1961), should be added to the gas/partcle drag coefficient proposed by the Ergun equation.

When comparing the pressure drop over a granular packed bed to the pressure drop over ceramic foams, Dietrich et al. (2009) suggested to use $\epsilon = 0.40$ as the average porosity for granular packed beds, as opposed to the average porosity of $\epsilon = 0.80$ for the ceramic foams, since a granular packed bed of $\epsilon = 0.80$ is not a real packing. Based on this argument and the fact that an average porosity of $\epsilon = 0.43$ has been used in the present study as a more refined value associated with a granular packed bed, the pressure drop

147
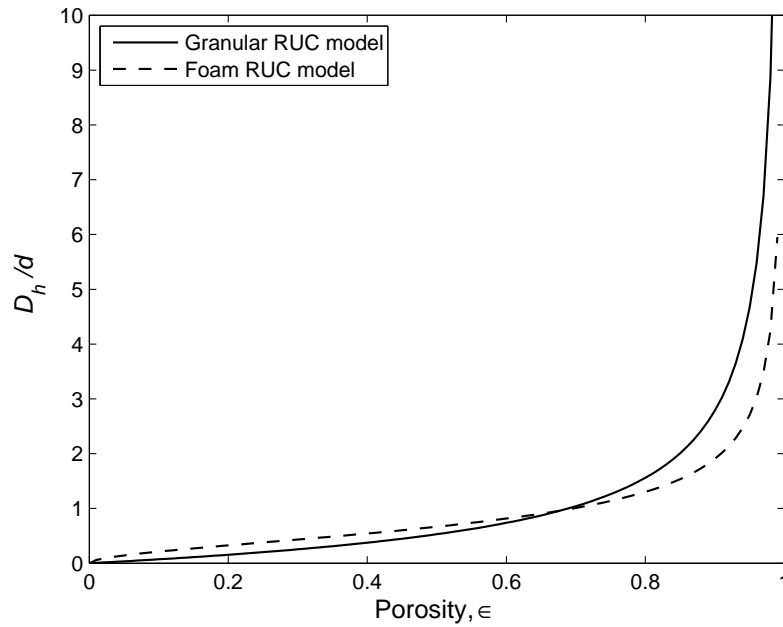
Figure 5.10: Ratio of hydraulic diameter and RUC cell size as a function of porosity.

over granular packed beds of average porosity $\epsilon = 0.43$ is compared in Figure 5.11 (p 149) to the pressure drop over the ceramic foams of average porosity $\epsilon = 0.80$. Note that the latter porosity of 0.80 is the average porosity of the Aluminium foams used by Dietrich et al. (2009) in their experiments and does not represent the average porosity associated with foamlike media in general. Such an average is difficult to determine since there is, to the knowledge of the author of this dissertation, no mention made in the literature of a lower porosity limit for foamlike media.

When Dietrich et al. (2009) compared their empirical foam model (for $\epsilon = 0.80$) with the Ergun equation (for $\epsilon = 0.40$) they used the same value for the hydraulic diameter, D_h. For granular and foamlike media of different porosities the hydraulic diameter will not necessarily be the same when different porosities are considered. In equation (5.47) this is an important issue as the hydraulic diameter is squared in the Darcy term. According to the RUC models, the ratio of the hydraulic diameter to the RUC cell size d in Figure 5.10 yields more or less the same value for a porosity of 0.80 for both granular and foam models, but this value is higher than the value at $\epsilon = 0.43$. The value of D_h/d for the foam RUC model at $\epsilon = 0.80$ is 1.30, whereas the value of D_h for the granular RUC model at $\epsilon = 0.43$ is 0.42. This discrepancy is squared in equation (5.47) which leads to a significant effect on the pressure gradient, as shown in Figure 5.11. The pressure gradient predicted by the granular RUC model in which the same hydraulic diameter is used as for the foam RUC model is significantly lower than the pressure gradient prediction in which the hydraulic diameter differs from that of the foam RUC model.

The pressure gradient predicted by the granular RUC model, with $\epsilon = 0.43$ and in which

148
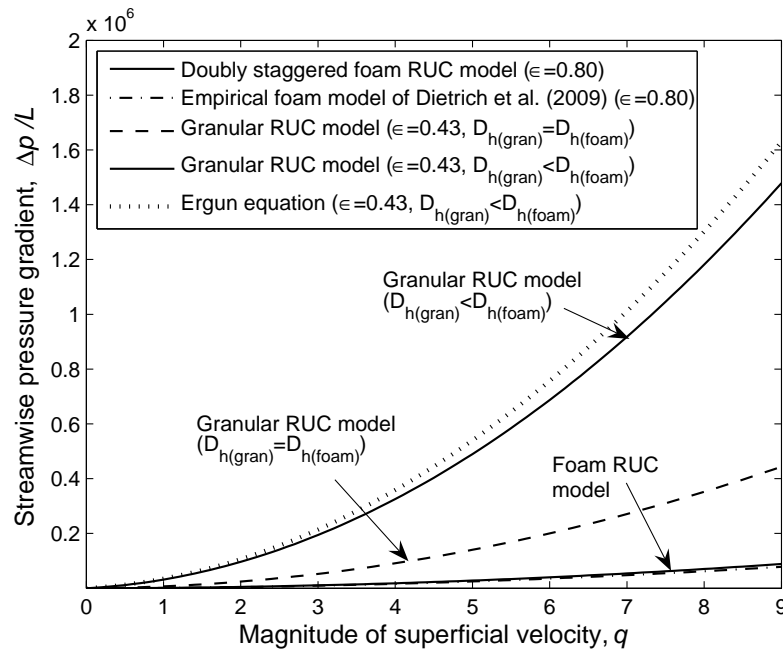
Figure 5.11: Streamwise pressure gradient as a function of the magnitude of the superficial velocity for foamlike and granular media of porosity 0.80 and 0.43, respectively.

the same hydraulic diameter is used as in the foam RUC model, is 80% higher than the pressure gradient predicted by the foam RUC model. If the lower value for the hydraulic diameter is used in the granular RUC model, the pressure gradient prediction increases with another 72%, which is a significant difference. The pressure drop predicted by the granular RUC model with $\epsilon = 0.43$ and in which the lower hydraulic diameter is used, is thus in total 152% higher than that predicted by the foam RUC model at $\epsilon = 0.8$. This result corresponds to the observation from the literature that the pressure drop predicted for granular media is significantly higher than that for foamlike media.

Figure 5.11 shows that the foam RUC model is in satisfactory agreement with the empirical foam model of Dietrich et al. (2009). The same hydraulic diameter values were used in both models. The granular RUC model, in which the lower value for the hydraulic diameter is used, is in satisfactory agreement with the Ergun equation, in which the same lower hydraulic diameter value is used.

The higher pressure drop for granular media in comparison with foamlike media in Figure 5.11 may partly be contributed to the lower porosity associated with a granular packed bed than with foamlike media. The lower porosity represents more solid material in the sample volume which leads to a higher flow resistance and hence a higher pressure drop. The fact that foamlike media have a lower pressure drop than granular media is one of the advantageous properties of foamlike media for use in industrial applications, since a lower pressure drop requires less energy for fluid flow (Innocentini et al. (1999b)). Figures 5.7 and 5.8 (p 144) furthermore show that both the coefficient values A' and B' of the granular RUC model at $\epsilon = 0.43$ are higher than the coefficient values of the foam RUC

149

model at $\epsilon = 0.80$. As already mentioned, the hydraulic diameter of the granular RUC model at $\epsilon = 0.43$ is lower than the value for the foam model at $\epsilon = 0.80$. Since the hydraulic diameter appears as denominators in equation (5.47), the lower D_h value leads to a higher pressure gradient.

According to Dietrich et al. (2009), their newly proposed empirical Ergun-type equation for foamlike media (i.e. equation (5.47)) can alternatively be used to determine the hydraulic diameter of new ceramic foam samples if the pressure drop measurements and porosity values are known. Then from equation (5.62) the dynamic specific surface area can be obtained. Dietrich et al. (2009) state that being able to determine the hydraulic diameter, and hence d_{strut} and d_{window}, from pressure drop data eliminates the need to perform expensive, time-consuming experiments to determine the morphology of the porous medium. By knowing the dynamic specific surface area of a foam sample, it is however, not possible to calculate d_{strut} and d_{window} from equation (5.30), if the values of both of these parameters are unknown. More information is needed. The advantage of the foam RUC model is that two separate equations are provided for A_{vd}, i.e. equations (5.33) and (5.34) from which $d_{strut} = d_s$ and $d_{window} = d - d_s$ can respectively be obtained.

5.5 Fibre RUC model

Jackson & James (1986) provide a comprehensive collection of experimental data from numerous authors, based on flow through various types of fibrous porous media. Jackson & James (1986) and Skartsis et al. (1992) furthermore provide summaries of theoretical models for predicting the permeability of fibrous porous media.

Since fibrous porous materials typically fall within the range of medium to high porosities, models predicting the permeability of fibrous materials are often expressed in terms of the solid volume fraction ϕ (Section 2.8.1, p 17), instead of the porosity. The vast majority of analytical models from the literature regard fibrous materials as arrays of unidirectional cylinders with uniform radius, a. The relation between the solid width, d_s, and the radius, a, of the cylinders is given by $d_s = 2\,a$ (Section 3.16.5, p 78).

In the literature both flow perpendicular and parallel to the fibre axes are considered. However, in the present study only the former case will be considered. The dimensionless permeability, k/a^2, as a function of the solid volume fraction, ϕ, for cross-flow through two-dimensional isotopic fibre beds, predicted by the transversely isotropic fibre RUC model, is given by

$$\frac{k}{a^2} = \frac{(1 - \sqrt{\phi})^3}{3.38\,\phi^{3/2}}\,.$$

(5.66)

Equation (5.66) results from the equation for the permeability prediction of the fibre RUC model presented in Table 4.4 (p 94) together with the relationship, $d_s = 2\,a$. In cross-flow through two-dimensional isotopic fibre beds the fibre axes are all perpendicular to the streamwise direction, but oriented at random angles with respect to each other in those

planes (Spielman & Goren (1968)).

5.5.1 Comparison with experimental data and models from the literature

In this section the transversely isotropic fibre RUC model, given by equation (5.66), will be compared to experimental data and other analytical models from the literature. All these models and data concern cross-flow through a system of unidirectional fibrous media at Reynolds numbers within the Darcy flow regime. The vast majority of theoretical studies involving flow through arrays of unidirectional fibres are based on a circular unit cell approach and an adaptation of the Stokes equations (Section 2.10, p 26). As a result, the models based on the latter approach are mostly valid at low solid volume fractions, i.e. for $\phi < 0.2$.

Happel (1959) was one of the first to predict the permeability of cross-flow though an array of unidirectional cylinders. He solved the Stokes equations theoretically by making use of a free-surface unit cell model (Section 2.11.2, p 32). The free-surface model of Happel (1959) for cross-flow (i.e. equation (2.37)) is given by Jackson & James (1986) as

$$\frac{k}{a^2} = \frac{1}{8\,\phi}\left[-\ln\phi + \frac{\phi^2 - 1}{\phi^2 + 1}\right] . \tag{5.67}$$

The model of Kuwabara (1959) (i.e. equation (2.40)) is given by (Jackson & James (1986))

$$\frac{k}{a^2} = \frac{1}{8\,\phi}\left(-\ln\phi - \frac{3}{2} + 2\,\phi\right) , \tag{5.68}$$

and the model of Hasimoto (1959) (i.e. equation (2.39)) is given by (Jackson & James (1986))

$$\frac{k}{a^2} = \frac{1}{8\,\phi}\left(-\ln\phi - 1.476 + 2\,\phi + \mathcal{O}(\phi^2)\right) . \tag{5.69}$$

Sangani & Acrivos (1982) extended the work of Hasimoto (1959) by making use of a least-squares technique to solve the Stokes equations. Their expression for a hexagonal array is given by (Jackson & James (1986))

$$\frac{k}{a^2} = \frac{1}{8\,\phi}\left(-\ln\phi - 1.490 + 2\,\phi - \frac{\phi^2}{2} + \mathcal{O}(\phi^4)\right) . \tag{5.70}$$

Drummond & Tahir (1984) made use of a matching technique in which a solution outside one of the cylinders is matched with solutions, having the same number of singularities,
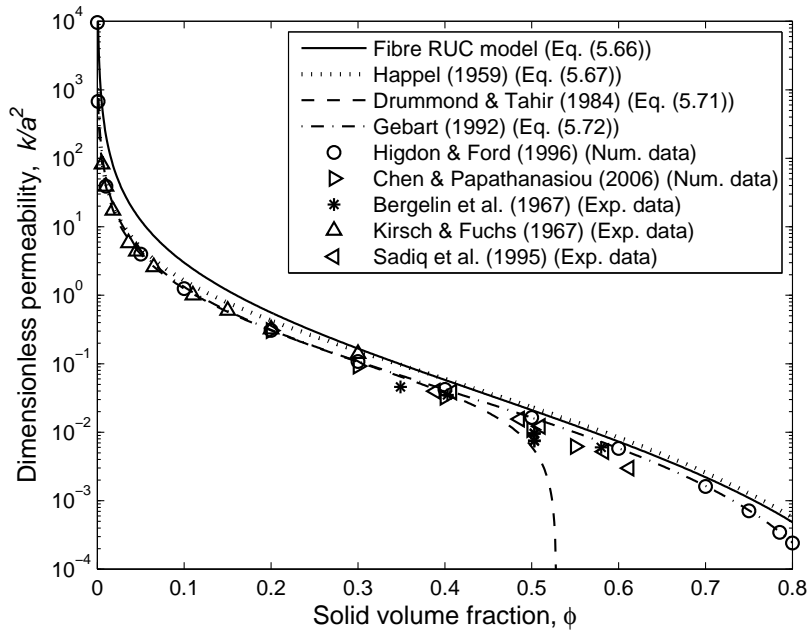
Figure 5.12: Dimensionless permeability for cross-flow through fibrous media.

inside every cylinder of an infinite array. With this approach they added terms to the expression of Sangani & Acrivos (1982), which, for a triangular array, is given by

$$\frac{k}{a^2} \;=\; \frac{1}{8\,\phi}\left(-\ln\phi - 1.4975 + 2\,\phi - \frac{\phi^2}{2} - 0.739\,\phi^4 + \mathcal{O}(\phi^5)\right) . \qquad (5.71)$$

Gebart (1992) solved the Stokes equations by also making use of the unit cell approach for an array of cylinders. The resulting equation for a hexagonal array is given by

$$\frac{k}{a^2} \;=\; \frac{16}{9\,\pi\sqrt{6}}\left(\sqrt{\frac{\pi}{2\sqrt{3}\,\phi}} - 1\right)^{5/2} . \qquad (5.72)$$

Higdon & Ford (1996) computed numerically the resistance force per unit length for flow through two-dimensional arrays of cylinders as a function of the solid volume fraction. Chen & Papathanasiou (2006) also provide numerical data for cross-flow through arrays of unidirectional cylinders. Bergelin et al. (1950) obtained experimental pressure drop data for cross-flow through banks of heat exchanger tubes. Kirsch & Fuchs (1967) also performed experiments on cross-flow through arrays of unidirectional cylinders and Sadiq et al. (1995) considered cross-flow through solid aluminium and nylon rods.

A comparison of the dimensionless permeability, predicted by the fibre RUC model (i.e. equation (5.66)), with the various analytical models (presented above) and numerical and experimental data from the literature is shown in Figure 5.12.

The models of Kuwabara (1959), Hasimoto (1959) and Sangani & Acrivos (1982) are not shown in Figure 5.12 (p 152), since the model of Drummond & Tahir (1984) serves as an extension, with respect to number of terms, of the latter models. From Figure 5.12 it is evident that for $\phi < 0.2$ the RUC model slightly over-predicts the permeability. This may be attributed to the model assumption of flow between parallel plates which becomes less applicable at these low solid volume fractions. In the range of $0.2 < \phi < 0.8$ the RUC model, however, yields satisfactory predictions and corresponds well with the model of Happel (1959) and the data provided. Thus, despite the simple rectangular geometry of the RUC model the balance between accuracy and simplicity of the RUC model is well maintained.

5.6   Kozeny constant

The Kozeny constant was introduced by Carman (1937) into the Carman-Kozeny equation (Appendix C.2, p 287) to obtain correlation between the capillary model and experimental results. From equations (C.10) and (C.14), the Kozeny constant can, alternatively, be expressed as (Bourbie & Zinszner (1985))

$$k_{koz} = \frac{\epsilon\, R_h^2}{k} \, , \tag{5.73}$$

where R_h is the hydraulic radius (Section 2.8.5, p 20). The Kozeny constant is not a *true* constant (Kaviany (1995)): it averages to *more or less* the same value for all random porous media, independently of the size of the particles and porosity (Happel & Brenner (1965)).

For the granular RUC model it follows from equation (3.31) and the expression for the granular permeability in Table 4.4 (p 94) that the Kozeny constant may be expressed as

$$k_{koz} = \frac{\epsilon^3}{1.4\,(1-\epsilon)^{2/3}(1-(1-\epsilon)^{1/3})(1-(1-\epsilon)^{2/3})^2} \, . \tag{5.74}$$

Similarly, for the fibre RUC model it follows from equation (3.64) and the expression for the permeability in Table 4.4 for the fibre RUC model that

$$k_{koz} = \frac{\epsilon^3}{1.19\,\sqrt{1-\epsilon}\,(1-\sqrt{1-\epsilon})^3} \, . \tag{5.75}$$

From equations (3.32) and (2.36), the following expression is obtained for the concentric spherical cell model of Happel (1958):

$$k_{koz} = \frac{\epsilon^3}{2\,(1-\epsilon)}\left[\frac{3+2\,(1-\epsilon)^{5/3}}{3-(9/2)(1-\epsilon)^{1/3}+(9/2)(1-\epsilon)^{5/3}-3\,(1-\epsilon)^2}\right] \, . \tag{5.76}$$

Table 5.7: Model predictions for the Kozeny constant, k_{koz}.

| | Kozeny constant, k_{koz} | | | |
| | RUC | | Happel | |
ϵ	Granular	Fibre	Sphere	Cylinder
0.10	4.83	6.55	4.44	5.73
0.20	4.84	6.39	4.42	5.51
0.30	4.87	6.22	4.44	5.36
0.40	4.93	6.06	4.54	5.30
0.50	5.02	5.91	4.74	5.37
0.60	5.12	5.78	5.11	5.62
0.70	5.43	5.69	5.79	6.20
0.80	5.95	5.70	7.22	7.46
0.90	7.33	6.06	11.34	11.03
0.99	20.93	11.19	71.64	53.83

Similarly, for the concentric cylindrical cell model of Happel (1959), it follows from equations (3.65) and (2.37) that the Kozeny constant may be expressed as

$$k_{koz} = \frac{2\,\epsilon^3}{(1-\epsilon)[-\ln(1-\epsilon) + ((1-\epsilon)^2 - 1)/((1-\epsilon)^2 + 1)]} \ . \tag{5.77}$$

Table 5.7 gives the values for the Kozeny constant, as predicted by the equations presented above, and Figure 5.13 (p 155) shows a comparison between the k_{koz}−values obtained by the different drag models. According to Happel & Brenner (1965), the experimentally determined average value of the Kozeny constant is $k_{koz} = 5.0$ for porosities in the range $0.4 < \epsilon < 0.8$, as indicated by the solid line in Figure 5.13. Figure 5.14 (p 155) shows the absolute relative percentage error for the k_{koz}−values (calculated with the aid of equation (I.2) in Appendix I, p 320).

The Kozeny constant can also be expressed as $k_{koz} = k_o\chi^2$ (Appendix C.2, p 287), where k_o is a shape factor introduced by Carman (1937) and χ is the tortuosity. For cylinders $k_o = 2$. Carman (1937) determined that in a bed of spheres the average value of the slope of the traversing fluid with respect to the column axis is 45°, thus yielding $\chi = L_e/L = \sqrt{2}$. In order to obtain the value of $k_{koz} = k_o\chi^2 = 5$, it follows that $k_o = 2.5$. The latter value of k_o was consequently introduced as an average value for the shape factor of a granular porous medium. This transition from $k_o = 2$ for cylindrical capillary tube flow to the average value of $k_o = 2.5$ was accompanied by the transition from the capillary tube model to modelling flow through a granular packed bed in order to match the experimental
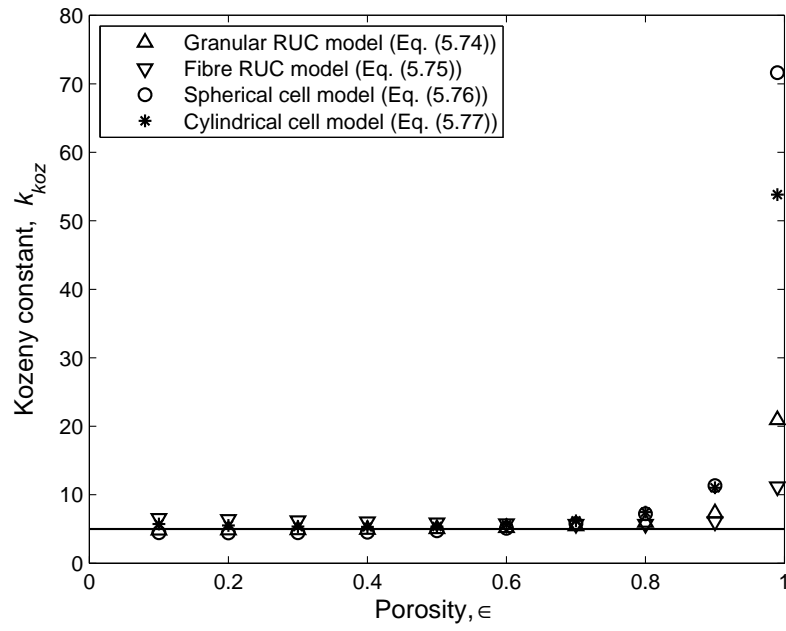
Figure 5.13: Kozeny constant as a function of porosity.
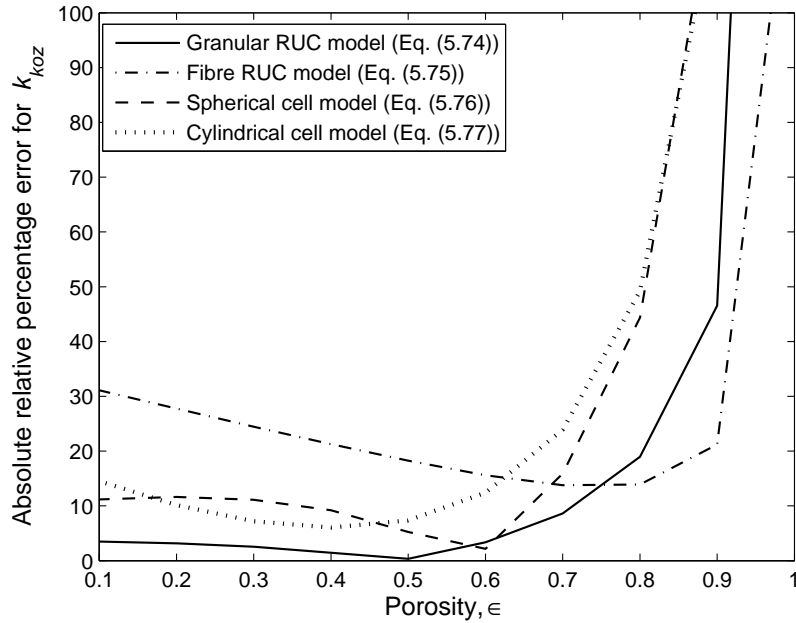
Figure 5.14: Absolute relative percentage error for the Kozeny constant.

results. A reason why the cylindrical cell model yields a slightly higher k_{koz}-value for $\epsilon < 0.8$ than the spherical cell model (as evident in Table 5.7, p 154), may be that the flow through a bed of uniform cylinders is more restricted than flow through a bed of uniform spheres of the same porosity, yielding a higher value for the geometrical tortuosity χ. The effect of a higher tortuosity is larger than a smaller shape factor because the geometrical tortuosity is squared in the latter definition given for the Kozeny constant.

The value of k_o for cubes and rectangular rods are, to the knowledge of the author of this dissertation, not specified in the literature. If, for example, the same relative difference in shape factor is applicable for cubes and rectangular rods as for spheres and cylinders, then the same reasoning for the higher k_{koz}-value (at $\epsilon < 0.8$) for rectangular rods as for cubes applies as in the case of spheres and cylinders.

Given the conditions under which the Kozeny constant was introduced into the Carman-Kozeny equation, i.e. at moderate porosities ranging from 0.38 to 0.47, the Kozeny constant is strictly not applicable at $\epsilon > 0.8$. The deviations of the predicted values from the constant average value of 5 in this range are thus to be expected. From another point of view, the sharp deviations at $\epsilon > 0.8$ may be attributed to the fact that the porous medium concept breaks down at these high porosities. The difference in physical flow processes between the cell models of Happel (1958) and Happel (1959), which is based on an extension of the Stokes equations (Section 2.10, p 26), and the capillary tube model in which the Kozeny constant was introduced, becomes significant at these high porosities. The cell models of Happel (1958) and Happel (1959) were derived on the basis of *flow by* whereas the capillary tube model is based on *flow through*. In the case of the RUC models, the concept of *flow through* becomes *flow by* at high porosities and the assumption of flow between parallel plates (i.e. plane-Poiseuille flow) breaks down.

A reason why the value of the Kozeny constant is higher for the fibre RUC model, than for the cylindrical cell model of Happel (1959) may be because the tortuosity, based on the definition $\chi = L_e/L$, is higher for the fibre RUC model than for the cylindrical cell model due to the sharp corners of the rectangular geometry. In comparison of all the model predictions for the Kozeny constant, the granular RUC model yields the most accurate prediction for the Kozeny constant in the porosity range associated with a packed bed, i.e. $0.4 < \epsilon < 0.6$. The relative percentage error is less than 3.5%. For the fibre RUC model the relative percentage error is less than $\pm 20\%$.

The constancy of the Kozeny constant may also be viewed in respect of the definition in terms of the hydraulic radius (i.e. equation (5.73)). The actual solid diameter does not enter into the definition of the hydraulic diameter, it rather determines an average diameter of an assemblage of non-uniformly sized solids (Happel & Brenner (1965)). The hydraulic diameter plays a similar role as the shape factor by providing an estimate for the average solid size whereas the shape factor gives an estimate for the average shape of solids.

Happel & Brenner (1965) argue that the constancy of the Kozeny constant lends support to the cylindrical capillary tube model as approximation to flow through a packed bed of spheres. The same reasoning may apply to the rectangular geometry of the RUC model

156

in which the granular RUC model is used to model flow through a packed bed of spheres. The rectangular geometry is thus also an acceptable and adequate approximation to the average geometry of the porous micro-structure. The relative percentage error in Figure 5.14 (p 155) is even less for the granular RUC model than for the spherical cell model of Happel (1958).

5.7 Critical Reynolds number for unconsolidated media

The critical Reynolds number indicates the transition between the Darcy and Forchheimer regimes (Section 2.9, p 23) and is defined as that Reynolds number at which the asymptotes intersect.

Equating the two terms of the equation for the granular RUC model in Table 4.19 (p 112) and solving for the Reynolds number, yields the following expression for the critical particle Reynolds number for Re_{qds}, i.e.

$$Re_{c_{qds}} = \frac{50.8\,\epsilon\,(1-\epsilon)^{1/3}}{c_d\,(1-(1-\epsilon)^{1/3})}\,. \tag{5.78}$$

Zeng & Grigg (2006) proposed an alternative criteria for determining the critical point of transition between the Darcy and Forchheimer regimes. They make use of the Forchheimer number (Section 2.9) instead of the Reynolds number. The Reynolds number is used in the present study since, apart from the interstitial form drag coefficient c_d, it can be quantified in terms of the porosity only, whereas for the Forchheimer number a pore-scale linear dimension, i.e. d_s, in addition to other parameters, also need to be known.

The porosity dependence of the critical particle Reynolds number predicted by the granular model is shown in Figure 5.15 (p 158). A value of $c_d = 1.9$ is used for the interstitial form drag coefficient (Section 3.14.4, p 51).

Scheidegger (1957) proposed a range of $0.1 < Re_{c_{qds}} < 75$ for the critical particle Reynolds number of various unconsolidated porous media. As mentioned in Section 2.9, the large margin of uncertainty is attributed partly to the difference in pore structure (including the curvature of the pores), surface roughness and the criteria used to describe the critical point of transition between the Darcy and Forchheimer regimes. Also, the use of different definitions for the Reynolds number by different authors in the literature makes direct comparison difficult. Zeng & Grigg (2006) presented various ranges proposed by several authors in the literature for the critical particle Reynolds number for granular media. They also specified the Reynolds number used in each case. They concluded that for a particle Reynolds number, as defined by equation (4.5), all the ranges they found in the literature for the critical particle Reynolds numbers fall within the range $1 < Re_{c_{qds}} < 100$. The critical particle Reynolds number range proposed by the granular RUC model is $30 \leq Re_{c_{qds}} \leq 75$ for a porosity range of $0.1 \leq \epsilon \leq 0.8$.
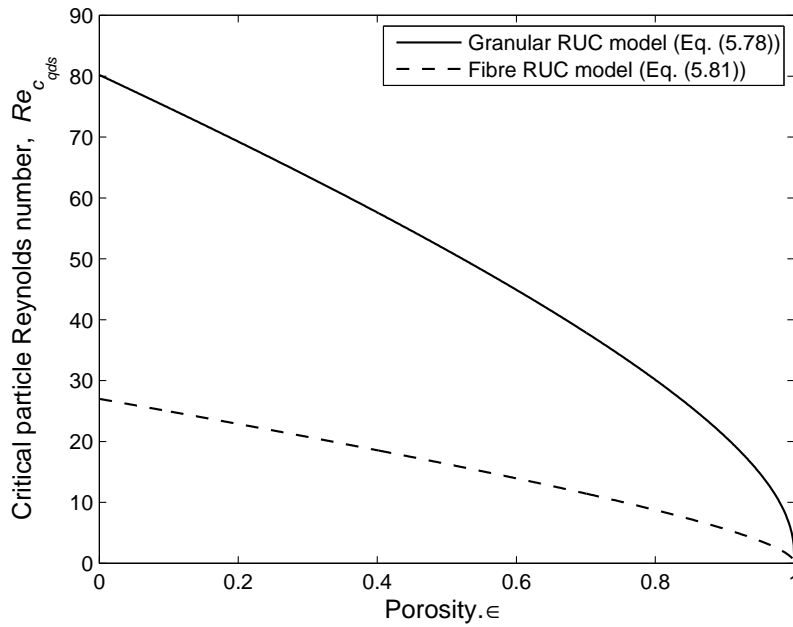
Figure 5.15: Porosity dependence of the critical particle Reynolds number.

Equation (5.78) can be simplified by series expansions followed by the method of throwback, as described in Section 5.3.2 (p 123). Series expansion of the porosity terms appearing in brackets in equation (5.78) (by application of the formulas presented in Appendix J, p 321), leads to

$$Re_{c_{qds}} = 80.2 \left(1 - \frac{2}{3}\epsilon - \frac{2}{27}\epsilon^2 - ...\right) . \tag{5.79}$$

Truncation after the first power of ϵ and application of the throwback method at $\epsilon = 0.43$ leads to

$$Re_{c_{qds}} = 80.2 \left(1 - 0.708\,\epsilon\right) \approx 56 . \tag{5.80}$$

Equation (5.80) is thus a simplification of equation (5.78) for porosities near the throwback porosity of 0.43 and predicts a value of 56 for the critical particle Reynolds number associated with a granular packed bed. A model prediction for the critical particle Reynolds number could not be found in the literature for comparison with the value of 56 predicted by the granular RUC model. This value and the range of $30 \le Re_{c_{qds}} \le 75$ predicted by the granular RUC model, however, falls within the range of $1 \le Re_{c_{qds}} \le 100$ proposed by Zeng & Grigg (2006).

Similarly to the granular model, the critical particle Reynolds number predicted by the fibre RUC model as a function of porosity is given by

$$Re_{c_{qds}} = \frac{27\,\epsilon\sqrt{1-\epsilon}}{c_d\left(1 - \sqrt{1-\epsilon}\right)} . \tag{5.81}$$

158

Equation (5.81) will not be simplified by series truncation and the method of throwback, as was done in the case of the granular RUC model, due to the fact that an average porosity value for fibre beds could not be found in the literature.

The porosity dependence of the critical particle Reynolds number predicted by the fibre RUC model is also shown in Figure 5.15 (p 158). For the fibre model a value of $c_d = 2$ is used for the interstitial form drag coefficient (Section 3.16.4, p 75). Figure 5.15 shows that the critical particle Reynolds number range is narrower for the fibre RUC model than for the granular model. For porosities in the range $0.1 \leq \epsilon \leq 0.8$, the fibre RUC model predicts a critical particle Reynolds number range of $9 \leq Re_{c_{qds}} \leq 25$. This range is about three times lower than that predicted by the granular RUC model. The RUC models therefore predict that inertial effects will initiate at much lower Reynolds numbers (i.e. three times lower) in fibre beds than in granular media.

The advantage of the RUC model of being applicable over the entire porosity range allows for equations (5.78) and (5.81) to be produced. With equations (5.78) and (5.81) the critical particle Reynolds number can be predicted in granular media and fibre beds, respectively. Equations for the critical particle Reynolds number as a function of porosity for unconsolidated media, similar to equations (5.78) and (5.81), could not be found in the literature.

For foamlike media a pore Reynolds number rather than a particle Reynolds number is usually specified. The critical pore Reynolds number for the foam RUC model will be discussed in Chapter 6.

5.8   Summary

In this chapter a historical overview is presented of the development of the RUC models over the past three decades.

It is then illustrated that the granular RUC model can be regarded as a theoretical derivation of the semi-empirical Ergun equation. The granular RUC model is graphically indistinguishable from the improved Ergun equation of Macdonald et al. (1979). The empirical coefficients of the Ergun equation are expressed in terms of the porosity by application of the granular RUC model. For the average porosity associated with a packed bed, i.e. $\epsilon = 0.43$, the granular model yields coefficient values of $A = 176$ and $B = 1.8$ which is in satisfactory agreement with the values of $A = 180$ and $B = 1.8$ proposed by Macdonald et al. (1979). The application of series expansion together with throwback at $\epsilon = 0.43$ yield simplified predictive equations for the granular RUC model. It is also shown that the granular RUC model presented in this study may be regarded as an improvement on the granular RUC models of Du Plessis & Masliyah (1991) and Du Plessis (1994).

The foam RUC model is used to predict the dynamic specific surface of ceramic foams. Model predictions for the dynamic specific surface are presented in terms of either the

solid width or the channel width. The predicted values are of the same order of magnitude as other model predictions from the literature. This is satisfactory, given the difficulty in accurately determining the average pore-scale linear dimensions and also due to the fact that the possibility of hollow struts, pore blockage and surface roughness are not accounted for in the model. The advantage of the RUC model is that either the solid width or the channel width needs to be known to predict the dynamic specific surface. For the theoretical and empirical models to which the foam RUC model are compared, both the strut and window diameters need to be known.

It is emphasized that in order to apply the Ergun equation to porous media other than granular media, the actual physical differences has to be remodelled to provide physical compliance between the model and reality. This is considered an important aspect as it is the only meaningful manner in which generalizations can be attempted. It is shown that the pressure gradient prediction of the foam RUC model can be regarded as a theoretical Ergun-type equation for foamlike media. The empirical coefficients of the Ergun-type equation for foamlike media proposed in the literature are expressed in terms of the porosity by application of the foam RUC model. It is thereby illustrated that the 'constant empirical' coefficients relate to the pore-scale geometry and therefore have physical meaning. Although the coefficient $A^{'}$ predicted by the foam RUC model remains more or less constant over the entire porosity range, the coefficient $B^{'}$ varies significantly. For the average porosity of $\epsilon = 0.79$ the foam RUC model predicts that $A^{'} = 109$ and $B^{'} = 1.69$, as opposed to $A^{'} = 110$ and $B^{'} = 1.45$ proposed by Dietrich et al. (2009). It is shown graphically that the model prediction for the coefficient $B^{'}$ is sensitive to the value of the interstitial form drag coefficient. The absolute relative percentage error of the model predictions for both coefficients, measured with respect to the values proposed by Dietrich et al. (2009), are less than the experimental error range of 20% provided by the latter authors.

The foam RUC model yields satisfactory predictions for the passability of both the Aluminium and Mullite foams. For the Aluminium foam the absolute relative percentage error ranges between 1% and 15% and for the Mullite foam the maximum error is 26%. Although a much wider range of absolute relative percentage errors are obtained for the predicted permeability values, the model prediction for $A^{'}$ is in satisfactory agreement with the empirical value. The wider range of absolute relative percentage errors for the predicted permeability values may be attributed to the fact that the A_{vd}-values are squared in the expression for the permeability. As a result the experimental error in the measurement of A_{vd} is also squared.

The different pressure drops predicted by the granular and foam RUC models can be explained from a physical point of view, whereas this cannot be done in the case of the empirical models. The higher pressure drop for the granular RUC model may partly be attributed to the lower porosity associated with a granular packed bed than with foamlike media, the higher coefficient values and a lower hydraulic diameter value.

For $\epsilon = 0.80$ the pressure drop predicted by the granular RUC model is about 79% lower than the pressure drop predicted by the foam RUC model. This can be attributed to the

coefficient values at $\epsilon = 0.80$ as well as to the value used for the hydraulic diameter. At this porosity value the Ergun equation over-predicts the pressure drop by 88% which can be attributed to the fact the Ergun equation is not applicable at porosities beyond the packed bed porosity.

It is shown that in comparing the pressure drop predicted by the granular RUC model at $\epsilon = 0.43$ to the pressure drop predicted by the foam RUC model at $\epsilon = 0.80$, the same hydraulic diameter cannot be used, as was done when the empirical models for granular and foamlike media were compared by Dietrich et al. (2009). The hydraulic diameter of the foam RUC model at $\epsilon = 0.80$ is higher than the hydraulic diameter of the granular RUC model at $\epsilon = 0.43$. This discrepancy has a significant effect on the pressure drop as the hydraulic diameter is squared in the Darcy term. The pressure gradient predicted by the granular RUC model, with $\epsilon = 0.43$ and in which the same hydraulic diameter is used as in the foam RUC model, is 80% higher than the pressure gradient predicted by the foam RUC model. If the lower value for the hydraulic diameter is used in the granular RUC model then the pressure drop prediction increases with 72%. The pressure drop predicted by the granular RUC model with $\epsilon = 0.43$ and in which the lower hydraulic diameter is used, is thus in total 152% higher than that predicted by the foam RUC model at $\epsilon = 0.8$.

It is shown that the two-dimensional transversely isotropic fibre RUC model yields satisfactory agreement with analytical models and numerical and experimental data from the literature, especially in the range $0.2 < \phi < 0.8$. The slight over-prediction at $\phi < 0.2$ may be attributed to the model assumption of flow between parallel plates which becomes less applicable at these low solid volume fractions.

A comparison of the Kozeny constant predicted by the granular and fibre RUC models with the spherical and cylindrical cell models of Happel (1958) and Happel (1959), respectively, shows that the granular RUC model yields the most accurate prediction for the Kozeny constant in the porosity range associated with a packed bed. The constancy of an average value of 5 for the Kozeny constant is well maintained by the unconsolidated RUC models. This shows that a balance between accuracy and simplicity is obtained with the RUC model. The relative percentage error is less than 3.5% for the granular model and less than about 20% for the fibre model for the porosity range $0.4 \leq \epsilon \leq 0.6$. Based on the argument that the constancy of the Kozeny constant lends support to the cylindrical capillary tube model as approximation to flow through a packed bed of spheres, the rectangular geometry of the granular RUC model is adequate for approximating flow through a packed bed of spheres. The same reasoning applies to the rectangular fibre RUC model being adequate as approximation for cross-flow through a bed of unidirectional cylinders.

Equations for the critical particle Reynolds number are provided for the unconsolidated RUC models. Similar equations could not be found in the literature. The critical Reynolds number range predicted by the granular RUC model, falls within the range proposed by Zeng & Grigg (2006). For the same porosity range, the range of critical particle Reynolds numbers predicted by the fibre RUC model is three times lower than the range predicted by the granular RUC model. The RUC models therefore predict that inertial effects

will initiate at much lower Reynolds numbers in fibre beds than in granular media. The information provided by the model predictions for the critical Reynolds number may be crucial for optimization and design purposes for the various engineering applications in which unconsolidated porous media are used.

The satisfactory model verification of the three RUC models presented in this chapter provides confidence in the analytical modelling procedure.

Chapter 6

Short duct foam RUC model

In this chapter the foam RUC model is adapted to account for the effect of developing flow on the pressure drop. This model will henceforth be referred to as the "short duct foam RUC model" as opposed to the foam model presented in Chapters 4 and 5 that will be referred to as the "long duct foam RUC model".

Due to the high porosities, and consequently, the relatively short duct sections present in foamlike media, the assumption of fully developed flow breaks down. The short duct sections prevent the fully developed velocity profile to be reached. The effect of developing flow is therefore incorporated into the apparent friction factor which is in turn incorporated into the pressure drop. The pores are approximated as square ducts and, in analogy thereof, as double pairs of parallel plates. An existing unified equation for the apparent friction factor, applicable over any duct length, is quantified for the two duct geometries. Model predictions are obtained for the critical Reynolds number at which the effects of fully developed and developing flow weigh equally. The dimensionless total drag factor predicted by the short duct model is compared to experimental data of aluminium and stainless steel foams. It is illustrated graphically that developing flow is already present at very low Reynolds numbers (i.e. in the Darcy flow regime) and that the effect of developing flow is to increase the pressure drop, or equivalently, to decrease the permeability. It is also shown that the short duct model reduces back to the long duct model for a Reynolds number of zero. Through application of the power addition technique an equation is proposed for the pressure drop prediction applicable over the entire steady laminar flow regime.

A method is furthermore proposed in which to express the interstitial form drag coefficient, used in the foam model, as a function of porosity. This porosity dependent form drag coefficient, then implicitly takes into account the variation in cross-sectional shape of the fibres, as observed in the literature. The newly proposed form drag coefficient is then used to predict the inertial coefficient and passability. The model predictions are compared with available experimental data from the literature. For aluminium foams, a comparison is drawn between the use of a constant and a porosity dependent from drag coefficient.

6.1 Introduction

In modern day technological advancements in process engineering, such as nano-technology, the use of short tubular devices is becoming an important design parameter. In addition to the knowledge about fully developed flow conditions, present day accuracies needed for such high technology engineering designs and scientific analysis necessitate the need for careful consideration of developing flow in ducts.

In studies on porous media, one is frequently confronted with short straight channel sections, each in which flow development is invariably taking place (Du Plessis & Collins (1992)). This necessitates knowledge about flow development in short channels. Experimental results on flow through porous media show that the effect of developing flow on the pressure becomes significant if the ratio of the diameter-to-duct length becomes of the order of unity, which is typically the case (Dybbs & Edwards (1984)). Another physical reason for the occurrence of flow development in the pores of actual porous media may be the irregular pore-sizes of the complex porous micro-structures.

Molale (2007) performed numerical simulations to verify the assumption of fully developed plane-Poiseuille flow in the fibre RUC model. It was found that the parabolic velocity profile in the streamwise channels prevails for porosities up to 0.5. At higher porosities developing flow is observed. Developing flow was also observed in the transverse channels of a fully staggered array because the transverse duct sections are half the length of that of the streamwise duct sections. This observation provides confirmation that for short ducts developing flow has to be accounted for. Although these results were obtained for the fibre RUC model, the information is also useful for the foam RUC model since the same modelling assumptions (e.g. plane-Poiseuille flow) apply to the foam RUC model.

6.2 Developing flow

In the hydrodynamic entrance region of a straight duct, flow development from a uniform (or other) inlet velocity profile takes place due to shear stresses imposed by the solid surfaces of the duct on the fluid. Flow development for a uniform inlet velocity profile is schematically illustrated in Figure 6.1 (p 165).

As the fluid enters the duct, the velocity boundary layer develops from a zero thickness to a thickness equal to the duct radius. The length, measured from the duct inlet, to this position along the duct length is called the entry length (Du Plessis & Collins (1992)), as indicated in Figure 6.1. Beyond the entry length, but still in the entrance region, the velocity profile continues to develop until it reaches a fully developed profile at the end of the entrance region. The length, measured from the duct inlet, to this position along the duct length is known as the entrance length. In the entrance length the flow conditions change dynamically from point to point and they differ considerably from the flow conditions that prevail in the fully developed domain. In the literature (e.g. Shah &

164
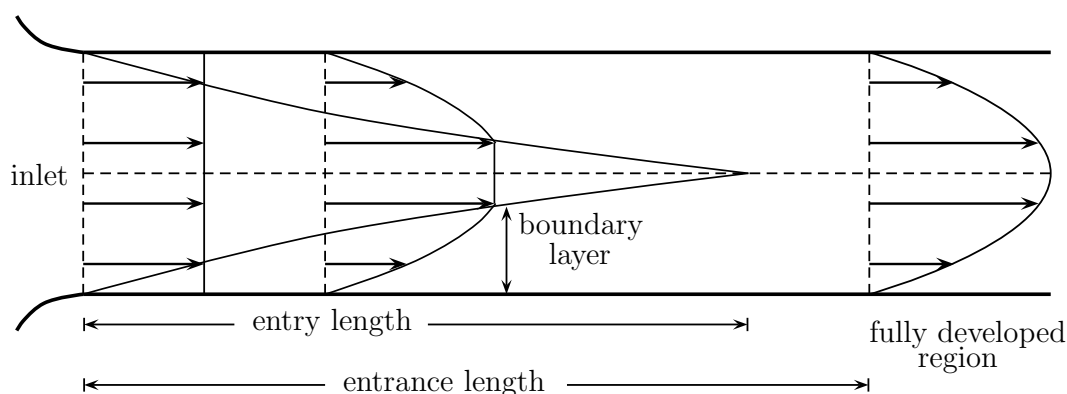
Figure 6.1: Schematic illustration of the developing velocity profile in the entrance region of a duct.

London (1978)) it is fairly common practice to define the entrance length as that length of duct necessary for flow, entering the duct with a uniform velocity profile, to attain a profile for which the maximum velocity is 99% of that of the fully developed profile.

In fully developed flow the pressure drop is caused by wall shear stresses only, whereas in developing flow the change in momentum flow rate, as the velocity develops, also needs to be taken into consideration when calculating the pressure drop. Due to an unbalanced shear drag, momentum is transferred towards the centre of the duct as the fluid moves downstream, until a balance is obtained with the resulting shear stresses within the fluid. At a duct inlet 39% of the pressure drop is caused by wall shear stresses and the remaining 61% by an increase in momentum flux (Shah & London (1978)). Radial flow towards the center in the entrance region can thus have a detrimental effect on the accuracy of analysis of transfer processes if only fully developed flow is considered. If the effect of developing flow on the pressure drop is accounted for, then the pressure drop is expected to be higher than the pressure drop associated with fully developing flow.

Evidently two asymptotic physical situations are involved during the development of the velocity profile. In the predominantly developing flow regime the laminar boundary layer is increasing steadily with distance along the duct. In the predominantly fully developed regime the boundary layers on the different flanks of the duct have already met and the velocity profile remains unchanged.

The attainment of a fully developed velocity profile is theoretically only possible in an infinitely long duct. The effect of flow development is thus omnipresent but, as the fluid moves further downstream, the effect becomes asymptotically insignificant.

165

6.3   Apparent friction factor

For an axial distance x along the duct, the dimensionless axial distance, x^+, is defined as

$$x^+ \equiv \frac{x}{D_h\, Re_{Dh}}\ . \tag{6.1}$$

The apparent friction factor, f_{app}, at any axial position x^+ from the inlet plane of the duct is defined as the pressure drop between the inlet plane at $x^+ = 0$ and the particular position (Shah & London (1978)), i.e.

$$f_{app}\ =\ \frac{\Delta p\, D_h}{2\,\rho\, u_m^2\, x}\ =\ \frac{\Delta p}{2\,\rho\, u_m^2\, Re_{Dh}\, x^+}\ , \tag{6.2}$$

where Re_{Dh} is the Reynolds number, defined in terms of the hydraulic diameter as

$$Re_{Dh}\ =\ \frac{\rho\, u_m\, D_h}{\mu}\ . \tag{6.3}$$

It then follows that the apparent friction factor-Reynolds number product is given by

$$f_{app}\, Re_{Dh}\ =\ \frac{\Delta p}{2\,\rho\, u_m^2\, x^+}\ , \tag{6.4}$$

where u_m is the magnitude of the average streamwise channel/duct velocity. The pressure drop in equations (6.2) and (6.4) is a result of the wall shear stresses *and* the change in the momentum flow rate in the entrance region.

In the asymptotic limit of a short duct section, starting at the inlet plane, it is reasonable to assume that the pressure drop over it will be caused only by the boundary layer development locally on the plate and that the duct inlet curvature will not have any influence. The apparent friction factor should thus be independent of the circumferential passage geometry and, as a result, also be similar to that of laminar flow development over a flat plate. Shah & London (1978) reported that the boundary layer behaviour at the entrance of any duct geometry of constant cross-sectional area along the duct is indeed identical to that on a flat plate when the thickness of the boundary layer is small compared to the duct dimensions. The apparent friction factor-Reynolds number product for laminar uniform entry flow in the asymptotic limit of a short duct of arbitrary but uniform cross-sectional geometry, can be approximated by (Shah & London (1978))

$$f_{app}\, Re_{Dh}\big|_{x^+ \to 0}\ =\ \frac{3.44}{\sqrt{x^+}}\ . \tag{6.5}$$

At the other extreme, i.e. in the fully developed flow regime,

$$f_{app}\, Re_{Dh}\big|_{x^+ \to \infty}\ =\ f_{fd}\, Re_{Dh}\ , \tag{6.6}$$

166

where f_{fd} is the friction factor for fully developed flow (Appendix A.3.2, p 282). By application of the power addition technique (Churchill & Usagi (1972)), an expression is obtained for the apparent friction factor-Reynolds number product over the entire duct length. This eliminates the necessity to analyze the combined effect of the two physical flow processes at intermediate duct lengths. The resulting expression for the apparent friction factor-Reynolds number product along the entire duct length, x^+, is given by (Du Plessis & Collins (1992))

$$f_{app} \, Re_{Dh} \;\; = \;\; [(f_{app} \, Re_{Dh}|_{x^+ \to \infty})^s \; + \; (f_{app} \, Re_{Dh}|_{x^+ \to 0})^s]^{1/s} \; , \tag{6.7}$$

$$= \;\; \left[(f_{fd} \, Re_{Dh})^s \; + \; \left(\frac{3.44}{\sqrt{x^+}} \right)^s \right]^{1/s} \; . \tag{6.8}$$

Two approaches will now be followed in the present study to describe the duct geometry: In the first case the pore-channels of the foam RUC model will be regarded as square ducts and secondly as double pairs of parallel plates.

6.3.1   Friction factor for square ducts

In the limit of fully developed flow in a long straight square duct, $f_{fd} Re_{Dh} = 14.23$ (Shah & London (1978)).

6.3.2   Friction factor for double pairs of parallel plates

Let Δp be the streamwise pressure drop, $(d - d_s)^2$ the cross-sectional duct area and d the length of the duct. It then follows that

$$\Delta p \, (d - d_s)^2 \;\; = \;\; \tau_w \, d \, 4 \, (d - d_s) \; . \tag{6.9}$$

The pressure gradient over the duct can then be expressed as

$$\frac{\Delta p}{d} \;\; = \;\; \frac{4}{d - d_s} \, \tau_w \; . \tag{6.10}$$

The definition for the friction factor-Reynolds number product for fully developed flow is given by (Appendix A.3.2)

$$f_{fd} \, Re_{Dh} \;\; \equiv \;\; \frac{D_h^2}{2 \, \mu \, u_m} \frac{\Delta p}{d} \; . \tag{6.11}$$

If the duct is approximated as two pairs of parallel plates, then $D_h = d - d_s$. For flow between parallel plates a distance $d - d_s$ apart, the wall shear stress may be expressed as:

$$\tau_w \;\; = \;\; \frac{d - d_s}{2} \left(\frac{\Delta p}{d} \right) \;\; = \;\; \frac{6 \, \mu \, u_m}{d - d_s} \; . \tag{6.12}$$

167

From equations (6.10) and (6.12) it then follows that

$$\frac{\Delta p}{d} = \frac{24\,\mu\,u_m}{(d - d_s)^2}\,.\tag{6.13}$$

Consequently, for double sets of parallel plates,

$$f_{fd}\,Re_{Dh} = \frac{D_h^2}{2\,\mu\,u_m}\frac{\Delta p}{d} = \frac{D_h^2}{2\,\mu\,u_m}\frac{24\,\mu\,u_m}{(d - d_s)^2} = 12\,,\tag{6.14}$$

as opposed to $f_{fd}\,Re_{Dh} = 24$ for a single set of parallel plates.

6.4   Short duct foam RUC model

The incorporation of the apparent friction factor into the RUC modelling theory will be based on a direct analytical modelling procedure. Let $f_{app}\,Re_{Dh}|_{x^+\to\infty} = f_{fd}\,Re_{Dh} = n$. For a square duct $n = 14.23$ and for double pairs of parallel plates $n = 12$. It then follows from equation (6.7) that

$$f_{app}\,Re_{Dh} = \left[\,n^s\,+\,(f_{app}\,Re_{Dh}|_{x^+\to 0})^s\,\right]^{1/s}\,.\tag{6.15}$$

From the discussion in Section 6.3 (p 166), the apparent friction factor-Reynolds number product in the limit of a short duct (i.e. equation (6.5)), is applicable to both a square duct and double pairs of parallel plates. To obtain the value for $f_{app}\,Re_{Dh}$ at the critical point of transition between the two limits, denoted by $(f_{app}\,Re_{Dh})_c$, the second term in the square brackets of equation (6.15) is deliberately set equal to the value of the first term, yielding $(f_{app}\,Re_{Dh})_c = 2^{1/s}\,n$. The numerical values for $f_{app}\,Re_{Dh}$, provided by Shah & London (1978) (in their Table 47) for square duct flow, was interpolated by Du Plessis & Masliyah (1988) to obtain $(f_{app}\,Re_{Dh})_c = 20.1$. If, in the present study, the value of the shifting exponent is chosen to be equal to 2, then $(f_{app}\,Re_{Dh})_c = 2^{1/s}\,n = \sqrt{2}\,(14.23) = 20.124$, which corresponds to the value obtained from the numerical work of Shah & London (1978). A shifting exponent of $s = 2$ will therefore be used in equation (6.15). The apparent friction factor-Reynolds number product then simplifies to

$$f_{app}\,Re_{Dh} = n\,\sqrt{1 + \frac{m}{x^+}}\,,\tag{6.16}$$

with

$$m = \left(\frac{3.44}{n}\right)^2\,.\tag{6.17}$$

For a square duct $m = 0.0584$ and for double pairs of parallel plates $m = 0.0822$. The values for n and m are presented in Table 6.1 (p 169) for the two duct geometries.

Table 6.1: Parameters for the square duct and double pairs of parallel plates models.

Duct	n	m
Square	14.23	0.0584
Parallel plates	12	0.0822

Equation (6.16) is valid for any duct length x^+. The value of x^+ at which the two asymptotes intersect is given by $x_c^+ = m$. Since values of $f_{app}\,Re_{Dh}$ for parallel plates in the vicinity of $x_c^+ = 0.0822$ are not provided by Shah & London (1978), the value of $(f_{app}\,Re)_c = 20.1$ will be assumed to also be applicable for the double pairs of parallel plates, although equation (6.16) leads to a value of $(f_{app}\,Re)_c = 16.97$ for a shifting exponent of 2. The accuracy of the value of 16.97 can, however, not be confirmed. A value of $s = 2$ will nevertheless also be used for the double sets of parallel plates model.

The hydraulic diameter for both the square duct and the duct formed by double pairs of parallel plates is $D_h = d - d_s$. For the case of a duct of length d_s, equation (6.16) can be expressed as

$$f_{app}\,Re_{Dh} \;=\; n\sqrt{1 + \frac{m\,(d - d_s)\,Re_{Dh}}{d_s}} \;=\; n\sqrt{1 + \frac{m\,(3 - \psi)\,Re_{Dh}}{(\psi - 1)}}, \qquad (6.18)$$

by application of equations (3.45) and (3.46). The relation between the pressure drop, over a duct of length x, and the apparent friction factor is given by (Shah & London (1978))

$$f_{app} \;=\; R_h \left(\frac{\Delta p}{x}\right) \frac{1}{\frac{1}{2}\,\rho\,w_\parallel^2}, \qquad (6.19)$$

with $\Delta p/x$ the pressure gradient and R_h the hydraulic diameter. In equation (6.19) the magnitude of the average channel velocity, u_m, is replaced with the magnitude of the streamwise average channel velocity, $w_\parallel$, for flow in the RUC. From equation (6.19) it follows that the pressure drop, Δp, over any duct length, x, can then be expressed as

$$
\begin{aligned}
\frac{\Delta p}{x} \;&=\; f_{app}\,\frac{1}{2}\,\rho\,w_\parallel^2\,\frac{4}{D_h} \\
&=\; \rho\,w_\parallel^2\,\frac{2}{D_h}\,\frac{f_{app}\,Re_{Dh}}{Re_{Dh}} \\
&=\; \rho\,\frac{q^2\,d^4}{(d - d_s)^4}\,\frac{2}{D_h}\,\frac{f_{app}\,Re_{Dh}}{Re_{Dh}}.
\end{aligned}
\qquad (6.20)
$$

The Reynolds number, defined in terms of the hydraulic diameter, i.e. Re_{Dh}, can be expressed in RUC notation as

$$Re_{Dh} \;=\; \frac{\rho\,w_\parallel\,D_h}{\mu} \;=\; \frac{4\,\rho\,q\,(d - d_s)}{(3 - \psi)^2\,\mu}. \qquad (6.21)$$

It then follows from equations (6.23), (6.21) and (3.45) that

$$\frac{\Delta p}{x} = \frac{8\,\mu\,q}{(d - d_s)^2\,(3 - \psi)^2}\, f_{app}\, Re_{Dh} \; . \tag{6.22}$$

The total streamwise pressure gradient over all the duct sections of the foam RUC model is assumed to be equal to the pressure gradient over the actual foam. Hence,

$$-\frac{\mathrm{d}p}{\mathrm{d}x} = \frac{\Delta p}{x}\frac{(3 - \sigma)\,d_s}{d} = \frac{(3 - \sigma)\,\psi^2\,(\psi - 1)}{\epsilon^2\,d^2}\,\mu\,q\,f_{app}\,Re_{Dh}$$
$$= \frac{(3 - \sigma)\,\psi^2\,(\psi - 1)(3 - \psi)^2}{4\,\epsilon^2\,(d - d_s)^2}\,\mu\,q\,f_{app}\,Re_{Dh} \; , \tag{6.23}$$

by application of equations (3.45), (3.46) and (3.49). Substituting the apparent friction factor-Reynolds number product (equation (6.18)) into equation (6.23), then yields

$$-\frac{\mathrm{d}p}{\mathrm{d}x} = \frac{(3 - \sigma)\,\psi^2\,(\psi - 1)(3 - \psi)^2}{4\,\epsilon^2\,(d - d_s)^2}\,\mu\,q\,n\,\sqrt{1 + \frac{m\,(3 - \psi)\,Re_{Dh}}{(\psi - 1)}} \; . \tag{6.24}$$

Equation (6.24) is expressed in terms of σ and is therefore applicable to the doubly, singly and non-staggered foam RUC models. Equation (6.24) confirms that the effect of developing flow is to increase the pressure drop. Molale (2007) showed numerically that the significance of the effect of developing flow depends on the porosity and Reynolds number, which is also portrayed by the model prediction of equation (6.24). Since $-\mathrm{d}p/\mathrm{d}x = \mu\,q\,f_0$ (equation (4.30)), it follows from equation (6.24) that the drag factor in the asymptotic limit of low Reynolds number flow in terms of $d - d_s$, is given by

$$f_{0dds} = \frac{(3 - \sigma)\,\psi^2\,(\psi - 1)(3 - \psi)^2}{4\,\epsilon^2\,(d - d_s)^2}\,n\,\sqrt{1 + \frac{m\,(3 - \psi)\,Re_{Dh}}{(\psi - 1)}} \; , \tag{6.25}$$

and the dimensionless drag factor in the asymptotic limit of low Reynolds number flow, normalized with $(d - d_s)^2$, is given by

$$F_{0dds} = f_{0dds}(d - d_s)^2 = \frac{(3 - \sigma)\,\psi^2\,(\psi - 1)(3 - \psi)^2}{4\,\epsilon^2}\,n\,\sqrt{1 + \frac{m\,(3 - \psi)\,Re_{Dh}}{(\psi - 1)}} \; . \tag{6.26}$$

In the next section the effect of developing flow will be incorporated into the short duct foam RUC model.

6.5 Incorporation of inertial effects

The drag factor in the steady laminar limit of the inertial flow regime in terms of $d - d_s$ results from equations (4.43) and (4.45) and is given by

$$f_{\infty dds} = \frac{c_d\,(2 - \sigma)(\psi - 1)(3 - \psi)^2\psi^2}{16\,\mu\,\epsilon^3\,(d - d_s)}\,\rho\,q$$

$$= \frac{c_d\,(2-\sigma)(\psi-1)(3-\psi)^4\,\psi^2}{64\,\epsilon^3\,(d-d_s)^2}\,Re_{Dh}\,. \tag{6.27}$$

The dimensionless drag factor in the steady laminar limit of the inertial flow regime, normalized with $(d-d_s)^2$, is given by

$$F_{\infty dds} \;=\; f_\infty (d-d_s)^2 \;=\; \frac{c_d\,(2-\sigma)(\psi-1)(3-\psi)^4\,\psi^2}{64\,\epsilon^3}\,Re_{Dh}\,. \tag{6.28}$$

Application of the power addition technique (Churchill & Usagi (1972)) leads to the following expression for the total drag factor in terms of $d-d_s$,

$$f_{dds} \;=\; [f_{0dds}^t + f_{\infty dds}^t]^{1/t} \;=\; \left[\left\{\frac{(3-\sigma)\,\psi^2\,(\psi-1)(3-\psi)^2}{4\,\epsilon^2\,(d-d_s)^2}\,n\,\sqrt{1+\frac{m\,(3-\psi)\,Re_{Dh}}{(\psi-1)}}\right\}^t\right.$$
$$\left.+\;\left\{\frac{c_d\,(2-\sigma)(\psi-1)(3-\psi)^4\,\psi^2}{64\,\epsilon^3\,(d-d_s)^2}\,Re_{Dh}\right\}^t\right]^{1/t}\,, \tag{6.29}$$

where t denotes another shifting exponent. The dimensionless total drag factor, normalized with $(d-d_s)^2$, is given by

$$F_{dds} \;=\; [F_{0dds}^t + F_{\infty dds}^t]^{1/t} \;=\; \left[\left\{\frac{(3-\sigma)\,\psi^2\,(\psi-1)(3-\psi)^2}{4\,\epsilon^2}\,n\,\sqrt{1+\frac{m\,(3-\psi)\,Re_{Dh}}{(\psi-1)}}\right\}^t\right.$$
$$\left.+\;\left\{\frac{c_d\,(2-\sigma)(\psi-1)(3-\psi)^4\,\psi^2}{64\,\epsilon^3}\,Re_{Dh}\right\}^t\right]^{1/t}\,. \tag{6.30}$$

Equation (6.30) is shown graphically in Figure 6.2 (p 172) as a function of the Reynolds number, Re_{Dh}, together with the various asymptotes. Although a shifting exponent of $t = 1$ will be chosen for simplicity, it is clear from Figure 6.2 that a shifting exponent of $t = 2$ yields more accurate results in the transition region of the asymptotes.

The resulting expression for the short duct foam RUC model applicable over the entire steady laminar flow regime (with $s = 2$ and $t = 1$) is given by

$$f_{dds} \;=\; \frac{(3-\sigma)\,\psi^2\,(\psi-1)(3-\psi)^2}{4\,\epsilon^2\,(d-d_s)^2}\,n\,\sqrt{1+\frac{m\,(3-\psi)\,Re_{Dh}}{(\psi-1)}}$$
$$+\;\frac{c_d\,(2-\sigma)(\psi-1)(3-\psi)^4\,\psi^2}{64\,\epsilon^3\,(d-d_s)^2}\,Re_{Dh}\,. \tag{6.31}$$

The streamwise pressure gradient may then be expressed as

$$-\frac{\mathrm{d}p}{\mathrm{d}x} \;=\; \frac{(3-\sigma)\,\psi^2\,(\psi-1)(3-\psi)^2}{4\,\epsilon^2\,(d-d_s)^2}\,\mu\,q\,n\,\sqrt{1+\frac{m\,(3-\psi)\,Re_{Dh}}{(\psi-1)}}$$
$$+\;\frac{c_d\,(2-\sigma)(\psi-1)(3-\psi)^4\,\psi^2}{64\,\epsilon^3\,(d-d_s)^2}\,\mu\,q\,Re_{Dh}\,, \tag{6.32}$$

171
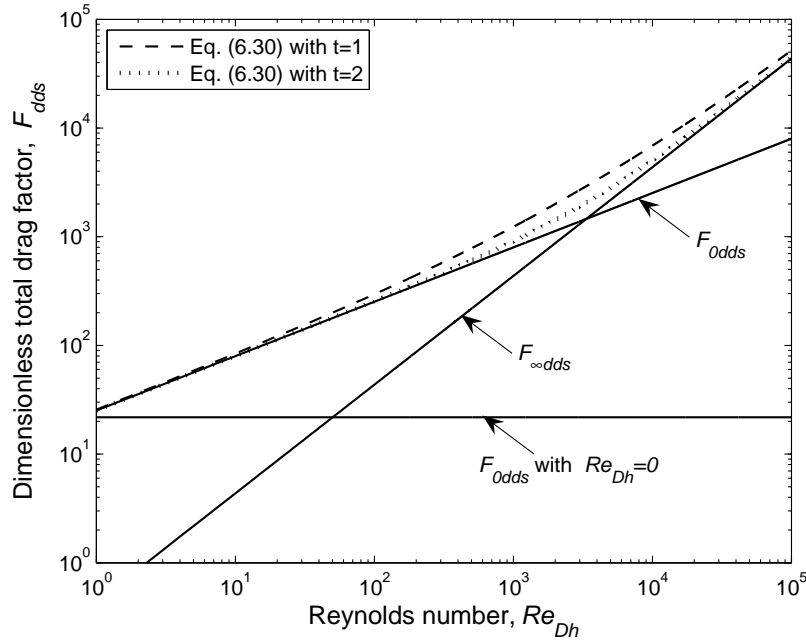
Figure 6.2: Dimensionless total drag factor F_{dds} as a function of the Reynolds number, Re_{Dh}, for $\epsilon = 0.9$, $\sigma = 0$ and $c_d = 2$.

or in terms of the magnitude of the superficial velocity, instead of the Reynolds number,

$$
-\frac{\mathrm{d}p}{\mathrm{d}x} = \frac{(3-\sigma)\,\psi^2\,(\psi-1)(3-\psi)^2}{4\,\epsilon^2\,(d-d_s)^2}\,\mu\,q\,n\,\sqrt{1 + \frac{4\,m\,\rho\,q\,(d-d_s)}{\mu\,(\psi-1)(3-\psi)}}
$$
$$
+ \frac{c_d\,(2-\sigma)(\psi-1)(3-\psi)^2\,\psi^2}{16\,\epsilon^3\,(d-d_s)}\,\rho\,q^2\,. \quad (6.33)
$$

Equations (6.32) and (6.33) are presented in Tables 6.2 (p 173) and 6.3 (p 174), respectively, for the doubly staggered foam RUC model ($\sigma = 0$). The corresponding equations for the singly staggered foam RUC model ($\sigma = 1$) are presented in Tables 6.4 (p 175) and 6.5 (p 176). In Appendix D (Tables D.13 to D.20, pp 302-307) equations for the streamwise pressure gradient, similar to those in Tables 6.2 to 6.5, are presented but as a function of d and d_s (instead of $(d-d_s)$).

The permeability as a function of $d - d_s$ is given by

$$
k_{dds} = \frac{4\,\epsilon^2\,(d-d_s)^2}{(3-\sigma)\,n\,\psi^2\,(\psi-1)(3-\psi)^2}\left[1 + \frac{m\,(3-\psi)\,Re_{Dh}}{(\psi-1)}\right]^{-1/2}, \quad (6.34)
$$

and the passability in terms of $d - d_s$ by

$$
\eta_{dds} = \frac{16\,\epsilon^3\,(d-d_s)}{c_d\,(2-\sigma)(\psi-1)(3-\psi)^2\,\psi^2}\,. \quad (6.35)
$$

172

Table 6.2: Expressions for the streamwise pressure gradient, $-\mathrm{d}p/\mathrm{d}x$, as a function of Re_{Dh} and $d - d_s$, predicted by the doubly staggered foam models.

Streamwise pressure gradient for the doubly staggered foam model:
Doubly staggered long duct foam model: $$-\frac{\mathrm{d}p}{\mathrm{d}x} = \frac{9\,\psi^2\,(\psi - 1)(3 - \psi)^2}{\epsilon^2\,(d - d_s)^2}\,\mu\,q \;+\; \frac{(\psi - 1)(3 - \psi)^4\,\psi^2}{32\,\epsilon^3(d - d_s)^2}\,c_d\,\mu\,q\,Re_{Dh}$$
Doubly staggered parallel plate short duct foam model: $$-\frac{\mathrm{d}p}{\mathrm{d}x} = \frac{9\,\psi^2\,(\psi - 1)(3 - \psi)^2}{\epsilon^2\,(d - d_s)^2}\,\mu\,q\,\sqrt{1 + \frac{0.0822\,(3 - \psi)\,Re_{Dh}}{(\psi - 1)}} \\ + \frac{(\psi - 1)(3 - \psi)^4\,\psi^2}{32\,\epsilon^3\,(d - d_s)^2}\,c_d\,\mu\,q\,Re_{Dh}$$
Doubly staggered square short duct foam model: $$-\frac{\mathrm{d}p}{\mathrm{d}x} = \frac{10.67\,\psi^2\,(\psi - 1)(3 - \psi)^2}{\epsilon^2\,(d - d_s)^2}\,\mu\,q\,\sqrt{1 + \frac{0.0584\,(3 - \psi)\,Re_{Dh}}{(\psi - 1)}} \\ + \frac{(\psi - 1)(3 - \psi)^4\,\psi^2}{32\,\epsilon^3\,(d - d_s)^2}\,c_d\,\mu\,q\,Re_{Dh}$$

For $Re_{Dh} = 0$ the permeability prediction of equation (6.34) reduces to that of the long duct foam sub-models, as expected.

6.6 Critical Reynolds numbers

The Reynolds number at which the effects of developing and fully developed flow weigh equally, denoted by Re_{Dh_c}, can be determined from equation (6.24) by equating the two terms in the square root and solving for the Reynolds number. The result is given by

$$Re_{Dh_c} = \frac{(\psi - 1)}{m\,(3 - \psi)}, \tag{6.36}$$

and is an implicit function of porosity. The porosity dependence of Re_{Dh_c} is shown in Figure 6.3 (p 175) for the square duct and parallel plates models. In the legend of Figure 6.3 the word 'parallel' in "double parallel plates model" is abbreviated as ||.

It is evident that as the porosity increases the critical Reynolds number decreases. This

Table 6.3: Expressions for the streamwise pressure gradient, $-\mathrm{d}p/\mathrm{d}x$, as a function of q and $d - d_s$, predicted by the doubly staggered foam models.

Streamwise pressure gradient for the doubly staggered foam model:

Doubly staggered long duct foam model:

$$-\frac{\mathrm{d}p}{\mathrm{d}x} = \frac{9\,\psi^2\,(\psi-1)(3-\psi)^2}{\epsilon^2\,(d-d_s)^2}\,\mu\,q \;+\; \frac{(\psi-1)(3-\psi)^2\,\psi^2}{8\,\epsilon^3\,(d-d_s)}\,c_d\,\rho\,q^2$$

Doubly staggered parallel plate short duct foam model:

$$-\frac{\mathrm{d}p}{\mathrm{d}x} = \frac{9\,\psi^2\,(\psi-1)(3-\psi)^2}{\epsilon^2\,(d-d_s)^2}\,\mu\,q\,\sqrt{1+\frac{0.33\,\rho\,q\,(d-d_s)}{\mu\,(3-\psi)(\psi-1)}}$$
$$+\;\frac{(\psi-1)(3-\psi)^2\,\psi^2}{8\,\epsilon^3\,(d-d_s)}\,c_d\,\rho\,q^2$$

Doubly staggered square short duct foam model:

$$-\frac{\mathrm{d}p}{\mathrm{d}x} = \frac{10.67\,\psi^2\,(\psi-1)(3-\psi)^2}{\epsilon^2\,(d-d_s)^2}\mu\,q\,\sqrt{1+\frac{0.23\,\rho\,q\,(d-d_s)}{\mu\,(3-\psi)(\psi-1)}}\;+$$
$$+\;\frac{(\psi-1)(3-\psi)^2\,\psi^2}{8\,\epsilon^3\,(d-d_s)}\,c_d\,\rho\,q^2$$

---

is to be expected since the effect of developing flow becomes more and more significant as the porosity increases and the duct length decreases.

The Reynolds number at which the effects of developing flow and the inertial effects of the Forchheimer regime weigh equally, denoted by Re_c, can be obtained by setting equations (6.26) and (6.28) equal and solving for the Reynolds number. This leads to

$$Re_c = \frac{\frac{m\,(3-\psi)}{(\psi-1)} + \sqrt{\left(\frac{m\,(3-\psi)}{(\psi-1)}\right)^2 + 4\left(\frac{c_d\,(2-\sigma)(3-\psi)^2}{16\,\epsilon\,(3-\sigma)\,n}\right)^2}}{2\left(\frac{c_d\,(2-\sigma)(3-\psi)^2}{16\,\epsilon\,(3-\sigma)\,n}\right)^2}\,. \tag{6.37}$$

Equation (6.37) is also an implicit function of porosity. The porosity dependence of Re_c is shown in Figure 6.4 (p 177) for $\sigma = 0$ and $c_d = 2$. The porosity dependence of the square duct and parallel plate models is graphically indistinguishable. The Re_c-range for $0.8 \leq \epsilon \leq 0.99$ is approximately given by $35 \leq Re_c \leq 220$. The Reynolds numbers of this critical Reynolds number range is higher than those of the Re_{Dh_c}-values, as expected.

According to the short duct foam RUC model, the higher the porosity, the higher the Reynolds number at which the effects of developing flow and inertia weigh equally.

174

Table 6.4: Expressions for the streamwise pressure gradient, $-\mathrm{d}p/\mathrm{d}x$, as a function of Re_{Dh} and $d - d_s$, predicted by the singly staggered foam models.

Streamwise pressure gradient for the singly staggered foam model:
Singly staggered long duct foam model $-\dfrac{\mathrm{d}p}{\mathrm{d}x} \;=\; \dfrac{6\,\psi^2\,(\psi - 1)(3 - \psi)^2}{\epsilon^2\,(d - d_s)^2}\,\mu\,q \;+\; \dfrac{(\psi - 1)(3 - \psi)^4\,\psi^2}{64\,\epsilon^3\,(d - d_s)^2}\,c_d\,\mu\,q\;Re_{Dh}$
Singly staggered parallel plate short duct foam model: $-\dfrac{\mathrm{d}p}{\mathrm{d}x} \;=\; \dfrac{6\,\psi^2\,(\psi - 1)(3 - \psi)^2}{\epsilon^2\,(d - d_s)^2}\,\mu\,q\,\sqrt{1 + \dfrac{0.0822\,(3 - \psi)\,Re_{Dh}}{(\psi - 1)}}$ $\qquad\qquad\qquad + \dfrac{(\psi - 1)(3 - \psi)^4\,\psi^2}{64\,\epsilon^3\,(d - d_s)^2}\,c_d\,\mu\,q\;Re_{Dh}$
Singly staggered square short duct foam model: $-\dfrac{\mathrm{d}p}{\mathrm{d}x} \;=\; \dfrac{7.12\,\psi^2\,(\psi - 1)(3 - \psi)^2}{\epsilon^2\,(d - d_s)^2}\,\mu\,q\,\sqrt{1 + \dfrac{0.0584\,(3 - \psi)\,Re_{Dh}}{(\psi - 1)}}$ $\qquad\qquad\qquad + \dfrac{(\psi - 1)(3 - \psi)^4\,\psi^2}{64\,\epsilon^3\,(d - d_s)^2}\,c_d\,\mu\,q\,Re_{Dh}$
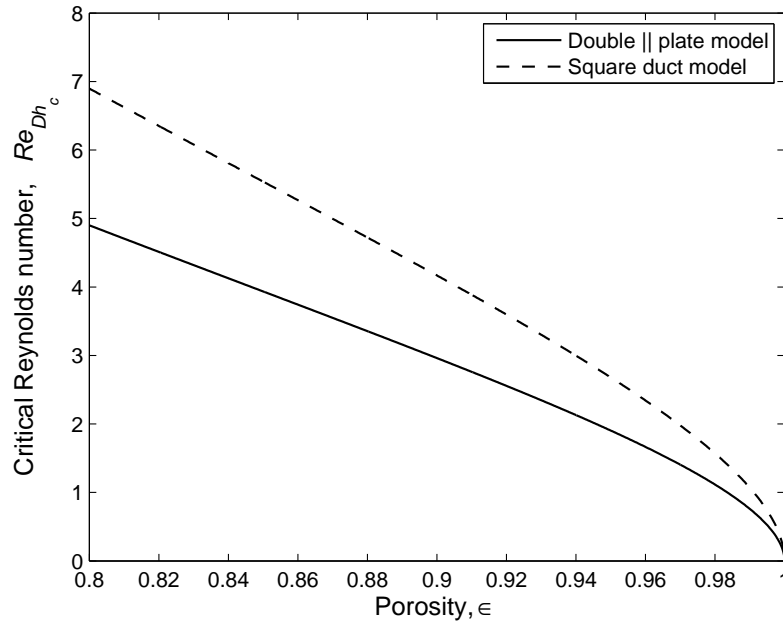
Figure 6.3: Critical Reynolds number for the transition between developing and fully developed flow as a function of porosity.

175

Table 6.5: Expressions for the streamwise pressure gradient, $-\mathrm{d}p/\mathrm{d}x$, as a function of q and $d - d_s$, predicted by the singly staggered foam models.

Streamwise pressure gradient for the singly staggered foam model:

Singly staggered long duct foam model

$$-\frac{\mathrm{d}p}{\mathrm{d}x} = \frac{6\,\psi^2(\psi-1)(3-\psi)^2}{\epsilon^2\,(d-d_s)^2}\,\mu\,q \;+\; \frac{(\psi-1)(3-\psi)^2\,\psi^2}{16\,\epsilon^3\,(d-d_s)}\,c_d\,\rho\,q^2$$

Singly staggered parallel plate short duct foam model:

$$-\frac{\mathrm{d}p}{\mathrm{d}x} = \frac{6\,\psi^2\,(\psi-1)(3-\psi)^2}{\epsilon^2\,(d-d_s)^2}\,\mu\,q\,\sqrt{1 + \frac{0.33\,\rho\,q\,(d-d_s)}{\mu\,(3-\psi)(\psi-1)}} \\ + \frac{(\psi-1)(3-\psi)^2\,\psi^2}{16\,\epsilon^3\,(d-d_s)}\,c_d\,\rho\,q^2$$

Singly staggered square short duct foam model:

$$-\frac{\mathrm{d}p}{\mathrm{d}x} = \frac{7.12\,\psi^2\,(\psi-1)(3-\psi)^2}{\epsilon^2\,(d-d_s)^2}\,\mu\,q\,\sqrt{1 + \frac{0.23\,\rho\,q\,(d-d_s)}{\mu\,(3-\psi)(\psi-1)}} \\ + \frac{(\psi-1)(3-\psi)^2\,\psi^2}{16\,\epsilon^3\,(d-d_s)}\,c_d\,\rho\,q^2$$

6.7   Effect of developing flow on pressure drop

Figure 6.5 (p 177) shows the dimensionless total drag factor, F_{dds}, as a function of Re_{Dh} predicted by the doubly staggered long duct and short duct foam RUC models (both the parallel plates and square duct models) for an arbitrary porosity value of $\epsilon = 0.9$ and $c_d = 2$.

Figure 6.5 shows that the parallel plate and square duct models are graphically almost indistinguishable. Since flow between parallel plates was assumed in the long duct model, the parallel plates model will henceforth be used as the short duct model. Also shown is the doubly staggered long duct model (for Darcy and Forchheimer flow). At very low Reynolds numbers (i.e. at $Re_{Dh} \approx 1$) the long duct and short duct models yield more or less the same model predictions, as expected. A figure with similar trends predicted, as in Figure 6.5, can also be obtained for the singly staggered short duct model. Also in this case, the parallel plates model will henceforth be used to predict the pressure gradient.

Crosnier et al. (2006) performed experiments on airflow through stainless steel (i.e. POR-VAIR) and aluminium (i.e. ERG) foams with PPI numbers of 5, 10, 20 and 40. The notation will be followed that ERG20, for example, denotes the aluminium foam with a
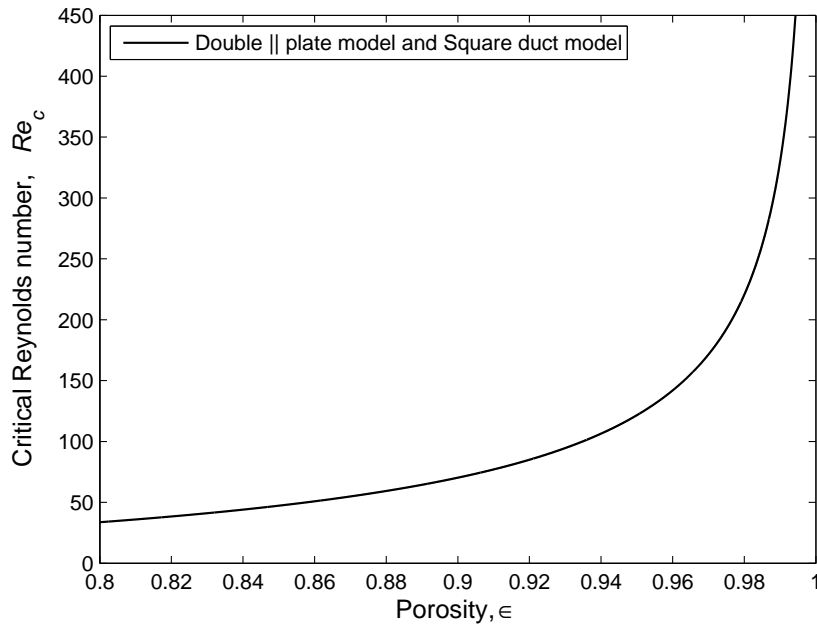
Figure 6.4: Critical Reynolds number for the transition between developing flow and the Forchheimer flow regime as a function of porosity ($\sigma = 0$ and $c_d = 2$)
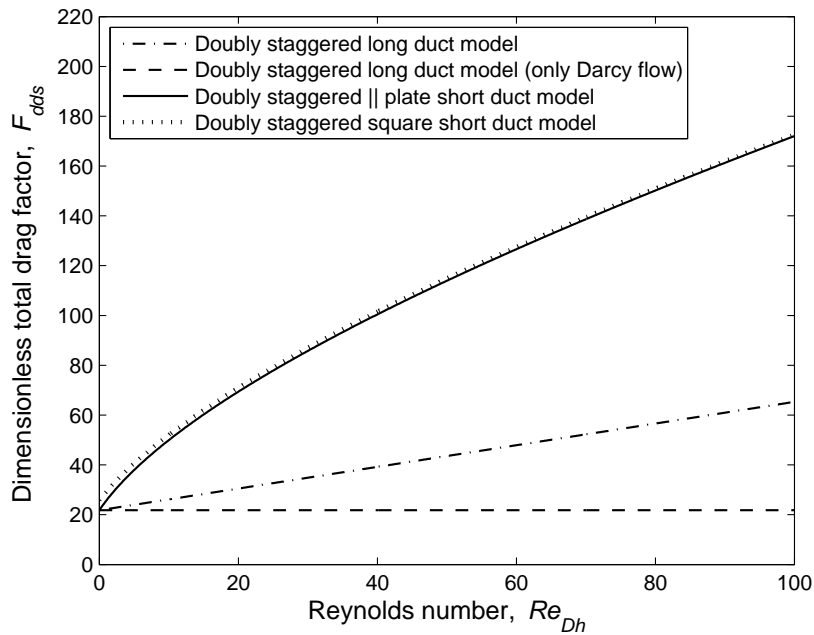
Figure 6.5: Dimensionless total drag factor as a function of the Reynolds number, Re_{Dh}, for $\epsilon = 0.9$ and $c_d = 2$.

PPI number of 20 and POR20, for example, denotes the stainless steel foam with a PPI number of 20. The average strut diameter of the metallic foams was obtained through image analysis. Lumps of material at the intersection of struts as well as covered (or closed) faces are observed in the PORVAIR foams. Assuming that this leads to the presence of stagnant fluid domains, the singly staggered short duct model will be applied to the PORVAIR foams.

Dybbs & Edwards (1984) state that for $1 < Re_{Dh} < 18$ developing laminar flow is present in the pores of a porous medium. Although Dybbs & Edwards (1984) did not specify for which types of porous media and porosities the latter range is applicable, it may be used as a rough indication of the onset of developing flow in foamlike media. Application of equation (6.36) for the parallel plates short duct model to the ERG and PORVAIR foams both yield critical Reynolds numbers in the vicinity of 2, i.e. 2.2 for the ERG foams and 2.1 for the PORVAIR foams. Since at the critical Reynolds number developing flow and fully developed flow contribute equally to the pressure drop, the effect of developing flow is not negligible at Reynolds numbers below 1. For flow to occur, the Reynolds number cannot be zero, so it is evident that developing flow will have an effect which needs to be accounted for.

The pressure gradient as a function of the superficial velocity could not be presented graphically for the ERG and PORVAIR foams, since the experimental superficial velocity values or Reynolds numbers are not provided by Crosnier et al. (2006). Since the exact Reynolds numbers at which the experiments were performed are unknown, the critical Reynolds number will be used to indicate the presence of developing flow.

ERG foams

For the ERG foams the doubly staggered parallel plate short duct foam RUC model is used to predict the pressure drop. Figure 6.6 (p 179) shows the dimensionless total drag factor, F_d, as a function of porosity for the ERG foams of Crosnier et al. (2006). Due to the narrow porosity range associated with the ERG foams all the data points are in the range $0.92 < \epsilon < 0.94$. For the ERG foams the average critical Reynolds number was calculated as $Re_{Dh_c} = 2.2$.

For all the data points, except some of the ERG5 data points, the doubly staggered long duct model under-predicts the pressure drop. As the Reynolds number increases from 0 to the average critical Reynolds number of 2.2, the pressure drop prediction increases due to the effect of developing flow. The relative percentage difference between the long and short duct foam RUC models at the average porosity of the ERG foams and the critical Reynolds number is about 28.5%.

There seems to be no correlation between the PPI number and the porosity of the ERG foams. Similarly, there seems to be no correlation between the PPI number of the ERG foams and the degree of influence of developing flow. As a result, no useful information can be extracted from the PPI number. Related to the discussion on the PPI number in Section 3.15.7 (p 67), this number should rather not be used in model predictions.
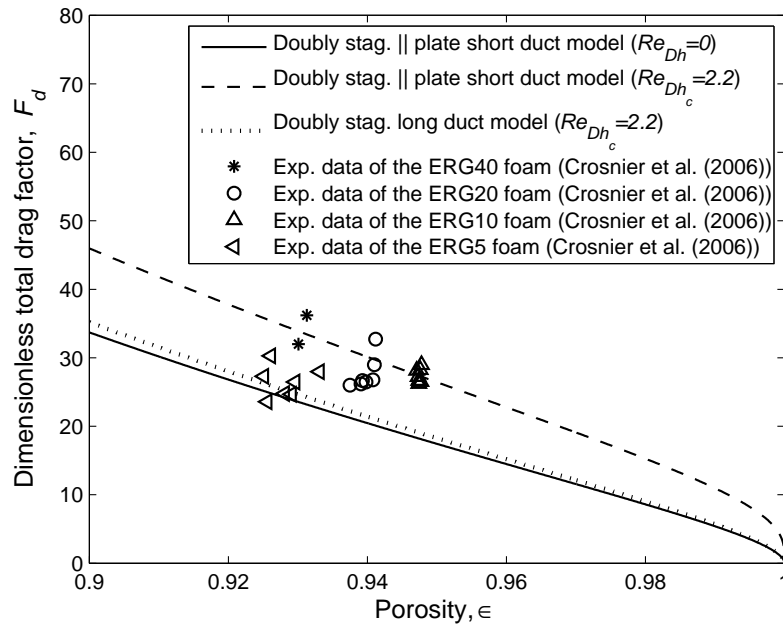
Figure 6.6: Dimensionless total drag factor as a function of porosity for the ERG foams of Crosnier et al. (2006).

The model prediction at a Reynolds number of zero provides a lower bound for the data (with the exception of one ERG5 data point). It is satisfactory that the data are scattered from this lower bound to regions of increasing Reynolds number up to and slightly beyond the model prediction at the average critical Reynolds number. The increase in the dimensionless total drag factor with an increase in Reynolds number illustrates the effect of developing flow.

PORVAIR foams

As already mentioned, the singly staggered parallel plate short duct foam RUC model was used to predict the pressure drop of the PORVAIR foams. Figure 6.7 (p 180) shows the dimensionless total drag factor, F_d, as a function of porosity for the PORVAIR foams of Crosnier et al. (2006) for which the average critical Reynolds number is calculated as $Re_{Dh_c} = 2.1$.

Shown for comparison in Figure 6.7 are both the doubly staggered and singly staggered short duct models at $Re_{Dh_c} = 2.1$. The doubly staggered model over-predicts the pressure gradient, as expected. Also in this case, the singly staggered model prediction at a Reynolds number of zero may be regarded as a lower bound from which the data is scattered towards and slightly beyond the model prediction at the average critical Reynolds number.

The relative percentage difference between the long and short duct foam RUC models at
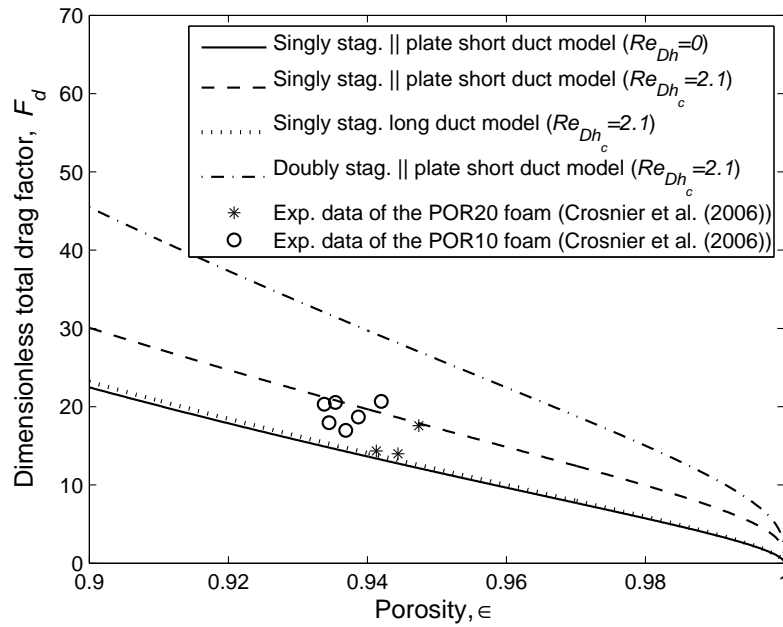
Figure 6.7: Dimensionless total drag factor as a function of porosity for the PORVAIR foams of Crosnier et al. (2006).

the average porosity of the PORVAIR foams and the critical Reynolds number is here also about 28.5%. Crosnier et al. (2006) owes the under-prediction of the long duct model to the lumps of solid material at the intersection of struts which is not accounted for in the model. They suggest that the foam model should be modified to take the lumps into account. They then recommend a combined granular and foam RUC model. In this section it was, however, illustrated that the under-prediction can be attributed to the effect of developing flow since the same under-prediction was observed for the ERG foams containing no lumps.

6.8   Extended permeability due to developing flow

Bhattacharya et al. (2002) performed experiments on airflow through aluminium and carbon foams with PPI numbers of 5, 10, 20 and 40 and porosities in the range $0.89 < \epsilon < 0.98$. The long duct foam RUC model of Du Plessis et al. (1994) was used by Bhattacharya et al. (2002) to predict the permeability of the metallic foams. The model prediction was compared with their experimental permeability data.

Bhattacharya et al. (2002) found that the long duct foam RUC model of Du Plessis et al. (1994) over-predicts the experimental permeability data by factors of $1.4 - 2.7$. This is equivalent to an under-prediction in the total drag factor (or pressure drop), as was observed in Section 6.7 (p 176). Bhattacharya et al. (2002) then stated that the expression

for the tortuosity, given by the foam RUC model, i.e.

$$\chi = 2 + 2\cos\left[\frac{4\pi}{3} + \frac{1}{3}\cos^{-1}(2\epsilon - 1)\right] ,$$
(6.38)

is not applicable for determining χ for their metallic foam samples. (Equation (6.38) is the same for the doubly staggered models of the present study and that of Du Plessis et al. (1994).) Similarly to Crosnier et al. (2006), Bhattacharya et al. (2002) also attributed the deviations to the irregular lumps of solid material at the intersection of struts that are not accounted for in the RUC model. They state that the solid lumps cause an extra flow resistance that will lead to an increase in pressure drop and consequently a decrease in permeability. It was illustrated in Section 6.7 (p 176) that the under-prediction in pressure drop can be resolved by incorporating the effect of developing flow into the model, regardless of the presence of lumps.

Bhattacharya et al. (2002) then adapted the expression for the tortuosity, given by equation (6.38), to account for the extra flow resistance provided by the lumps of solid material. In order to find an expression for the pore diameter as a function of porosity and the cylindrical fibre diameter, they combined the dodecahedron model with the cubic unit cell model (Section 5.4.1, p 128). The dodecahedron model was used to represent the accumulation of solid material at the intersection of fibres. Through geometrical calculations they found that the relationship between the cubic cell size, d', and the cell size, a', of the dodecahedron, is given by

$$d' = 0.59\,a' .$$
(6.39)

The resulting equation for the ratio of the cylindrical fibre diameter, d'_f, and their proposed pore diameter, d'_p, is a function of porosity, i.e.

$$\frac{d'_f}{d'_p} = 1.18\sqrt{\frac{1-\epsilon}{3\pi}\frac{1}{G}} ,$$
(6.40)

where G is an empirical shape function which accounts for the lump of solid material at the intersection of fibres. It takes the variation in fibre cross-section with porosity into account and is given by

$$G = 1 - \epsilon^{-(1-\epsilon)/0.04} .$$
(6.41)

In order to adapt the equation for the tortuosity, given by equation (6.38), they made use of the relation,

$$\chi = \frac{\epsilon\,d'^2_p}{A_{p_\parallel}} ,$$
(6.42)

where $A_{p_\parallel}$ is the streamwise cross-sectional flow area in the RUC model. Equation (6.42) is, however, incorrect and should be expressed in terms of the cell size instead of the pore

181
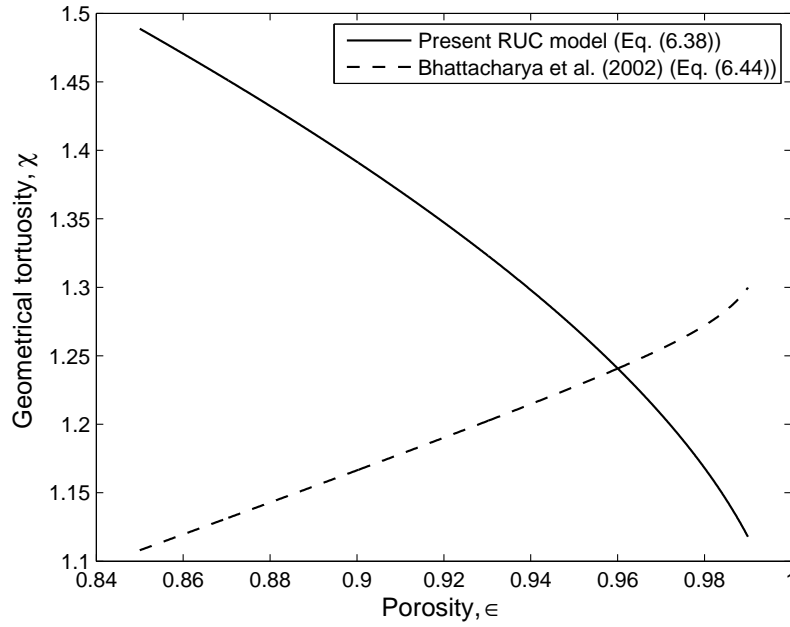
Figure 6.8: Geometrical tortuosity of the doubly staggered foam model as a function of porosity.

size, as was done in the RUC model. They then substituted $A_{p_\parallel}$ into equation (6.42), with $A_{p_\parallel}$ given by

$$A_{p_\parallel} = \frac{\pi}{4}\left(d_p'^2 - d_f'^2\right) . \tag{6.43}$$

They furthermore substituted equation (6.40) into equation (6.43) to obtain

$$\chi = \frac{4\,\epsilon}{\pi}\left\{1 - \left(1.18\sqrt{\frac{1-\epsilon}{3\,\pi}}\frac{1}{G}\right)^2\right\}^{-1} . \tag{6.44}$$

In Figure 6.8 the geometrical tortuosity predicted by equation (6.38) is compared to the adapted geometrical tortuosity of Bhattacharya et al. (2002) (i.e. equation (6.44)).

The increase in geometrical tortuosity with an increase in porosity, proposed by the adapted tortuosity equation of Bhattacharya et al. (2002), does not comply with the definition of the geometrical tortuosity on which equation (6.38) is based. The geometrical tortuosity of the RUC model was defined as the ratio of the average length of the tortuous flow path to the streamwise cell size of the RUC (Section 3.9, p 45). According to this definition the tortuosity should decrease with an increase in porosity, as illustrated graphically by equation (6.38) in Figure 6.8. For the doubly staggered foam RUC model the geometrical tortuosity of equation (6.38) is the same as the expression for the geometric factor ψ, since the only difference between the tortuosity and geometric factor is

the presence of stagnant fluid volumes and in the doubly staggered model stagnant fluid volumes are absent.

Next it will be shown that the combined RUC, cubic unit cell and dodecahedron model of Bhattacharya et al. (2002) is not needed to improve the predictive capabilities of the RUC model, since this can be achieved by simply using another choice of pore diameter in the RUC model.

Equation (6.39), resulting from the dodecahedron model of Bhattacharya et al. (2002), shows that the cubic cell size, d', is smaller than the pentagonal cell size, a', by a factor of 0.59. Recall that the relationship between the two-dimensional pore diameter, $d - d_s$, of the foam RUC model and the three-dimensional pore diameter, d_p, was determined in Section 3.15.7 (p 67) to be

$$d - d_s \;=\; \frac{1}{\sqrt{3}}\, d_p \approx 0.58\, d_p \; . \tag{6.45}$$

When applying the foam RUC model to the experimental permeability data of Bhattacharya et al. (2002), the three-dimensional pore diameter, d_p, will be used instead of the two-dimensional pore or channel width $d - d_s$, since Bhattacharya et al. (2002) also worked with the cell size, a', instead of d'.

If the experimental values provided by Bhattacharya et al. (2002) for the pore diameter are used as the three-dimensional pore diameter, d_p, in the doubly staggered parallel plate short duct foam RUC model, then satisfactory agreement is obtained between the model prediction for the permeability and the experimental data, as shown in Figure 6.9 (p 184).

The dimensionless permeability predicted by the doubly staggered parallel plate short duct foam RUC model, in terms of d_p, is given by

$$K_{dp} \;=\; \frac{k}{d_p^2} \;=\; \frac{\epsilon^2}{27\,\psi^2\,(\psi - 1)(3 - \psi)^2}\left[1 + \frac{0.0822\,(3 - \psi)\,Re_{Dh}}{(\psi - 1)}\right]^{-1/2} . \tag{6.46}$$

Figure 6.9 shows that the dimensionless permeability predicted by the doubly staggered parallel plate short duct foam RUC model at the average critical Reynolds number of $Re_{Dh_c} = 2.2$ is in satisfactory agreement with the experimental data of Bhattacharya et al. (2002). The relative percentage difference between the long duct RUC model of Du Plessis (1994) and the short duct foam RUC model at the average foam porosity and the critical Reynolds number is 85%. More accurate model predictions are obtained at Reynolds numbers slightly higher than the critical Reynolds number. Since the exact Reynolds number corresponding to the experimental data was not specified, the model prediction corresponding to the exact Reynolds number cannot be shown in Figure 6.9. It is nevertheless satisfactory that the RUC model follows a similar trend as the experimental data and yields model predictions of the same order of magnitude.

Figure 6.9 also shows that the doubly staggered long duct model over-predicts the experimental permeability data. Wilms (2006) also observed this over-prediction of the doubly
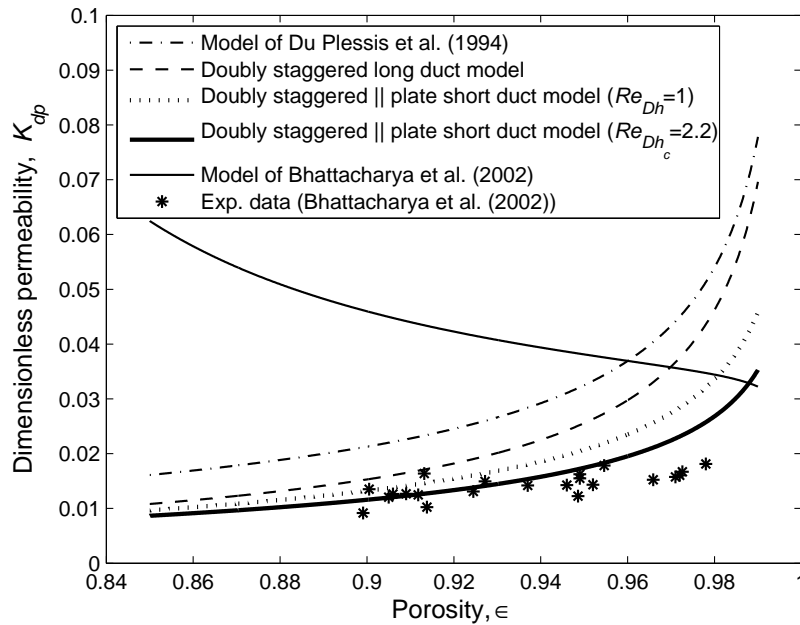
Figure 6.9: Dimensionless permeability as a function of porosity for the aluminium and carbon foams of Bhattacharya et al. (2002).

staggered long duct model. She obtained the same permeability prediction for the doubly staggered long duct model as in the present study. The doubly staggered long duct model is equivalent to the doubly staggered parallel plate short duct foam RUC model with $Re_{Dh} = 0$. Figure 6.9 shows that the over-prediction of the latter long duct model is less than that of the long duct model of Du Plessis (1994). The relative percentage difference between the long duct RUC model of Du Plessis (1994) and the long duct model of the present study is 30%. The difference between the two models is an additional tortuosity/geometric factor that appears in the model of the present study which results from the incorporation of the Lloyd correction (Section 4.4.1, p 85). The relative percentage difference between the long duct and short duct models of the present study is 40%. It is satisfactory that the over-prediction at a Reynolds number of zero becomes significantly less as the Reynolds number is increased towards the critical value. This once again illustrates the influence of developing flow.

Figure 6.9 shows furthermore that the dimensionless permeability prediction of Bhattacharya et al. (2002) decreases with an increase in porosity, as opposed to the dimensionless permeability prediction of the RUC model which increases with porosity. They regard their model prediction resulting from the combined geometrical models as an improvement to the permeability prediction of the RUC model. They then state that the model of Du Plessis et al. (1994) is accurate only at low porosities, whereas their newly adapted 'RUC' model can be applied over a wide range of porosities.

It was illustrated here that the RUC model has the potential to be adapted through sound physical principles (i.e. of developing flow) to improve its predictive capabilities.

The increase in flow resistance caused by developing flow together with the use of the three-dimensional pore diameter, d_p, as a more "observable pore diameter", as stated by Du Plessis et al. (1994), compensates for the over-predicted permeability values. The RUC model does not discriminate between foams with and without solid lumps. It is important to note that the RUC model geometry should not be regarded as the exact geometry of the actual foam, but rather as the *average* geometry and that the effect of solid lumps is implicitly incorporated into the model through the average *measured* pore diameter. It is therefore important to know exactly which pore-scale linear dimension of the actual foam was measured in order to know which of the various pore-scale linear dimensions specified for the foam RUC model resembles this measured value. It is therefore not necessary to combine the RUC model with another model geometry and adapt the expression for the tortuosity of the RUC model to account for the effect of the solid lumps in the RUC model.

6.9 Porosity dependence of the interstitial form drag coefficient

The value used throughout this study for the interstitial form drag coefficient, c_d, of the foam RUC model is the empirical value for flow past a single square rod, i.e. $c_d = 2$ (Section 3.15.6, p 63). This constant value of $c_d = 2$ will thus be regarded as an average value for the complex micro-structures of foamlike media.

According to Bhattacharya et al. (2002), for the foam samples they considered, the form drag coefficient is a function of porosity for $0.85 < \epsilon < 0.97$, after which it is assumed to be constant. In analogy of the work of Bhattacharya et al. (2002), Crosnier et al. (2006) observed that the cross-sectional shape of the struts of the PORVAIR foams are close to a circular form whereas in the ERG foams the cross-section of the struts changes from a circle at $\epsilon = 0.85$ to an inner concave triangle at $\epsilon = 0.97$ and should therefore be a function of porosity.

In this section a semi-empirical method will be discussed for determining the interstitial form drag coefficient as a function of porosity. The first part of the method is based on the work of Du Plessis et al. (1994) and the second part of the method is proposed by the author of this dissertation.

In the empirical method of Du Plessis et al. (1994), the value of c_d can be inferred from experimental pressure drop data by expressing the experimental pressure gradient in the form of a Forchheimer-type equation, i.e.

$$\left(-\frac{\mathrm{d}p}{\mathrm{d}x} \right)_{exp} = N_{exp}\, q_{exp} + M_{exp}\, q_{exp}^2 , \qquad (6.47)$$

with $N_{exp} = \mu/k_{exp}$ and $M_{exp} = \rho/\eta_{exp}$. Dividing throughout by the magnitude of the

185

superficial velocity leads to

$$\frac{1}{q_{exp}} \left(-\frac{\mathrm{d}p}{\mathrm{d}x} \right)_{exp} = N_{exp} + M_{exp} \, q_{exp} \,. \tag{6.48}$$

Equation (6.48) shows a linear dependence in q_{exp} with N_{exp} as the y-intercept of the straight line and M_{exp} the gradient. Expressing the foam RUC model (i.e. the long duct model of the present study, for simplification purposes) in the same form as equation (6.48) yields

$$\frac{1}{q} \left(-\frac{\mathrm{d}p}{\mathrm{d}x} \right) = \frac{12 \, \mu \, (3 - \sigma)(\psi - 1) \, \psi^2}{\epsilon^2 \, d^2} + \frac{(2 - \sigma)(\psi - 1)(3 - \psi) \, \psi^2 \, c_d \, \rho \, q}{8 \, \epsilon^3 \, d} \,. \tag{6.49}$$

It then follows that

$$N_{an} = \frac{12 \, \mu \, (3 - \sigma) \, (\psi - 1) \, \psi^2}{\epsilon^2 \, d^2} \,, \tag{6.50}$$

and

$$M_{an} = \frac{(2 - \sigma)(\psi - 1)(3 - \psi) \, \psi^2 \, \rho \, c_d}{8 \, \epsilon^3 \, d} \,. \tag{6.51}$$

If the porosity is known, the following analytical value can be obtained

$$\left(\frac{N d^2}{\mu} \right)_{an} = \frac{12 \, (3 - \sigma) \, (\psi - 1) \, \psi^2}{\epsilon^2} \,. \tag{6.52}$$

If it is known that there are stagnant fluid volumes present in the foam, then $\sigma = 1$, otherwise $\sigma = 0$. If the viscosity of the fluid is also known, then the linear dimension d can be obtained from

$$d = \sqrt{\left(\frac{\mu}{N} \right)_{exp} \left(\frac{N \, d^2}{\mu} \right)_{an}} = \sqrt{k_{exp} \left(\frac{N \, d^2}{\mu} \right)_{an}} \,. \tag{6.53}$$

Having determined the value of d, if follows from equation (6.51) that

$$\left(\frac{M}{c_d} \right)_{an} = \frac{(2 - \sigma)(\psi - 1)(3 - \psi) \, \psi^2 \, \rho}{8 \, \epsilon^3 \, d} \,. \tag{6.54}$$

Finally the interstitial form drag coefficient, c_d, can be determined from

$$c_d = M_{exp} \left(\frac{c_d}{M} \right)_{an} = \frac{\rho}{\eta_{exp}} \left(\frac{c_d}{M} \right)_{an} \,. \tag{6.55}$$

Bhattacharya et al. (2002) classified the domain (i.e. $0.85 < \epsilon < 0.97$) in which the form drag coefficient is a function of porosity and the fibre cross-section changes from a circle to

186

a concave triangle, as Domain I. Domain II is the domain, where $\epsilon > 0.97$ and the cross-section of the fibres retains its shape of a concave triangle. In Domain II the form drag coefficient thus remains unchanged. The porosity dependence of the form drag coefficient in Domain I is determined from the experimental values for the inertial coefficient of Bhattacharya et al. (2002), $f_{B_{exp}}$, defined as

$$f_{B_{exp}} = \frac{M_{exp}\sqrt{k_{B_{exp}}}}{\rho} \ .$$

(6.56)

They then use two different equations for the inertial coefficient, $f_{B_{exp}}$, based on the different porosity dependencies of the form drag coefficient in the two domains.

Bhattacharya et al. (2002) stated that the long duct foam RUC model of Du Plessis (1994) is applicable for fibre cross-sections of concave triangles only and does not take into account the variation in cross-section for $0.85 < \epsilon < 0.97$. The form drag coefficient used by them for the foam RUC model is, however, 2.05, which is the empirical value for flow past a single square rod and not the value of $c_d = 1.75$ used by them for concave triangles.

Next in this study an expression for the porosity dependence of the form drag coefficient will be proposed by the author of this dissertation that is applicable over the entire porosity range and that can be used as the interstitial form drag coefficient in the foam RUC model. Thereafter the expression for the interstitial form drag coefficient will be used to propose a single equation for the inertial coefficient.

From the experimental data of Bhattacharya et al. (2002) and Crosnier et al. (2006) two asymptotic limits are identified, i.e.

$$\text{Lower limit:} \qquad c_d = c_{d_o} = 1.2 \qquad \text{for} \qquad \epsilon < 0.9 \qquad (6.57)$$
$$\text{Upper limit:} \qquad c_d = c_{d_\infty} = 3.5 \qquad \text{for} \qquad \epsilon > 0.97 \qquad (6.58)$$

These limits, together with the experimental data, are shown in Figure 6.10 (p 188). It is noted from the upper limit that the experimental values for the form drag coefficient extend well beyond the value of 1.75 for a concave triangle. A possible reason for this is that the form drag coefficient over a single object in an infinite stream, may differ from that associated with a solid in a porous medium due to the presence of neighbouring solids.

The next step is to determine an expression for the central function, c_{d_c}, between the two asymptotic limits. It will be assumed that the central function, c_{d_c}, takes on the form:

$$c_{d_c} = A' e^{m'\epsilon} \ .$$

(6.59)

The coefficients A' and m' can be determined as follows: The average value of c_{d_o} and c_{d_∞} is given by $c_{d_a} = (c_{d_o} + c_{d_\infty})/2 = 2.35$. From the data points in Figure 6.10 the porosity
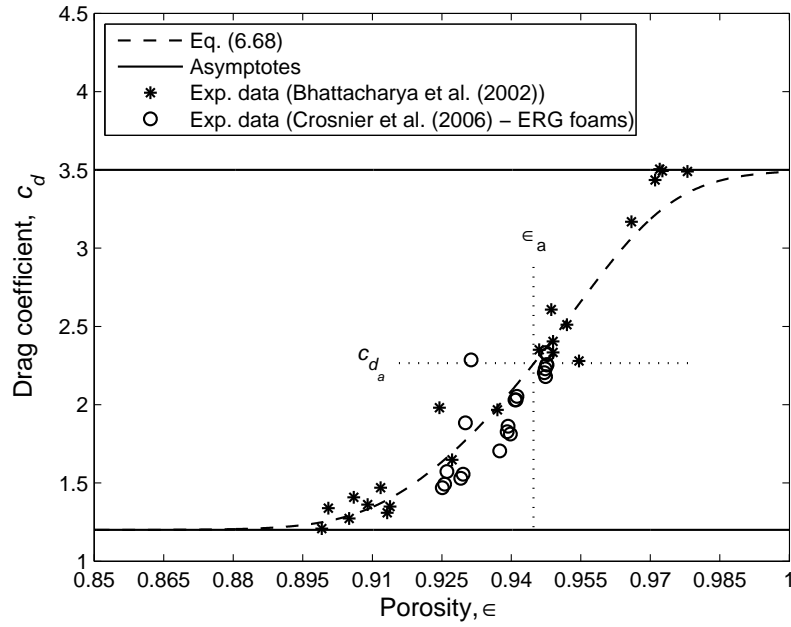
Figure 6.10: Interstitial form drag coefficient as a function of porosity.

value ϵ_a, where the data intersect the line c_{d_a} can be determined. This value is given by $\epsilon_a = 0.946$. From equation (6.59) it follows that the gradient of the function c_{d_c} at ϵ_a is

$$\left. \frac{\mathrm{d}c_{d_c}}{\mathrm{d}\epsilon} \right|_a = A' m' e^{m' \epsilon_a} \,, \tag{6.60}$$

and the function c_{d_c} evaluated at ϵ_a is given by

$$c_{d_c}|_a = A' e^{m' \epsilon_a} \,, \tag{6.61}$$

with $c_{d_c}|_a = c_{d_a}$. Solving for A' and m' from equations (6.60) and (6.61), leads to

$$m' = \frac{1}{c_{d_c}|_a} \left. \frac{\mathrm{d}c_{d_c}}{\mathrm{d}\epsilon} \right|_a \,, \tag{6.62}$$

and

$$A' = c_{d_c}|_a \, e^{-m' \epsilon_a} \,. \tag{6.63}$$

From the data in Figure 6.10 it follows that

$$\left. \frac{\mathrm{d}c_{d_c}}{\mathrm{d}\epsilon} \right|_a = 41.2 \,, \tag{6.64}$$

188

and consequently, $m' = 17.5$ and $A' = 1.5 \times 10^{-7}$, yielding

$$c_{d_c} = 1.5 \times 10^{-7} e^{17.5\epsilon} . \qquad (6.65)$$

Application of the power addition technique (Churchill & Usagi (1972)) to the asymptotes, c_{d_o} and c_{d_c}, leads to

$$c_{d_l} = \left[(c_{d_o})^s + (c_{d_c}^s) \right]^{1/s} , \qquad (6.66)$$

with s a shifting exponent. Applying the power addition technique once more, i.e. to the asymptotes c_{d_l} and c_{d_∞} then yields for a shifting exponent t,

$$c_d = \left[(c_{d_l})^{-t} + (c_{d_\infty})^{-t} \right]^{-1/t} . \qquad (6.67)$$

The resulting expression for the interstitial form drag coefficient is then given by:

$$
\begin{aligned}
c_d &= \left[((c_{d_o})^s + (c_{d_c})^s)^{1/s})^{-t} + (c_{d_\infty})^{-t} \right]^{-1/t} \\
&= \left[\left[\left((1.2)^s + \left(1.5 \times 10^{-7} e^{17.5\epsilon} \right)^s \right)^{1/s} \right]^{-t} + (3.5)^{-t} \right]^{-1/t} . \qquad (6.68)
\end{aligned}
$$

A value of 7 is used for both shifting parameters s and t, as this value provided the most satisfactory correspondence with the experimental data. Equation (6.68) for $s, t = 7$ is shown in Figure 6.10 (p 188) to correspond well with the experimental values of c_d.

6.9.1 Inertial coefficient

The dimensionless inertial coefficient of Du Plessis et al. (1994), used by Bhattacharya et al. (2002) (denoted by $f_{B_{an}}$), is given by

$$f_{B_{an}} = \frac{(2 - \sigma)(\psi - 1)(3 - \psi)\,\psi^2\, c_d\, \sqrt{k_{B_{an}}}}{8\,\epsilon^3\, d} = \frac{2.05\,(\psi - 1)\,\psi\,\sqrt{k_{B_{an}}}}{\epsilon^2\,(3 - \psi)\, d} , \qquad (6.69)$$

by application of equation (3.49) and using $\sigma = 0$ and $c_d = 2.05$. (Recall that for the doubly staggered foam model $\psi = \chi$). Equation (6.69) was incorrectly given by Bhattacharya et al. (2002) as

$$f_{B_{an}} = \frac{2.05\,(\psi - 1)\,\psi\,\sqrt{k_{B_{an}}}}{\epsilon^2\,(3 - \psi)\, d^2} . \qquad (6.70)$$

The permeability of Du Plessis et al. (1994), used by Bhattacharya et al. (2002) (denoted by $k_{B_{an}}$), is given by

$$k_{B_{an}} = \frac{\epsilon^2\, d^2}{36\,\chi\,(\chi - 1)} . \qquad (6.71)$$

Table 6.6: Expressions for the inertial coefficient.

Model	Inertial coefficient
Du Plessis et al. (1994):	$f_{B_{an}} = \dfrac{2.05\,\sqrt{\chi - 1}\sqrt{\chi}}{6\,\epsilon\,(3 - \chi)}$
Doubly staggered long duct:	$f = \dfrac{(2 - \sigma)\sqrt{\psi - 1}(3 - \psi)\,\psi\,c_d}{8\,\epsilon^2\,\sqrt{12}\,\sqrt{3 - \sigma}}$
Parallel plate short duct:	$f = \dfrac{(2 - \sigma)\sqrt{\psi - 1}(3 - \psi)\,\psi\,c_d}{8\,\epsilon^2\,\sqrt{12}\,\sqrt{3 - \sigma}} \times$ $\left[1 + \dfrac{0.0822\,(3 - \psi)\,Re_{Dh}}{(\psi - 1)}\right]^{-1/4}$

Expressions for the inertial coefficient predicted by the doubly staggered long duct model of Du Plessis et al. (1994), the doubly staggered long duct model of the present study and the parallel plate short duct foam RUC model are presented in Table 6.6.

The inertial coefficient is thus a function of porosity, ϵ, (since χ and ψ are functions of porosity only) and the interstitial form drag coefficient, c_d. The parallel plate short duct foam RUC model is given as a function of σ and is therefore applicable to the doubly staggered model (for $\sigma = 0$) and to the singly staggered model (for $\sigma = 1$).

Bhattacharya et al. (2002) found that the inertial coefficient of Du Plessis et al. (1994) exhibit relative percentage errors of 30 to 70% for $\epsilon < 95\%$ and concluded that the model of Du Plessis et al. (1994) is applicable only in the higher porosity range, i.e. for $\epsilon > 95\%$. Bhattacharya et al. (2002) also found that the inertial coefficient predicted by the model of Du Plessis et al. (1994) decreases with ϵ over the entire porosity range under consideration. This is also evident in Figure 6.11 (p 191), which is a graphical representation of the inertial coefficient as a function of porosity. Bhattacharya et al. (2002) state that the inertial coefficient only decreases with an increase in porosity for their samples in the range of $\epsilon > 0.97$. For porosities in the range $\epsilon < 0.97$ their experimental data shows that the inertial coefficient increases with an increase in porosity. This phenomena was not accounted for in the model of Du Plessis et al. (1994). The reason they give for this phenomenon is the fact that the inertial coefficient is a measure of the drag experienced by the fluid when flowing past the fibres and is therefore expected to depend strongly on the variation in cross-sectional shape of the fibres. Bhattacharya et al. (2002) then
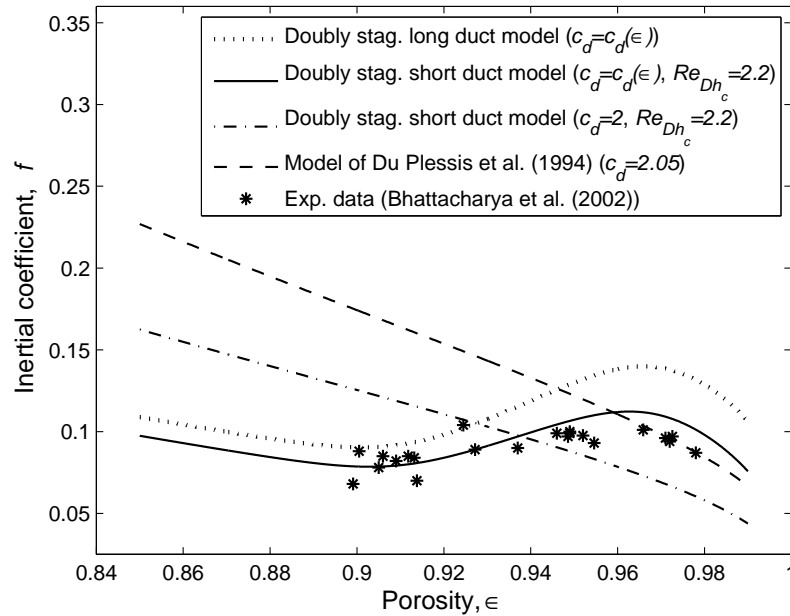
Figure 6.11: Inertial coefficient as a function of porosity.

adapted the expression for the form drag coefficient by incorporating the variation in cross-sectional shape of the fibres into c_d through an empirical shape function which is related to their expression for G (given by equation (6.41)). Their empirical expressions for c_d are however different for Domains I and II. Furthermore, in the model of Du Plessis et al. (1994), which they used for the inertial coefficient, they incorporated their adapted tortuosity function χ (equation (6.41)). According to Bhattacharya et al. (2002), their model prediction provides satisfactory agreement with their experimental data.

Next it will be shown that by making use of the porosity dependence of the form drag coefficient, given by equation (6.68), the short duct foam RUC model yields accurate predictions for the inertial coefficient. The RUC model then also accounts for the variation in cross-sectional shape of the fibres.

The model prediction for the inertial coefficient given in Table 6.6 (p 190) for the doubly staggered long duct foam RUC model and the doubly staggered parallel plate short duct model, into which equation (6.68) (with $s, t = 7$) is substituted, are shown in Figure 6.11. The doubly staggered long duct foam RUC model again corresponds to the doubly staggered parallel plate short duct model for $Re_{Dh} = 0$. Figure 6.11 shows that the long duct model, in which the porosity dependence of the interstitial form drag coefficient is incorporated, is a considerable improvement on the model prediction in which a constant form drag coefficient of 2 is used. A further improvement in the foam RUC model is the incorporation of the effect of developing flow which, once again, improves the model prediction. The critical Reynolds number of $Re_{Dh_c} = 2.2$ used here is the same value used to illustrate the effect of developing flow on permeability in Section 6.8 (p 180).

6.9.2   Passability

The passability predicted by the foam RUC model in terms of the RUC cell size, d, can be expressed as

$$\eta_d \;=\; \frac{2\,\epsilon^3\,U_o}{c_d\,S_{face}\,\psi^2} \;=\; \frac{8\,\epsilon^3\,d}{c_d\,(2-\sigma)(\psi-1)(3-\psi)\,\psi^2}\;. \qquad (6.72)$$

The resulting equations for the doubly staggered and singly staggered models are given in Table 4.12 (p 105). The relationship between the passability and the inertial coefficient, f, is given by

$$\eta \;=\; \frac{\sqrt{k}}{f}\;. \qquad (6.73)$$

The model prediction of Crosnier et al. (2006) is given by

$$\eta_d \;=\; \frac{2\,\epsilon^2\,(3-\psi)\,d}{c_d\,\psi^2\,(\psi-1)(2-\sigma)}\;. \qquad (6.74)$$

The reason for the difference between equations (6.72) and (6.74) is due to the fact that Crosnier et al. (2006) also incorporated the Lloyd correction in the closure modelling procedure at higher Reynolds numbers (Section 4.5, p 97).

A comparison of the model predictions for the dimensionless passability, η_d/d, as a function of porosity is shown in Figures 6.12 and 6.13 (p 193) for the doubly staggered ERG and singly staggered PORVAIR foams of Crosnier et al. (2006), respectively.

Figure 6.12 shows that the dimensionless passability in which the porosity dependence of the form drag coefficient is incorporated follows the trend of the experimental data more accurately than the model prediction in which a constant form drag coefficient is used. It also performs better than the model prediction of Crosnier et al. (2006).

Since the cross-section of the fibres of the PORVAIR foams retains its shape, a constant form drag coefficient is used in the model prediction for these foams. In Figure 6.13 the model prediction for both the singly staggered and doubly staggered foam models are shown for comparison. The experimental data lie between the two model predictions. A reason for this may be that the combination of lumps of solid material at the intersection of struts as well as the closed faces present in the PORVAIR foams result in stagnant zones that are in total less than one third of the total fluid volume of the porous medium. The only values that σ takes on is 0, 1 and 2, representing the number of duct sections (three in total) of the foam RUC model that are stagnant. The RUC model can therefore only distinguish between stagnant fluid volumes making up one third or two thirds of the total fluid domain. For the PORVAIR foams the model of Crosnier et al. (2006) corresponds well with the experimental data.
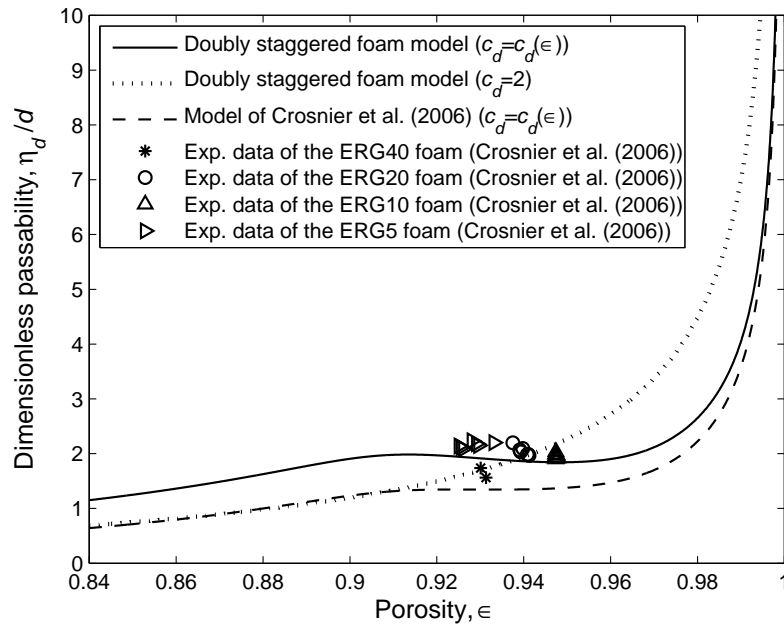
Figure 6.12: Passability as a function of porosity for the ERG foams of Crosnier et al. (2006).
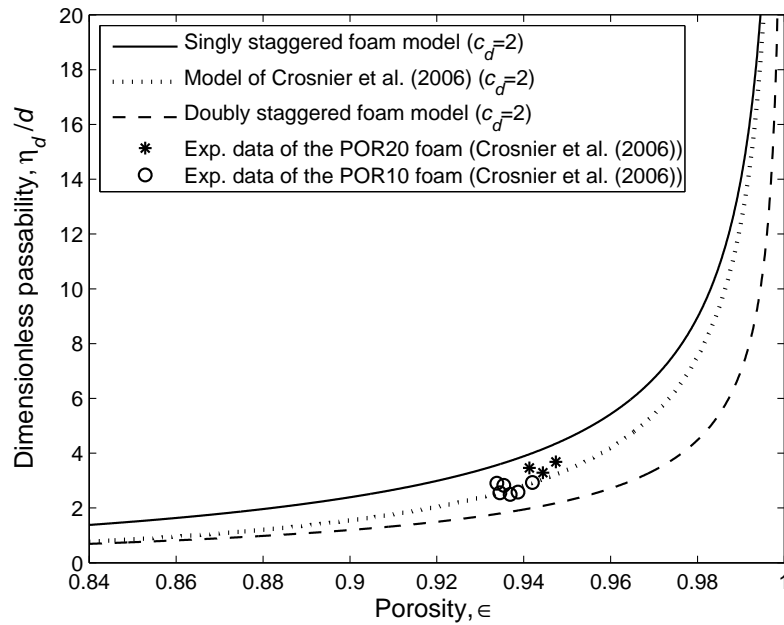
Figure 6.13: Passability as a function of porosity for the PORVAIR foams of Crosnier et al. (2006).

6.10 Summary

The effect of developing flow on the pressure drop was illustrated through the adaptation of the long duct foam RUC model to obtain the short duct model. This was done through the incorporation of the apparent friction factor into the pressure drop. A duct or pore was approximated as either rectangular or consisting of double pairs of parallel plates. The two representations yielded similar results for the pressure drop prediction. Since, throughout the RUC modelling theory, flow between parallel plates is assumed, the double pairs of parallel plates model was adopted and used in the remainder of the chapter.

The permeability prediction for developing flow is a function of the Reynolds number. The short duct foam RUC model thus reduces back to the long duct model for a Reynolds number of zero. Since, for flow to occur, the Reynolds number is greater than zero, developing flow will play a role. For all the experimental pressure drop data considered, the critical Reynolds number was in the vicinity of 2, which also supports the fact that developing flow will already have an effect at very low Reynolds numbers. It was illustrated that the over-prediction in permeability observed by previous authors, who have utilized the RUC model, may be attributed to the effect of developing flow, in addition to possibly other effects such as the lump of solid material at the intersection of fibres and closed faces.

It was shown that the significant over-prediction by factors as much as 2.7 observed by Bhattacharya et al. (2002), when applying the model of Du Plessis et al. (1994) to their experimental data, can be diminished by accounting for the effect of developing flow in the model together with the use of the three-dimensional pore diameter, d_p. The short duct foam RUC model reduced the over-prediction in dimensionless permeability of the model of Du Plessis (1994) by 85%, measured at the average foam porosity and the average critical Reynolds number. The effect of solid lumps is implicitly accounted for by the presence of stagnant fluid volumes and by the average solid geometry in the RUC model and hence by the pore-scale linear dimension used in the model. It is therefore not necessary to introduce another geometrical model (i.e. the dodecahedron model) to account for the presence of solid lumps at the intersection of struts.

A method was proposed in which the variation in the cross-sectional shape of the fibres can be incorporated into the foam RUC model. This serves as an improvement to the constant value previously used by authors who have utilized the foam RUC model. A unified semi-empirical equation was proposed for the interstitial form drag coefficient to be used in the RUC model in order to improve on the different empirical equations proposed by Bhattacharya et al. (2002).

The over-prediction observed by Bhattacharya et al. (2002) in the inertial coefficient, when applying the long duct model of Du Plessis et al. (1994), was diminished through the incorporation of the porosity dependent interstitial form drag coefficient and the effect of developing flow. The porosity dependent interstitial form drag coefficient also improves the model prediction of Crosnier et al. (2006) for the passability of the ERG foams, of which the cross-sectional shape varies.

Boomsma & Poulikakos (2002) report that the values for the permeability and inertial coefficient depend on the flow velocity range over which these parameters are calculated. The use of different flow velocity ranges will yield different values for the permeability and inertial coefficient. They stress the fact that when values for the permeability and inertial coefficient are reported then the velocity range over which the values were calculated should also be specified. The author of this dissertation agrees to this. If the values of the superficial velocity and/or Reynolds number values are provided, then the effect of developing flow can be determined without the use of the average critical Reynolds number.

Chapter 7

Geometrically adapted foam RUC model

In this chapter the foam RUC model is adapted to determine the effect of compression of a fibrous porous medium on permeability. A complicating condition caused by the compression is that it yields an anisotropic structure. The transversely isotropic foam RUC model is therefore adapted geometrically to an anisotropic structure by shortening the strut in the direction of compression. The anisotropic foam RUC model is used to determine the effect of compression on permeability. In the first case study, the anisotropic foam RUC model is applied to a non-woven glass fibre filter, and in the second case study the model is applied to soft compressible polyester material typically found in pillows. In both case studies different stages of compression of the porous medium are considered. The effect of compression on the micro-structural parameters is determined, because it directly affects the permeability and pressure drop predictions. In the second case study the anisotropic foam RUC model is adapted to account for the combined effects of compression and developing flow on permeability.

7.1   Introduction

The thermal and mechanical properties of metallic foams (typically of porosities larger than 0.9) can be enhanced considerably by decreasing its porosity to within the range $0.7 < \epsilon < 0.8$. Compression of metallic foams increases the foams's structural rigidity as well as the dynamic specific surface (Dukhan & Patel (2008)). This leads to improved thermal performance of heat exchanger devices in which metallic foams find application (Gerbaux et al. (2009)). The thermal efficiency of these devices depends on the hydraulic parameters, such as the pressure drop, permeability and inertial coefficient (Antohe et al. (1997)).

Dukhan (2006) performed experiments to determine the permeability and inertial coefficients of compressed aluminium foams. He states that the existing geometrical foam

196

models of Du Plessis et al. (1994), Bhattacharya et al. (2002) and Fourie & Du Plessis (2002) are all based on the assumption of uniform cell size and therefore they are not applicable to compressed foams since the cells are deformed after compression. He then concludes that there has to be relied on experimental correlations to investigate the influence of compression on permeability.

Other authors who also performed experiments on the compression of metallic foams (e.g. Antohe et al. (1997), Boomsma & Poulikakos (2002), Gerbaux et al. (2009)) also reverted to direct curve fitting of experimental results, due to the lack of geometrical foam models in the literature that can account for the effect of compression on permeability and inertial coefficients. The aim of this chapter is to show that the anisotropic foam RUC model can serve as a first attempt to fulfil this need in the literature.

7.2 Anisotropic foam RUC model

The foam RUC model is adapted geometrically from the transversely isotropic structure, as presented in Figure 7.1(a), to the anisotropic structure, shown in Figure 7.1(b). This is done by shortening the strut in the direction of compression, which for the two cases to be studied, corresponds to the streamwise direction. The anisotropic structure is introduced in order to predict physical flow phenomena in fibrous porous media that have been subjected to one-dimensional compression, i.e. compression only in the streamwise direction.

(a) Transversely isotropic model　　(b) Anisotropic model
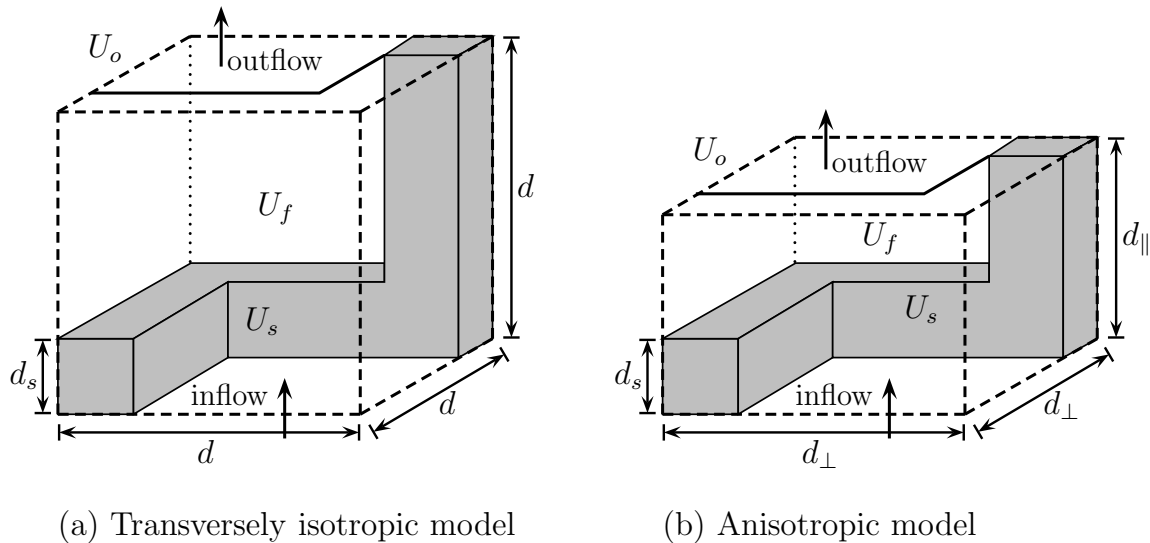
Figure 7.1: High porosity (a) transversely isotropic and (b) anisotropic foam RUC model.

The two transverse struts, i.e. those perpendicular to the streamwise direction are of equal length $d_\perp$, as indicated in Figure 7.1(b). The strut in the streamwise direction is

197

shortened to $d_\parallel (< d_\perp)$ in order to resemble the compressed nature of the fibrous porous medium. The latter condition yields the anisotropy effect. The dimensions of the RUC in the plane perpendicular to the streamwise direction are therefore $d_\perp \times d_\perp$, whereas in the streamwise direction the RUC extends over a distance $d_\parallel$. The dimension $d_\parallel$ will either be referred to as the RUC thickness in the streamwise direction or as the short strut length of the RUC in the streamwise direction. It will be implicitly assumed that $d_\parallel \geq 2\,d_s$, so that maximum compression excludes deformation of the struts from their original shape. A complication resulting from the compression in the streamwise direction is that *both* RUC dimensions change, i.e. both $d_\perp$ and $d_\parallel$ become smaller under compression. This has to be accounted for in the mathematical modelling procedure.

The total volume of the RUC, U_o, the total solid volume, U_s, and the total fluid volume, U_f, can be expressed in terms of the linear dimensions of the anisotropic RUC model, as follows:

$$U_o = d_\perp^2 d_\parallel \,, \tag{7.1}$$

$$U_s = d_s^2 \left(2\,d_\perp - 2\,d_s + d_\parallel \right) \,, \tag{7.2}$$

$$U_f = d_\perp^2 d_\parallel - d_s^2 \left(2\,d_\perp - 2\,d_s + d_\parallel \right) \,. \tag{7.3}$$

The porosity may then be expressed as

$$\epsilon = \frac{U_f}{U_o} = \frac{d_\perp^2 d_\parallel - d_s^2 \left(2\,d_\perp - 2\,d_s + d_\parallel \right)}{d_\perp^2 d_\parallel} \,. \tag{7.4}$$

Equation (7.4) will be used to obtain the relationship between $d_\parallel$ and $d_\perp$.

In the first case study, presented in the next section, the anisotropic RUC model will be applied to the compression of a non-woven glass fibre filter.

7.3 Case study 1: Non-woven glass fibre filter

Experiments were performed on airflow through a non-woven glass fibre filter consisting of a bed of uniform fibres of length 900 µm and fibre diameter of 2.7 µm each. (Figure 2.3, presented in Section 2.2 (p 8), is a picture of the micro-structure of such a filter.) Each filter consists of more or less randomly distributed glass fibres in the plane of the filter, as shown in Figure 7.2 (p 199). In the direction perpendicular to the plane of the filter the structure is anisotropic.

Different stages of compression of the filter were studied by Le Coq (2008). The filter is mechanically compressed, after which a pressure drop, Δp, is applied over the porous material to obtain airflow through it. The permeability and tortuosity of airflow through the filter were measured to investigate the effect of compression on these parameters.
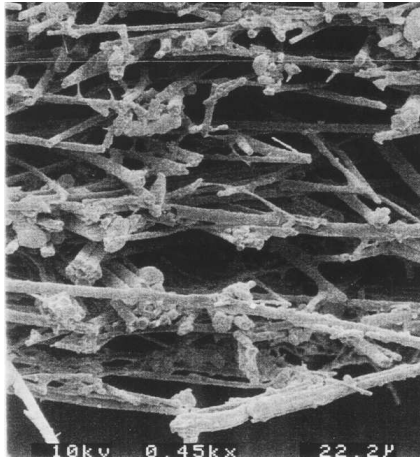
Figure 7.2: Vertical section of the porous micro-structure of a non-woven glass fibre filter (Picture supplied by Prof. L. Le Coq).

7.3.1   Experimental results of Le Coq (2008)

Since permeability is a property of the porous micro-structure and independent of the fluid properties, the influence of the compression on the micro-structural parameters needs to be determined. The method of mercury porosimetry (Section 2.3, p 10) was used by Le Coq (2008) to determine experimentally the modification of the micro-structural parame-ters (e.g. porosity and pore size) under compression. Three reproducibility experiments were performed for each porous sample. With mercury porosimetry an accurate characterization of the micro-structural parameters can be obtained from which the hydrodynamic permeability, k_{exp}, can be determined. By measuring the volume of mercury penetrating the porous medium at different pressures, pore sizes (or mean hydraulic pore diameters, D_h) at various porosity values are obtained. The ϵ and D_h-values were obtained within an experimental error range of 2 and 15%, respectively (Le Coq (2010)).

The values of the micro-structural parameters obtained from the mercury porosimetry measurements are given in Table 7.1 (p 200) for four stages of compression. The Δp-values given in Table 7.1 are the pressure drop values for airflow through the filter. The different stages of compression are characterized by the filter thickness relative to its uncompressed state, denoted by e_{exp}. (This definition differs from the notation used by Le Coq (2008), who worked with the compression ratio, $1 - e_{exp}$.) The values of e_{exp} were measured by Le Coq (2008) within an experimental error of 5% (Le Coq (2010)).

Two methods were used by Le Coq (2008) to calculate the permeability for the different stages of compression, i.e. either from the values obtained for the micro-structural parameters from mercury porosimetry or from the method of permeametry (Section 2.3).

Following the method based on mercury porosimetry measurements, the permeability is

Table 7.1: Experimental results for airflow through a non-woven glass fibre filter with fibre diameter 2.7 µm and fibre lengths of 900 µm (Le Coq (2008)).

| Δp [kPa] | e_{exp} | Mercury porosimetry | | | | Permeameter |
		ϵ	D_h [µm]	k_{exp} [µm^2]	T	k_{exp} [µm^2]
0	1	0.94	28	8.2	2.8	10
14	0.85	0.92	17	2.0	4.1	2.1
27	0.75	0.89	16.5	1.4	5.5	–
80	0.55	0.86	16.0	0.17	41.6	–

calculated from the following relation (Le Coq (2008)):

$$k_{exp} = \frac{\epsilon \, (D_h/4)^2}{2\,T} \, . \tag{7.5}$$

In equation (7.5) T denotes a kinematical tortuosity (Section 2.8.4, p 19) since it can be expressed as a function of permeability. The kinematical tortuosity values for the four different stages of compression, as presented in Table 7.1, were measured within an estimated experimental error range of 20% (Le Coq (2010)). In equation (7.5) the mean hydraulic pore diameter is defined by equation (2.9) (Section 2.8.5, p 20).

The permeability, obtained from the method of permeametry, was determined from the following modification of Darcy's law, i.e.

$$k_{exp} = \frac{t_{\parallel} \, \mu \, q_{exp}}{\Delta p} \, , \tag{7.6}$$

where $t_{\parallel}$ denotes the sample thickness in the streamwise direction, μ is the dynamic viscosity of the traversing fluid (in this case air) and q_{exp} is the experimentally determined magnitude of the superficial velocity.

7.3.2 Application of the anisotropic foam RUC model

The uniform width of the struts of the foam RUC model, d_s, is set equal to the fibre diameter, i.e. $d_s = 2.7$ µm. Although the fibre diameter is known, it is not evident what the dimensions $d_{\parallel}$ and $d_{\perp}$ of the foam RUC model should be. In order to apply the model, more information on the micro-structure is needed. The information can be inferred from the experimental mean hydraulic pore diameter data.
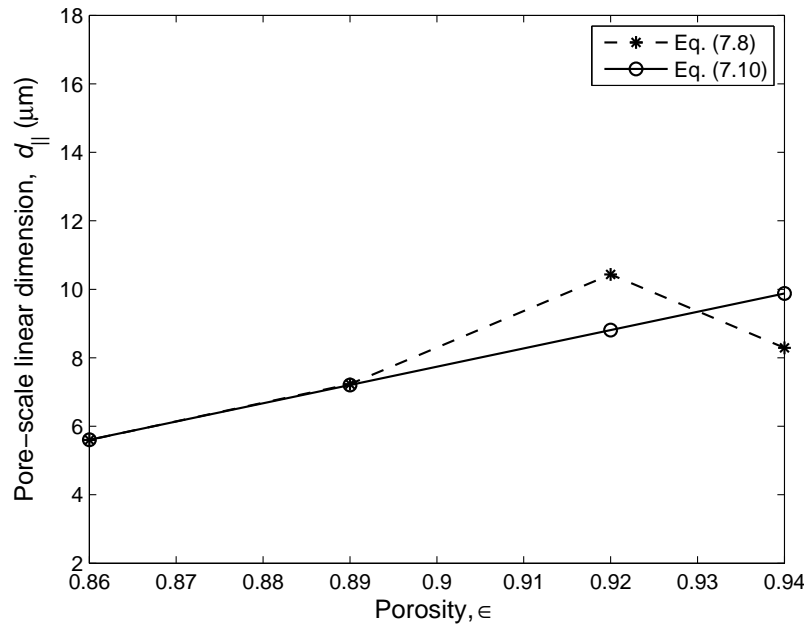
Figure 7.3: Model prediction for the short strut length in the streamwise direction.

Calculation of micro-structural parameters

In RUC notation the mean hydraulic pore diameter, D_h, with respect to the streamwise direction, is $d_\perp - d_s$. Whence

$$d_\perp = (d_\perp - d_s) + d_s = D_h + d_s . \tag{7.7}$$

From equations (7.4) and (7.7) it follows that

$$d_\parallel = \frac{2\, d_s^2\, D_h}{(D_h + d_s)^2\, (1 - \epsilon) - d_s^2} . \tag{7.8}$$

Equation (7.8) represents the RUC thickness in the streamwise direction in any of the four stages of compression because data for D_h is provided for the four different stages of compression. Equation (7.8) is presented graphically in Figure 7.3. The decrease in the value of $d_\parallel$ from $\epsilon = 0.92$ to 0.94 is a result of the experimental data.

From the experimental data given in Table 7.1 (p 200) for the filter thickness relative to its uncompressed state, e_{exp}, and the porosity, ϵ, the following relation is obtained from a linear regression of the data points:

$$e = 5.34\,\epsilon - 4.03 . \tag{7.9}$$

The R^2 value for the linear regression provided by equation (7.9) is 0.98. An alternative

201

Table 7.2: Micro-structural parameters of the compressed non-woven fibre filter predicted by the anisotropic foam RUC model.

e_{exp}	ϵ	$d_{\parallel}$ [µm] Eq. (7.10)	$d_{\perp}$ [µm] Eq. (7.12)	Pore size, D_h [µm] Exp.	RUC model $d_{\perp} - d_s$
1	0.94	10.0	26.4	28	23.7
0.85	0.92	8.9	22.1	17	19.4
0.75	0.89	7.2	19.3	16.5	16.6
0.55	0.86	5.5	19.0	16	16.3

expression for the RUC thickness in the streamwise direction can then be proposed as:

$$d_{\parallel} = d_{\parallel_o}\, e = d_{\parallel_o}\, (5.34\,\epsilon - 4.03) \ , \tag{7.10}$$

where $d_{\parallel_o}$ is the short strut length in the uncompressed state. By using equation (7.8) for $d_{\parallel}$ in the following relation:

$$d_{\parallel_o} = \frac{d_{\parallel}}{e_{exp}} \ , \tag{7.11}$$

values for $d_{\parallel_o}$ are obtained for the four different states of compression. The latter values yield an average value of $d_{\parallel_o} = 10.0\,\mu$m, which is used as the streamwise dimension of the RUC in the uncompressed state. The values of $d_{\parallel}$ for the different states of compression, predicted by equation (7.10), are given in Table 7.2 and presented graphically in Figure 7.3 (p 201). The RUC thickness in the streamwise direction, provided by equation (7.10), decreases with a decrease in porosity over the entire porosity range, which, from a physical point of view, yields a desired result. Knowing $d_{\parallel}$, the transverse RUC dimension, $d_{\perp}$, can be obtained from equation (7.4), yielding

$$d_{\perp} = \frac{d_s \left(d_s + \sqrt{d_s^2 + (1-\epsilon)\,d_{\parallel}\,(d_{\parallel} - 2\,d_s)}\right)}{(1-\epsilon)\,d_{\parallel}} \ . \tag{7.12}$$

The values of $d_{\perp}$, predicted by equation (7.12) for the different states of compression, are also given in Table 7.2.

Predictions for the pore-size, or mean hydraulic pore diameter, is given by $d_{\perp} - d_s$. The values of $d_{\perp} - d_s$ for the four states of compression, are presented in Table 7.2. From Table 7.2 it is evident that the assumption of $d_{\parallel} \geq 2\,d_s$ is adhered to, i.e. for the maximum compression of $e_{exp} = 0.55$ considered, $d_{\parallel} = 5.5$µm> 5.4µm $(2 \times 2.7$µm$)$. Although this restriction is placed on the model, the actual struts may deform under compression,
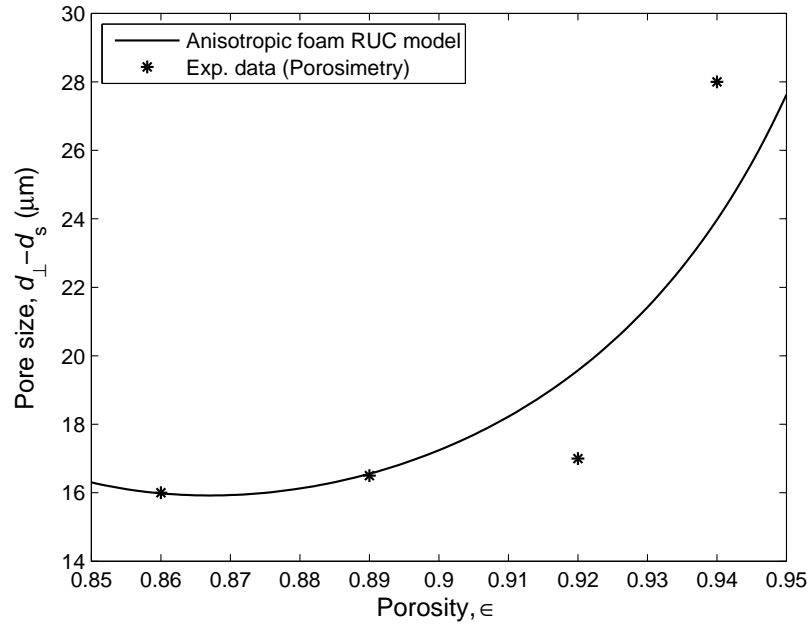
Figure 7.4: Model prediction for the pore size (or mean hydraulic pore diameter).

depending on the type of material under compression as well as the compression ration. In this case glass fibres were used which are unlikely to deform. Figure 7.4 shows the pore size predictions as a function of porosity together with the experimental mean hydraulic pore diameter values obtained from mercury porosimetry.

The upward curvature of the model prediction in Figure 7.4 at porosities lower than about 0.87 is due to the quadratic dependence of $d_\perp$ on ϵ (i.e. resulting from equation (7.4)), which is a direct result of the rectangular model geometry.

Permeability prediction

The streamwise direction is chosen to be parallel to the direction of compression, i.e. normal to the plane of the filter. From mass conservation the following relation between the magnitudes of the streamwise average channel velocity and the superficial velocity is deduced:

$$w_\parallel \;=\; \frac{q\,\psi}{\epsilon} \;=\; \frac{q\,d_\perp^2}{(d_\perp - d_s)^2} \;, \tag{7.13}$$

where the geometric factor ψ (Section 3.11, p 47) is given by

$$\psi \;=\; \frac{\epsilon\,d_\perp^2}{(d_\perp - d_s)^2} \;. \tag{7.14}$$

The wall shear stress for plane-Poiseuille flow in the streamwise channel can be expressed

as

$$\tau_{w_\parallel} = \frac{6\,\mu\,w_\parallel}{(d_\perp - d_s)} \, , \tag{7.15}$$

and for the two transverse channels

$$\tau_{w_{\perp_1}} = \frac{6\,\mu\,w_\perp}{(d_\parallel - d_s)} \qquad \text{and} \qquad \tau_{w_{\perp_2}} = \frac{6\,\mu\,w_\perp}{(d_\perp - d_s)} \, . \tag{7.16}$$

The coefficient β (Section 3.8, p 45) may be expressed as

$$\beta = \frac{w_\perp}{w_\parallel} = \frac{A_{p_\parallel}}{A_{p_\perp}} = \frac{d_\perp - d_s}{d_\parallel - d_s} \, . \tag{7.17}$$

The parameters $A_{p_\parallel}$ and $A_{p_\perp}$ denote the streamwise and transverse cross-sectional flow areas, respectively. For the transversely isotropic foam RUC model, $\beta = 1$, since $d_\perp = d_\parallel$. For the anisotropic foam model, it follows from equation (7.17) that $\beta > 1$, since $d_\perp > d_\parallel$. As a result $A_{p_\parallel} > A_{p_\perp}$, leading to $w_\perp > w_\parallel$.

The total pressure drop over the RUC, Δp, in the limit of low Reynolds number flow may be expressed as (Section 4.4.2, p 91)

$$\Delta p = \frac{S_\parallel \tau_{w_\parallel}}{A_{p_\parallel}} + \frac{\xi\, S_\perp \tau_{w_\perp}}{A_{p_\parallel}} \, . \tag{7.18}$$

From equations (7.13) and (7.15) to (7.17), it follows that

$$\Delta p = \frac{24\,d_s\,d_\perp^2\,\mu\,q}{(d_\perp - d_s)^2} \left[\frac{1}{A_{p_\parallel}} + \frac{\xi\,(d_\perp - d_s)}{A_{p_\perp}(d_\parallel - d_s)} + \frac{\xi\,(d_\parallel - d_s)}{A_{p_\perp}(d_\perp - d_s)} \right] \, . \tag{7.19}$$

Since $A_{p_\parallel} = (d_\perp - d_s)^2$, $A_{p_\perp} = (d_\perp - d_s)(d_\parallel - d_s)$, $\xi = 1$ for the foam RUC model (Section 3.15.6, p 63) and the pressure drop over the streamwise extent, $d_\parallel$, of the RUC is assumed to be the same as the pressure gradient over the filter, it follows immediately that

$$\frac{\Delta p}{d_\parallel} = \frac{24\,d_s\,d_\perp^2\,\mu\,q}{d_\parallel\,(d_\perp - d_s)^2} \left[\frac{2}{(d_\perp - d_s)^2} + \frac{1}{(d_\parallel - d_s)^2} \right] \, . \tag{7.20}$$

Consequently, the permeability is given by

$$k = \frac{d_\parallel\,(d_\perp - d_s)^2}{24\,d_s\,d_\perp^2} \left[\frac{2}{(d_\perp - d_s)^2} + \frac{1}{(d_\parallel - d_s)^2} \right]^{-1} \, . \tag{7.21}$$

Incorporated into equation (7.19) is the hydraulic diameter with respect to the streamwise direction, i.e. $d_\perp - d_s$, and the hydraulic diameter with respect to the two transverse

204

Table 7.3: Permeability and tortuosity values predicted by the anisotropic foam RUC model for airflow through a compressed non-woven fibre filter.

e_{exp}	ϵ	Permeability [µm²]		Tortuosity	
		Exp.	RUC model	Exp.	RUC model
1	0.94	8.2/10	5.4	2.8	3.1
0.85	0.92	2.0/2.1	3.3	4.1	3.6
0.75	0.89	1.4	1.4	5.5	5.2
0.55	0.86	0.17	0.50	41.6	13.7

directions, i.e. $d_{\parallel} - d_s$ for one of the two transverse directions and $d_{\perp} - d_s$ for the other. Similarly as was done by Giani et al. (2005a), who also studied compression of metallic foams, and distinguished between the hydraulic diameter in the streamwise and transverse directions, the anisotropic foam RUC model also distinguishes between hydraulic diameters in the latter two flow directions. The experimentally measured hydraulic diameter specified is, however, only the one measured with respect to the streamwise direction. The modelling procedure presented above can thus be simplified accordingly (as was done by Du Plessis et al. (2010)), but since a primary focus of the present study is to generalize the RUC model as far as possible, it is chosen deliberately that the model will not be restricted by the limiting experimental values specified. If the hydraulic diameter values with respect to the two transverse directions can be provided from future experimental measurements, the modelling procedure presented above need not be amended.

Although equations (7.20) and (7.21) are not expressed explicitly in terms of porosity, they are, however, implicit functions of porosity, since $d_{\parallel}$ is a function of porosity (i.e. equation (7.10)) and $d_{\perp}$ is a function of $d_{\parallel}$ (i.e. equation (7.12)). Figure 7.5 (p 206) shows the experimental and predicted permeability as a function of porosity. The permeability values predicted by the anisotropic foam RUC model for the four different states of compression are given in Table 7.3. It shows that the permeability is significantly influenced by compression, since the values change with more than an order of magnitude over the relative small porosity range of 0.08. Boomsma & Poulikakos (2002) also found the effect of compression on the pressure drop of foams to be profound. For one type of foam considered, a 6.1% increase in porosity yielded a 58% increase in permeability and for another type of foam considered an increase in porosity of only 0.8% led to a 21% increase in permeability. As expected, and also found by other authors in the literature (e.g. Antohe et al. (1997), Boomsma & Poulikakos (2002), Gerbaux et al. (2009)), the permeability decreases with an increase in compression.

At the level of no compression (i.e. at $\epsilon = 0.94$), the model prediction deviates significantly from the experimental data. The deviation, is however, less significant if it is noted that the relative percentage difference between the permeability data points obtained from the methods of mercury porosimetry and permeametry is 18%. This is despite the fact
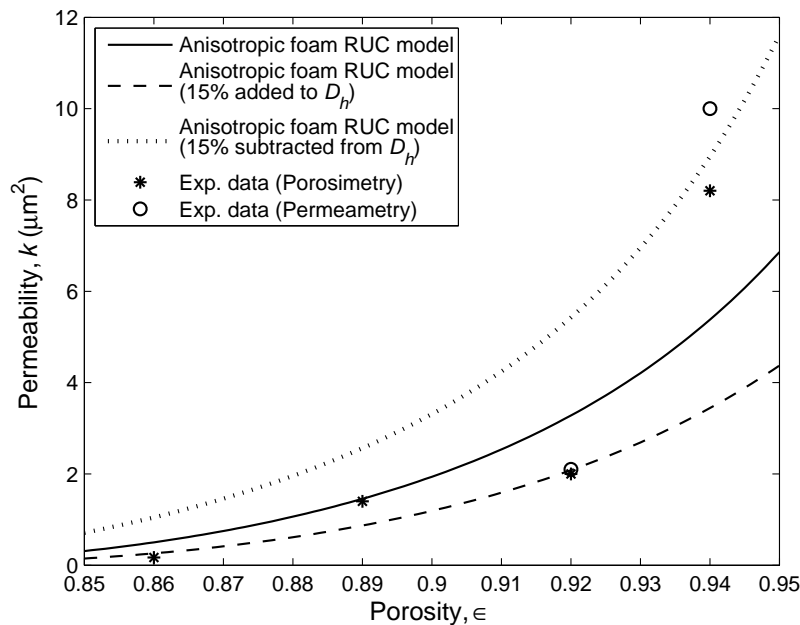
Figure 7.5: Influence of a 15% error in D_h on the permeability of a compressed non-woven fibre filter predicted by the anisotropic foam RUC model.

that for each experimental technique, three reproducibility experiments were performed of which the average is determined and represented in Figures 7.5 to 7.8. From a modelling perspective the deviation may be attributed to the fact that a consolidated foam model is used to represent the fibrous porous medium whereas the actual structure consists of unconsolidated or "loose" fibres.

Table 7.4 (p 207) presents the values for the absolute relative percentage errors for k (calculated with the aid of equation (I.2) in Appendix I, p 320).

The absolute relative percentage errors are rather high. Le Coq (2008) concluded that, although permeability is completely determined by the porous micro-structure, surface roughness does *not* have a significant effect on permeability. Therefore, to investigate other possible causes for the high deviations, the effect of experimental errors in the measured micro-structural parameters and the compression ratio relative to its uncompressed state (i.e. e_{exp}) are investigated in the following subsection.

Sensitivity analysis

A sensitivity analysis is performed on the experimental values of D_h, e_{exp} and ϵ, based on the reported percentage errors of 15%, 5% and 2%, respectively (Le Coq (2010)). The influence of a 15% error in *all* the D_h-values is shown in Figure 7.5. The influence of a 5% error in *all* the e_{exp}-values is shown in Figure 7.6 (p 207) and the influence of a 2%

Table 7.4: Absolute relative percentage error in permeability of a compressed non-woven fibre filter predicted by the anisotropic foam RUC model.

e_{exp}	ϵ	Absolute relative percentage error for k (%)			Absolute relative percentage difference of Condition (ii) relative to Condition (i)
		Calculated from Eq. (7.21)	Calculated from Eq. (7.21) together with		
			Condition (i)	Condition (ii)	
1	0.94	34.4	82.7	86.1	975.4
0.85	0.92	63.9	57.5	341.3	937.5
0.75	0.89	3.9	76.2	208.7	1195.7
0.55	0.86	194.7	50.7	1137.9	2408.5
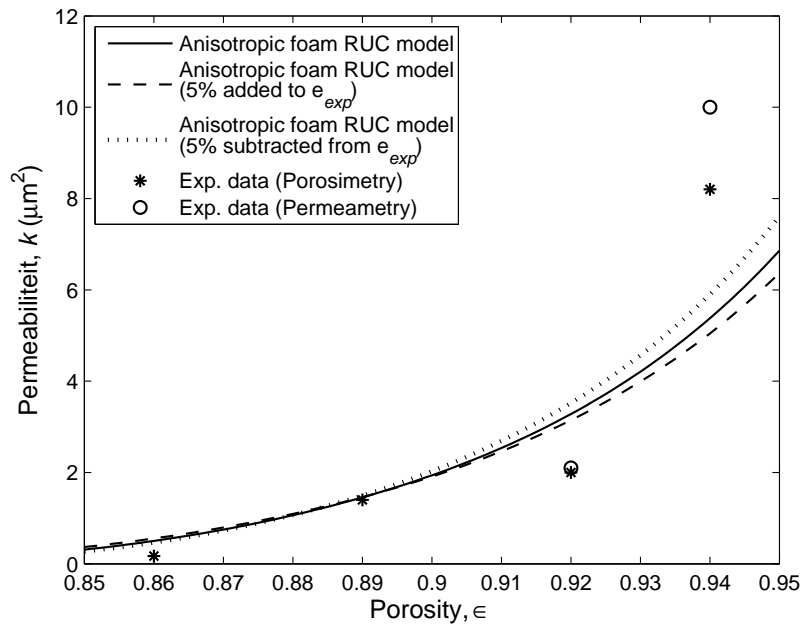
Figure 7.6: Influence of a 5% error in e_{exp} on the permeability of a compressed non-woven fibre filter predicted by the anisotropic foam RUC model.

error in *all* the ϵ-values on permeability is shown in Figure 7.7 (p 208).

Figures 7.5 (p 206) and 7.7 (p 208) show that the influence of a 15% error in D_h and a 2% error in ϵ, respectively, on permeability are of the same order of magnitude, based on the margin of deviation of the predicted error curves relative to the permeability curve (with no errors assumed). Figure 7.6, however, shows that the influence of a 5% error in e_{exp} is far less.
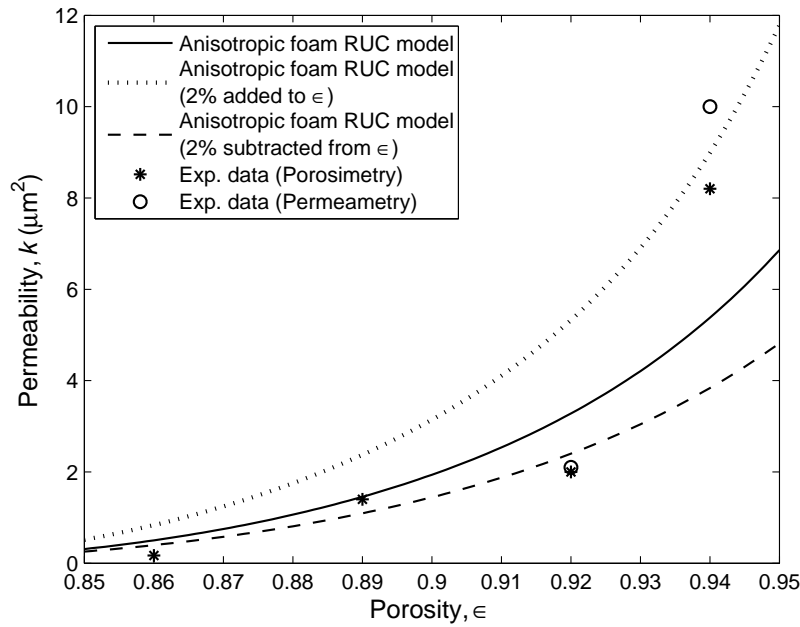
Figure 7.7: Influence of a 2% error in ϵ on the permeability of a compressed non-woven fibre filter predicted by the anisotropic foam RUC model.

Next, the influence of combinations of a 15% error in D_h, a 5% error in e_{exp} and a 2% error in ϵ will be investigated. It was found that the following two combinations lead to the largest deviation in permeability from the predicted permeability curve (with no errors assumed), i.e. :

- **Condition (i)**: 15% added to all the values of D_h; 5% added to all the values of e_{exp} and 2% subtracted from all the values of ϵ

- **Condition (ii)**: 15% subtracted from all the values of D_h; 5% subtracted from all the values of e_{exp} and 2% added to all the values of ϵ

A change in D_h affects the value of $d_{\parallel o}$ (resulting from equations (7.8)) and (7.11)). A change in e_{exp} affects the expression for e (given by equation (7.9)) and, hence, the value of $d_{\parallel o}$. A change in ϵ also affects the expression for e and the value of $d_{\parallel o}$. The influence of the experimental error ranges of Conditions (i) and (ii) on the predicted permeability is shown graphically in Figure 7.8 (p 209). Condition (i) can be regarded as a lower bound for the permeability prediction provided by the anisotropic foam RUC model and Condition (ii) as an upper bound.

The absolute relative percentage error values, based on Conditions (i) and (ii), are presented in Table 7.4 (p 207).

Although the absolute relative percentage error provided by the model prediction for $e_{exp} = 0.55$ in Table 7.4 (i.e. 194.7%) appears to be high, it is still less than the maximum
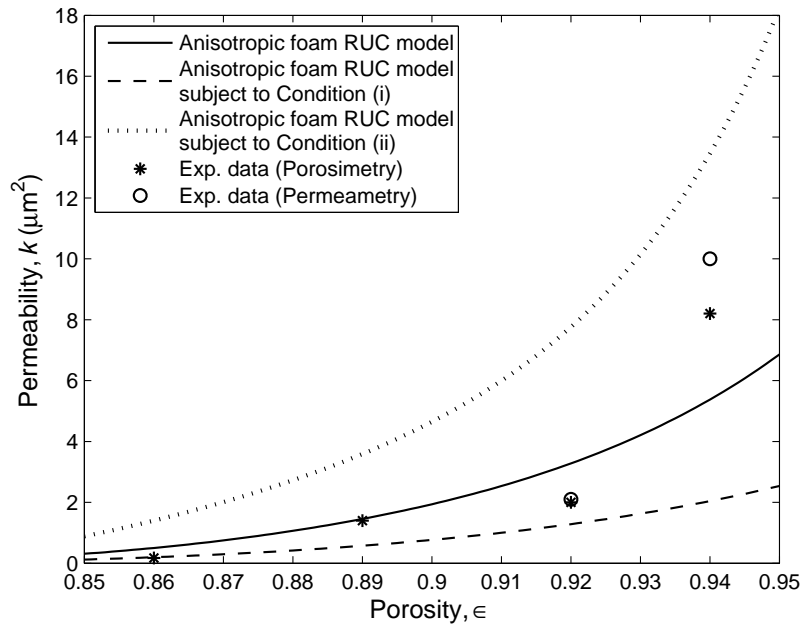
Figure 7.8: Influence of a 15% error in D_h, a 5% error in e_{exp} and a 2% error in ϵ on the permeability predicted by the anisotropic foam RUC model.

absolute relative percentage error of 1137.9% that can be associated with this predicted permeability value according to Condition (ii). The absolute relative percentage errors associated with the other predicted permeability values are also less than the maximum of the corresponding percentage errors provided by either Conditions (i) or (ii).

Values for the absolute relative percentage difference of Condition (ii) measured relative to Condition (i) are also shown in Table 7.4 (p 207). It follows that Conditions (i) and (ii), representing the minimum and maximum permeability predictions, respectively, lead to percentage differences in permeability predictions of more than 900 % and up to about 2400%. Marginal experimental errors, i.e. according to Conditions (i) and (ii), thus have a significant effect on the permeability prediction of the anisotropic foam RUC model. The model is therefore very sensitive to deviations in the measured micro-structural parameters used to predict the permeability.

A graphical representation of the absolute relative percentage error in k is given in Figure 7.9 (p 210). It shows that the absolute relative percentage errors in k associated with the anisotropic foam RUC model (with no experimental errors assumed) are all less than the percentage errors associated with Condition (ii). This provides confidence in the predictive capabilities of the anisotropic foam RUC model.
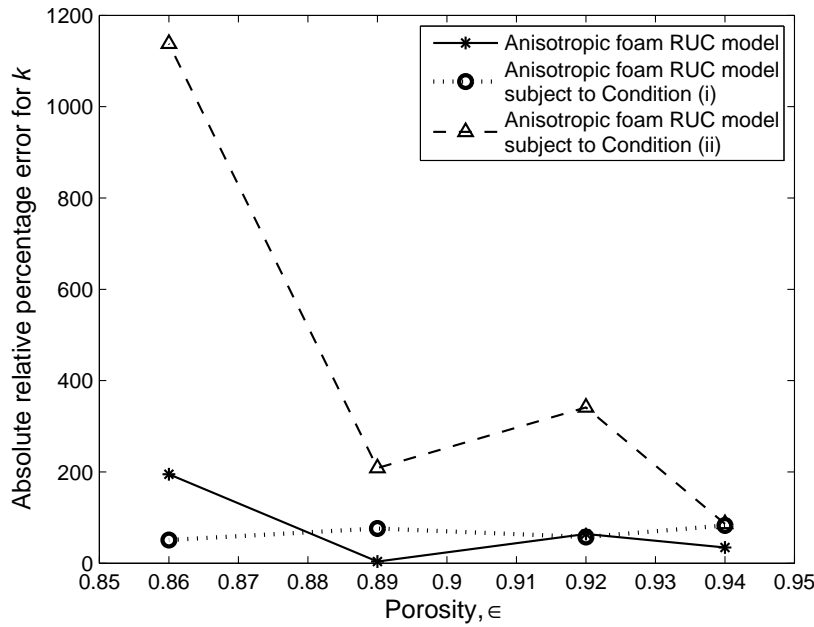
Figure 7.9: Absolute relative percentage error in permeability of a compressed non-woven fibre filter predicted by the anisotropic foam RUC model.

Determining the influence of developing flow and inertial effects

The experimental values for the magnitude of the superficial velocity can be determined from equation (7.6), i.e.

$$q_{exp} = \frac{k_{exp}\,\Delta p}{\text{t}_{\parallel}\,\mu}\;. \tag{7.22}$$

The values for k_{exp} and Δp are given in Table 7.1 (p 200). The values for the sample thickness in the streamwise direction, i.e. $\text{t}_{\parallel}$, for the four different states of compression can be determined as follows:

$$\text{t}_{\parallel} = \text{e}_{\parallel o}\text{e}_{exp}\;, \tag{7.23}$$

where $\text{e}_{\parallel o} = 440\,\mu\text{m}$ is the sample thickness in the uncompressed state. Superficial velocity magnitudes of nanometers per second are obtained. For the Reynolds number, defined for developing flow as (equation (6.3)),

$$Re_{Dh} = \frac{\rho\,w_{\parallel}\,D_h}{\mu} = \frac{\rho\,q_{exp}\,d_{\perp}^2\,D_h}{\mu\,(d_{\perp} - d_s)^2}\;, \tag{7.24}$$

the mean hydraulic diameter, D_h, is set equal to the experimental values provided for D_h. By using the measured values for q_{exp} and D_h, equation (7.24) leads to Reynolds numbers of the order of nanometers. These low Reynolds numbers lead to a negligible effect of
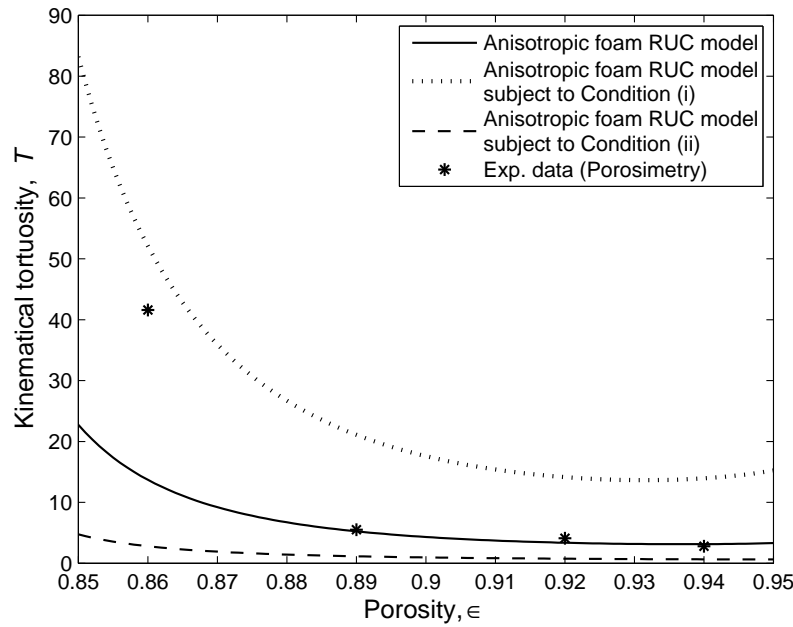
Figure 7.10: Kinematical tortuosity of a compressed non-woven fibre filter predicted by the anisotropic foam RUC model.

developing flow and inertial effects on the streamwise pressure drop (see for example the equations presented in Table 6.2 (p 173) for the short duct models).

Tortuosity prediction

Although the tortuosity plays no explicit role in the RUC model, information about this frequently mentioned parameter may be obtained from the geometric pore-scale model presented. The kinematical tortuosity, T, (Section 2.8.4, p 19) measured with respect to the streamwise direction, can be obtained from equation (7.5) as

$$T = \frac{\epsilon D_h^2}{32\,k} = \frac{\epsilon\,(d_\perp - d_s)^2}{32\,k} \; . \tag{7.25}$$

In equation (7.25) k is given by equation (7.21). In Figure 7.10 the tortuosity predicted by the anisotropic foam RUC model (i.e. equation (7.25)) is compared to the experimental tortuosity data of Le Coq (2008), obtained from mercury porosimetry measurements. Also shown in Figure 7.10 are the tortuosity predictions subject to Conditions (i) and (ii).

The upward curvature of the model prediction for the kinematical tortuosity, represented by the dotted curve in Figure 7.10 at porosities higher than 0.94, is due to the implicit quadratic dependence of $d_\perp$ on ϵ (i.e. resulting from equation (7.4)), which is again a direct result of the rectangular model geometry.

The tortuosity values predicted by the anisotropic foam RUC model for the four experimental porosity values are given in Table 7.3 (p 205). The anisotropic RUC model prediction, without any experimental errors assumed, yields satisfactory agreement with the experimental data for $\epsilon = 0.94, 0.92$ and 0.89. For $\epsilon = 0.86$ the RUC model under-predicts the tortuosity. The latter predicted value, however, still lies within the bounding experimental error ranges indicated for the kinematical tortuosity prediction in Figure 7.10 (p 211).

In the second case study, presented in the next section, the anisotropic RUC model will be applied to the compression of a soft polyester material found in pillows.

7.4 Case study 2: Soft fibrous media

Akaydin et al. (2011) investigated experimentally the effect of compression of soft fibrous porous media on permeability. The compressible soft fibrous material used is polyester pillow material, consisting of fibres with an average diameter of $10\,\mu\text{m}$. Each test sample of soft fibrous material was built up of several layers of randomly distributed fibres. The streamwise direction corresponds to the direction of compression. The permeability of airflow was measured by Akaydin et al. (2011) at seven different stages of compression.

7.4.1 Experimental results of Akaydin et al. (2011)

The values of the experimental measurements are given in Table 7.5 for the seven stages of compression.

Table 7.5: Experimental results for airflow through layers of soft polyester pillow material with average fibre diameter of $10\,\mu\text{m}$ (Akaydin et al. (2011)).

i	$h\,[\text{mm}]$	e_{exp}	ϵ	$k_{exp}\,[10^{-9}\,\text{m}^2]$	$C_f\,[10^4\,\text{m}^{-1}]$	Re_k	$q_{exp}\,[\text{m/s}]$
1	16	0.15	0.9780	0.62	2.58	0.07	0.0419
2	30	0.27	0.9883	1.34	0.24	0.10	0.0412
3	41	0.37	0.9914	2.11	0.19	0.13	0.0428
4	50	0.45	0.9930	2.82	0.16	0.15	0.0428
5	60	0.55	0.9941	3.72	0.21	0.17	0.0423
6	86	0.78	0.9959	6.17	0.15	0.22	0.0426
7	110	1.0	0.9968	9.22	0.08	0.26	0.0412

The different stages of compression are characterized by the sample thickness relative to its uncompressed state, e_{exp}. (This definition differs from the notation used by Akaydin et al. (2011). They worked with the compression ratio, $1 - e_{exp}$, instead of e_{exp}). In Table 7.5 (p 212), i represents the number of the data point and h denotes the sample thickness in the direction of compression. The parameter, C_f, is the coefficient of the pressure gradient term in the Forchheimer flow regime, i.e.

$$-\frac{\mathrm{d}p}{\mathrm{d}x} = \frac{\mu\, q_{exp}}{\epsilon\, k_{exp}} + \frac{C_f}{\epsilon^2}\rho\, q_{exp}^2\;, \qquad (7.26)$$

with the x-direction corresponding to the direction of compression and μ and ρ being the dynamic viscosity and density of air, respectively. The Reynolds number, Re_k, is defined as

$$Re_k = \frac{\rho\, q_{exp}\sqrt{k_{exp}}}{\epsilon\, \mu}\;. \qquad (7.27)$$

An experimental error range of 4% in the k_{exp}-values is reported by Akaydin et al. (2011).

7.4.2 Application of the anisotropic foam RUC model

The width of the struts of the foam RUC model is set equal to the average diameter of the fibres, i.e. $d_s = 10\,\mu\mathrm{m}$. As explained in Section 7.3.2 (p 200), the effect of compression on both $d_\parallel$ and $d_\perp$ has to be determined. Apart from knowing the value of d_s, more information on the micro-structural geometry is needed.

The difficulty, however, in the application investigated by Akaydin et al. (2011) on soft porous media, is that the measured values for the mean hydraulic pore diameter, at the different stages of compression, were not provided. As a result, the short strut length in the uncompressed state, $d_{\parallel_o}$, cannot be determined from the experimental mean hydraulic pore diameter values, as was done in Section 7.3.2 in the application for non-woven fibre filters. Although not being an optimal approach, one has to rely on the predictions for the micro-structural parameters provided by the *isotropic* foam RUC model to determine the value of $d_{\parallel_o}$.

Calculation of micro-structural parameters

Due to the lack of information on the average hydraulic diameter of the actual fibrous micro-structure, the value of the short strut length in the uncompressed state, $d_{\parallel_o}$, is obtained from the relation between the pore-scale linear dimensions provided by the transversely isotropic RUC model (Section 3.15.6, p 63), i.e.

$$d_{\parallel_o} = \frac{2\, d_s}{\psi_o - 1}\;, \qquad (7.28)$$

213

where ψ_o denotes the geometric factor in the uncompressed state, i.e.

$$\psi_o = 2 + 2\cos\left[\frac{4\pi}{3} + \frac{1}{3}\cos^{-1}(2\epsilon_o - 1)\right] . \tag{7.29}$$

In equation (7.29), ϵ_o denotes the porosity of the uncompressed state, i.e. $\epsilon_o = 0.9968$. The latter porosity value yields $d_{\|_o} = 302.8\,\mu\text{m}$. An underlying assumption in the latter procedure of determining the value of $d_{\|_o}$ is that $d_\| = d_\perp$ for $\epsilon_o = 0.9968$, which is not necessarily the case, since even in the uncompressed state it may be that $d_\| < d_\perp$. The value of $d_{\|_o} = 302.8\,\mu\text{m}$ should thus be regarded as a first order approximation.

For this application on soft fibrous porous media, the dependence of the sample thickness relative to its uncompressed state, i.e. e_{exp}, on porosity is not linear. To find an equation that fits the experimental data for e_{exp} as a function of porosity, the power addition technique (Churchill & Usagi (1972)) will once again be applied. It will be assumed that the asymptotes passing through the first two data points in Table 7.5 (p 212) for which $i = 1, 2$ (and through the last two data points for which $i = 6, 7$) takes on the following form:

$$e_i = A\,e^{m\,\epsilon_i} . \tag{7.30}$$

The coefficient values A and m of each of the two asymptotes can be obtained by taking the logarithm of equation (7.30), i.e.

$$\ln e_i = \ln A + m\,\epsilon_i . \tag{7.31}$$

For the asymptote passing through the first two data points , it follows that

$$m = \frac{\ln e_2 - \ln e_1}{\epsilon_2 - \epsilon_1} . \tag{7.32}$$

The corresponding coefficient A can then be obtained from equation (7.31), i.e.

$$A = e^{(\ln e_i - m\,\epsilon_i)} , \tag{7.33}$$

for $i = 1$ and $i = 2$. For the asymptote passing through the first two data points it follows that $m = 57.1$ and $A = 8.66 \times 10^{-26}$, yielding

$$e = 8.66 \times 10^{-26}\,e^{57.1\,\epsilon} . \tag{7.34}$$

Similarly the values of m and A can be obtained for the asymptote passing through the last two data points (for which i=6,7). The results are given by $m = 276.1$ and $A = 3.08 \times 10^{-120}$, yielding

$$e = 3.08 \times 10^{-120}\,e^{276.1\,\epsilon} . \tag{7.35}$$
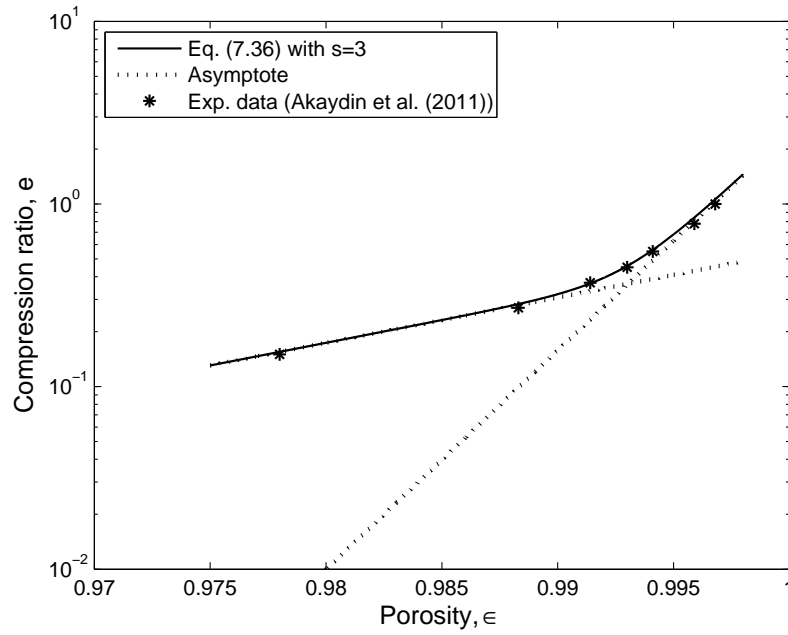
Figure 7.11: Log-linear plot of the sample thickness relative to its uncompressed state as a function of porosity.

Application of the power-addition technique (Churchill & Usagi (1972)) then leads to

$$\mathrm{e} \; = \; \left[(8.66 \times 10^{-26}\, e^{57.1\,\epsilon})^s + (3.08 \times 10^{-120}\, e^{276.1\,\epsilon})^s \right]^{1/s} , \qquad (7.36)$$

where s is the shifting exponent. A logarithmic plot of the asymptotes and equation (7.36) is given in Figure 7.11 for $s = 3$ and the corresponding linear plot is given in Figure 7.12 (p 216).

The RUC thickness in the streamwise direction, $d_{\parallel}$, can be obtained by assuming the same relation as given by equation (7.10), i.e.

$$d_{\parallel} \; = \; d_{\parallel_o} \mathrm{e} \; . \qquad (7.37)$$

The values of $d_{\parallel}$ for the different stages of compression are given in Table 7.6 (p 216). Also for this application the assumption of $d_{\parallel} \geq 2\,d_s$ is adhered to, as can be seen from Table 7.6: for the maximum compression of $\mathrm{e}_{exp} = 0.15$ considered, $d_{\parallel} = 43.4\,\mu\mathrm{m} > 2\,(10\,\mu\mathrm{m})$.

Knowing $d_{\parallel}$, the transverse RUC dimension, $d_{\perp}$, can be obtained from equation (7.12). The latter values are also given in Table 7.6.
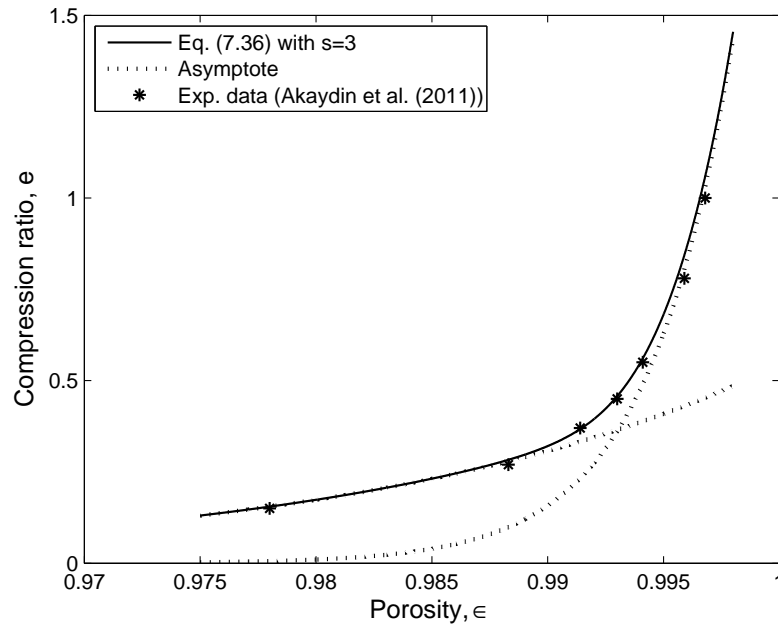
Figure 7.12: Linear plot of the sample thickness relative to its uncompressed state as a function of porosity.

Table 7.6: Micro-structural parameters of the compressible soft fibrous porous medium predicted by the anisotropic foam RUC model.

e_{exp}	ϵ	$d_{\parallel}$ (µm) Eq. (7.37)	$d_{\perp}$ (µm) Eq. (7.12)
0.15	0.9780	43.4	220.4
0.27	0.9883	82.3	235.1
0.37	0.9914	109.6	250.1
0.45	0.9930	139.1	253.6
0.55	0.9941	169.9	257.6
0.78	0.9959	243.9	280.0
1.0	0.9968	294.4	307.1

Permeability prediction

For the present application, the streamwise direction is also chosen to be parallel to the direction of compression. The streamwise pressure gradient in the limit of low Reynolds number flow may be predicted by the use of equation (7.20) and the permeability by
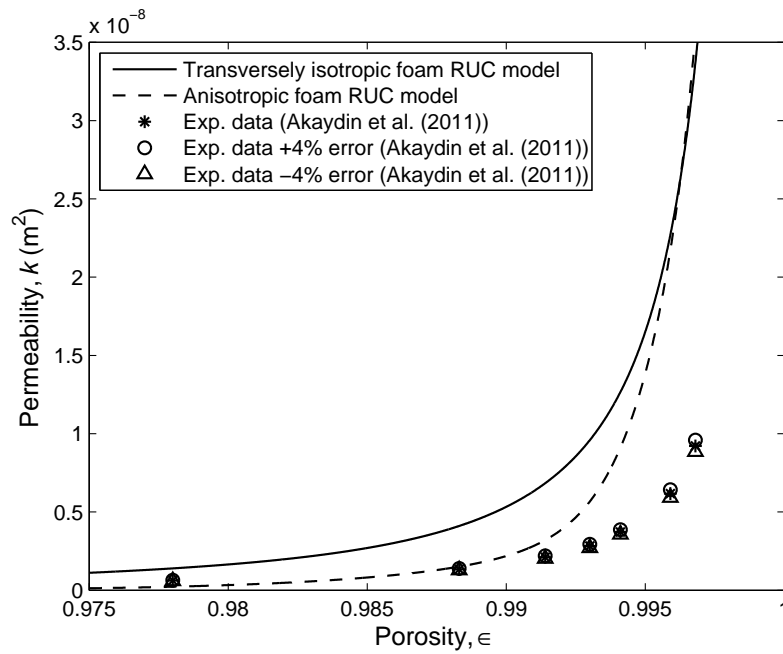
Figure 7.13: Permeability of compressible soft fibrous media predicted by the transversely isotropic and anisotropic foam RUC models.

equation (7.21). Figure 7.13 compares the permeability predicted by the anisotropic foam RUC model with the experimental permeability data of Akaydin et al. (2011). Also shown for comparison is the permeability predicted by the transversely isotropic (doubly staggered) foam RUC model (given in Table 4.4, p 94) and a 4% error in the experimental permeability data. The two model predictions yield the same values for no-compression (i.e. at $\epsilon = 0.9968$), as expected.

Table 7.7 (p 218) gives the experimental and predicted permeability values for the different stages of compression. Also presented in Table 7.7 are the geometrical tortuosity values predicted by the anisotropic foam RUC model. These values were obtained from the following expression for the geometrical tortuosity (Section 3.9, p 45):

$$\chi = 2 + 2\cos\left[\frac{4\pi}{3} + \frac{1}{3}\cos^{-1}(2\epsilon - 1)\right] . \tag{7.38}$$

(Equation (7.38) is the same as the corresponding equation presented for the doubly staggered model in Table 3.5 (p 63).) The values for ϵ in equation (7.38) are determined by the aid of equation (7.4) and the corresponding values for $d_\parallel$ and $d_\perp$ given in Table 7.6 (p 216).

Given the high porosity values under consideration, Akaydin et al. (2011) assumed a value of unity for the geometrical tortuosity. Their assumption is justified by the geometrical tortuosity values, all close to unity, predicted by the anisotropic foam RUC model in Table 7.7.

Table 7.7: Permeability and tortuosity predicted by the transversely isotropic and anisotropic foam RUC models for airflow through compressible soft fibrous porous media.

e_{exp}	ϵ	Exp.	Transversely isotropic RUC model	Anisotropic RUC model	Anisotropic RUC model
			Permeability $[10^{-9}\,\mathrm{m}^2]$		Tortuosity
0.15	0.9780	0.62	1.40	0.23	1.18
0.27	0.9883	1.34	4.10	1.51	1.13
0.37	0.9914	2.11	6.84	3.20	1.11
0.45	0.9930	2.82	9.58	5.66	1.10
0.55	0.9941	3.72	12.65	9.10	1.09
0.78	0.9959	6.17	22.72	21.74	1.07
1.0	0.9968	9.22	33.71	35.57	1.07

From Figure 7.13 (p 217) and Table 7.7 it is evident that both the transversely isotropic and anisotropic foam RUC models over-predict the experimental permeability values. The absolute relative percentage errors (calculated with the aid of equation (I.2) in Appendix I, p 320) are given in Table 7.8 (p 221). The anisotropic model decreases the over-prediction of the transversely isotropic model by an average of 94.0%. The anisotropic model, however, still over-predicts the permeability. This over-prediction tends to increase with an increase in porosity. Possible physical explanations for the over-prediction are investigated in the following subsection.

Determining the influence of inertial effects

The values for q_{exp} are presented in Table 7.5 (p 212). The average of these q_{exp}-values is $q_{exp} = 0.042$ m/s.

The Reynolds number for developing flow is defined by equation (7.24), i.e. in terms of the hydraulic diameter. As already mentioned, the anisotropic foam RUC model distinguishes between the hydraulic diameter in the three principal flow directions. The Reynolds numbers associated with the latter hydraulic diameters, i.e. $D_h = d_\perp - d_s$ and $D_h = d_\parallel - d_s$, are all of the order of 10^{-1}. The inertial forces are therefore negligible in comparison with the viscous forces.

Although the Reynolds numbers are low, they are much higher than the Reynolds numbers of the order of nanometers obtained in the previous case study. Consequently, the effect

of developing flow on permeability is investigated in the following subsection.

Determining the influence of developing flow

In order to account for the effect of developing flow on permeability the streamwise pressure gradient may be expressed as (resulting from equation (6.19), with $R_h = D_h/4$ and $x = d_\parallel$)

$$
\begin{aligned}
\frac{\Delta p}{d_\parallel} &= f_{app}\, \frac{1}{2}\, \rho\, w_\parallel^2\, \frac{4}{D_h} \;+\; f_{app}\, \frac{1}{2}\, \rho\, w_\perp^2\, \frac{4}{D_h} \\
&= \frac{d_\perp^2\, \mu\, q_{exp}}{2\, \chi\, d_\parallel\, (d_\perp - d_s)^2} \left[f_{app}\, Re_{Dh}\, \frac{S_\parallel}{A_{p_\parallel}\, D_h} \;+\; f_{app}\, Re_{Dh}\, \frac{\xi\, S_\perp}{A_{p_\perp}\, D_h} \right], \quad (7.39)
\end{aligned}
$$

by application of equations (2.9), (7.24), (7.17), (7.13) and (3.11). In Table 7.7 (p 218) all the values for χ predicted by the anisotropic foam RUC model are close to unity. It was therefore assumed that $\chi = 1$. (For the doubly staggered array, which is considered here, $\chi = \psi$.) The apparent friction factor-Reynolds number product results from equation (6.18) (with $n = 12$ and $m = 0.0822$), and is given by

$$
f_{app}\, Re_{Dh} = 12\sqrt{1 + \frac{0.0822\, D_h\, Re_{Dh}}{d_s}} \,. \quad (7.40)
$$

The streamwise pressure gradient may consequently be expressed as

$$
\begin{aligned}
\frac{\Delta p}{d_\parallel} &= \frac{d_\perp^2\, \mu\, q_{exp}}{2\, d_\parallel\, (d_\perp - d_s)^2} \left[12\sqrt{1 + \frac{0.0822\, D_h^2\, \rho\, q_{exp}\, d_\perp^2}{d_s\, \mu\, (d_\perp - d_s)^2}}\, \frac{4\, d_s\, (d_\perp - d_s)}{(d_\perp - d_s)^2 (d_\perp - d_s)} \right. \\
&\quad + 12\sqrt{1 + \frac{0.0822\, D_h^2\, \rho\, q_{exp}\, d_\perp^2}{d_s\, \mu\, (d_\perp - d_s)^2}}\, \frac{4\, \xi\, d_s\, (d_\perp - d_s)}{(d_\perp - d_s)(d_\parallel - d_s)(d_\parallel - d_s)} \\
&\quad \left. + 12\sqrt{1 + \frac{0.0822\, D_h^2\, \rho\, q_{exp}\, d_\perp^2}{d_s\, \mu\, (d_\perp - d_s)^2}}\, \frac{4\, \xi\, d_s\, (d_\parallel - d_s)}{(d_\perp - d_s)(d_\parallel - d_s)(d_\perp - d_s)} \right].
\end{aligned}
$$
$$(7.41)$$

Since for the foam RUC model, $\xi = 1$, it follows that the streamwise pressure gradient predicted by the anisotropic short duct foam RUC model reduces to

$$
\begin{aligned}
\frac{\Delta p}{d_\parallel} = = \frac{24\, d_\perp^2\, \mu\, q_{exp}}{d_\parallel\, (d_\perp - d_s)^2} &\left[2\sqrt{1 + \frac{0.0822\, \rho\, q_{exp}\, d_\perp^2}{\mu\, d_s}}\, \frac{d_s}{(d_\perp - d_s)^2} \right. \\
&\quad \left. + \sqrt{1 + \frac{0.0822\, (d_\parallel - d_s)^2\, \rho\, q_{exp}\, d_\perp^2}{\mu\, d_s\, (d_\perp - d_s)^2}}\, \frac{d_s}{(d_\parallel - d_s)^2} \right]. \quad (7.42)
\end{aligned}
$$
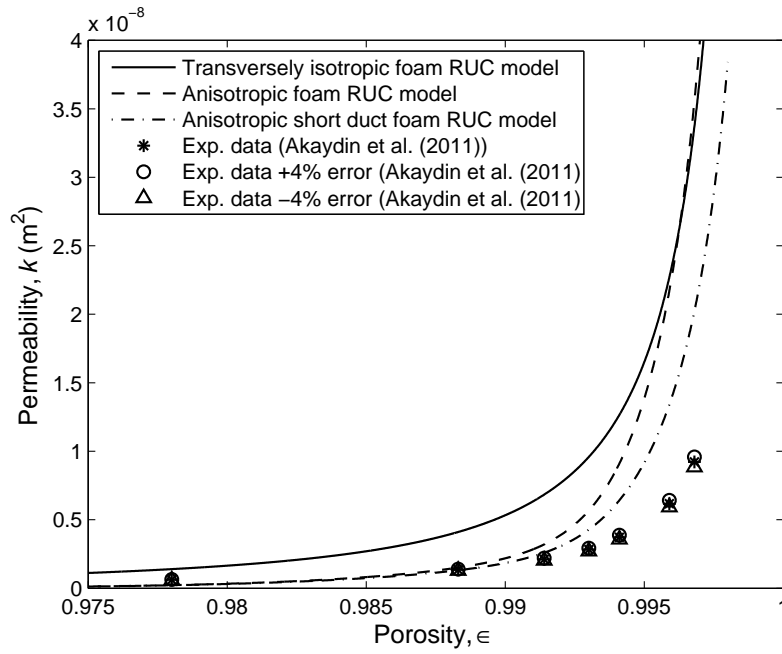
Figure 7.14: Permeability of compressible soft fibrous media predicted by the isotropic, anisotropic and anisotropic short duct foam RUC models.

The permeability predicted by the anisotropic short duct foam RUC model is then given by

$$
k = \frac{d_\| \, (d_\perp - d_s)^2}{24 \, d_\perp^2} \left[2 \sqrt{1 + \frac{0.0822 \, \rho \, q_{exp} \, d_\perp^2}{\mu \, d_s} \frac{d_s}{(d_\perp - d_s)^2}} \right.
$$
$$
\left. + \sqrt{1 + \frac{0.0822 \, (d_\| - d_s)^2 \, \rho \, q_{exp} \, d_\perp^2}{\mu \, d_s \, (d_\perp - d_s)^2} \frac{d_s}{(d_\| - d_s)^2}} \right]^{-1} . \tag{7.43}
$$

The permeability prediction of equation (7.43) is shown graphically in Figure 7.14 as a function of porosity for the different stages of compression. The predicted permeability values and the absolute relative percentage errors (calculated with the aid of equation (I.2) in Appendix I, p 320) are given in Table 7.8 (p 221) from which one can see the significant effect of compression on permeability. For the narrow porosity range of less than 0.02 the permeability changes with more than an order of magnitude.

As mentioned in the application on the glass fibre filter, the equation for the permeability (i.e. equation (7.43)) is an implicit function of porosity, since $d_\|$ is a function of porosity (i.e. equations (7.36) and (7.37)) and $d_\perp$ is a function of $d_\|$ (i.e. equation (7.12)).

The incorporation of the effect of developing flow into the modelling procedure of the anisotropic foam RUC model reduced the over-prediction of the anisotropic model significantly (i.e. with 65.7%, on average). The absolute relative percentage errors, however,

Table 7.8: Permeability and absolute relative percentage error values predicted by the anisotropic short duct foam RUC model for airflow through compressible soft fibrous porous media.

e_{exp}	ϵ	Permeability $[10^{-9}\,\mathrm{m}^2]$		Absolute relative percentage error for k (%)		
		Exp.	Anisotropic short duct	Transversely isotropic	Anisotropic	Anisotropic short duct
0.15	0.9780	0.62	0.22	125.0	63.7	65.1
0.27	0.9883	1.34	1.31	206.2	12.5	2.0
0.37	0.9914	2.11	2.60	224.2	51.8	23.0
0.45	0.9930	2.82	4.28	239.8	100.9	51.6
0.55	0.9941	3.72	6.42	240.1	144.6	72.5
0.78	0.9959	6.17	13.42	268.2	252.3	117.5
1.0	0.9968	9.22	20.24	265.6	285.8	119.5

still range from 2.0% to 119.5%. The resulting discrepancies between the measured and predicted values will be investigated by performing a sensitivity analysis on the predicted $d_{\parallel_o}$-value as well as on the experimental values for e_{exp}, ϵ, d_s and q_{exp}.

Sensitivity analysis

Although estimates for experimental error ranges in e_{exp} are not provided by Akaydin et al. (2011), an experimental error range of 5% was assumed for this parameter (as was done in the previous case study involving non-woven fibre filters). For ϵ an appropriate experimental error range of 0.1% was used (ranges larger than 0.5% lead to values in ϵ larger than unity.). For q_{exp} an experimental error range of 5% was chosen but it was found that this error range has a negligible effect on permeability.

A value for the error range in the predicted value of $d_{\parallel_o}$ had to be proposed. In the previous case study in which the anisotropic foam RUC model was applied to a non-woven fibre filter, experimental values for the mean hydraulic pore diameter were provided. The mean hydraulic pore diameter values were then used to determine the value of $d_{\parallel_o}$. If, however, the transversely isotropic foam RUC model was used to determine the value of $d_{\parallel_o}$, as was done in the present case study, then a 80% over-prediction in the value of $d_{\parallel_o}$ is obtained. This 80% uncertainty includes the assumption of equal $d_{\parallel}$ and $d_{\perp}$-values in the determination of $d_{\parallel_o}$. The values of $d_{\parallel}$ and $d_{\perp}$ need not be equal before compression, as the sample may be anisotropic before compression. The range of 80% will be used to give
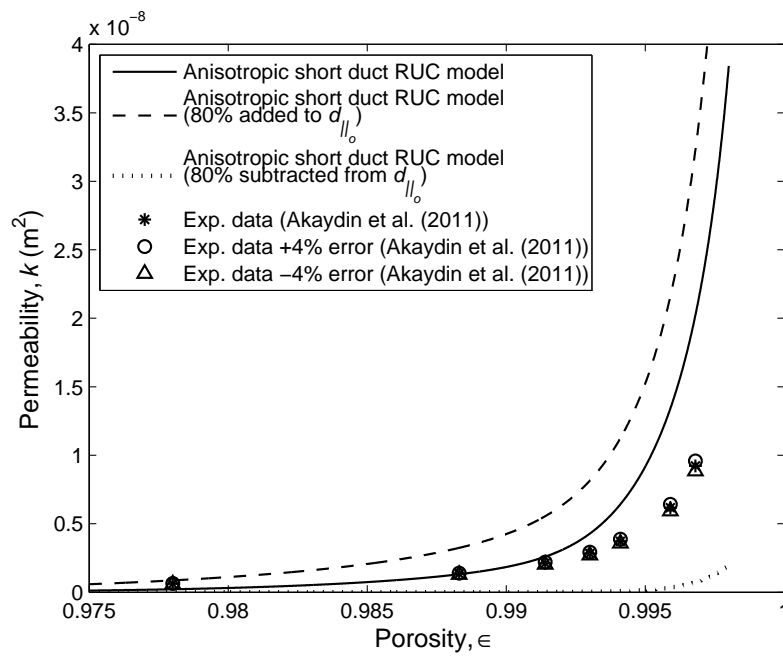
Figure 7.15: Influence of a 80% error in $d_{\|_o}$ on the permeability of compressible soft fibrous media predicted by the anisotropic short duct foam RUC model.

an indication of the order of magnitude in error range that should be considered for the value of $d_{\|_o}$. A sensitivity analysis on a 80% error in the value of $d_{\|_o}$ is shown in Figure 7.15. It shows that the value of $d_{\|_o}$ has a significant effect on the permeability prediction due to the large deviation in permeability predictions provided by an 80% error in $d_{\|_o}$.

The influence of a 0.1% error in *all* the ϵ-values on the permeability prediction is shown in Figure 7.16 (p 223) and the influence of a 5% error in *all* the e_{exp}-values is shown in Figure 7.17 (p 224).

In view of the specific error ranges considered for $d_{\|_o}$, e_{exp}, and ϵ, as shown in Figures 7.15, 7.16 and 7.17, respectively, the proposed error range in $d_{\|_o}$ has the largest effect on permeability. This is to be expected, given the large error range considered for $d_{\|_o}$. However, for the very narrow percentage error range of 0.1% in ϵ, deviations in the permeability prediction from the experimental permeability values ranging between 0.5 and 158% is obtained, which is not insignificant.

The influence of combinations of a 80% error in $d_{\|_o}$, a 0.1% error in ϵ and a 5% error in e_{exp} were investigated. Compared to the previous case study, a similar combination of percentage errors leads to the largest deviation in the permeability prediction, i.e.

- **Condition (i):** 80% added to all the values of $d_{\|_o}$; 5% added to all the values of e_{exp} and 0.1% subtracted from all the values of ϵ
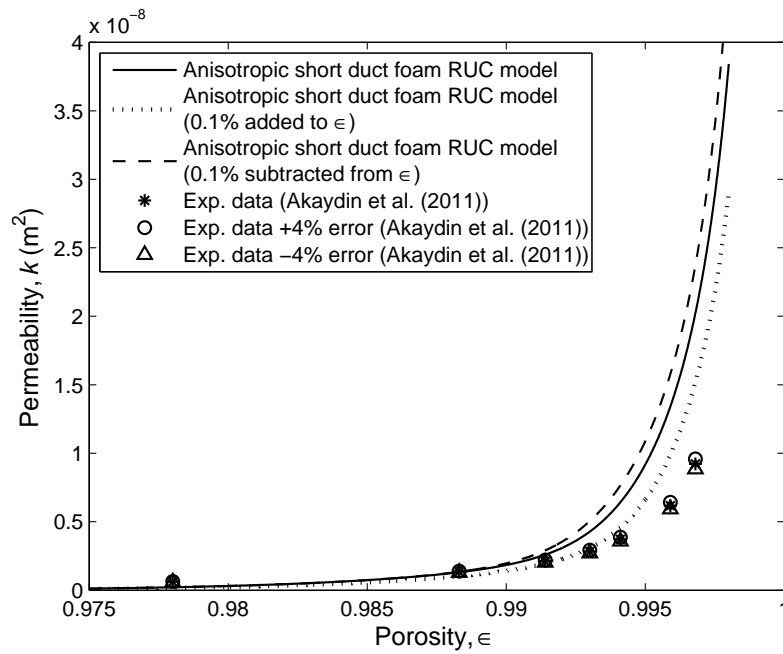
Figure 7.16: Influence of a 0.1% error in ϵ on the permeability of compressible soft fibrous media predicted by the anisotropic short duct foam RUC model.

- **Condition (ii)**: 80% subtracted from all the values of $d_{\|_o}$; 5% subtracted from all the values of e_{exp} and 0.1% added to all the values of ϵ

As in the previous case study, a change in e_{exp} affects the expression for e, given by equation (7.36) and, consequently, the value of $d_{\|_o}$. A change in ϵ also affects the expression for e and the value of $d_{\|_o}$. The influence of the experimental percentage errors of Conditions (i) and (ii) on the predicted permeability is shown in Figure 7.18 (p 224).

Since Figures 7.18 and 7.15 (p 222) show similar trends, it is clear that the experimental error range considered for $d_{\|_o}$ has the largest effect on the permeability prediction of the experimental error ranges of the various parameters considered. Condition (i) can be regarded as an upper bound for the permeability prediction of the anisotropic short duct foam RUC model and Condition (ii) as a lower bound. The permeability prediction provided by the anisotropic short duct foam RUC model is enveloped between the two bounding curves.

Although the absolute relative percentage errors provided by the anisotropic short duct foam RUC model in Table 7.9 (p 225) ranges between 2.0% and 119.5%, all these percentage errors are still less than the maximum of the corresponding percentage errors provided by either Conditions (i) or (ii). Values for the absolute relative percentage difference of Condition (ii) measured relative to Condition (i) are also shown in Table 7.9. These values range between 149.9% and 415.0%, which once again illustrates that the model is sensitive to deviations in the measured micro-structural parameters used to predict the
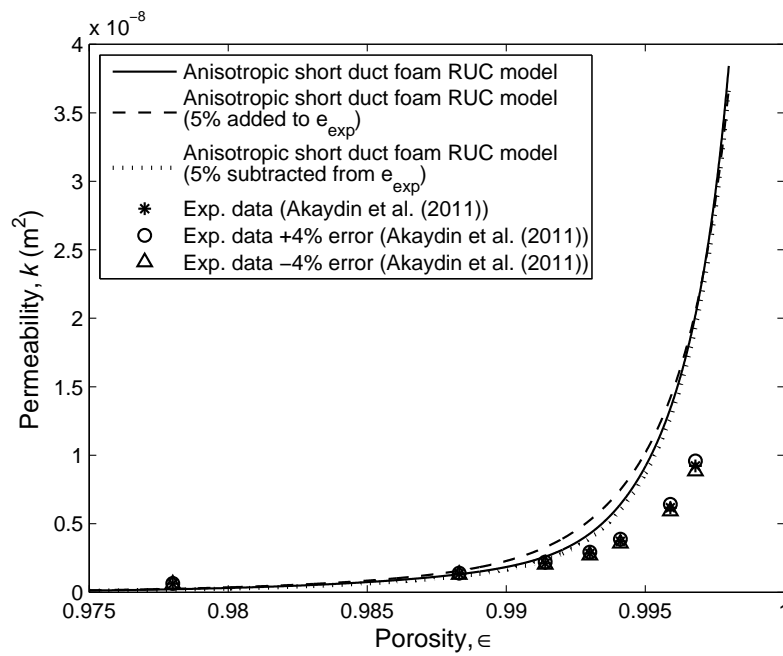
Figure 7.17: Influence of a 5% error in e$_{exp}$ on the permeability of compressible soft fibrous media predicted by the anisotropic short duct foam RUC model.
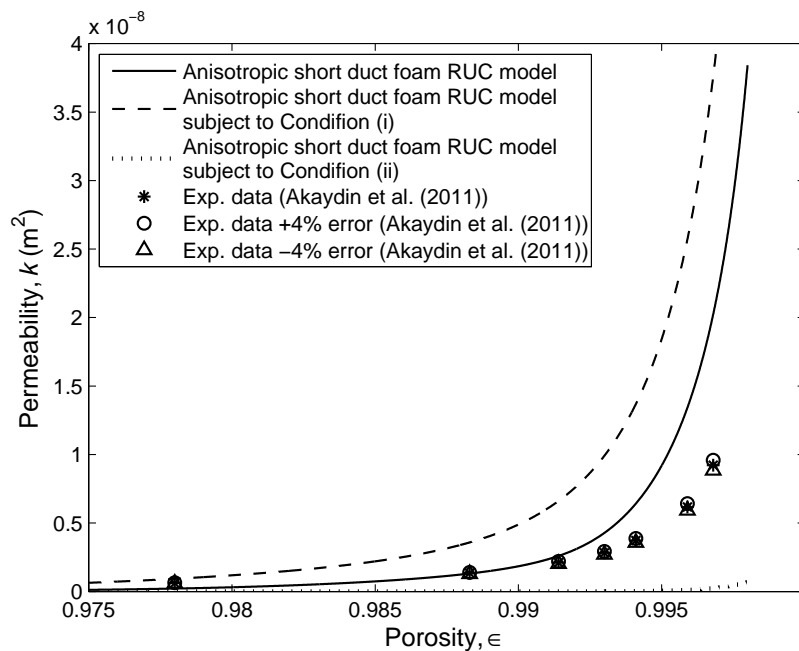
Figure 7.18: Influence of Conditions (i) and (ii) on the permeability of a compressed fibre filter predicted by the anisotropic foam RUC model.

Table 7.9: Absolute relative percentage error in permeability of a compressed non-woven fibre filter predicted by the anisotropic foam RUC model.

e_{exp}	ϵ	Absolute relative percentage error for k (%)			Absolute relative percentage difference of Condition (ii) relative to Condition (i)
		Calculated from Eq. (7.43)	Calculated from Eq. (7.43) together with		
			Condition (i)	Condition (ii)	
0.15	0.9780	65.1	49.9	100.0	149.9
0.27	0.9883	2.0	167.6	99.9	267.5
0.37	0.9914	23.0	213.2	99.7	313.0
0.45	0.9930	51.6	251.3	99.5	350.9
0.55	0.9941	72.5	267.9	99.3	367.2
0.78	0.9959	117.5	316.8	98.2	415.0
1.0	0.9968	119.5	307.8	97.4	405.2

permeability.

Since in the case study involving the application of the anisotropic foam RUC model to a non-woven fibre filter, the isotropic foam RUC model *over-predicted* the value of $d_{\parallel o}$ by 80%, various decreasing percentage errors, starting from 80% up to 5% are incorporated into Condition (ii) and shown in Figure 7.19 (p 226). It illustrates that, although the experimental error range in the value of $d_{\parallel o}$ cannot be justified, since the hydraulic diameter is not specified for this specific case study, the model shows that it has the ability to yield satisfactory predictions. The model prediction takes on a similar trend as the experimental data. It is worth mentioning that in the sensitivity analysis performed in the present study, the specific error range considered for each parameter was assumed to be applicable to *all* the data points. It may happen that some data points were measured with more accuracy than others. Knowing this information may improve the model prediction even more.

From Table 7.9 it is evident that the model predictions for the intermediate compression ratios are more accurate than the model prediction at $e_{exp} = 0.15$ and for $e_{exp} > 0.55$. A possible physical reason for the under-prediction at maximum compression (i.e. for $e_{exp} = 0.15$) may possibly be due to an alteration of the geometric porous micro-structure at this high level of compression. The fibres may possibly re-align themselves yielding less staggering in the streamwise direction. Although the model predicts that the condition of $d_{\parallel} \geq 2\,d_s$ is not violated, it may physically be the case. These secondary effects are not accounted for by the anisotropic short duct foam RUC model. The over-predicted values for $e > 0.55$, i.e. where the porosity approaches unity, may be attributed to the assumption of flow between parallel plates that breaks down at these high porosity values.
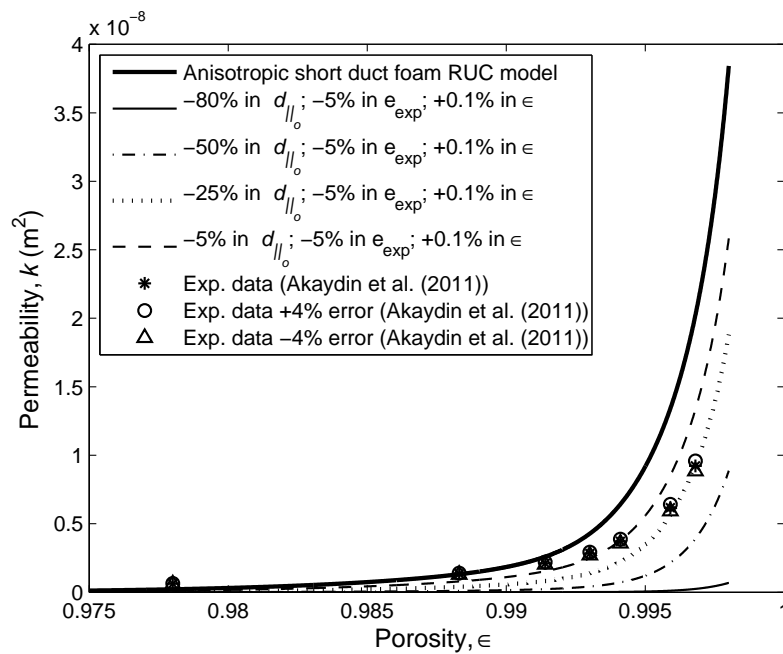
Figure 7.19: Influence of Condition (ii) together with various experimental error ranges in $d_{\|_o}$ on the permeability of a compressed fibre filter predicted by the anisotropic foam RUC model.

To the knowledge of the author of this dissertation, there do not exist analytical models in the literature that have the predictive capabilities as the anisotropic short duct foam RUC model. The model could therefore not be compared to other analytical models from the literature that can resemble the geometric porous micro-structure and account for the effects of compression and developing flow on permeability. Due to the lack of such analytical models, Akaydin et al. (2011) applied the semi-empirical model of Mirbod et al. (2009) to their experimental permeability data. The model of Mirbod et al. (2009) is based on a modification of the semi-empirical Carman-Kozeny equation (Appendix C.2, p 287). The soft fibrous medium is regarded as a random array of cylindrical fibres of uniform diameter. Mirbod et al. (2009) then used the model predictions for the Kozeny constant proposed by the cylindrical cell model of Happel (1959) for flow parallel and perpendicular to the cylinders. To resemble a random array of fibres, the weighted average, proposed by Happel & Brenner (1965), was performed by giving a weight of two to the Kozeny constant for flow perpendicular to the fibres and a weight of unity for parallel flow. Application of the model of Mirbod et al. (2009) to the porosities presented in Tables 7.5 to 7.9 (pp 212-225) will, however, not account for the effect of compression nor developing flow on permeability. It will yield the same permeability values as for an isotropic structure of the same porosity values in the absence of compression. In addition, since the model of Mirbod et al. (2009) is based on an empirical relation it cannot be physically adapted to incorporate these physical phenomena to improve its predictive capabilities.

Pressure gradient prediction

Although the inertial forces are negligible in comparison with the viscous forces, the higher
Reynolds number term will be included in this section into the pressure drop prediction
to show that the anisotropic short duct foam RUC model can be extended to higher
Reynolds numbers.

From Section 4.5 (equation (4.41), p 101) it follows that the pressure gradient in the
steady laminar limit of the inertial flow regime can be expressed as

$$
\begin{aligned}
\frac{\Delta p}{d_{\|}} &= \frac{S_{face}}{2\,\epsilon\,U_o}\,c_d\,\rho\,w_{\|}^2 \\
&= \frac{d_s\,(d_\perp - d_s) + \xi\,d_s\,(d_\perp - d_s) + \xi\,d_s\,(d_{\|} - d_s)}{2\,\epsilon\,d_\perp^2\,d_{\|}}\,\frac{c_d\,d_\perp^4}{(d_\perp - d_s)^4}\,\rho\,q^2\,.
\end{aligned}
\tag{7.44}
$$

Since $\xi = 1$ for the foam RUC model, it follows that

$$
\frac{\Delta p}{d_{\|}} = \frac{2\,d_s\,(d_\perp - d_s) + d_s\,(d_{\|} - d_s)}{2\,\epsilon\,d_\perp^2\,d_{\|}}\,\frac{c_d\,d_\perp^4}{(d_\perp - d_s)^4}\,\rho\,q^2\,.
\tag{7.45}
$$

Thus, for the anisotropic short duct foam RUC model the pressure drop over the entire
steady laminar flow regime is obtained by application of the power addition technique
(Churchill & Usagi (1972)) with a shifting parameter of unity to equations (7.45) and
(7.42), yielding

$$
\begin{aligned}
\frac{\Delta p}{d_{\|}} = \;=\; & \frac{24\,d_\perp^2\,\mu\,q_{exp}}{d_{\|}\,(d_\perp - d_s)^2}\left[2\sqrt{1 + \frac{0.0822\,\rho\,q_{exp}\,d_\perp^2}{\mu\,d_s}\,\frac{d_s}{(d_\perp - d_s)^2}}\right. \\
& \left. + \sqrt{1 + \frac{0.0822\,(d_{\|} - d_s)^2\,\rho\,q_{exp}\,d_\perp^2}{\mu\,d_s\,(d_\perp - d_s)^2}\,\frac{d_s}{(d_{\|} - d_s)^2}}\right] \\
& \frac{2\,d_s(d_\perp - d_s) + d_s(d_{\|} - d_s)}{2\,\epsilon\,d_\perp^2\,d_{\|}}\,\frac{c_d\,d_\perp^4}{(d_\perp - d_s)^4}\,\rho\,q^2\,.
\end{aligned}
\tag{7.46}
$$

Figure 7.20 (p 228) shows the effect of compression on the streamwise pressure gradient as
a function of the compression ratio, $1 - \mathrm{e}_{exp}$. The pressure gradient increases non-linearly
with the compression ratio. The anisotropic short duct RUC model yields a significant
over-prediction at maximum compression whereas for the other stages of compression sat-
isfactory agreement is obtained with the experimental pressure drop data. It is clear that
for very high ratios of compression, i.e. larger than 0.8, there exist factors that influence
the pressure drop that are not taken into consideration in the anisotropic short duct foam
RUC model. These discrepancies between the model prediction and the experimental
data may be investigated in future studies.
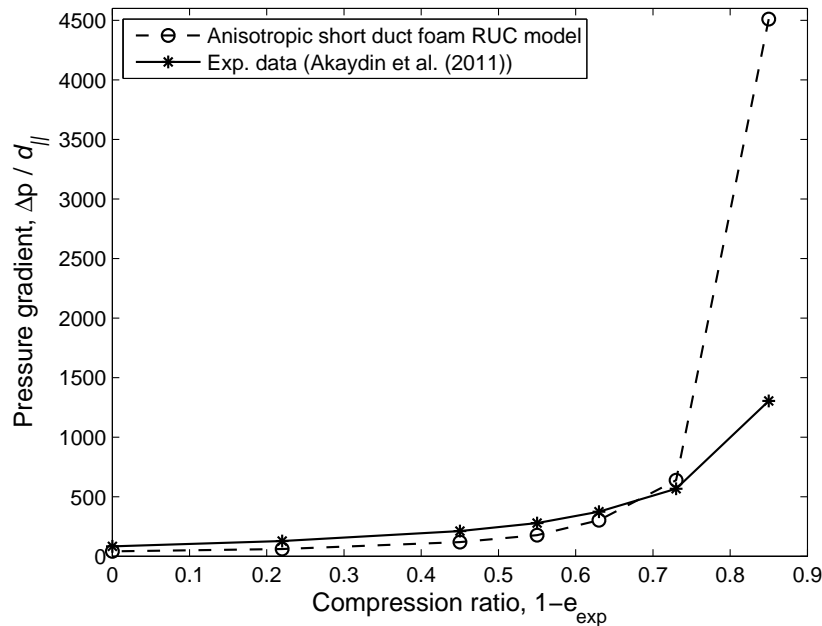
Figure 7.20: Pressure drop prediction as a function of the compression factor $1 - e_{exp}$ for compressible soft fibrous media predicted by the anisotropic short duct foam RUC model.

7.5   Summary

The foam RUC model was used to predict the permeability of fibrous porous media subject to different stages of compression in the streamwise direction. In order to account for anisotropy, the RUC model for foamlike media was adapted geometrically from an isotropic structure to an anisotropic one by shortening the strut in the streamwise direction. A direct analytical modelling procedure was followed into which the RUC thickness in the streamwise direction was incorporated as a new variable. Since the streamwise and transverse pore-scale linear dimensions of the RUC are related through the porosity, the compression not only affects the streamwise dimension of the RUC, but also the transverse dimension.

In the first case study, the anisotropic foam RUC model was used to predict the permeability of a non-woven glass fibre filter. From the given experimental values for the filter thickness relative to its uncompressed state, the porosity, and the mean hydraulic pore diameter values, the short strut length in the streamwise direction could be expressed as a function of the short strut length in the uncompressed state and the porosity. Knowing the values of the short strut length in the streamwise direction for the different stages of compression, the corresponding transverse dimensions of the RUC could be obtained. The permeability, expressed in terms of the known pore-scale linear dimensions of the RUC, could then be predicted for the different stages of compression. Although the measured mean hydraulic pore diameter values are measured only with respect to the streamwise

direction, the RUC model distinguishes between the hydraulic diameter values in the three principal flow directions.

The influence of developing flow and inertial effects on the streamwise pressure drop was found to be negligible, based on the low Reynolds numbers (i.e. of the order of nanometers) under consideration. The kinematical tortuosity predicted by the RUC model is in satisfactory agreement with three of the four experimental values. The under-prediction of the fourth data point is, however, still within the bounding experimental error ranges indicated for the kinematical tortuosity prediction.

In the second case study, the anisotropic foam RUC model is used to predict the permeability of a compressible soft polyester material. The difficulty was that measurements on the mean hydraulic pore diameter, at the different stages of compression, were not provided. As a result, the short strut length in the uncompressed state could not be determined from the experimental mean hydraulic pore diameter values. As a first order approximation, the relation between the pore-scale linear dimensions of the isotropic foam RUC model were used to determine the value of the short strut length in the uncompressed state. In this case study it was shown that the anisotropic model decreases the over-prediction of the isotropic model by an average of 94.0%. The Reynolds numbers calculated for this case study are of the order of 10^{-1}. The permeability prediction of the anisotropic foam RUC model was then adapted to account for the effect of developing flow. It was illustrated that already at these low Reynolds numbers the effect of developing flow is significant and has to be accounted for in the permeability prediction. The incorporation of the effect of developing flow reduced the over-prediction of the anisotropic model by another 65.7%, on average.

A sensitivity analysis was performed on the model predictions. In the first case study specified experimental percentage error ranges were provided, but not in the second case study. For the latter case study, error ranges were chosen based on the results of the first case study. For both cases studies it was found that the permeability prediction is very sensitive to deviations in the values of the pore-scale linear dimension of the uncompressed state and in the porosity values used in the model. In both case studies, the permeability ranges over more than an order of magnitude over the relatively low porosity ranges involved. The permeability prediction is affected to a much lesser degree by the compression ratio. Combinations of the specified experimental percentage error ranges were determined that yield an upper bound and lower bound for the permeability prediction. In both case studies the model prediction lie between the two bounding error curves.

The absolute relative percentage differences between the two bounding permeability curves are more than 900 % for the first case study and up to about 150% for the second case study. This shows that the anisotropic foam RUC model is very sensitive to deviations in the measured micro-structural input parameters. The absolute relative percentage errors associated with the model prediction are all less than the maximum absolute relative percentage error of the two bounding curves. This is promising and provides confidence in the predictive capabilities of the anisotropic foam RUC model.

The application of the anisotropic foam RUC model to experimental data on compressed fibres, presented in this chapter, excluded the studies of Antohe et al. (1997), Boomsma & Poulikakos (2002), Dukhan (2006) and Gerbaux et al. (2009), as these authors have either not supplied hydraulic diameter values or estimates for e_{exp}, or both.

Chapter 8

Contributions to other applications of the RUC models

This chapter is partitioned into three sections. In the first section the permeability predictions of the transversely isotropic granular and foam RUC models are adapted to predict the permeability of Fontainebleau sandstone by accounting for the effect of block throats at very low porosities. The question arises as to whether Fontainebleau sandstone should be regarded as a consolidated (i.e. foamlike) or an unconsolidated (i.e. granular) porous medium. Doyen (1988), for instance, regarded Fontainebleau sandstone as a consolidated porous medium. According to Adler et al. (1990), Fontainebleau sandstone was originally unconsolidated sand after which various geological processes, such as the accretion of sand particles took place, which led to a decrease in porosity. The objective is to provide an answer to the question being posed as to whether Fontainebleu sandstone should be regarded as a consolidated or unconsolidated porous medium by application of the granular and foam RUC models.

Secondly, the transversely isotropic granular and fibre RUC models are used to predict the diffusivity ratio of unconsolidated porous media in the absence of fluid motion and in which the diffusion process can be regarded as isotropic. The diffusivity ratio of two-dimensionally staggered and non-staggered arrays of anisotropic solid rectangles is computed numerically and an existing weighted average model is applied to verify the numerical data. A particular case of a staggered array of solid squares, for which this weighted average model is no longer adequate, is outlined and a weighted average RUC model is proposed instead to predict the diffusivity ratio.

Lastly, a summary is given of contributions made to the RUC models over the past three decades, with emphasis on the involvement of the author of this dissertation in some of the applications.

8.1 Predicting the permeability of sandstones

Sandstones make up about 25% of the sedimentary rocks in the world (Dullien (1979)). The ability to accurately predict the permeability of groundwater seepage through granular soils and rock formations, such as sandstones, has received considerable attention as aid to the management thereof, both naturally and industrially. Sandstones are consolidated sedimentary rocks formed by the natural cementation of unconsolidated sands (Collins (1961)). The pore space is thus partially filled with cementing material and as a result the porosity is considerably low.

Numerous experimental measurements for determining the permeability of Fontainebleau sandstone have been performed (e.g. Bourbie & Zinszner (1985), Doyen (1988), Adler et al. (1990)) due to its simple geometric micro-structure and its large porosity variation. Fontainebleau sandstone is composed primarily of fine impermeable quartz grains cemented by silica (Bourbie & Zinszner (1985), Doyen (1988)). The constant composition and grain size of Fontainebleau sandstone as well as the well-sortedness of the grains make the material remarkably homogeneous. Another important feature is that the geometric structure is conserved with variation in porosity. These characteristics of Fontainebleau sandstone make it well-suited for modelling purposes.

8.1.1 Application of the granular RUC model

The permeability prediction of the transversely isotropic granular RUC model in terms of the linear dimension d_s is given in Table 4.4 (p 94) as

$$k_{ds} \; = \; \frac{d_s^2 \left(1 - (1 - \epsilon)^{1/3}\right) \left(1 - (1 - \epsilon)^{2/3}\right)^2}{25.4 \left(1 - \epsilon\right)^{4/3}} \; . \tag{8.1}$$

Note that in Woudberg & Du Plessis (2008) the granular RUC model of Woudberg (2006) was used whereas in this study the improved granular model presented in Chapter 4 will be used. The difference between the two models lie in the value of the coefficient, i.e. the value of 25.4 in equation (8.1). The model of Woudberg (2006) resulted in a coefficient of 26.8 as opposed to the value of 25.4 obtained for the granular model proposed in this study (Section 3.14.4, p 51).

Du Plessis & Roos (1994b) regarded a well-sorted sandstone as a granular porous medium and the grain size is used as characteristic length. The relation between the grain size, d_g, and the solid width, d_s, of the granular RUC model is obtained by setting the volume of a sphere equal to the volume of a cube and is given by

$$d_s \; = \; \left(\frac{\pi}{6}\right)^{1/3} d_g \; . \tag{8.2}$$

The granular permeability, k_{gran}, for sandstones may then be expressed as

$$k_{gran} \;=\; \frac{d_g^2 \left[1 - (1 - \epsilon)^{1/3}\right] \left[1 - (1 - \epsilon)^{2/3}\right]^2}{39.1 \, (1 - \epsilon)^{4/3}} \;.$$

(8.3)

8.1.2   Application of the foam RUC model

The permeability prediction of the transversely isotropic foam RUC model in terms of
the linear dimension d is given in Table 4.4 (p 94) for the doubly staggered model as

$$k_{foam} \;=\; \frac{\epsilon^2 \, d_s^2}{9 \, \psi^2 \, (\psi - 1)^3} \;,$$

(8.4)

with the geometric factor ψ given by

$$\psi \;=\; 2 + 2 \cos \left[\frac{4 \, \pi + \cos^{-1}(2 \, \epsilon - 1)}{3} \right] \;.$$

(8.5)

As already mentioned, for the doubly staggered foam model the geometric factor ψ equals
the tortuosity χ. The next step is to relate the solid width, d_s, of the foam RUC model to
the grain diameter, d_g. Doyen (1988) modelled the transport properties of Fontainebleau
sandstone as a consolidated network of narrow struts, similar to the foam RUC model,
but he used circular struts with complicated orientations. He assumed that the length of
the narrow struts connecting the pore chambers is constant and approximately equal to
the grain diameter, which means that in RUC notation $d = d_g$. Alternatively, consider
the low porosity foam RUC model in Figure 8.1 (p 234). In order to find the relation
between d_g and d_s a similar approach will be followed as in Section 3.15.7 (p 67).

From Figure 8.1 the following relation can be deduced:

$$d_s \;=\; \frac{c_s}{\sqrt{3}} \;=\; 0.58 \, c_s \;.$$

(8.6)

The diagonal length, c_s, will be assumed to be equivalent to the grain diameter, i.e.
$c_s = d_g$. Consequently, the foam permeability in terms of the grain diameter, d_g, is given
by

$$k_{foam} \;=\; \frac{\epsilon^2 \, d_g^2}{27 \, \psi^2 \, (\psi - 1)^3} \;.$$

(8.7)

The variation in grain diameter, d_g, of different samples of Fontainebleau sandstone is
given by Doyen (1988) as $150 < d_g < 300 \, \mu m$. Bourbie & Zinszner (1985) give an average
diameter of $d_g \approx 250 \, \mu m$ for Fontainebleau sandstone. The experimental permeability
values provided by Bourbie & Zinszner (1985), Doyen (1988) and Adler et al. (1990) are

233
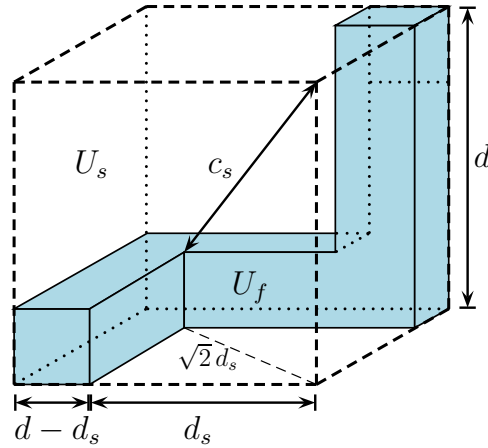
Figure 8.1: Illustration of the diagonal length, c_s, in the low porosity foam RUC model.

shown in Figure 8.2 together with the two curves representing the permeability predictions of equations (8.3) and (8.7) corresponding to the limiting grain diameter values of 150 and 325 µm. The latter diameter value is determined as the average of 300 and 350 µm.

The fluctuations in the permeability data at certain porosity values by almost a factor of 10 is a known phenomenon in sandstones (Adler et al. (1990)). The curves representing the permeability prediction of the granular RUC model capture the experimental data of Bourbie & Zinszner (1985) within an envelope for porosities greater than about 0.08. For
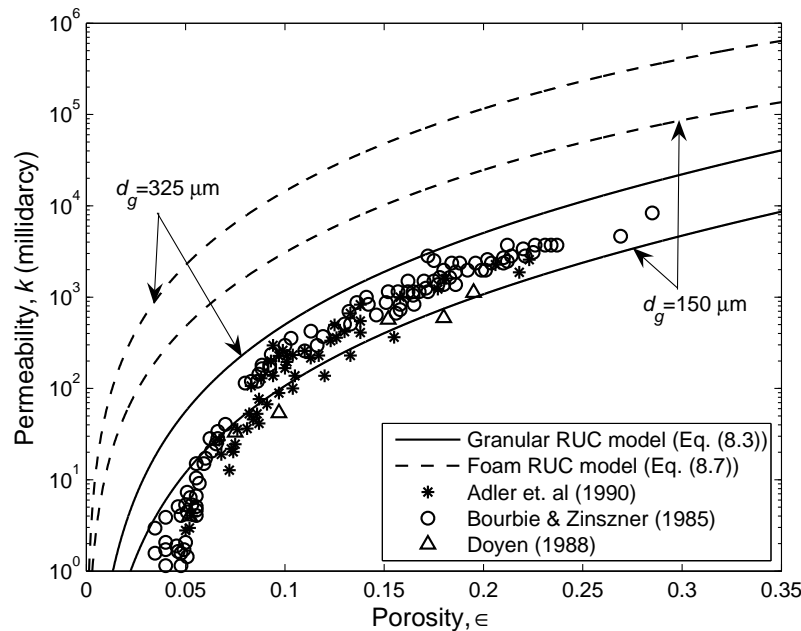
Figure 8.2: Permeability prediction of Fontainebleau sandstone.

porosities less than 0.08 a significant deviation is evident. It appears from the data that below this porosity all throats are blocked, prohibiting any fluid motion and thus causing an almost zero permeability.

The permeability predicted by the foam RUC model is about two orders of magnitude larger than the experimental permeability data. The significant deviation of the foam RUC model from the experimental data, as well as the deviation of the granular RUC model from the experimental data at porosities below 0.08, are to be addressed next.

8.1.3 Blocking of throats

Du Plessis & Roos (1994b) have developed a model for the permeability prediction of granular porous media with grain size, d_g, based on the granular RUC model of Du Plessis & Masliyah (1991). The model was applied to predict the permeability of several well-sorted sandstones. As in the present study, significant discrepancies were observed at very low porosities between the permeability prediction and published experimental values for Fontainebleau sandstone. This was attributed to the blocking of throats and resulting isolated pore space. The effective porosity was expressed as a second order polynomial of which the coefficients are a function of the porosity at which pore blockage start to occur and the porosity at which no more seepage takes place. It was shown that the permeability prediction could be enhanced considerably through the incorporation of the effective porosity. The challenge was to find the coefficient values for a particular sandstone.

The deviation of the granular RUC model from the experimental data in Figure 8.2 (p 234) at porosity values below about 0.08 may similarly be attributed to the occurrence of blocked throats which are not accounted for in both RUC models. Blocked throats result when the porosity becomes so low that regions within the interstitial pore sections randomly become clogged. Stagnant zones appear and at a certain porosity, called the percolation threshold porosity (Bourbie & Zinszner (1985)), no more seepage takes place, leading to an impermeable porous medium. The percolation threshold porosity, ϵ_c, is a characteristic property of the particular porous structure and the particular clogging mechanism and needs to be determined experimentally for the specific sandstone under consideration. Certainly the occurrence of blocked throats should also be accounted for in the foam RUC model since clogging will take place, but not necessarily at the same porosity as in granular media.

According to the experimental data, the percolation threshold porosity seems to lie in the vicinity of 0.04. Du Plessis (1999) proposed the following analytical approach based on the power addition technique (Churchill & Usagi (1972)) to physically account for blocked throats: The effective or backbone porosity, ϵ_B, is introduced as the porosity in which the effect of blocked throats is incorporated. At the percolation threshold, the backbone porosity should tend to zero, i.e.

$$\epsilon_B \to 0 \qquad \text{when} \qquad \epsilon \to \epsilon_c \,, \tag{8.8}$$

235

and secondly, at porosities well above the threshold, pore blockage is non-existent and the
backbone porosity should take on the same values as the porosity, i.e.

$$\epsilon_B \to \epsilon \qquad \text{when} \qquad \epsilon \to 1 \; . \tag{8.9}$$

Two different physical processes thus take place, each of which predominates in a differ-
ent porosity regime. At very low porosities the transport properties are predominantly
affected by pore-blockage and at low to high porosities maximum inter-connectivity of the
pore space is assumed. A general expression for the backbone porosity satisfying both
limiting conditions may be obtained through application of the power addition technique
(Churchill & Usagi (1972)), i.e. :

$$\epsilon_B \;=\; (\epsilon^s - \epsilon_c^s)^{1/s} \; , \tag{8.10}$$

where s denotes a shifting exponent. It was established by inspection of the data (Du
Plessis (1999)) that the value of s which led to the best correspondence of the granular
RUC model with many sets of experimental data found in the literature (e.g. Bourbie
& Zinszner (1985), Adler et al. (1990)) is $s = 3/2$. The value of s for the foam RUC
model is yet unknown and also needs to be determined by correlation with experimental
data. Substituting ϵ_B with $s = 3/2$ into equation (8.3) yields the following granular
permeability prediction for Fontainebleau sandstones in which the effect of pore blockage
at low porosities is accounted for:

$$k_{gran} \;=\; \frac{d_g^2 \left(1 - (1 - \epsilon_B)^{1/3}\right)\left(1 - (1 - \epsilon_B)^{2/3}\right)^2}{39.1\,(1 - \epsilon_B)^{4/3}} \; . \tag{8.11}$$

The permeability prediction obtained by application of the foam RUC model is given by

$$k_{foam} \;=\; \frac{\epsilon_B^2\, d_g^2}{27\,\psi_B^2\,(\psi_B - 1)^3} \; , \tag{8.12}$$

with

$$\psi_B \;=\; 2 + 2\cos\left[\frac{4\,\pi + \cos^{-1}(2\,\epsilon_B - 1)}{3}\right] \; , \tag{8.13}$$

Equations (8.11) and (8.12) provide permeability predictions for Fontainebleau sandstone
over the entire porosity range applicable to the porous material, in terms of four pa-
rameters, i.e. the porosity ϵ, grain size d_g, percolation threshold porosity ϵ_c and shifting
exponent s.

8.1.4   Percolation

Du Plessis (1999) provided an analytical expression that relates the percolation threshold
porosity of granular sandstone samples with different grain sizes, but was presented incor-
rectly. The expression for the granular model to be presented in this section follows the

236

same analogy as was used by Du Plessis (1999), but the result is different. In addition, a corresponding expression for the foam model is proposed.

Let d_{g_i}, with $i = 1, 2$, denote the grain diameter of a sandstone sample and ϵ_{c_i} denote the percolation threshold porosity of the sample with grain size, d_{g_i}. A reasonable assumption is that the percolation threshold porosity does not depend on the grain size, but on the pore width (Du Plessis (1999)). The pore width in the granular RUC model may be expressed as

$$d - d_s = \left[(1 - \epsilon)^{-1/3} - 1\right] \left(\frac{\pi}{6}\right)^{1/3} d_g . \tag{8.14}$$

For samples of known d_{g_i}-values it is possible to obtain an expression for the percolation threshold porosity ϵ_{c_i}, if either the value of ϵ_{c_1} or ϵ_{c_2} is known and subject to the assumption that the samples have an equivalent uniform pore width in which the same clogging processes took place. For a sample of grain diameter, d_{g_1}, and a known threshold porosity, ϵ_{c_1}, the threshold porosity, ϵ_{c_2}, of a sample with known grain diameter, d_{g_2}, may be obtained by application of equation (8.14), i.e.

$$\left[(1 - \epsilon_{c_1})^{-1/3} - 1\right] d_{g_1} = \left[(1 - \epsilon_{c_2})^{-1/3} - 1\right] d_{g_2} . \tag{8.15}$$

Solving for ϵ_{c_2} yields, for granular media,

$$\epsilon_{c_2} = 1 - \left[\frac{d_{g_2}}{d_{g_1} \left[(1 - \epsilon_{c_1})^{-1/3} - 1\right] + d_{g_2}}\right]^3 . \tag{8.16}$$

The pore width in the foam RUC model as a function of d_s can be obtained from equations (3.45) and (3.46). Assuming again that the percolation threshold porosity does not depend on the grain size, but on the pore width, yields

$$\frac{3 - \psi|_{\epsilon_{c_1}}}{\psi|_{\epsilon_{c_1}} - 1} 0.58 \, d_{g_1} = \frac{3 - \psi|_{\epsilon_{c_2}}}{\psi|_{\epsilon_{c_2}} - 1} 0.58 \, d_{g_2} , \tag{8.17}$$

with

$$\psi|_{\epsilon_{c_i}} = 2 + 2 \cos\left[\frac{4\pi + \cos^{-1}(2\epsilon_{c_i} - 1)}{3}\right] \qquad \text{for} \qquad i = 1, 2 . \tag{8.18}$$

Solving for ϵ_{c_2} from equations (8.17) and (8.18), leads to

$$\epsilon_{c_2} = \frac{1}{2} \cos\left[3 \cos^{-1}\left[\frac{d_{g_2} - \gamma \, d_{g_1}}{2 \, d_{g_2} + 2 \, \gamma \, d_{g_1}}\right] - 4\pi\right] + \frac{1}{2} , \tag{8.19}$$

with

$$\gamma = \frac{1 - 2 \cos\left[\frac{4\pi + \cos^{-1}(2\epsilon_{c_1} - 1)}{3}\right]}{1 + 2 \cos\left[\frac{4\pi + \cos^{-1}(2\epsilon_{c_1} - 1)}{3}\right]} . \tag{8.20}$$

237

Equation (8.16) for granular media and equation (8.19) for foamlike media each provides a prediction for the percolation threshold porosity, ϵ_{c_2}, of a sample with average grain diameter, d_{g_2}, if the average grain diameter, d_{g_1}, and the percolation threshold porosity, ϵ_{c_1}, of another sample are known.

8.1.5 Granular versus foam RUC model predictions for sandstones

The variation in porosity of different samples of Fontainebleau sandstone is given by Doyen (1988) and Fredrich et al. (1993) respectively as $0.05 < \epsilon < 0.22$ and $0.04 < \epsilon < 0.2$. According to Adler et al. (1990), the porosity range is given by $0.03 < \epsilon < 0.35$ and Bourbie & Zinszner (1985) proposes the range $0.03 < \epsilon < 0.28$. From the experimental data in Figure 8.2 (p 234) it is evident that a reasonable estimate for the percolation threshold porosity, ϵ_{c_1}, corresponding to the limiting grain diameter of $d_{g_1} = 150\,\mu m$ is $\epsilon_{c_1} = 0.04$. Substituting the latter values, together with $d_{g_2} = 325\,\mu m$, into equations (8.16) and (8.19) yields $\epsilon_{c_2} = 0.0187$ and $\epsilon_{c_2} = 0.0102$, respectively. The permeability predictions for the granular and foam RUC models, in which pore blockage at very low porosities is accounted for (i.e. equations (8.11) and (8.12), respectively), are shown in Figure 8.3 (p 239) for the limiting grain diameter values of 150 and 325 μm. The value of s which leads to the most satisfactory permeability prediction of the foam RUC model is $s = 1/2$. In Figure 8.4 (p 239) are shown the permeability predictions of the foam RUC model for different s-values. It is evident that the lower the value of s, the more gradual the transition from the one physical flow process where pore blockage occurs to the other flow process in which all the pore sections are inter-connected. A value lower than $1/2$ for s for the foam RUC model will result in an under-prediction of the data.

Comparison of Figures 8.2 and 8.3 leads to the conclusion that blocked throats at very low porosities have a significant effect on the permeability prediction. The analytical modelling thereof seems to justify the observed physical phenomenon. The granular RUC model provides satisfactory enclosure of the experimental data between the two limiting grain diameter values. The foam RUC model, however, provides a much broader region of feasibility for the same limiting grain diameter values. The foam RUC model predicts much higher permeability values than the granular RUC model for the 325 μm grain size. The reason for this phenomenon may be attributed to the different solid geometries of the foam and granular RUC models. In the derivation of the analytical expressions for ϵ_{c_2} for both the granular and foam RUC models it was assumed that the pore width remains the same for sandstone samples of different grain sizes, but the different granular and foam RUC model geometries lead to different porosity dependencies of the pore-scale linear dimensions. In the case of the granular RUC model the flow in the pores are predominantly modelled as flow between single sets of parallel plates, whereas in the foam model the flow in the pores are regarded as flow between double sets of parallel plates, thus resembling tube-like flow behaviour. In addition, for the granular model the relation $d_s = (\pi/6)^{1/3} d_g$ was used and for the foam model $d_s = d_g/\sqrt{3}$. A combination of the latter effects leads to the larger difference between the ϵ_{c_1} and ϵ_{c_2}-values for the foam
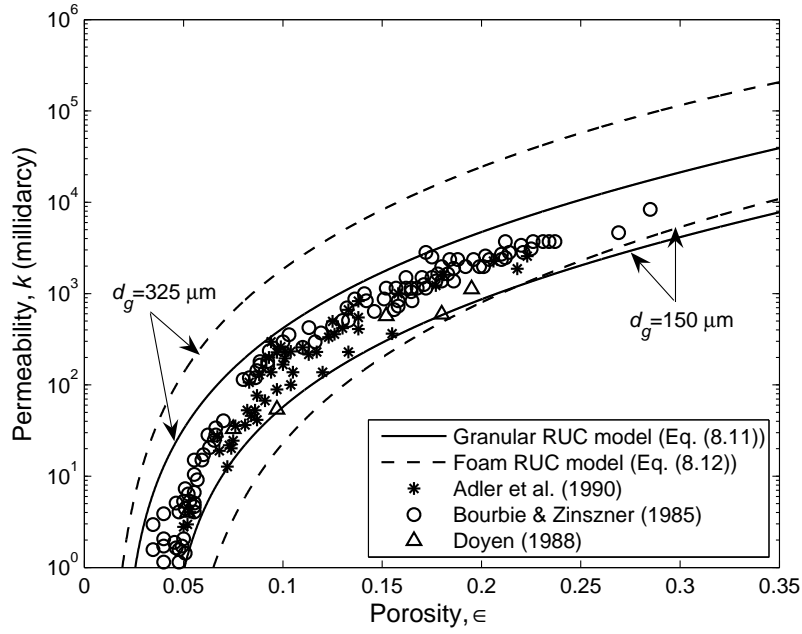
Figure 8.3: Permeability prediction of Fontainebleau sandstone with pore blockage.
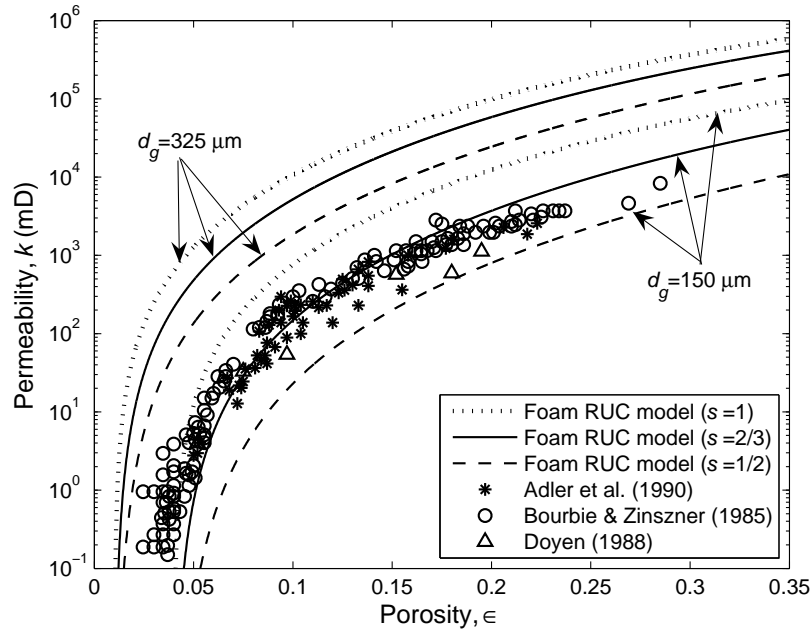
Figure 8.4: Predictions of the foam permeability for different s-values.

model and hence larger permeability predictions for a grain diameter of $325\,\mu m$.

In the literature sandstones are believed to provide both kinds of apertures to a traversing fluid. The goal in this section was to determine which of the granular or foam RUC models is superior to the other in predicting the permeability of sandstones, and in specific, Fontainebleau sandstone. Success of both models, the granular RUC model predictions just being more refined than that of the foam model, leads to the conclusion that Fontainebleau sandstone exhibit both granular and tubular properties, with the granular characteristics being more prominent. This supports both modelling approaches in the literature where Fontainebleau sandstone is treated as consolidated or unconsolidated porous media.

8.2   Diffusion in unconsolidated porous media

Molecular diffusion in porous media plays an important role in chemical reactor design (Kim et al. (1987)) and in the process of mass transfer in catalyst pellets (Ryan et al. (1981)). Diffusion also plays a major role in the transport of contaminants in soils surrounding toxic waste disposal sites (Sáez et al. (1991)). The rate of drying of wood and granular materials is, under certain circumstances, controlled by diffusion of water vapor through the porous medium (Kim et al. (1987)). Diffusion is also important in many processes in the coal industry, e.g. the recovery of methane from coal beds (Kim et al. (1987)).

8.2.1   Diffusion equation

Fick's second law of diffusion (Appendix A.2, p 280), or simply the diffusion equation, applies to a stationary incompressible fluid without chemical production of the particular diffusing species under consideration and is given by

$$\frac{\partial \phi_c}{\partial t} + \nabla \cdot D \nabla \phi_c \;=\; 0 \,, \tag{8.21}$$

where D is the diffusion coefficient, also known as the mass diffusivity, of the particular diffusing species under consideration and ϕ_c is the concentration of the particular diffusing species. The diffusive flux, $\underline{j}_c$, described by Fick's first law of diffusion (Appendix A.1, p 279), i.e.

$$\underline{j}_c \;=\; -D \nabla \phi_c \,, \tag{8.22}$$

is incorporated into the second term of equation (8.21). For steady diffusion and a constant diffusion coefficient, the Laplace equation for mass transport is obtained (e.g. Welty (1978)), i.e.

$$\nabla^2 \phi_c \;=\; 0 \,. \tag{8.23}$$

Equation (8.23) is to be solved numerically, with suitable boundary conditions, in order to predict the effective diffusion coefficient for porous media from the diffusive flux. For the present analysis the pressure and temperature are regarded as constant and neither adsorption nor chemical reaction is assumed at the gas-solid interfaces. No mass transfer between the phases will be considered. It will furthermore be assumed that the fluid is stationary and that the solid particles are impenetrable, i.e. the diffusion coefficient for the solid phase is zero.

8.2.2 Effective diffusion coefficients for porous media

The ratio of the effective diffusion coefficient for porous media, D_{eff}, with respect to the diffusion coefficient D, i.e. D_{eff}/D, is to be determined. This ratio is a dimensionless number less than unity and is also referred to as the diffusivity ratio or the diffusibility (Hoogschagen (1955)). It is a material property, rather than a process parameter (Ryan et al. (1981)). In the context of a porous medium, the diffusion coefficient, D, is the diffusion coefficient of the fluid in the absence of the solid phase (Kim et al. (1987)).

According to Whitaker (1969) and Kim et al. (1987), the diffusivity ratios in the streamwise and transverse directions of a regular array (i.e. in the $x-$ and $y-$directions of a two-dimensional rectangular Cartesian coordinate system) differ by less than 1% and are essentially equal, which means that the system may be regarded as transversely isotropic with respect to the diffusion process. This is also true for the fully staggered array, even though the diffusion path is more tortuous in the streamwise direction than in the transverse direction (Kim et al. (1987)). Thus, both the regular and fully staggered arrays are transversely isotropic with respect to the diffusion process even though both arrays are not geometrically transversely isotropic (Section 3.4, p 42). The term "isotropic", or rather "transversely isotropic" in the case of the RUC models, will henceforth refer to porous media in which the *diffusion process* is isotropic (or transversely isotropic).

Quintard (1993) confirmed, through three-dimensional numerical computations, that for unconsolidated isotropic systems the porosity is an essential parameter for the determination of the diffusivity ratio. Kim et al. (1987) also stated that for unconsolidated isotropic porous media the diffusivity ratio is independent of the details of the geometry and that the diffusivity ratio can be expressed as a function of porosity alone. This is however not the case for unconsolidated media which are anisotropic with respect to the diffusion process.

For unconsolidated isotropic (with respect to the diffusion process) porous media two-dimensional models are sufficient to predict the effective diffusivity (Kim et al. (1987), Sáez et al. (1991), Quintard (1993)). Two and three-dimensional analytical and numerical models yield more or less the same predictions for the diffusivity ratio when the models are evaluated at the same porosities (Quintard (1993)). This also confirms that for unconsolidated isotropic porous media (or transversely isotropic in the case of the RUC models) the diffusivity ratio is essentially determined by porosity. However, in the case of unconsolidated media, which are anisotropic with respect to the diffusion process,

two-dimensional models are no longer adequate to predict the diffusivity ratio (Sáez et al. (1991), Quintard (1993)).

Ryan et al. (1981) state that reliable theoretical models are absolutely essential because the diffusivity ratio cannot be measured directly and needs to be extracted from flux measurements and calculated in conjunction with a reliable theoretical model. They also express the need to characterize actual porous media by constructing a realistic geometrical model. Quintard (1993) mentioned that, although it is realistic to compute the transport properties by describing the actual porous medium, three-dimensional computations require advanced computer resources and that diffusivity ratios close to the actual measurements can be obtained by using the representative unit cell approach. There are, however, several models available in the literature for predicting diffusivity ratios in isotropic porous media. The approaches followed can be classified into two different categories (Sáez et al. (1991)), i.e. statistical models and deterministic models. In the statistical models the random local distribution of the phases in the porous medium is described using statistical theories and the deterministic models are based on a geometrical representation of the porous medium in the form of a unit cell. The deterministic approach will be followed in the present study. The diffusivity ratio will be determined analytically for unconsolidated isotropic systems as a function of porosity by application of the granular and fibre RUC models. For two-dimensional staggered and non-staggered arrays of solid rectangles, the diffusivity ratio will be computed numerically.

8.2.3   Diffusivity ratios predicted by the RUC models

Similarly as in the case of convective transport through the fibre RUC model, only diffusion perpendicular to the prism axis will be considered. It will thus be assumed that the properties of diffusion do not change in the direction parallel to the prism axis. The fibre RUC model will therefore also be referred to as the 2D (two-dimensional) RUC model and the granular RUC model as the 3D (three-dimensional) RUC model. The direction of the streamwise average diffusive pore flux is defined as the streamwise average diffusive pore flux, $\underline{j}_{c_\parallel}$, divided by its magnitude, i.e.

$$\widehat{\underline{n}} \;=\; \frac{\underline{j}_{c_\parallel}}{|\underline{j}_{c_\parallel}|} \;.$$
(8.24)

In the modelling procedure for convective flow, piece-wise straight streamlines were assumed, which, together with the parallel plate geometry allow for the fluid domain within an RUC to be partitioned into different sub-volumes (Section 3.6, p 43). The notation will be kept the same as was used in the modelling procedure for convective flow, except that the streamlines will be replaced with piece-wise straight diffusive lines. The total fluid-filled volume, U_f, within the RUC may thus be expressed the same as previously (Section 3.6), i.e.

$$U_f \;=\; U_\parallel \;+\; U_\perp \;+\; U_g \;+\; U_t \;,$$
(8.25)

242

where the streamwise volume, $U_\parallel$, denotes the total fluid volume parallel to the stream-wise direction (i.e. $\underline{j}_{c_\parallel} \parallel \hat{n}$) and the transverse volume, $U_\perp$, is the total fluid volume perpendicular to the streamwise direction (i.e. $\underline{j}_{c_\perp} \perp \hat{n}$, with $\underline{j}_{c_\perp}$ being the transverse average diffusive pore flux). The transfer fluid volume, U_t, was defined for convective flow as a fluid volume in which no friction occurs due to the absence of adjacent solid surfaces. In order to keep the notation the same, the streamwise and transfer fluid volumes, $U_\parallel$ and U_t, will be treated similarly, since in the case of diffusion the presence of solid walls adjacent to U_t has no effect. For convective flow the fluid volume, U_g, was defined as a stagnant fluid volume in which the fluid remains stationary. For the process of diffusion the diffusive flux will, however, not be zero in these fluid regions and will therefore be treated similarly as the transverse fluid volumes, $U_\perp$.

Recall that the geometrical tortuosity, χ_{geo}, was defined for convective flow in the RUC as the ratio of the average length of the tortuous flow path, d_e, to the streamwise cell size, d, of the RUC for fluid traversing through a constant cross-sectional flow area, $A_{p_\parallel}$. Assuming that the geometrical tortuosity is also applicable to the diffusional flux, it may be expressed as (Section 3.9, p 45)

$$\chi_{geo} \equiv \frac{d_e}{d} = \frac{U_\parallel + U_t + U_\perp}{A_{p_\parallel} d} = \frac{U_\parallel + U_t + U_\perp}{U_\parallel + U_t} . \tag{8.26}$$

For the regular array of both unconsolidated RUC models, $\chi = 1$, for the fully staggered array of the 2D RUC model $\chi = \epsilon/(1 - \sqrt{1 - \epsilon})$ and for the fully staggered array of the 3D RUC model $\chi = \epsilon/(1 - (1 - \epsilon)^{2/3})$ (Tables 3.2 (p 52) and 3.8 (p 76), respectively). The geometric factor was defined as (Section 3.11, p 47)

$$\psi \equiv \frac{U_f}{U_\parallel + U_t} = \frac{U_f}{A_{p_\parallel} d} = \frac{U_\parallel + U_t + U_\perp + U_g}{U_\parallel + U_t} . \tag{8.27}$$

In the absence of stagnant fluid volumes the geometric factor, ψ, is equal to the tortuosity χ. For both the fully staggered and regular arrays of the 2D RUC model, the geometric factor is given by (Table 3.8)

$$\psi_{2D} = \frac{\epsilon}{1 - \sqrt{1 - \epsilon}} , \tag{8.28}$$

and for both the fully staggered and regular array of the 3D RUC model (Table 3.2),

$$\psi_{3D} = \frac{\epsilon}{1 - (1 - \epsilon)^{2/3}} . \tag{8.29}$$

The advantage of the geometric factor above the tortuosity is that, for both models, the same expressions are obtained for a fully staggered and a regular array of the same model. This is because the stagnant fluid volume, U_g, and the transverse fluid volume, $U_\perp$, contribute equally to the total fluid volume, U_f. For a fully staggered array, $U_g = 0$, and for a regular array, $U_\perp = 0$.

243

The geometric factor, ψ, is used to obtain the relation between the total average diffusive flux, $\underline{J}_c$, and the streamwise average diffusive pore flux, $\underline{j}_{c_{\parallel}}$, which is given by

$$\underline{j}_{c_{\parallel}} = \frac{\underline{J}_c \, \psi}{\epsilon} \, .$$

(8.30)

In the literature the diffusivity ratio for isotropic diffusion processes is commonly expressed as (e.g. Kim et al. (1987))

$$\frac{D_{eff}}{D} = \frac{\epsilon}{\chi} \, .$$

(8.31)

Although equation (8.31) is often used without stating where it originates from, it does have some physical meaning. In the context of the RUC theory, let A_e be the uniform cross-sectional area of the rectangular ducts in the RUC model and let d_e be the total piece-wise winding duct length. The total fluid volume in the RUC can then be expressed as $U_f = A_e d_e$ and, consequently, the porosity is given by

$$\epsilon = \frac{A_e d_e}{A \, d_{\parallel}} \, ,$$

(8.32)

where $A \, (> A_e)$ is the perpendicular face of the RUC through which the diffusive flux enters and $d_{\parallel} \, (d_{\parallel} < d_e)$ is the streamwise RUC dimension. It then follows that

$$\frac{A_e}{A} = \frac{d_{\parallel}}{d_e} \epsilon \, .$$

(8.33)

Assuming a concentration gradient of unity, the magnitude of the total diffusive flux through the RUC can be expressed as the product of the effective diffusion coefficient and the cross-sectional area, i.e. $D_{eff} \, A$. The flux in the ducts of the RUC can similarly be expressed as $D \, A_e$. Equating the two magnitudes of the diffusive fluxes leads to

$$\frac{D_{eff}}{D} = \frac{A_e}{A} = \frac{d_{\parallel}}{d_e} \epsilon = \frac{\epsilon}{\chi} \, ,$$

(8.34)

which is equivalent to equation (8.31). Alternatively, equation (8.31) follows directly from equation (8.30) as the ratio of the two fluxes and with $\chi = \psi$.

In the present study the following expression for the diffusivity ratio in terms of the geometric factor, ψ (rather than the tortuosity, χ), is proposed, i.e.

$$\frac{D_{eff}}{D} = \frac{\epsilon}{\psi} \, .$$

(8.35)

Recall that the tortuosity, as defined for the RUC models, takes on different values for a regular and fully staggered array, whereas this is not the case with the geometric factor.

244

The diffusivity ratio expressed in terms of the geometric factor thus supports findings
from the literature that the diffusivity ratios are essentially equal for the streamwise
and transverse directions of a fully staggered array, of which the transverse directions
corresponds to that of a regular array (Section 4.4.1, p 85). This is true even though the
diffusion path is more tortuous in the streamwise direction of a fully staggered array than
in the transverse direction (Kim et al. (1987)).

The geometric factor, as opposed to the tortuosity, furthermore, takes into account dif-
fusion that may take place in the hydrodynamically stagnant fluid volumes, U_g. The 2D
RUC model yields the following expression for the diffusivity ratio for isotropic processes:

$$\left(\frac{D_{eff}}{D}\right)_{2D} = 1 - \sqrt{1-\epsilon} \, , \tag{8.36}$$

and application of the 3D RUC model leads to

$$\left(\frac{D_{eff}}{D}\right)_{3D} = 1 - (1-\epsilon)^{2/3} \, . \tag{8.37}$$

The RUC models thus confirm findings from the literature that for unconsolidated isotropic
systems the diffusivity ratio is only a function of porosity. Note that equation (8.36) is
only applicable for diffusion *perpendicular* to the fibre axes.

Currie (1960) and Epstein (1989) proposed the following relation for predicting the diffu-
sivity ratio:

$$\frac{D_{eff}}{D} = \frac{\epsilon}{\chi^2} \, . \tag{8.38}$$

The only difference between equations (8.38) and (8.31) is the additional tortuosity factor
in equation (8.38), which results from the definition of tortuosity. Recall from Section
2.8.4 (p 19) that some authors in the literature define the tortuosity as $T = (L_e/L)^2$,
instead of only $\chi = (L_e/L)$. Analogous to equation (8.38) the diffusivity ratio can, in
RUC notation, also be expressed as

$$\frac{D_{eff}}{D} = \frac{\epsilon}{\psi^2} \, . \tag{8.39}$$

8.2.4 Model predictions for the diffusivity ratio from the liter-
ature

Models from the literature for predicting the diffusivity ratio in porous media involving
isotropic diffusion processes include the model of Maxwell (Kim et al. (1987)). He was
the first to analyze a dilute suspension of spheres analytically to obtain the following
expression for the diffusivity ratio:

$$\frac{D_{eff}}{D} = \epsilon \left[1 + \frac{1}{2}(1-\epsilon)\right]^{-1} \, . \tag{8.40}$$

Maxwell's equation serves as an upper bound for the diffusivity ratio for any value of ϵ (Kim et al. (1987)), even for non-spherical particles (Weissberg (1963)). Weissberg (1963) made use of a variational approach to describe the random geometry of a bed of spheres statistically, leading to the following expression for the diffusivity ratio:

$$\frac{D_{eff}}{D} = \epsilon \left[1 - \frac{1}{2} \ln \epsilon \right]^{-1} . \tag{8.41}$$

The micropore-macropore model of Wakao & Smith (1962) is given by

$$\frac{D_{eff}}{D} = \epsilon^2 . \tag{8.42}$$

Based on their experimental data, Kim et al. (1987) proposed the following empirical equation for the diffusivity ratio:

$$\frac{D_{eff}}{D} = \epsilon^{1.4} \qquad \text{for} \qquad 0 \leq \epsilon \leq 0.5 . \tag{8.43}$$

A comparison between the latter models from the literature and the 2D and 3D RUC models is shown in Figure 8.5 (p 247). It shows that the model of Maxwell (i.e. equation (8.40)) indeed forms an upper bound. The experimental data of Hoogschagen (1955), Currie (1960) and Kim et al. (1987) are for diffusion in randomly packed beds of spheres. The close correspondence between the model predictions of the 2D and 3D RUC models and the experimental data confirms that for unconsolidated isotropic porous media 2D models are adequate to predict the diffusivity ratio. The model predictions of the 2D and 3D RUC models capture the experimental data between them. An advantage of the RUC models is that they provide a relatively simple manner of describing the pore geometry. The close correspondence between the RUC model predictions and the diffusivity ratios predicted by the models form literature is satisfactory.

Figure 8.6 (p 247) shows a comparison between the 2D and 3D RUC model predictions for the diffusivity ratio based on equations (8.35) and (8.39). It is evident that the model predictions based on equation (8.35) leads to more accurate predictions than those based on equation (8.39).

8.2.5   Series-parallel formulae for anisotropic systems

The following subsections are devoted to the models that are used to verify the numerical data obtained for predicting the diffusivity ratio.

A popular concept to model diffusion in arbitrary composites is to mix two formulae that apply to composites made up of elements (or laminates) of different diffusion coefficients, namely the series and parallel formulae (Crank (1975)).
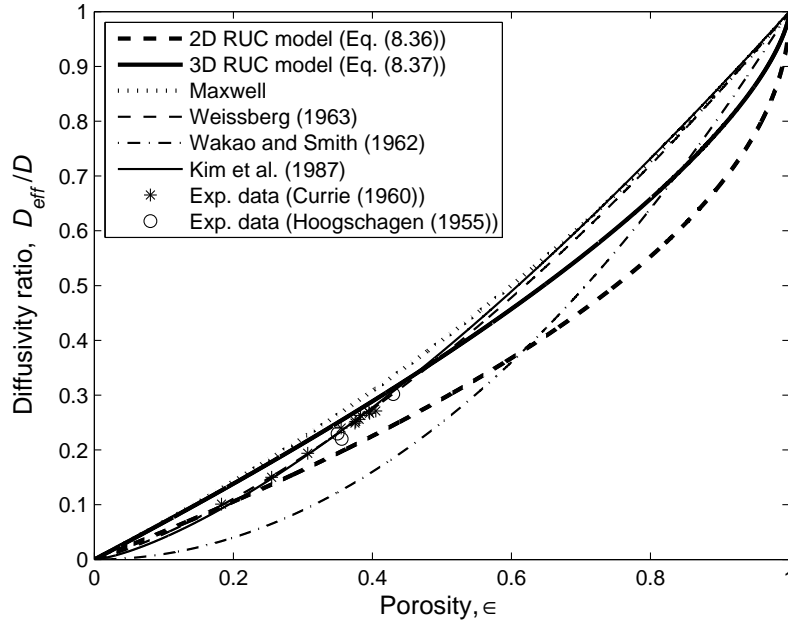
Figure 8.5: Diffusivity ratio as a function of porosity.
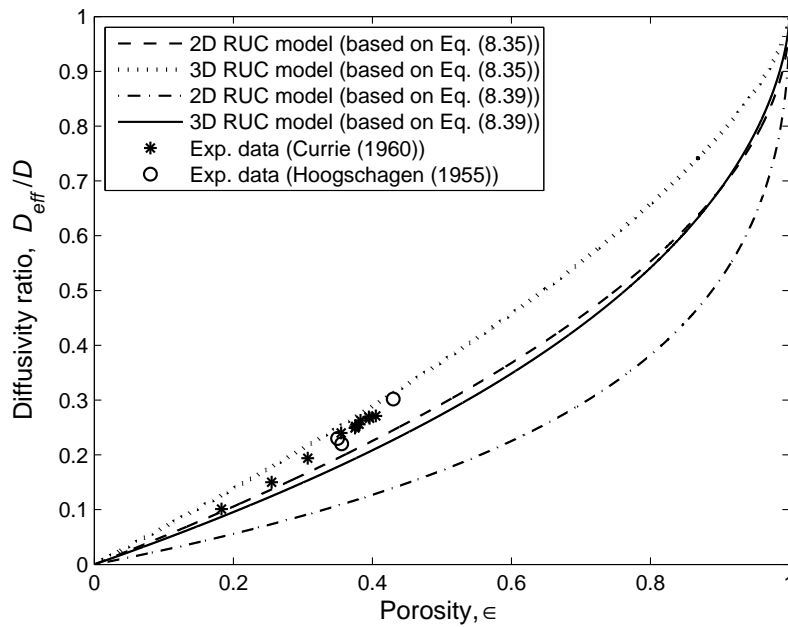
Figure 8.6: Comparison between diffusivity ratios predicted by equations (8.35) and (8.39).

In Figure 8.7 is shown a stacking of thin elements of a composite in series, i.e. perpendicular to the streamwise direction. Each element has a length, ℓ_i, and diffusion coefficient, D_i. The total length of the composite consisting of n elements is L and D represents the diffusion coefficient of the composite. A stacking of thin elements of a composite in parallel is shown in Figure 8.8. Each element of the composite of total length, L', in Figure 8.8, has a length of ℓ'_i.
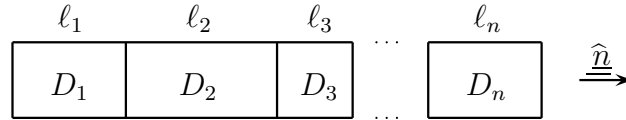
Figure 8.7: Series stacking of elements in a composite (Du Plessis (2010)).
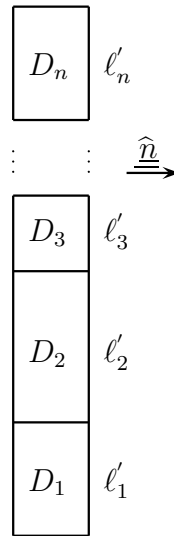
Figure 8.8: Parallel stacking of elements in a composite (Du Plessis (2010)).

The series and parallel formulae based on Figures 8.7 and 8.8 are respectively given by (Crank (1975))

$$\frac{L}{D} = \sum_i \frac{\ell_i}{D_i} = \frac{\ell_1}{D_1} + \frac{\ell_2}{D_2} + ... + \frac{\ell_n}{D_n} , \tag{8.44}$$

and

$$L'D = \sum_i \ell'_i D_i = \ell'_1 D_1 + \ell'_2 D_2 + ... + \ell'_n D_n . \tag{8.45}$$

The assumptions for these models are that each laminate has uniform diffusive properties

248

and that the diffusive transport is uni-directional. The solids are also assumed to be impenetrable.

Series-parallel (SP) model

In the SP model (Crank (1975)) the composite is split into elements perpendicular to the streamwise direction (as illustrated by the series stacking in Figure 8.7 (p 248)), after which a diffusion coefficient is calculated for each element in terms of the diffusion coefficient of the composite using the parallel formula and, finally, by summing the elements in series an effective diffusion coefficient is obtained for the composite as a whole. Thus, in the SP-model the parallel formula (equation (8.45)) is applied first, followed by the series formula (equation (8.44)).

Parallel-series (PS) model

In the PS model (Crank (1975)) the composite is split into elements parallel to the streamwise direction (as illustrated by the parallel stacking in Figure 8.8 (p 248)), after which a diffusion coefficient is calculated for each element in terms of the diffusion coefficient of the composite using the series formula and, finally, by summing the elements in parallel an effective diffusion coefficient is obtained for the composite as a whole. Thus, in the PS-model the series formula (equation (8.44)) is applied first, followed by the parallel formula (equation (8.45)).

8.2.6   Weighted average of SP and PS models

The following weighted average of the SP and PS approximations was suggested by Bell & Crank (1974) to predict the diffusivity ratio:

$$\frac{D_{eff}}{D} \;=\; \theta \frac{D_{SP}}{D} \;+\; (1-\theta)\frac{D_{PS}}{D} \;, \tag{8.46}$$

where D_{SP} and D_{PS} are the estimates produced by the SP and PS models, respectively, and

$$\theta \;=\; 0.56 \;-\; 0.5\sigma \;+\; 0.4h \;, \tag{8.47}$$

where σ is the streamwise solid width and h is the so-called window space or rather transverse pore width. The latter dimensions used by Bell & Crank (1974) are indicated in Figure 8.9(a) (p 250).

The coefficients in equation (8.47) were derived for a square cell size of dimensions 1 by 1 and chosen such that the weighted average proposed by Bell & Crank (1974) would yield a reasonable fit for both the staggered and non-staggered arrays for all values of h and

(a) Notation used by Bell and Crank (1974)

(b) Notation used for 2D RUC model
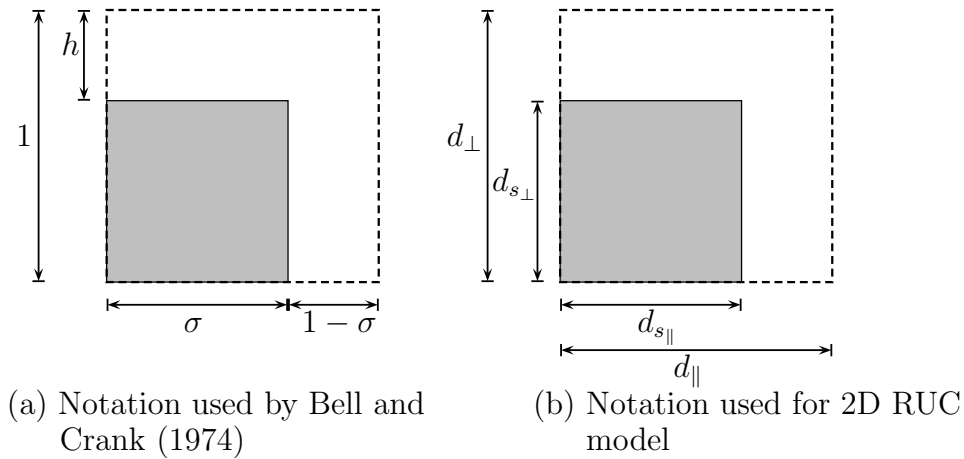
Figure 8.9: Illustration of the linear dimensions used in (a) Bell & Crank (1974) and (b) the numerical computations with the 2D RUC model.

σ. The parameters, h and σ, in equation (8.47) should therefore rather be expressed as a ratio of the cell size so that the expression for θ is dimensionless, i.e.

$$\theta = 0.56 - 0.5\frac{\sigma}{1} + 0.4\frac{h}{1}. \tag{8.48}$$

The linear dimensions used in the numerical computations with the 2D RUC model are shown in Figure 8.9(b). The streamwise and transverse solid widths are denoted by $d_{s_\parallel}$ and $d_{s_\perp}$, respectively, and the streamwise and transverse cell sizes by $d_\parallel$ and $d_\perp$, respectively.

8.2.7   Numerical computations

Bell & Crank (1974) obtained numerical solutions for the diffusivity ratio of two-dimensional arrays of impermeable solid rectangles. A finite-difference numerical method was used to solve Laplace's equation for various sizes of rectangles and for different staggered arrangements. The ends at $x = 0$ and $x = l$ were held at unit and zero concentrations, respectively. The diffusion coefficient, D, was assumed to be constant. The vertical and horizontal linear dimensions of the cell size were held fixed at unity, while h and σ were allowed to vary.

A similar numerical method was used in the present study to predict the diffusivity ratio for two-dimensional arrays of impermeable rectangles. A tri-diagonal matrix algorithm was used to compute the concentration gradients from the discritized form of equation (8.23) which was then used to calculate the diffusivity ratio from the diffusive flux. The diffusivity ratio is computed numerically for different arrays of solid rectangles, namely a regular array, a non-overlapping fully staggered array, an overlapping streamwisely fully staggered array and an overlapping transversely fully staggered array. The latter arrays are presented schematically in Figures 8.10 to 8.13 (pp 251-255), respectively.
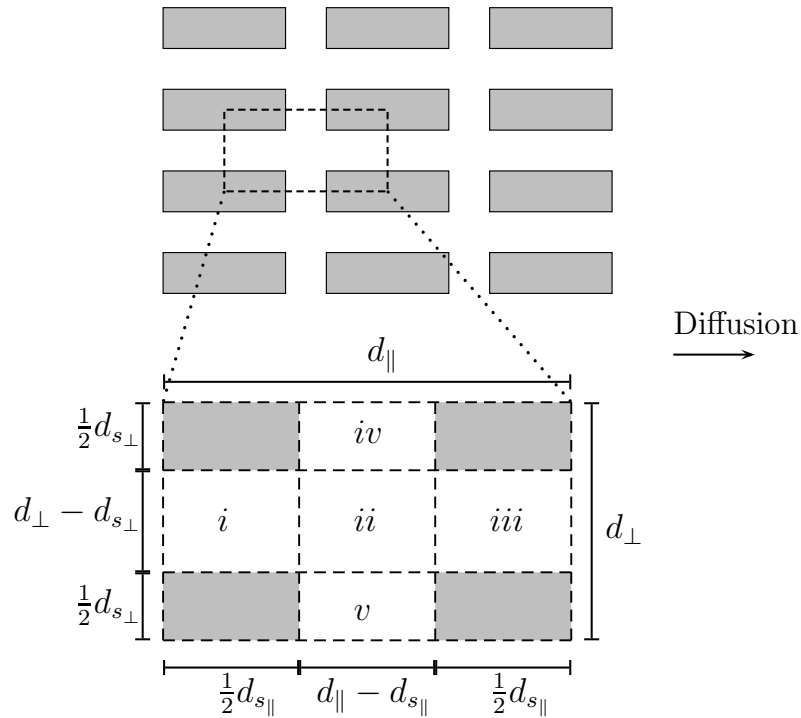
Figure 8.10: Unit cell of regular array.

For the regular array, non-overlapping fully staggered array and the overlapping stream-wisely fully staggered array the expressions for σ and h in RUC notation are given by $h = \frac{1}{2}(d_\perp - d_{s_\perp})$ and $\sigma = \frac{1}{2}d_{s_\parallel}$, as illustrated in Figures 8.10, 8.11 (p 253) and 8.12 (p 254), respectively. For the overlapping transversally fully staggered array $h = d_\perp - \frac{1}{2}d_{s_\perp}$ and $\sigma = \frac{1}{2}d_{s_\parallel}$, as illustrated in Figure 8.13 (p 255).

The derivation of the SP and PS models of only the regular array will be given. The SP and PS models for the other arrays can be derived in a similar way (Du Plessis (2010)). Only the results will be given in the present study (i.e. in Table 8.1, p 256).

Regular array

A schematic representation of a unit cell associated with a regular array is shown in Figure 8.10. In the regular array no staggering and no overlap of the solids occur in any of the two principal directions.

SP model

In the SP model the diffusion coefficients are first added along the columns marked i, ii

251

and iii, according to the parallel formula (equation (8.45)). For column i this yields

$$d_\perp D_i = d_\perp D - d_{s_\perp} D \qquad \text{so that} \qquad D_i = D \left(\frac{d_\perp - d_{s_\perp}}{d_\perp} \right) .$$

Similarly, for column ii,

$$d_\perp D_{ii} = d_\perp D \qquad \text{so that} \qquad D_{ii} = D .$$

For column iii,

$$d_\perp D_{iii} = d_\perp D - d_{s_\perp} D \qquad \text{which leads to} \qquad D_{iii} = D \left(\frac{d_\perp - d_{s_\perp}}{d_\perp} \right) .$$

Application of the series formula (equation (8.44)) then yields

$$\frac{d_\|}{D_{SP}} = \frac{d_{s_\|}/2}{D_i} + \frac{d_\| - d_{s_\|}}{D_{ii}} + \frac{d_{s_\|}/2}{D_{iii}} .$$

The diffusivity ratio according to the SP model is then given by

$$\frac{D_{SP}}{D} = \left[1 + \frac{d_{s_\|} d_{s_\perp}}{d_\|(d_\perp - d_{s_\perp})} \right]^{-1} . \tag{8.49}$$

PS model

In the PS model the diffusion coefficients are first added along the rows marked iv, ii and v, according to the series formula (equation (8.44)). For row ii this yields

$$\frac{d_\|}{D_{ii}} = \frac{\frac{1}{2}d_{s_\|}}{D} + \frac{d_\| - d_{s_\|}}{D} + \frac{\frac{1}{2}d_{s_\|}}{D} \qquad \text{so that} \qquad D_{ii} = D .$$

For rows iv and v:

$$D_{iv} = D_v = 0 .$$

Application of the parallel formula (equation (8.45)) yields

$$D_{PS}\, d_\perp = D_{ii}\, (d_\perp - d_{s_\perp}) .$$

The diffusivity ratio according to the PS model is then given by

$$\frac{D_{PS}}{D} = \frac{d_\perp - d_{s_\perp}}{d_\perp} . \tag{8.50}$$

252
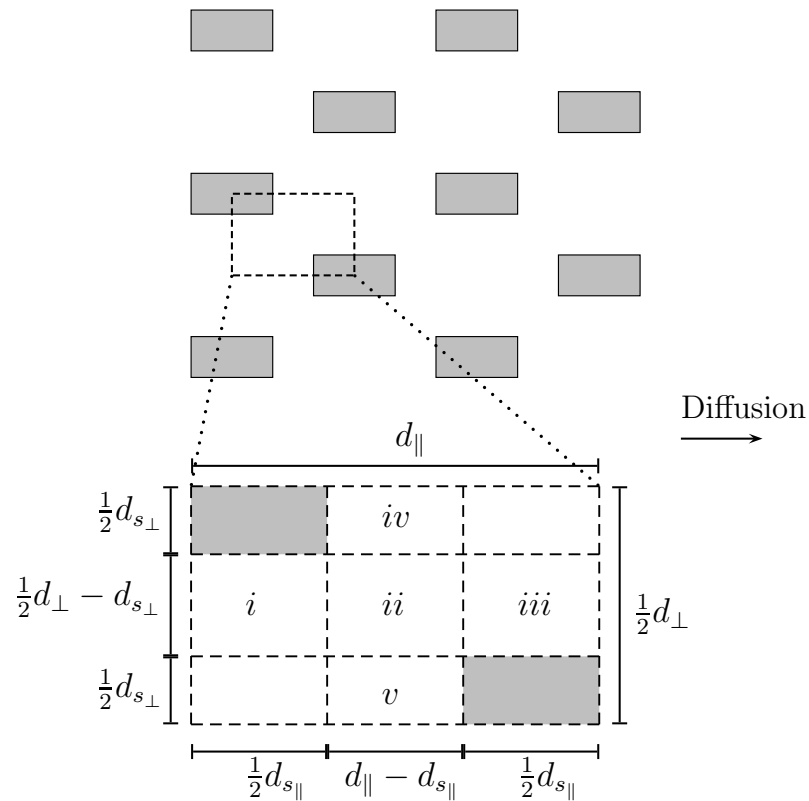
Figure 8.11: Unit cell of non-overlapping fully staggered array.

Non-overlapping fully staggered array

A schematic representation of a unit cell associated with a non-overlapping fully staggered array is shown in Figure 8.11. No overlap of the solids occurs in any of the two principal directions.

Overlapping streamwisely fully staggered array

A schematic representation of a unit cell associated with an overlapping streamwisely fully staggered array is shown in Figure 8.12 (p 254). Staggering and overlapping of the solids occur only in the streamwise direction.

Overlapping transversally fully staggered array

A schematic representation of a unit cell associated with an overlapping transversally fully staggered array is shown in Figure 8.13 (p 255). Staggering and overlapping of the solids

253
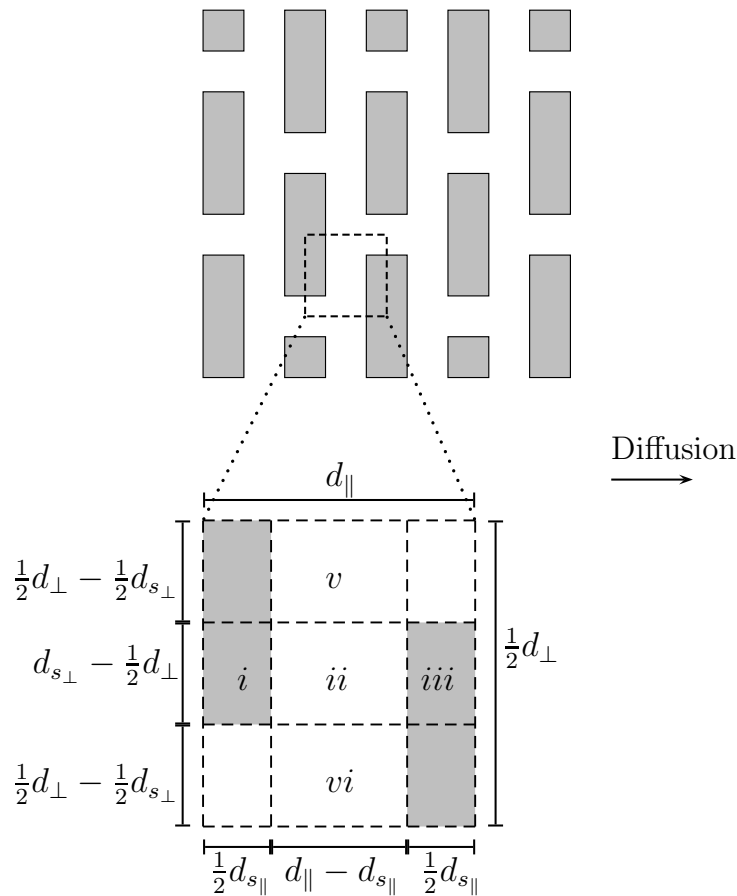
Figure 8.12: Unit cell of overlapping streamwisely fully staggered array.

occur only in the transverse direction.

Diffusivity ratios for arrays of rectangles

Table 8.1 (p 256) gives the expressions resulting from application of the SP and PS models to the unit cells of the respective arrays of rectangles in terms of $d_{\parallel}$, $d_{\perp}$, $d_{s_{\parallel}}$ and $d_{s_{\perp}}$.

8.2.8   Numerical results for arrays of solid rectangles

The numerical data obtained for D_{eff}/D as a function of the transverse pore width, h, (expressed as a percentage) is presented in Figure 8.14 (p 257). For $0 \leq h \leq 0.5$ the SP and PS models for the overlapping streamwisely fully staggered array were used (Table 8.1). For $0.5 \leq h \leq 1$ the SP and PS models for the non-overlapping fully staggered

254

Figure 8.13: Unit cell of overlapping transversally fully staggered array.

array were used. Also shown is the weighted average model of Bell & Crank (1974) (i.e. equations (8.46) and (8.47)) for all h-values. The value used for the streamwise solid width, σ, is 0.2. (Figure 8.14 (p 257) corresponds to Figure 9(a) given in Bell & Crank (1974).)

Numerical data were generated for a uniform grid as well as a non-uniform grid. Both grids produced roughly the same numerical data. The breakpoint at $100h = 50\%$ in Figure 8.14 of the weighted average of the SP and PS models proposed by Bell & Crank (1974) may be attributed to the fact that the PS model is zero for values of $100h = 50\%$ and below whereas above $100h = 50\%$ it abruptly follows a linear trend. This discontinuity is then reflected in the weighted average model. A physical explanation for the zero values of the PS model is simply due to the modelling procedure on which it is based. First the series formula (equation (8.44)) is applied to the hypothetical rows (v, ii and vi in Figure 8.12 (p 254)) constructed in the specific unit cell. For each row, the diffusion coefficient is zero due to solid obstructions within each row of the unit cell so that the diffusing species cannot exit the unit cell in the streamwise direction.

Figure 8.15 (p 257) is not given in Bell & Crank (1974). It presents D_{eff}/D as a function

255

Table 8.1: SP and PS models for arrays of rectangles.

Array	SP model	PS model
Regular array	$$\frac{D_{SP}}{D} = \left[1 + \frac{d_{s_\parallel} d_{s_\perp}}{d_\parallel (d_\perp - d_{s_\perp})}\right]^{-1}$$	$$\frac{D_{PS}}{D} = \frac{d_\perp - d_{s_\perp}}{d_\perp}$$
Non-overlapping fully staggered array	$$\frac{D_{SP}}{D} = \left[1 + \frac{d_{s_\parallel} d_{s_\perp}}{d_\parallel (d_\perp - d_{s_\perp})}\right]^{-1}$$	$$\frac{D_{PS}}{D} = \frac{d_\perp - 2d_{s_\perp}}{d_\perp}$$
Overlapping streamwisely fully staggered array	$$\frac{D_{SP}}{D} = \left[1 + \frac{d_{s_\parallel} d_{s_\perp}}{d_\parallel (d_\perp - d_{s_\perp})}\right]^{-1}$$	$$\frac{D_{PS}}{D} = 0$$
Overlapping transversally fully staggered array	$$\frac{D_{SP}}{D} = \frac{d_\parallel}{2d_\perp}\left[\frac{\frac{1}{2}d_\parallel d_\perp + \frac{1}{4}d_{s_\perp}(2d_{s_\parallel} - 3d_\parallel)}{(d_\perp - \frac{1}{2}d_{s_\perp})(d_\perp - d_{s_\perp})}\right]^{-1}$$	$$\frac{D_{PS}}{D} = \frac{d_\perp - d_{s_\perp}}{d_\perp}$$

of σ for the non-overlapping and overlapping transversally fully staggered arrays with $h = 0.8$.

For $0 \leq \sigma \leq 0.5$ the SP and PS models for the non-overlapping fully staggered array were used together with the weighted average model of Bell & Crank (1974). For $0.5 \leq \sigma \leq 1$ the SP and PS models for the overlapping transversally fully staggered array were used.

Although only plotted figures of *staggered arrays* of rectangles are given, similar figures for the regular arrays of rectangles can be constructed in which either the transverse pore width, h, or the streamwise solid width, σ, may be varied.
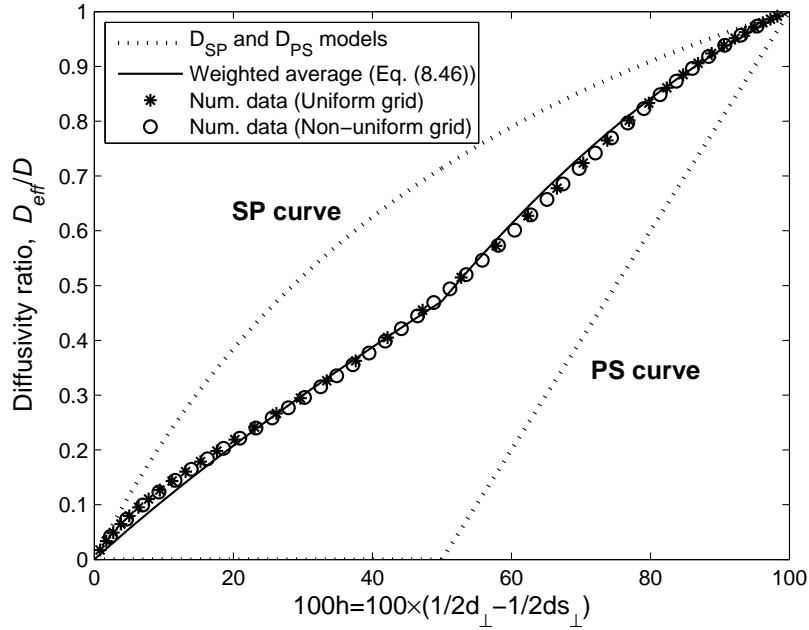
Figure 8.14: Diffusivity ratio for the non-overlapping and overlapping streamwisely fully staggered arrays as a function of h for $\sigma = 0.2$.
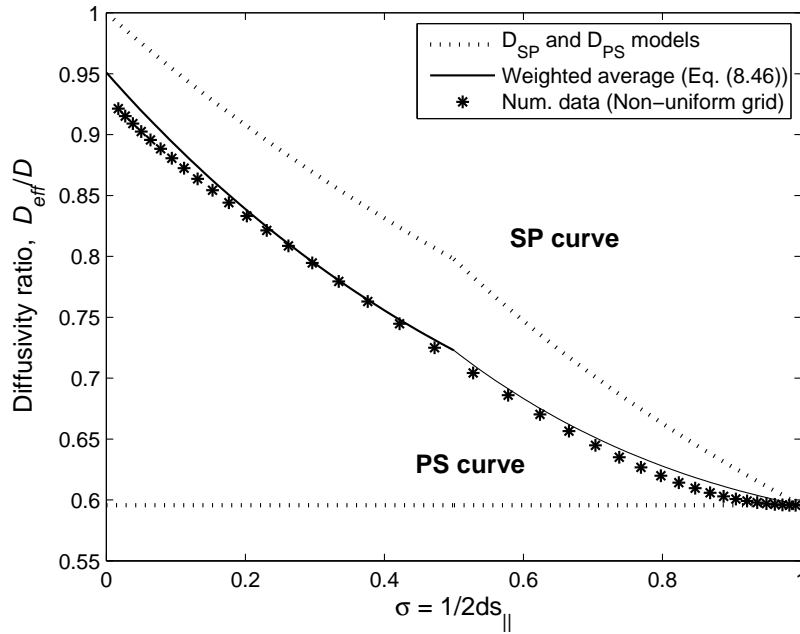
Figure 8.15: Diffusivity ratio for the non-overlapping and overlapping transversally fully staggered arrays as a function of σ for $h = 0.8$.
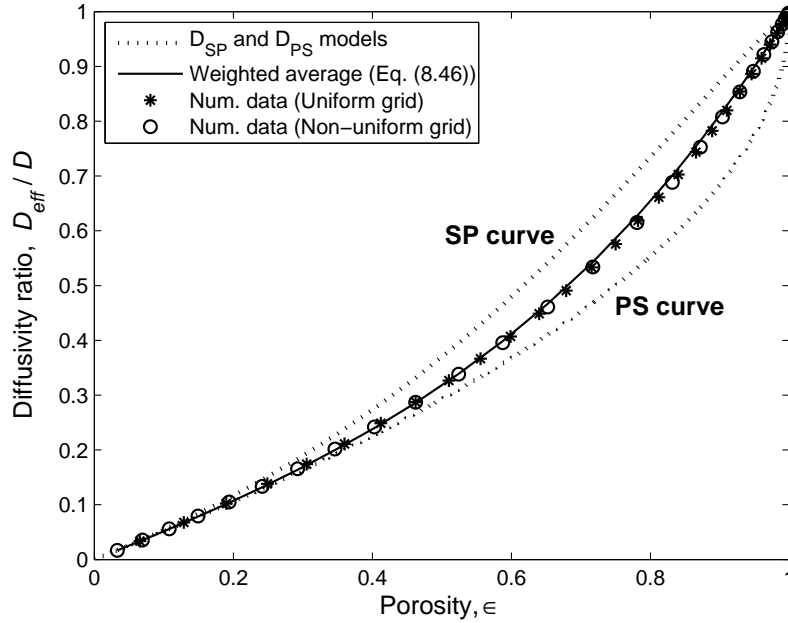
Figure 8.16: Diffusivity ratio for a regular array of squares as a function of porosity.

8.2.9 Numerical results for arrays of solid squares

The diffusivity ratios for arrays of solid squares can be obtained by setting $d_\parallel = d_\perp = d$ and $d_{s_\parallel} = d_{s_\perp} = d_s$ in the expressions presented in Table 8.1 (p 256). Expressions for the SP and PS models as a function of porosity alone can then be obtained for both the 2D and 3D RUC models by making use of equations (3.20) and (3.61), respectively, which relate the linear dimensions of the respective RUC models to the porosity. Figure 8.16 shows the diffusivity ratio for a regular array of solid squares as a function of porosity. The correspondence with the weighted average model of Bell & Crank (1974) is satisfactory.

The numerical computations for a fully staggered array of solid squares cannot be obtained by using a cell size of dimensions 1 by 1. This is because the solid squares begin to physically intersect and overlap at porosities of 0.5 and lower. In order to obtain values for the diffusivity ratio over the entire porosity range, i.e. from zero to unity, a cell size with a streamwise dimension of 2 and a transverse dimension of 1 was used. The numerical data for a fully staggered array of squares is shown in Figure 8.17 (p 259). The weighted average model of Bell & Crank (1974) (i.e. equations (8.46) and (8.47)) does not agree well with the numerical data. The reason for this is because the coefficients of the weighted average model are only applicable to a cell size of 1 by 1 (equation (8.48)). This may be the reason why Bell & Crank (1974) did not present a figure such as Figure 8.17 in their work.

In Figure 8.18 (p 259) the numerical data obtained for a fully staggered array of squares is compared to numerical and experimental data from the literature.
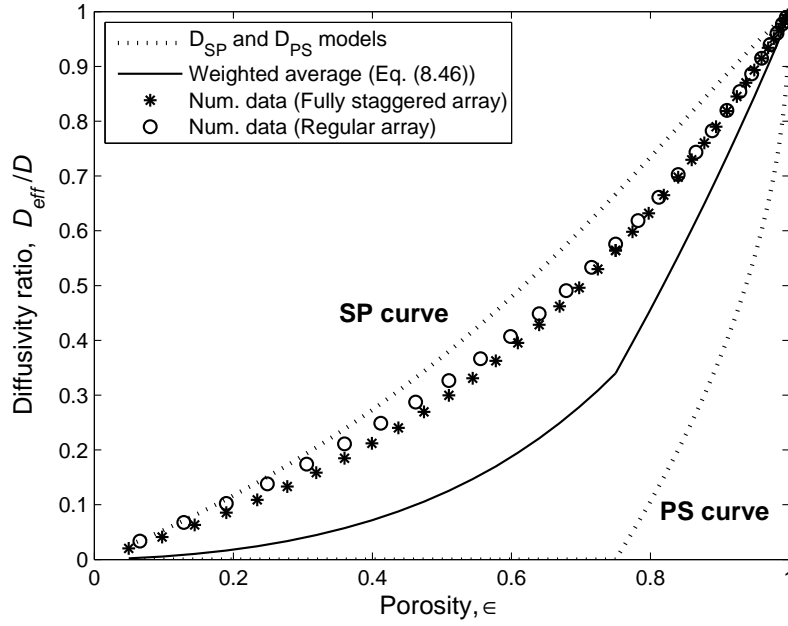
Figure 8.17: Diffusivity ratio for a fully staggered array of squares as a function of porosity.
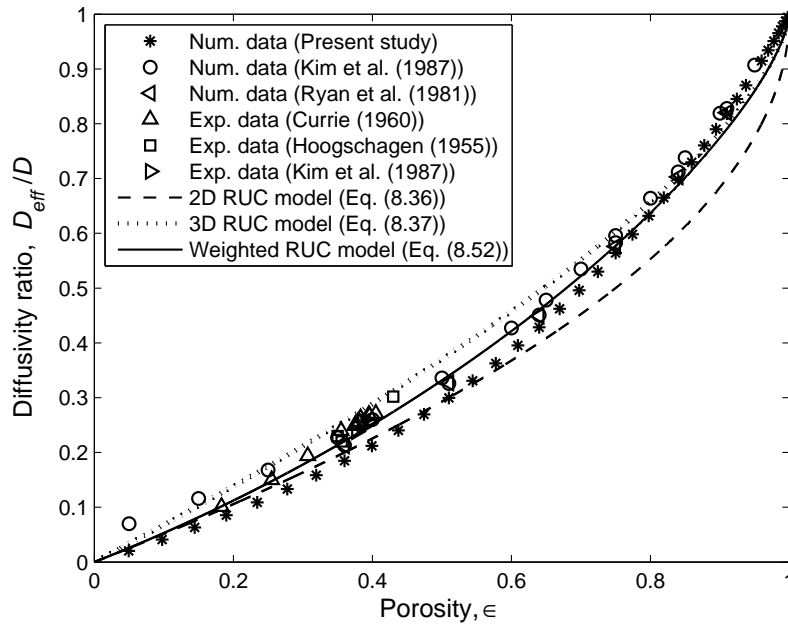
Figure 8.18: Diffusivity ratio for a fully staggered array of squares predicted by the 2D and 3D fibre RUC models.

Also shown in Figure 8.18 (p 259) are the model predictions of the 2D and 3D RUC models. Both models show satisfactory agreement with the data. The present study therefore confirms findings from the literature that two-dimensional geometric models are adequate to predict the diffusivity ratio of unconsolidated isotropic porous media. The physical reason as to why this is the case is (to the knowledge of the author of this dissertation) given nowhere in the literature and therefore still remains unknown. Although both the 2D and 3D RUC models provide adequate predictions, the diffusivity ratio predicted by the 2D model is less accurate than the 3D model at high porosities whereas the 3D model is less accurate than the 2D model at low porosities. In this regard, a weighted average is performed on the two RUC models such that at low porosities the resulting weighted average model approximates the 2D RUC model and at high porosities it approximates the 3D RUC model. The resulting weighted average model, which is similar the weighted average model of Bell & Crank (1974), is given by

$$\left(\frac{D_{eff}}{D}\right)_{RUC} = (1-\epsilon)\left(\frac{D_{eff}}{D}\right)_{2D} + \epsilon\left(\frac{D_{eff}}{D}\right)_{3D} , \qquad (8.51)$$

or as a function of porosity,

$$\left(\frac{D_{eff}}{D}\right)_{RUC} = (1-\epsilon)(1 - \sqrt{1-\epsilon}) + \epsilon\left(1 - (1-\epsilon)^{2/3}\right) . \qquad (8.52)$$

The weighted average RUC model for a fully staggered array of squares is shown in Figure 8.18. The agreement of the weighted average RUC model with the numerical and experimental data over the entire porosity range is satisfactory. The weighted average RUC model thus provides an alternative to the weighted average model of Bell & Crank (1974) which fails for a fully staggered array of squares with a cell size of 2 by 1.

In Figure 8.17 (p 259) it is shown that the numerical data obtained for a fully staggered array of squares almost coincide with the data obtained for a regular array and may be regarded as essentially the same. Although this result is not expected, due to the difference in the tortuous pathlines between a fully staggered and regular array, these findings agree with the numerical results of Crank (1975) which confirm that the values of D_{eff}/D obtained for the non-staggered and staggered arrays differ by only 2 or 3%. The numerical data of Ryan et al. (1981) showed this difference to be only 1%. These findings are also supported by Whitaker (1969) and Kim et al. (1987) and in effect justifies the use of the geometric factor in the expression for the diffusivity ratio rather than the tortuosity.

8.3 Contributions of previous authors to the RUC model

Below is a time-line, in authors-year format, of authors who have contributed to *applications* of the various RUC models. In Table 8.2 (p 262) the authors are categorized

according to the respective RUC models they have worked on and in Table 8.3 (p 263) the specific fields of application of the various authors are indicated.

Roos (1992) used the foam RUC model of Du Plessis & Masliyah (1988), the granular RUC model of Du Plessis & Masliyah (1991) and the fibre RUC model of Du Plessis (1991)) to predict the permeability of synthetic membranes. The predictive equations were simplified by means of a series truncation and the errors introduced by the truncations were investigated. For the granular model a throwback method was applied at a certain porosity to minimize the error introduced by the series truncation. A two-dimensional FORTRAN-code, based on the control-volume discretization method of Patankar (1980), was implemented to simulate flow through the membranes. This work was published by Du Plessis (1992).

Diedericks (1992) derived the macroscopic mass balance equation for a tracer traversing a porous medium. The foam RUC model of Du Plessis & Masliyah (1988) and the granular RUC model of Du Plessis & Masliyah (1991) were used to obtain a macroscopic expression for the dispersive flux in the absence of molecular diffusion.

Du Plessis & Roos (1993) simplified the equations produced by the granular RUC model of Du Plessis & Masliyah (1991) for predicting the permeability through very low porosity granular porous media.

Du Plessis & Van der Westhuizen (1993) used the fibre RUC model to predict the pressure drop over heat transfer tube banks.

Du Plessis & Roos (1994a) improved the simplified equations of the granular RUC model of Du Plessis & Roos (1993) by incorporating the modelling procedure of Du Plessis & Van der Westhuizen (1993).

Du Plessis & Roos (1994b) adapted the modelling procedure of the granular RUC model of Du Plessis & Masliyah (1991) to predict the permeability of very low porosity sandstones in which the effect of blocked throats was accounted for.

Van der Westhuizen & Du Plessis (1994) proposed, in addition to the fibre RUC model of Du Plessis (1991) for cross-flow, a fibre RUC model for longitudinal flow, i.e. flow parallel to the prism axis. For low porosities the friction factor for square duct flow, proposed by Shah & London (1978), was used and for higher porosities the friction factor for flow between parallel plates was used. The power addition technique (Churchill & Usagi (1972)) was used to present a unified expression for the permeability applicable over the entire porosity range.

Du Plessis & Roos (1995) used the granular RUC model, based on the modelling procedure of Du Plessis & Van der Westhuizen (1993), to analyze numerically the effect of near-wall channeling in a packed bed where the average porosity varies with distance from the container wall.

Table 8.2: Applications of the various RUC models.

	RUC model		
Reference	**Granular**	**Foam**	**Fibre**
Roos (1992) and Du Plessis (1992)	×	×	×
Diedericks (1992)	×	×	
Du Plessis & Roos (1993)	×		
Du Plessis & Van der Westhuizen (1993)			×
Du Plessis & Roos (1994a) and			
Du Plessis & Roos (1994b)	×		
Van der Westhuizen & Du Plessis (1994)			×
Du Plessis & Roos (1995)	×		
Van der Westhuizen & Du Plessis (1996)			×
Diedericks & Du Plessis (1996)	×	×	×
Diedericks & Du Plessis (1997)		×	
Smit (1997)	×	×	×
Smit & Du Plessis (1997)	×		
Diedericks et al. (1998)		×	
Diedericks (1999)	×	×	×
Smit & Du Plessis (1999)		×	
Du Plessis (1999)	×		
Smit & Du Plessis (2000)	×	×	×
Fourie & Du Plessis (2002) and		×	
Du Plessis (2002) and Smit et al. (2007)			×
Smit et al. (2005)		×	
Crosnier et al. (2006)		×	
Woudberg (2006)	×		
Molale (2007)			×
Rautenbach (2009)	×	×	
De Wet (2010) and De Wet et al. (2011)	×		

Table 8.3: Specific applications of the various RUC models.

Reference	Application
Roos (1992) and Du Plessis (1992)	Synthetic membranes
Diedericks (1992)	Tracer dispersion
Du Plessis & Roos (1993)	Low porosity granular media
Du Plessis & Van der Westhuizen (1993)	Heat transfer tube banks
Du Plessis & Roos (1994a) and	
Du Plessis & Roos (1994b)	Sandstones
Du Plessis & Roos (1995)	Near-wall channeling
Van der Westhuizen & Du Plessis (1996)	Woven roving cloth
Diedericks (1999) and	
Diedericks & Du Plessis (1996)	Electrical conductance
Diedericks & Du Plessis (1997)	Anisotropic foamlike media
Smit (1997)	Non-Newtonian flow
Smit & Du Plessis (1997)	Power-law flow
Diedericks et al. (1998)	Multifilament knit
Smit & Du Plessis (1999)	power-law flow
Du Plessis (1999)	Sandstones
Smit & Du Plessis (2000)	Non-Newtonian flow
Fourie & Du Plessis (2002)	Metallic foams
Du Plessis (2002) and Smit et al. (2007)	Timber-drying kiln
Smit et al. (2005)	Non-Newtonian flow
Crosnier et al. (2006)	Metallic foams
Woudberg (2006)	Non-Newtonian flow,
	fluidized beds and sandstones
Molale (2007)	Timber-drying kiln
Rautenbach (2009)	CO_2 absorption tower & Fluidized beds
De Wet (2010) and De Wet et al. (2011)	Fluidized beds & Non-Newtonian flow

263

Van der Westhuizen & Du Plessis (1996) made use of the fibre RUC model of Du Plessis & Van der Westhuizen (1993) and constructed an alternative fibre RUC model to predict the permeability of woven roving clothing.

Diedericks & Du Plessis (1996) and Diedericks & Du Plessis (1997) used the granular RUC model of Du Plessis (1994), the foam RUC model of Du Plessis et al. (1994) and the fibre RUC model of Du Plessis & Van der Westhuizen (1993) to predict the formation factor for electrical conduction, i.e. charge transport in isotropic porous media.

Diedericks et al. (1998) used the anisotropic foam model of Diedericks & Du Plessis (1997) to predict the pressure drop over a highly porous multifilament knit.

Smit (1997) adapted the modelling theory of Du Plessis & Van der Westhuizen (1993) to predict time-independent purely viscous non-Newtonian flow through all three RUC models. Different streamwise and transverse average channel velocities were assumed. The dependence of the apparent viscosity on the shear rate was incorporated through the wall shear stress. A generalized shear-thinning model was proposed for predicting shear-thinning flow in all three RUC models. The modelling theory was furthermore extended to account for normal stress effects due to the extensional nature of polymeric liquids. The granular RUC model for predicting power-law flow was published by Smit & Du Plessis (1997) and the adaptation of the foam RUC model to predict power-law flow was published by Smit & Du Plessis (1999). The generalized shear-thinning model and the adaptation of the granular RUC model to account for normal stress effects were published by Smit & Du Plessis (2000).

Du Plessis (1999) adapted the modelling theory of Du Plessis & Roos (1994b) to account for pore blockage in very low porosity sandstones.

Fourie & Du Plessis (2002) proposed an alternative geometric pore-scale model for foam-like media. The objective was to improve on the empirical approach of Du Plessis et al. (1994) for determining the linear dimension d for isotropic cellular high porosity metal-lic foams so that no information regarding the flow behaviour of the particular metallic foam need to be known beforehand. A morphological model was introduced in which each strut of the foam is approximated by a prism of uniform triangular cross-section and arranged to form the edges of an array of tetrakaidecahedra to account for the lump of solid material at the intersection of struts.

Du Plessis (2002) and Smit et al. (2007) applied the anisotropic fibre RUC model of Diedericks (1999) to cross-flow in tube-banks and airflow through a stack in a timber-drying kiln. Both staggered and non-staggered arrays were considered and experimental data was generated for a scale model of a timber stack in a wind tunnel. The center part of the timber stack was modelled with a standard duct flow model while flow through the staggered timber stack ends, resulting from the mode of stacking, was modelled by application of the fibre RUC model of Van der Westhuizen & Du Plessis (1994).

Smit et al. (2005) improved on the modelling procedures of Smit & Du Plessis (1999) and Smit & Du Plessis (2000) involving the RUC model for foamlike media. Stagnant fluid

volumes were accounted for and the Lloyd correction (Section 4.4.1, p 85) was introduced into the modelling procedure to predict shear-thinning power-law flow in the Darcy regime.

Crosnier et al. (2006) also introduced stagnant fluid volumes and the Lloyd correction (Section 4.4.1) into the modelling procedure of the foam RUC model and applied the doubly staggered foam RUC model to predict the pressure drop over high porosity aluminium and stainless steel foams.

Molale (2007) verified numerically the experimental data of Du Plessis (2002) for airflow through a stack in a timber-drying kiln. The model predictions of Diedericks (1999), Lloyd et al. (2004) and Cloete (2006) were also compared to the experimental and numerical data. The models of Diedericks (1999) and Lloyd et al. (2004) provided satisfactory agreement with the data.

Rautenbach (2009) applied the granular RUC model of Du Plessis & Woudberg (2008) and the foam RUC model of Crosnier et al. (2006) to a CO_2 cooling tower with raschig rings as packing material. The porosity was adapted by incorporating the Sonntag correction according to which approximately 20% of the inner volume of a raschig ring is available for flow. The singly staggered foam model yielded more accurate predictions for the pressure drop than the doubly staggered model which is a confirmation of the presence of stagnant fluid volumes. The granular RUC model was also used to predict the minimum fluidization velocity of a fluidized bed with spherical glass particles as packing material.

De Wet (2010) and De Wet et al. (2011) applied the granular RUC model of Du Plessis & Woudberg (2008) to predict the pressure drop and minimum fluidization velocity of fluidized beds.

8.4   Contributions of the author of this dissertation

Below is a summary of the research papers of which the author of this dissertation is a co-author. First a description of the content of each paper will be given, followed by the reference.

Woudberg (2006) adapted the analytical modelling procedure of Smit & Du Plessis (2000), involving the granular RUC model, to predict shear-thinning power-law flow in the Darcy regime by introducing stagnant fluid volumes and the Lloyd correction (Section 4.4.1) into the modelling procedure. The dependence of the apparent viscosity on the shear rate was incorporated through the wall shear stress. A unified equation was also proposed for the wall shear stress applicable over the entire shear rate domain. Satisfactory agreement was obtained between the predicted and experimental pressure drop values. This work was published in:

Woudberg, S., Du Plessis, J.P. and Smit, G.J.F. (2006). *Non-Newtonian purely viscous flow through isotropic granular porous media*, Chemical Engineering Science, vol.

61, no. 13, pp. 4299-4308.

Woudberg (2006) also adapted the granular RUC model to serve as drag model in a
fluidized bed and predicted the minimum fluidization velocity. A drag term applicable
at high porosities was added to the granular model for it to be applicable over the wide
porosity range associated with fluidized beds. It was found that the computational bubble
behaviour is influenced significantly by the drag model used in the numerical simulations.
The adapted RUC model was used to determine the drag at different radial positions from
the center of the bed, as the drag is directly related to the particle concentration. The
drag model was also used to determine the bed expansion as this may influence continuous
bubble formation over time and the symmetry of the bed regarding bubble formation. At
the time when the first bubble erupted during fluidization, the RUC drag model gave the
best agreement with the experimental bubble (of all the drag models used) according to
shape and size. This work was published in:

B.M. Halvorsen, Du Plessis, J.P. and **Woudberg, S.** (2006). *The performance of drag
models on flow behaviour in the CFD simulation of a fluidised bed*, Advances in Fluid
Mechanics (Editors: Rahman, M. & Brebbia, C.A.), Proceedings of the Sixth Inter-
national Conference on Advances in Fluid Mechanics (AFM VI), vol. VI, Skiatos,
Greece, 8-10 May 2006, WIT Press, United Kingdom, pp. 3-12.

The granular and foam RUC models presented in Chapters 3 and 4 were adapted to
predict the pressure drop over a packed bed with raschig rings as packing material. A
shape factor was introduced as well as the Sontagg correction according to which only
20% of the inner volume of a Raschig ring is available for flow. The model prediction
for the pressure drop was in satisfactory agreement with the experimental pressure drop
data. This work was published in:

Rautenbach, C., Halvorsen, B.M., Du Plessis, E., **Woudberg, S.** and Du Plessis, J.P.
(2009). *Measurement and prediction for air flow drag in different packing materials*,
Computational Methods in Multiphase Flow V (Editors: A.A. Mammoli and C.A.
Brebbia), Proceedings of the Fifth International Conference on Computational and
Experimental Methods in Multiphase and Complex Flow (Multiphase Flow V), New
Forest, UK, 15-17 June 2009, WIT Press, United Kingdom, pp. 409-419.

The permeability predictions of the granular and fibre RUC models presented in Chapters
3 and 4 were used to investigate the effect of rough surfaces on laminar liquid flow in micro-
channels. The rough surface is regarded as a porous layer. To obtain an analytical solution
the entire domain was split into two regions, i.e. a porous layer domain and an open
channel domain. To account for discontinuities between the porous layer and the open
channel a function was introduced that smooths out the porosity variation between the
two regions. Volume averaging of the momentum transport and continuity equations was
performed over the two domains together with appropriate coupling boundary conditions.
Numerical computations were performed and the transport equations solved in the two

flow domains subject to two appropriate interfacial boundary conditions, i.e. one for the
pressure and another for the jump in stress. Satisfactory agreement was obtained between
the numerical and analytical predictions for the dimensionless pressure gradient. This
work was published in:

> Izquierdo, S., Valdés, J.R., Martínez, M., Accolti, M., **Woudberg, S.**, Asinari, P.,
> Miana, M. and Du Plessis, J.P. (2010). *Porous-layer model for laminar liquid flow in
> rough microchannels*, Microfluidics and Nanofluidics, vol. 9, no. 6, pp. 1063-1075.

The granular RUC model presented in Chapters 3 and 4 was used to predict the pressure
drop over a fluidized bed consisting of spherical glass particles through which air was
forced upwards. The pressure drop predicted by the granular model was used as lower
asymptote in the power addition technique (Churchill & Usagi (1972)). The constant
pressure drop that prevails after the bed is fluidized is used as the higher asymptote to
obtain a unified expression for the pressure drop. In the vicinity of the critical point,
i.e. the point of intersection between the two asymptotes, a hump was observed in the
experimental data such that some data points crossed the upper limit. The amended
power addition technique of Churchill & Usagi (1974) was then applied, which, with a
suitable choice of shifting exponent resulted in a satisfactory model prediction for the
pressure drop over the bed. This work was published in:

> De Wet, P.D., Du Plessis, J.P. and **Woudberg, S.** (2011). *Application of power ad-
> dition as modelling technique for flow processes: Two case studies*, Chemical Engineer-
> ing Science, vol. 66, no. 9, pp. 1923-1931.

8.5   Summary

The permeability predictions of the transversely isotropic granular and foam RUC models
are adapted to predict the permeability of Fontainebleau sandstone for samples of different
grain diameters. In both RUC models the average grain diameter of a sample is used as
linear dimension. The effect of blocked throats at very low porosities is accounted for in the
permeability predictions by expressing the effective or backbone porosity in terms of the
percolation threshold porosity and by application of the power addition technique. The
percolation threshold porosity was determined from the experimental data. Equations
are proposed for determining the percolation threshold porosity of a sandstone sample if
the average grain diameter of the sample is known as well as the percolation threshold
porosity and grain diameter of another sample. It is found that the effect of blocked
throats at very low porosities has a significant effect on the permeability prediction.

Although both the granular and foam RUC model predictions provide satisfactory enclo-
sure of the experimental data between the two limiting grain diameter values, the enclosure
of the experimental data by the granular model is much more refined than that of the
foam model. The microscopic geometry of Fontainebleau sandstone may therefore be re-

garded to exhibit both granular and tubular properties, with the granular characteristics being more prominent. This supports findings from the literature to treat Fontainebleau sandstones as consolidated or unconsolidated media.

Predictions for the diffusivity ratio of unconsolidated arrays of squares and cubes are obtained by application of the 2D (fibre) and 3D (granular) RUC models, respectively. It is assumed that the diffusion process is isotropic and that the fluid is stationary. The RUC model predictions for the diffusivity ratio are expressed in terms of the geometric factor rather than the geometrical tortuosity, since the geometric factor yields the same expression for a fully staggered and regular array, whereas this is not the case with the tortuosity. This is supported by findings from the literature that the diffusivity ratio is essentially equal for the streamwise and transverse directions of a fully staggered array. The geometric factor, as opposed to the tortuosity, furthermore takes into account diffusion that may take place in the hydrodynamically stagnant fluid volumes. The final equation for the diffusivity ratio predicted by both models is a function of the porosity alone which confirms findings from the literature that this should be the case for unconsolidated isotropic systems. By making use of the RUC theory it is shown that there is physical meaning behind the equation often used, and simply just provided in the literature, to predict the diffusivity ratio (i.e. equation (8.31)). Satisfactory correspondence is obtained between the RUC model predictions and other model predictions and experimental data from the literature. The close correspondence between the model predictions of the 2D and 3D RUC models once again confirms findings from the literature that for unconsolidated isotropic porous media 2D models are adequate to predict the effective diffusivity.

Numerical computations are performed to compute the diffusivity ratio for two-dimensional staggered and non-staggered arrays of solid rectangles. Satisfactory agreement is obtained between the weighted average model of Bell & Crank (1974) and the numerical data for solid rectangles. The numerical data obtained for the regular array of squares correspond satisfactorily with the weighted average model of Bell & Crank (1974). For the fully staggered array of squares significant discrepancies are observed. This is because the weighted average model of Bell & Crank (1974) is not applicable for cell sizes other than 1 by 1, i.e. it is only applicable for square unit cells. A weighted average RUC model is proposed instead. This is done because the 2D model yields more accurate predictions at low porosities and the 3D model, on the other hand, yields more accurate predictions at high porosities. According to findings from the literature 2D models are adequate to predict the effective diffusivity of unconsolidated isotropic porous media. The physical reason as to why this is the case still remains unknown. The numerical data obtained for both the non-staggered (i.e regular) array and staggered (i.e. fully staggered) array of squares are essentially the same which also agrees with the findings from the literature. The weighted average RUC model is applicable over the entire porosity range for both staggered and non-staggered arrays of solid squares (or cubes).

Lastly, a summary is given of contributions made to the RUC models by previous authors over the past three decades, with emphasis on the involvement of the author of this dissertation in some of the applications.

Chapter 9

Concluding remarks

The aim of this chapter is to give the contributions of the author to this study and give concluding remarks and recommendations for future work.

9.1 Overall contributions of the author of this dissertation

A unified and refined analytical closure modelling procedure is presented for the three RUC models resembling granular media, foamlike media and fibre beds.

The modelling procedures for each type of porous medium have been presented independently in the past. The validity of assumptions made in each of the separate modelling procedures, previously presented, had to be confirmed to ensure its applicability to the other model geometries. A generalized mathematical definition was proposed for the coefficient ξ that is applicable to all three RUC models. Previously, only the coefficient β was defined mathematically. The Lloyd correction was also verified for the fully staggered array of the fibre RUC model. The concept of transverse isotropy was furthermore introduced for the RUC models. Previously all three models were simply assumed to be isotropic, which, for the rectangular geometry of the RUC models, is less justifiable than the assumption of transverse isotropy. Weighted averages were applied to the coefficients of the staggered and non-staggered arrays of the unconsolidated models to provide transversely isotropic granular and fibre RUC models.

The streamwise pressure drop prediction of the foam RUC model presented in this study differs from the model predictions provided by Crosnier et al. (2006). These authors have also incorporated the Lloyd correction in the closure modelling procedure at higher Reynolds numbers. There is no evidence for the scientific correctness for such an approach,

269

since Lloyd et al. (2004) have verified numerically the validity of the Lloyd correction only in the Darcy regime where only low porosities were considered due to the assumption of flow between parallel plates. In the opinion of the author, the Lloyd correction will not be applicable in the higher Reynolds number limit where only high porosities are considered in the model, since the assumption of flow between parallel plates is no longer applicable in this limit.

The streamwise pressure drop prediction of the foam RUC model presented in this study also differs from the model predictions provided by Wilms (2006). She has weighed the surface integral not only in the lower Reynolds number limit, as was done in Section 4.2 (p 82), but also in the higher Reynolds number limit. This weighted average was not performed in the present study for the higher Reynolds number limit, because it is argued that there will be only one type of RUC to be considered. This is because interstitial recirculation is assumed to be present and the form drag condition is inferred which makes it a high porosity model.

It is illustrated that the direct analytical modelling procedure leads to the same result as the one based on volume averaging.

> Firdaouss & Du Plessis (2004) showed for the fibre model that the direct modelling procedure and the one based on volume averaging leads to the same result. In the present study it was confirmed that the direct modelling procedure is also applicable to the granular and foam RUC models. Although the direct approach is much shorter and compact, it is restricted to uniformly sized solids, since this is the only manner in which homogeneity is obtained when working with a unit cell.

The importance of providing accurate relations between the RUC pore-scale linear dimensions, and those of models from the literature based on other geometries was emphasized as well as its relation to actual measured dimensions. These relations affect the accuracy of the model predictions significantly, since the permeability, for instance, is a function of the square of the linear dimension. An additional three-dimensional foam diameter was introduced which improved the permeability prediction of the foams studied experimentally by Bhattacharya et al. (2002). Which diameter to use in the model predictions depends on how the actual dimension was measured. In the case of foams, either a cross-sectional pore diameter is measured from a two-dimensional image or a three-dimensional pore diameter is measured at a different angle than the two-dimensional one. The angle at which the measurement is performed will be the angle with respect to the streamwise direction at which the fluid flows perpendicular through the pore 'window'. The three-dimensional pore diameter will therefore represent the diameter of the pore window 'seen' by the fluid.

It is shown that the granular RUC model presented in this study is an improvement on the granular RUC models of Du Plessis & Masliyah (1991) and Du Plessis (1994).

270

It is furthermore shown that the granular RUC model can be regarded as qualitative and quantitative proof of the semi-empirical Ergun equation.

Since the analytical modelling procedure presented, is based on sound physical principles, the granular RUC model prediction can be regarded as a theoretical derivation of the Ergun equation. The granular RUC model provides expressions for the coefficients A and B of the Ergun equation as a function of porosity. The model prediction for the coefficient A is within 2% from the empirical value for A and the model prediction for the coefficient B corresponds exactly to the empirical value. It was also shown that the predictive equations can be simplified by application of series expansion of the powered terms together with the method of throwback.

It is satisfactory that it became clear from this study that the *transversely isotropic* foam RUC model is one of only four well recognized geometrical models for foamlike media in the literature. It was therefore meaningful in this study to adapt a model that has already received recognition in the literature, as it is a sound basis to work from. It was also shown that the foam RUC model predicts dynamic specific surfaces area values that are of the same order of magnitude as other model predictions from the literature. An advantage of the foam RUC model is that either the strut diameter or pore diameter needs to be known in order to predict the dynamic specific surface. This is not the case for the model predictions considered from the literature in which both the strut and pore diameters need to be known.

An Ergun-type equation is proposed for foamlike media.

The interstitial geometric configuration and the accompanying flow conditions were remodelled for foamlike media to obtain an expression for the streamwise pressure gradient that has a different functional dependency on porosity than in the case of granular media. It was shown that the empirical coefficients of the Ergun-type equation proposed by Dietrich et al. (2009) indeed have physical meaning by quantification thereof in terms of the geometric factor, which is a function of porosity. At an average porosity of $\epsilon = 0.79$ the foam RUC model predicts values for the coefficients $A^{'}$ and $B^{'}$ that are within 1% and 17%, respectively, of the corresponding empirical values. The latter percentage value still lies within the experimental error range of $\pm 20\%$ given by Dietrich et al. (2009).

It is shown that the same hydraulic diameter cannot be used when the pressure drop predicted by foamlike media (of average porosity, 0.80) is compared to the pressure drop predicted by granular media (of average porosity, 0.43).

The reason for this can be attributed to the different porous medium morphologies. The hydraulic diameter for foamlike media at $\epsilon = 0.80$ is higher than the hydraulic diameter for granular media at $\epsilon = 0.43$. The pressure gradient predicted by the granular RUC model at $\epsilon = 0.43$ and in which the same hydraulic diameter is used

as in the foam RUC model, is 80% higher than the pressure gradient predicted by the foam RUC model. If the lower value for the hydraulic diameter is used in the granular RUC model, the pressure gradient prediction increases with another 72%, which is a significant difference. The pressure drop predicted by the granular RUC model at $\epsilon = 0.43$ and in which the lower hydraulic diameter is used, is thus in total 152% higher than that predicted by the foam RUC model at $\epsilon = 0.80$.

The versatility of the RUC model is emphasized by the constancy of the Kozeny constant at a value of 5 in the range, $0.2 < \phi < 0.60$, by both the fibre and granular RUC models.

The relative percentage difference in the Kozeny constant predicted by the granular RUC model in the porosity range, $0.4 < \epsilon < 0.6$, is less than 3.5% from the constant average value of 5. For the fibre RUC model the relative percentage difference is less than $\pm20\%$. This confirms that the rectangular geometry on which the RUC models are based is adequate in approximating the pore-scale geometry of packed beds of granular media and fibre beds.

Equations are proposed to predict the critical Reynolds number for granular media and fibre beds as a function of porosity.

Similar equations could not be found in the literature. The critical particle Reynolds number range predicted by the fibre RUC model for the porosity range, $0.1 \leq \epsilon \leq 0.8$, is found to be three times lower than the range predicted by the granular RUC model. The RUC models therefore predict that inertial effects will initiate at much lower Reynolds numbers (i.e. three times lower) in fibre beds than in granular media.

The long duct foam RUC model is adapted to account for the effect of developing flow on the pressure drop.

This resulted in the short duct foam RUC model, which reduces back to the long duct model at a Reynolds number of zero. The short duct foam RUC model provides pressure drop predictions applicable over the entire steady laminar flow regime. The relative percentage difference between the long and short duct models at the average foam porosity and critical Reynolds number is about 28.5% for both the ERG and PORVAIR foams. In the case of the ERG foams it was illustrated that the under-prediction of the long duct foam RUC model may be attributed largely to the effect of developing flow. For the PORVAIR foams the under-prediction may be attributed to the effect of developing flow and stagnant fluid domains, rather than solely to the effect of the presence of solid lumps at the intersection of struts.

Du Plessis & Masliyah (1988) have also considered developing flow in the foam RUC model. They did, however, not add a higher Reynolds number term as was done in the present study. They regarded the permeability prediction, in which developing flow is accounted for, as applicable over the entire laminar flow regime. The model proposed in the present study also accounts for the presence of stagnant fluid domains which was not considered by Du Plessis & Masliyah (1988). Since the model of Du Plessis & Masliyah (1988) led to an under-prediction at Reynolds numbers within the inertial flow regime, this model was abandoned by authors who have used the RUC model in the following years.

Model predictions are proposed for the critical Reynolds number of the foam RUC model indicating the transition between fully developed and developing flow as well as for the critical Reynolds number indicating the transition between developing flow and the inertial flow regime.

It is shown that the significant over-prediction observed by Bhattacharya et al. (2002), when applying the model of Du Plessis et al. (1994) to their experimental data, can be diminished by accounting for the effect of developing flow in the model together with the use of the pore diameter, d_p.

> The short duct foam RUC model improved the model prediction of Du Plessis (1994) for the dimensionless permeability by 85%, measured at the average foam porosity and the average critical Reynolds number. It was shown that the analytical model predictions obtained by Bhattacharya et al. (2002), through adaptation of the foam RUC model of Du Plessis et al. (1994), lack physical meaning and that it is not necessary to introduce another geometrical model (i.e. the dodecahedron model) to account for the presence of solid lumps at the intersection of struts. The effect of solid lumps is implicitly accounted for by the average solid geometry of the RUC model.

A method is proposed in which the variation in the cross-sectional shape of the fibres can be incorporated into the foam RUC model.

> This serves as an improvement to the constant value previously used by authors who have utilized the foam RUC model. A unified semi-empirical equation was proposed for the interstitial form drag coefficient to be used in the RUC model. This serves as an improvement to the different empirical equations proposed by Bhattacharya et al. (2002) for each of the two distinct porosity domains associated with the variation in cross-sectional shape of the fibres.

> The over-prediction observed by Bhattacharya et al. (2002) in the inertial coefficient, when applying the long duct model of Du Plessis et al. (1994), was diminished through the incorporation of the porosity dependent interstitial form drag coefficient and the effect of developing flow. The porosity dependent interstitial

form drag coefficient also improves the model prediction of Crosnier et al. (2006) for the passability of the ERG foams of which the cross-sectional shape varies.

The transversely isotropic foam RUC is adapted to account for anisotropy resulting from compression.

The streamwise pressure drop prediction was adapted to determine the increase in pressure drop, or equivalently the decrease in permeability, at different stages of compression.

Diedericks (1999) and Diedericks & Du Plessis (1997) also adapted the foam RUC model to account for anisotropy. In the present study the dimensions of the struts in the transverse directions are assumed to be equal whereas the latter authors considered all the struts of the anisotropic foam model to have different dimensions. The latter authors proposed equations in tensor notation for each of the three principal flow directions. A different approach was followed in the present study. The model prediction was adapted based on the available experimental values an input parameters, by considering two case studies. The problem therefore to be solved was how to determine the effect of compression on the pressure drop, given the information at hand. Since in both case studies the compression was only in the streamwise direction, only the dimension of the *streamwise* strut was altered. It was illustrated that the compression not only affects the streamwise dimension, but also the transverse dimensions. Although the measured mean hydraulic pore diameter values were measured only with respect to the streamwise direction, the proposed RUC model distinguishes between the hydraulic diameter values in the three principal flow directions.

It was illustrated that changes in the level of anisotropy, as a result of compression, have a significant effect on permeability. It therefore has to be taken into consideration for the optimization and design of filtration devices in which fibrous media are used. In both case studies, the permeability ranged over more than an order of magnitude over the narrow porosity ranges of 0.08 and 0.02, respectively. In the case study involving the soft polyester material, it was shown that the anisotropic foam RUC model decreases the over-prediction of the isotropic model by an average of 94.0%.

The pressure drop prediction is adapted to account for the combined effects of compression and developing flow.

It was found in the second case study that the effect of developing flow is already significant at Reynolds numbers as low as 0.1 . The incorporation of the effect of developing flow reduced the over-prediction of the *anisotropic model* by an average of 65.7%.

274

For both case studies it was found that the permeability prediction is very sensitive to deviations in the values of the pore-scale linear dimension of the uncompressed state and to deviations in the porosity values used in the model. The permeability prediction is affected to a much lesser degree by the compression ratio. In both case studies the proposed model predictions lie between the two bounding error curves obtained from the combination of experimental error ranges leading to a maximum deviation in model prediction. The absolute relative percentage differences between the two bounding permeability curves are more than 900% for the first case study and up to about 150% for the second case study.

Equations are proposed for predicting the permeability of Fontainebleau sandstones of different grain diameters.

Both the transversely isotropic granular and foam RUC models were adapted by incorporating the percolation threshold porosity to account for the effect of blocked throats. This has previously been done only for the granular model, but for the previous granular model of Du Plessis (1999), and not the improved granular RUC model presented in this study. Equations were proposed for determining the percolation threshold porosity of a sandstone sample if the average grain diameter of the sample is known as well as the percolation threshold porosity and grain diameter of another sample. It was found that the effect of blocked throats at very low porosities has a significant effect on the permeability prediction. The model predictions of both RUC models for the two limiting grain diameter values enclosed the experimental data, but with the permeability prediction of the granular model being more refined than that of the foam model. This led to the conclusion that the microscopic geometry of Fontainebleau sandstone may be regarded as both granular and tubular, but with the granular characteristics being more prominent. This supports findings from the literature to treat Fontainebleau sandstones as consolidated or unconsolidated media.

Equations are proposed for predicting the diffusivity ratio of unconsolidated arrays of squares and cubes by application of the 2D (fibre) and 3D (granular) RUC models, respectively.

The diffusivity ratio was expressed in terms of the geometric factor, instead of tortuosity, because the geometric factor yields the same expression for a fully staggered and regular array, whereas this is not the case with the tortuosity. Different equations therefore need not be provided for the diffusivity ratio of the staggered and non-staggered arrays. (This supports findings from the literature that the diffusivity ratios are essentially equal for the streamwise and transverse directions of a fully staggered array.) The geometric factor, as opposed to the tortuosity, also takes into account diffusion that may take place in the hydrodynamically stagnant fluid volumes. Physical meaning was given to the equation often used, and simply just provided in the literature, to predict the diffusivity ratio (i.e. equation (8.31)).

The numerical data obtained for predicting the diffusivity ratio of the non-staggered (i.e regular) and staggered (i.e. fully staggered) arrays of squares were essentially the same which again agrees with findings from the literature. It was shown that the weighted average model of Bell & Crank (1974) is not adequate to predict the diffusivity ratio of a fully staggered array of squares. The reason is that the weighted average model is not applicable for rectangular cells. The weighted average RUC model was proposed instead and is applicable over the entire porosity range for both staggered and non-staggered arrays of solid squares (or cubes).

9.2   Final remarks and suggestions

This dissertation contains all the latest updated model predictions for the pressure drop, permeability, inertial coefficient and passsability in terms of all three pore-scale linear dimensions associated with the RUC models.

Other analytical models with the same predictive capabilities as the short duct foam RUC model could not be found in the literature. The predictive capabilities include the effect of compression and developing flow on pressure drop and permeability. In addition, a model characteristic not often found in the literature (if even possible) is that the RUC model predictions can be expressed in terms of any of the pore-scale linear dimensions, i.e. the cell size, pore diameter or solid diameter. The model prediction can easily be converted to any of the RUC dimensions through geometrical relationships. Another model characteristic counting in the favour of the RUC models is that they are applicable over the entire steady laminar flow regime and over the full range of porosities.

A primary focus throughout this study was to physically adapt the RUC models and eliminate empirical coefficients and parameters as far as possible. The incorporation of the effects of developing flow, compression, pore blockage in sandstones and diffusive transport in the analytical modelling procedure involving the RUC models, is an illustration of the ability of the models to be physically adaptable since the modelling procedure and all the adaptations thereof are based on sound physical principles. The modelling assumptions are also clearly stated so that generalization in a scientifically justifiable manner is possible. The physical adaptability and satisfactory correspondence of the RUC model predictions with models from the literature provides confidence in the analytical modelling procedure.

Wilms (2006) replaced the rectangular struts of the high porosity foam RUC model with cylindrical struts to validate the accuracy regarding the geometry of the RUC model. The cylindrical strut model proved to be more accurate by a factor of $\sqrt{\pi}$, but at the cost of a much larger increase in mathematical complexity than accuracy. The cylindrical strut model is also only applicable for Newtonian flow in the Darcy regime and cannot be adapted in a relatively simple manner to broaden its range of applicability. One can, however, put great effort into trying to construct the foam micro-structure with much more accuracy, but with loss in mathematical simplicity. In respect thereof the slight

gain in accuracy may not be worth the increased level of mathematical complexity. In the opinion of the author of this dissertation the attempt to maintain a balance between simplicity and accuracy of the RUC modelling theory was adhered to.

The validation of the RUC models relies on the availability of accurate experimental data. A more thorough validation can be performed if more data is available in the literature. In most papers dealing with the pressure drop and/or permeability prediction of foamlike media, data on the magnitude of the superficial velocities and/or Reynolds numbers corresponding to the measured pressure drop and/or permeability data are not provided. This information is crucial for the short duct foam RUC model to determine the effect of developing flow.

It is suggested that the PPI number should not be used in model predictions, as no reliable information regarding pore scale-linear dimensions can be extracted from it. It is also suggested that experimentalists not only provide the value of the pore diameter measured for foamlike media, in addition to the PPI number, but also specify which dimension of the actual material it represents and how it was measured. This will lead to more reliable model predictions.

For accurate model predictions to be obtained for the pressure drop of fibrous media in which the effects of compression and developing flow is accounted for, it is suggested that the porosity, pore diameter, fibre/strut diameter and superficial velocity and/or Reynolds number be specified. For granular media, however, the pore diameter need not be specified, as the grain diameter is sufficient. It is suggested that the flow velocity range over which the permeability and inertial coefficients are measured be specified. This will enable one to use the exact Reynolds number values in the model predictions instead of the average critical Reynolds number.

The RUC models, and in specific the anisotropic foam RUC model, appears to be reasonably accurate in portraying the physical flow conditions to such an extent that it could be used for further understanding and analysis of the processes involved. The models thus serve as mathematical tools for the quantification of transfer processes in complex porous structures.

9.3   Future work

The successful interim results presented in this study pave the way for more advanced studies towards analysis of coupled convective-diffusive processes in double porosity media which is important in the study of, for instance, coal processing. In the present study, only diffusion in isotropic unconsolidated granular media was modelled analytically to predict the diffusivity ratio. Diffusion through anisotropic media was computed numerically, but not analytically. A next step would be to propose an analytical model to predict the diffusivity ratio of anisotropic media.

A further extension of this work may involve the mathematical modelling of diffusion in high porosity consolidated media such as metallic foams.

The over-prediction in permeability of the fibre RUC model at solid volume fractions below 0.2 may also be investigated. The model assumption of fully developed flow between parallel plates becomes less applicable at these low solid volume fractions. Accounting for the effect of developing flow may thus lead to more accurate model predictions.

Future work may also involve the adaptation of the fibre RUC model to account for anisotropy as a result of compression.

Appendix A

Transport equations and parameters

In this appendix the constitutive equations, of relevance to the present study, are formulated, followed by the conservation equations. Transport parameters such as the friction factor and form drag coefficient are also defined.

A.1   Constitutive equations

The physical laws or constitutive (i.e. empirically formulated) equations for momentum, mass and heat transfer are Newton's law of viscosity, Fick's (first) law of diffusion and Fourier's law of heat conduction, respectively. In addition, Ohm's law is the governing constitutive equation for electrical conduction. Since only momentum and mass transfer will be considered in the present study, only Newton's and Fick's laws will be formulated here.

Newton's law of viscosity for flow between parallel plates, oriented parallel to the x-direction of a rectangular Cartesian coordinate system, may be expressed as follows (e.g. Bird et al. (2007))

$$\tau_{yx} = -\mu \frac{\mathrm{d}v_x}{\mathrm{d}y} \ , \tag{A.1}$$

where τ_{yx} is the magnitude of the shearing force per unit area, $\mathrm{d}v_x/\mathrm{d}y$ is the velocity gradient and the constant of proportionality, μ, is the viscosity. A fluid with a constant viscosity and of which the flow behaviour is described by Newton's law of viscosity (i.e. equation (A.1)), is known as a Newtonian fluid. Fluid flow behaviour in which the viscosity is no longer constant but a function of the velocity gradient (also known as shear rate), are referred to as non-Newtonian flow. Several empirical models describing the dependency of the viscosity on the shear rate are available in the literature. These dependencies on the shear rate differ according to the type of non-Newtonian flow under consideration.

Fick's (first) law of diffusion for a binary system of species A diffusing through species B

279

may be expressed as (e.g. Bird et al. (2007))

$$j_{A_x} = -\rho D_{AB} \frac{d\omega_A}{dx} , \qquad (A.2)$$

where j_{A_x} is the mass flux of species A in the x-direction of a rectangular Cartesian coordinate system, ρ is the density of the binary mixture, ω_A is the mass fraction of species A and the constant of proportionality, D_{AB}, is the diffusion coefficient (also known as the diffusivity).

The minus sign in both equations (A.1) and (A.2) indicates that the driving mechanism behind the respective transfer processes are directed from high to low values.

A.2   Conservation equations

The conservation equation of momentum transport is given by (e.g. Happel & Brenner (1965))

$$\rho \frac{\partial \underline{v}}{\partial t} + \nabla \cdot (\rho \, \underline{v} \, \underline{v}) = \rho \underline{f}_b - \nabla p + \nabla \cdot \underline{\underline{\tau}} , \qquad (A.3)$$

where $\underline{v}$ is the interstitial fluid velocity, p is the static pressure, ρ is the fluid density, $\underline{\underline{\tau}}$ is the local shear stress tensor and $\underline{f}_b$ denotes the resultant external body force per unit mass.

For conservation of mass, the continuity equation is given by (e.g. Happel & Brenner (1965))

$$\frac{\partial \rho}{\partial t} + \nabla \cdot (\rho \underline{v}) = 0 , \qquad (A.4)$$

and Fick's second law of diffusion for a stationary fluid with no sources or sinks is given by

$$\rho \frac{\partial \omega_A}{\partial t} + \nabla \cdot \rho \, D_{AB} \, \nabla \omega_A = 0 . \qquad (A.5)$$

A.3   Drag coefficients

The total drag force, $\mathcal{F}$, exerted by a fluid on a solid surface(s) may be regarded as the sum of two forces, i.e. the force exerted on the solid(s) even if the fluid is stationary, denoted by $\mathcal{F}_s$, and the force on the solid(s) due to the kinetic energy of the fluid, denoted by $\mathcal{F}_k$ (Bird et al. (2007)). The latter force may, in turn, be expressed as the sum of the viscous drag force, $\mathcal{F}_v$, and pressure drag force, $\mathcal{F}_p$ (Rohsenow & Choi (1961), Welty et al. (1969), Welty (1978), Mironer (1979), Roberson & Crowe (1985), Massey (1989)). Viscous drag is also referred to as skin-friction drag.

The viscous drag results from friction at the surface of the solid when immersed in a flowing fluid and depends on the amount of wetted surface area. The pressure drag results from the pressure difference due to boundary-layer separation. Its value depends on the location of the boundary-layer separation, and hence the Reynolds number, as well as the shape or form (but not the size) of the body. The pressure drag is therefore also known as form drag. Whereas the viscous drag force is the resultant of the forces tangential to the surface of the solid, the pressure drag force is the resultant of the forces normal to it.

A.3.1 Form drag coefficient

The form drag coefficient, C_d, results from the mathematical expression relating the pressure drag force, $\mathcal{F}_p$, the projected area of the solid normal to the flow direction, $\mathcal{A}_p$, and the kinetic energy of the fluid, i.e. (e.g. Welty (1978))

$$\mathcal{F}_p = C_d \mathcal{A}_p \frac{\rho \, v_\infty^2}{2} \, , \qquad (A.6)$$

where $\rho \, v_\infty^2/2$ denotes the kinetic energy of the fluid and v_∞ is the magnitude of the free stream velocity.

As the Reynolds number increases within the laminar flow regime, the form drag coefficient gradually becomes independent of the Reynolds number (Massey (1989)). According to Roberson & Crowe (1985), the flow pattern at these high Reynolds numbers remains virtually unchanged, thus leading to constant values of C_d for angular solid obstacles, whereas abrupt changes may occur for rounded obstacles. Mironer (1979), however, states that for solid obstacles with sharp corners, the boundary layer separates right at the corner, irrespective of the flow regime present, thus yielding a fairly constant form drag coefficient over *all* flow regimes.

Table A.1 (p 282) gives empirical values for the form drag coefficient, C_d, for flow past a single solid object, of different shapes, in an infinite stream. The particle Reynolds number Re_p in Table A.1 is defined as $Re_p = \rho \, v_\infty D_s/\mu$, where D_s is the diameter of the solid object. In the case of rectangular objects, the latter diameter is assumed to be equal to the width of the square cross-section. For these rectangular geometries one of the faces is oriented normal to the flow.

For flow in porous media the free stream velocity, $\underline{v}_\infty$, in equation (A.6) is replaced with the superficial velocity, $\underline{q}$. The interstitial form drag coefficients for porous media, as the ones for flow past a single object, cannot be determined analytically and need to be obtained from experiments (Welty (1978)). This is, especially for porous media, not an easy task because the form drag coefficient may be a function of porosity in certain porosity ranges.

Table A.1: Values of the form drag coefficient, C_d, for flow past objects of different shapes.

Object	Flow regime	C_d	Reference
Cube	$Re_p > 10^4$	1.1	Roberson & Crowe (1985)
	All	1.05	Mironer (1979)
Sphere	$10^3 < Re_p < 10^4$	0.4	Hughes (1979), Whitaker (1968)
	$10^4 < Re_p < 10^5$	0.5	Hughes (1979), Whitaker (1968)
	Laminar	0.47	Mironer (1979)
Square rod	$Re_p > 10^4$	2.0	Roberson & Crowe (1985)
	All	2.0	Mironer (1979)
Cylinder	$10^3 < Re_p < 10^5$	1.0	Hughes (1979), Whitaker (1968)
	Laminar	1.2	Mironer (1979)

A.3.2   Friction factor

The friction factor (e.g. Dullien (1979), Bird et al. (2007)), like the hydraulic diameter, was originally introduced for conduit flow. The *friction* (also Fanning friction) *factor* for fully developed flow, f_{fd}, relates the viscous drag force resulting from wall shear stresses, to the kinetic energy per unit volume of fluid, i.e.

$$f_{fd} \;=\; \frac{\tau_w}{\frac{1}{2}\,\rho\,u_m^2} \;=\; \frac{R_h}{\frac{1}{2}\,\rho\,u_m^2}\frac{\Delta p}{L} \;=\; \frac{D_h}{2\,\rho\,u_m^2}\frac{\Delta p}{L} \;, \tag{A.7}$$

where u_m is the magnitude of the mean axial velocity. Sometimes the factor $f_f = 4f_{fd}$ is used, which is then referred to as the Darcy-Weisbach friction factor (Shah & London (1978)). The pressure drop in equation (A.7) results from wall shear stresses only. The friction factor times Reynolds number may be expressed as

$$f_{fd}Re_{Dh} \;=\; \frac{D_h^2}{2\,\mu\,u_m}\frac{\Delta p}{L} \;, \tag{A.8}$$

where Re_{Dh} is the Reynolds number, defined in terms of the hydraulic diameter as

$$Re_{Dh} \;=\; \frac{\rho\,u_m\,D_h}{\mu} \;. \tag{A.9}$$

The hydraulic diameter represents the mean flow cross-section.

Appendix B

Volume averaging of the Navier-Stokes and continuity equations

The theory regarding the volume averaging of the Navier-Stokes and continuity equations presented in this appendix is an adaptation and extension to that presented in the work of Woudberg (2006). It is included here for the sake of completeness.

B.1 Volume averaging theory

Macroscopic volume averaged quantities may be obtained through the introduction of phase average operators (e.g. Whitaker (1969), Bachmat & Bear (1986)). The phase average operators determine averages of the variables under consideration over an REV.

The phase average $\langle \Psi \rangle$ of any finite, continuous and differentiable tensorial quantity, Ψ, within $\mathcal{U}_f$ is defined as

$$\langle \Psi \rangle \equiv \frac{1}{\mathcal{U}_o} \iiint\limits_{\mathcal{U}_f} \Psi \, d\mathcal{U} \,. \tag{B.1}$$

The intrinsic phase average $\langle \Psi \rangle_f$ is given by

$$\langle \Psi \rangle_f \equiv \frac{1}{\mathcal{U}_f} \iiint\limits_{\mathcal{U}_f} \Psi \, d\mathcal{U} \,. \tag{B.2}$$

In both equations (B.1) and (B.2) the integration is over the total fluid phase in the REV, with the only difference being the volume through which the integral is divided. From

283

the latter two definitions the following identities are obtained:

$$\langle \Psi \rangle = \epsilon \langle \Psi \rangle_f \ , \tag{B.3}$$

$$\langle \alpha \, \Psi \rangle = \alpha \, \langle \Psi \rangle \ , \quad \alpha = \text{constant} \ , \tag{B.4}$$

$$\langle \Psi_1 + \Psi_2 \rangle = \langle \Psi_1 \rangle + \langle \Psi_2 \rangle \ , \tag{B.5}$$

$$\langle \Psi_1 \, \Psi_2 \rangle = \langle \Psi_1 \rangle \langle \Psi_2 \rangle / \epsilon + \langle \{\Psi_1\}\{\Psi_2\} \rangle \ , \tag{B.6}$$

where the deviation, $\{\Psi\}$, is defined as $\{\Psi\} \equiv \Psi - \langle \Psi \rangle_f$. By application of identities (B.3) to (B.6), the average of a gradient (or divergence) may be expressed in terms of the gradient of an average (or divergence) (e.g. Slattery (1969), Whitaker (1969)), i.e.

$$\langle \nabla \Psi \rangle = \nabla \langle \Psi \rangle + \frac{1}{\mathcal{U}_0} \iint\limits_{\mathcal{S}_{fs}} \underline{n} \, \Psi \, \mathrm{d}\mathcal{S} \ , \tag{B.7}$$

and

$$\langle \nabla \cdot \underline{\Psi} \rangle = \nabla \cdot \langle \underline{\Psi} \rangle + \frac{1}{\mathcal{U}_0} \iint\limits_{\mathcal{S}_{fs}} \underline{n} \cdot \underline{\Psi} \, \mathrm{d}\mathcal{S} \ . \tag{B.8}$$

In equations (B.7) and (B.8), $\underline{n}$ is the inwardly (with respect to the solid) directed unit vector normal to the fluid-solid interface. From equation (B.7) it follows that

$$\nabla \epsilon = -\frac{1}{\mathcal{U}_0} \iint\limits_{\mathcal{S}_{fs}} \underline{n} \, \mathrm{d}\mathcal{S} \ . \tag{B.9}$$

The phase average of a time derivative may be expressed as

$$\left\langle \frac{\partial \, \Psi}{\partial \, t} \right\rangle = \frac{\partial \, \langle \Psi \rangle}{\partial \, t} - \frac{1}{\mathcal{U}_0} \iint\limits_{\mathcal{S}_{fs}} \underline{n} \cdot \underline{v} \, \Psi \, \mathrm{d}\mathcal{S} \ , \tag{B.10}$$

where $\underline{v}$ is the microscopic fluid velocity on $\mathcal{S}_{fs}$.

B.2 Volume averaging of the continuity equation

From equation (B.8) it follows that the phase average of the continuity equation for incompressible flow (equation (2.23)) may be expressed as

$$\langle \nabla \cdot \underline{v} \rangle = \nabla \cdot \langle \underline{v} \rangle + \frac{1}{\mathcal{U}_0} \iint\limits_{\mathcal{S}_{fs}} \underline{n} \cdot \underline{v} \, \mathrm{d}\mathcal{S} = \langle 0 \rangle \ . \tag{B.11}$$

The surface integral in equation (B.11) becomes zero for a no-slip boundary condition, leading to the following expression for the volume averaged continuity equation for incompressible flow:

$$\nabla \cdot \underline{q} \;=\; 0 \,. \tag{B.12}$$

B.3   Volume averaging of the Navier-Stokes equation

Volume averaging of the Navier-Stokes equation for incompressible flow (equation (2.22)), leads to

$$\left\langle \rho \frac{\partial \underline{v}}{\partial t} \right\rangle \;+\; \langle \nabla \cdot (\rho \underline{v}\,\underline{v}) \rangle \;+\; \langle \nabla p \rangle \;-\; \left\langle \nabla \cdot \underline{\underline{\tau}} \right\rangle \;=\; \langle \underline{0} \rangle \,. \tag{B.13}$$

Application of the averaging identities to each term on the left hand side of equation (B.13) respectively yields

$$\left\langle \rho \frac{\partial \underline{v}}{\partial t} \right\rangle \;=\; \rho \left\langle \frac{\partial \underline{v}}{\partial t} \right\rangle \;=\; \rho \frac{\partial \underline{q}}{\partial t} \;-\; \frac{\rho}{\mathcal{U}_0} \iint\limits_{\mathcal{S}_{fs}} \underline{n} \cdot \underline{v}\,\underline{v}\, \mathrm{d}\mathcal{S} \,, \tag{B.14}$$

$$\langle \nabla \cdot (\rho \underline{v}\,\underline{v}) \rangle \;=\; \rho \nabla \cdot \left(\underline{q}\,\underline{q}/\epsilon \right) \;+\; \rho \nabla \cdot \langle \{\underline{v}\}\,\{\underline{v}\} \rangle \;+\; \frac{\rho}{\mathcal{U}_0} \iint\limits_{\mathcal{S}_{fs}} \underline{n} \cdot \underline{v}\,\underline{v}\, \mathrm{d}\mathcal{S} \,, \tag{B.15}$$

$$\langle \nabla p \rangle \;=\; \nabla \langle p \rangle \;+\; \frac{1}{\mathcal{U}_0} \iint\limits_{\mathcal{S}_{fs}} \underline{n}\, p\, \mathrm{d}\mathcal{S} \,, \tag{B.16}$$

$$\left\langle \nabla \cdot \underline{\underline{\tau}} \right\rangle \;=\; \nabla \cdot \left\langle \underline{\underline{\tau}} \right\rangle \;+\; \frac{1}{\mathcal{U}_0} \iint\limits_{\mathcal{S}_{fs}} \underline{n} \cdot \underline{\underline{\tau}}\, \mathrm{d}\mathcal{S} \,. \tag{B.17}$$

Substituting equations (B.14) to (B.17) into equation (B.13), leads to

$$-\nabla \langle p \rangle \;=\; \rho \frac{\partial \underline{q}}{\partial t} \;+\; \rho \nabla \cdot \left(\underline{q}\,\underline{q}/\epsilon \right) \;+\; \rho \nabla \cdot \langle \{\underline{v}\}\,\{\underline{v}\} \rangle \;-\; \nabla \cdot \left\langle \underline{\underline{\tau}} \right\rangle$$

$$+\; \frac{1}{\mathcal{U}_0} \iint\limits_{\mathcal{S}_{fs}} \left(\underline{n}\, p - \underline{n} \cdot \underline{\underline{\tau}} \right) \mathrm{d}\mathcal{S} \,. \tag{B.18}$$

For a Newtonian fluid (Appendix A.1, p 279), it follows that the term in equation (B.18) containing the shear stress dyadic, can be expressed as

$$\nabla \cdot \left\langle \underline{\underline{\tau}} \right\rangle \;=\; \nabla \cdot \mu \langle \nabla \underline{v} \rangle$$

$$=\; \nabla \cdot \mu \nabla \langle \underline{v} \rangle \;+\; \nabla \cdot \frac{\mu}{\mathcal{U}_0} \iint\limits_{\mathcal{S}_{fs}} \underline{n}\,\underline{v}\, \mathrm{d}\mathcal{S}$$

$$=\; \mu \nabla^2 \underline{q} \,. \tag{B.19}$$

285

Appendix C

Derivation of the Ergun equation

In this appendix a derivation of the semi-empirical Ergun equation is presented. The Ergun equation is a capillary tube model according to which a packed column, of length L and spherical particles as packing material, is regarded as a bundle of tortuous, arbitrarily shaped, capillary tubes. The capillary tubes, however, have a uniform length of L_e. Each capillary tube is assumed to have a uniform diameter along its entire length. The effect of channeling, as discussed in Section 2.7.1 (p 15), is assumed to be negligible. It is furthermore assumed that the random packing of spheres is statistically uniform. The Ergun equation is a superposition of two asymptotic limits, i.e. the Blake-Kozeny equation for flow in the Darcy regime and the Burke-Plummer equation for, presumably, turbulent flow (e.g. Bird et al. (2007)).

C.1   Blake-Kozeny equation

As a starting point, the capillaries are assumed to be cylindrical and straight (i.e. of length L) and of uniform diameter (with radius R). The Hagen-Poiseuille equation (e.g. Bird et al. (2007)) is then used to describe steady one-dimensional flow in only one of the cylinders. The latter equation is then generalized to account for a bundle of tortuous capillaries of length L_e and of arbitrary, but uniform, cross-section. This is accomplished by inclusion of the hydraulic radius R_h (instead of the radius R) and a constant shape factor k_o which depends on the arbitrary shape of the cross-section of the capillaries. The generalized Hagen-Poiseuille equation is given by

$$u_m = \frac{\Delta p\, R_h^2}{k_o\, \mu\, L_e}\,,\qquad\qquad (C.1)$$

where u_m is the magnitude of the average channel velocity and Δp is the pressure drop over the capillary length, L_e. For a circular capillary, $k_o = 2$, and equation (C.1) reduces to the Hagen-Poiseuille equation. Introducing the Dupuit-Forchheimer velocity relationship

286

(equation (2.29)) (with $u_m = u$) and the hydraulic radius for porous media (equation (2.12)) into equation (C.1), yields

$$\Delta p = 36 \, k_o \, \frac{(1-\epsilon)^2}{\epsilon^3} \frac{\mu \, q \, L_e}{D_h^2} \, . \tag{C.2}$$

To account for the actual tortuous flow path of the traversing fluid an empirical correction factor of 25/12 was introduced for agreement with experimental data. The introduction of the factor of $L_e = 25/12 L$, together with $k_o = 2$, yields a coefficient of 150, i.e.

$$\frac{\Delta p}{L} = 150 \, \frac{(1-\epsilon)^2}{\epsilon^3} \frac{\mu \, q}{D_h^2} \, . \tag{C.3}$$

Equation (C.3) is known as the Blake-Kozeny equation. From Darcy's law (equation (2.4)) the permeability resulting from the Blake-Kozeny equation, k_{BK}, may be expressed as

$$k_{BK} = \frac{D_h^2}{150} \frac{\epsilon^3}{(1-\epsilon)^2} \, . \tag{C.4}$$

The friction factor (Appendix A.3.2, p 282) associated with the Blake-Kozeny equation, f_{BK}, is defined as

$$f_{BK} = \frac{\Delta p}{\rho \, q^2} \frac{D_h}{L} \frac{\epsilon^3}{(1-\epsilon)} \, , \tag{C.5}$$

and the corresponding Reynolds number, Re_{BK}, is given by

$$Re_{BK} = \frac{\rho \, q \, D_h}{\mu \, (1-\epsilon)} \, . \tag{C.6}$$

The friction factor may then be expressed as

$$f_{BK} = \frac{150}{Re_{BK}} = \frac{A}{Re_{BK}} \, . \tag{C.7}$$

C.2   Carman-Kozeny equation

Carman (1937) argued that the actual tortuous flow path, L_e, of the traversing fluid is greater than the column length, L, by a factor of χ. In addition, the real average velocity in a tortuous channel of length L_e is L_e/L times greater than the value q/ϵ in a straight channel of length L. Hence, substituting

$$L_e = \chi \, L \, , \tag{C.8}$$

and

$$u_m = \frac{q}{\epsilon} \frac{L_e}{L} \, , \tag{C.9}$$

into equation (C.2), yields

$$\frac{\Delta p}{L} \;=\; 36\, k_o\, \chi^2\, \frac{(1-\epsilon)^2}{\epsilon^3}\, \frac{\mu\, q}{D_h^2}\; . \tag{C.10}$$

The *Kozeny constant*, k_{koz}, was then introduced and defined as

$$k_{koz} \;=\; k_o\, \chi^2 \;=\; k_o \left(\frac{L_e}{L}\right)^2 \;=\; k_o\, T\; , \tag{C.11}$$

where the ratio $T = (L_e/L)^2$ is referred to as the tortuosity. From available experimental data from the literature, Carman (1937) proposed an average value for the Kozeny constant of $k_{koz} = 5.0$. He determined that in a bed of spheres the average value of the slope of the traversing fluid with respect to the column axis is $45°$, thus yielding, $\chi = L_e/L = \sqrt{2}$. This leads to an average value of 2.5 for the shape factor, k_o. Substituting these values into equation (C.10) lead to a coefficient of $A = 180$. The pressure gradient may consequently be expressed as

$$\frac{\Delta p}{L} \;=\; 180\, \frac{(1-\epsilon)^2}{\epsilon^3}\, \frac{\mu\, q}{D_h^2}\; . \tag{C.12}$$

Equation (C.2) is known as the Carman-Kozeny-Blake or simply the Carman-Kozeny equation. In analogy with equation (C.7), the friction factor associated with the Carman-Kozeny equation, f_{CK}, may be expressed as

$$f_{CK} \;=\; \frac{180}{Re_{BK}} \;=\; \frac{A}{Re_{BK}}\; . \tag{C.13}$$

From Darcy's law (equation (2.4)) the permeability resulting from the Carman-Kozeny equation, k_{CK}, may be expressed as

$$k_{CK} \;=\; \frac{D_h^2}{180}\, \frac{\epsilon^3}{(1-\epsilon)^2}\; . \tag{C.14}$$

C.3 Burke-Plummer equation

The higher Reynolds number limit of the Ergun equation was modelled as turbulent flow. As discussed in Section 2.9 (p 23), it is widely accepted in the literature (e.g. Happel & Brenner (1965), Bear (1972)) that the failure of Darcy's law cannot be attributed to turbulence, since laminar inertial effects precedes turbulence. Nevertheless, for highly turbulent flow, as stated in the literature by Bird et al. (2007), for example, the friction factor f_{BK} (or f_{CK}) no longer depends on the Reynolds number, Re_{BK} (or Re_{CK}). It only depends on tube roughness. Assuming that the tubes in all packed columns have the same uniform roughness, leads to

$$f_{BK} \;=\; \text{constant} \;=\; B\; . \tag{C.15}$$

From numerous experimental data a value of $B = 1.75$ was proposed, yielding

$$\frac{\Delta p}{L} = 1.75 \frac{(1 - \epsilon)}{\epsilon^3} \frac{\rho \, q^2}{D_h} . \tag{C.16}$$

Equation (C.16) is known as the Burke-Plummer equation.

C.4 Ergun equation

Ergun (1952) superimposed the Blake-Kozeny and Burke-Plummer equations to obtain an equation for the pressure gradient over a packed bed for Reynolds numbers in the range $1 < Re_{BK} < 3000$. The Ergun equation is given by

$$\frac{\Delta p}{L} = A \frac{(1 - \epsilon)^2}{\epsilon^3} \frac{\mu \, q}{D_h^2} + B \frac{(1 - \epsilon)}{\epsilon^3} \frac{\rho \, q^2}{D_h} , \tag{C.17}$$

with $A = 150$ and $B = 1.75$. Equation (C.17) usually gives good agreement with experimental data for $0.3 \leq \epsilon \leq 0.5$. For $Re_{BK} < 10$ the first term in equation (C.17) dominates and the Ergun equation reduces to the Blake-Kozeny equation. For $10 < Re_{BK} < 10^3$ a gradual transition occurs after which the flow, becomes 'turbulent'. Thus for $Re_{BK} > 10^3$ the second term in equation (C.17) predominates and the Ergun equation reduces to the Burke-Plummer equation.

The Ergun equation may be expressed in terms of the static specific surface, A_{vs}, (as defined in Section 2.8.6, p 21) by replacing the hydraulic diameter D_h for porous media with the effective particle diameter, D_s (equation (2.16)), i.e.

$$\frac{\Delta p}{L} = \frac{25}{6} \frac{(1 - \epsilon)^2}{\epsilon^3} A_{vs}^2 \, \mu \, q + \frac{7}{24} \frac{(1 - \epsilon)}{\epsilon^3} A_{vs} \, \rho \, q^2 . \tag{C.18}$$

The Ergun equation may also be expressed in the following dimensionless form:

$$f_{BK} = \frac{A}{Re_{BK}} + B . \tag{C.19}$$

Appendix D

Additional Tables

Additional tables to those given in the main text of this dissertation are given here as supporting documentation.

Table D.1: Volume and surface partitioning table of the granular RUC model in terms of d and ϵ.

Parameter	Granular RUC model	
U_o	d^3	
U_s	d_s^3	
U_f	$(1-\epsilon)d^3$	
U_t	$d^3(1-(1-\epsilon)^{1/3})^2(1+2(1-\epsilon)^{1/3})$	
$U_\parallel$	$2\,d^3(1-\epsilon)^{2/3}(1-(1-\epsilon)^{1/3})$	
S_{fs}	$6\,d^2(1-\epsilon)^{2/3}$	
$S_\parallel$	$4\,d^2(1-\epsilon)^{2/3}$	
	Fully staggered array	Regular array
$U_\perp$	$d^3(1-\epsilon)^{2/3}(1-(1-\epsilon)^{1/3})$	0
$S_\perp$	$2\,d^2(1-\epsilon)^{2/3}$	0
U_g	0	$2\,d^3(1-\epsilon)^{2/3}(1-(1-\epsilon)^{1/3})$
S_g	0	$2\,d^2(1-\epsilon)^{2/3}$

Table D.2: Volume and surface partitioning table of the foam RUC model in terms of d, ψ and σ.

Parameter	Foam RUC model
U_o	d^3
U_s	$\dfrac{d^3}{4}(4-\psi)(\psi-1)^2$
U_f	$\dfrac{d^3}{4}(3-\psi)^2\psi$
U_t	$\dfrac{d^3(3-\psi)^3}{8}$
$U_\parallel$	$\dfrac{d^3(3-\psi)^2(\psi-1)}{8}$
S_{fs}	$3\,d^2(3-\psi)(\psi-1)$
$S_\parallel$	$d^2(3-\psi)(\psi-1)$
$U_\perp$	$\dfrac{(2-\sigma)d^3(3-\psi)^2(\psi-1)}{8}$
$S_\perp$	$\dfrac{(8-4\,\sigma)}{4}\,d^2(3-\psi)(\psi-1)$
U_g	$\dfrac{\sigma\,d^3(3-\psi)^2(\psi-1)}{8}$
S_g	$\sigma\,d^2(3-\psi)(\psi-1)$

Table D.3: Volume and surface partitioning table of the fibre RUC model in terms of d, ϵ and L.

Parameter	Fibre model	
U_o	$d^2 L$	
U_s	$d^2(1 - \epsilon)L$	
U_f	$d^2 \epsilon L$	
U_t	$d^2(1 - \sqrt{1 - \epsilon})^2 L$	
$U_\parallel$	$d^2\sqrt{1 - \epsilon}(1 - \sqrt{1 - \epsilon})L$	
S_{fs}	$4\sqrt{1 - \epsilon}\,d\,L$	
$S_\parallel$	$2\sqrt{1 - \epsilon}\,d\,L$	
	Fully staggered array	Regular array
$U_\perp$	$d^2\sqrt{1 - \epsilon}(1 - \sqrt{1 - \epsilon})L$	0
$S_\perp$	$2\sqrt{1 - \epsilon}\,d\,L$	0
U_g	0	$d^2\sqrt{1 - \epsilon}(1 - \sqrt{1 - \epsilon})L$
S_g	0	$2\sqrt{1 - \epsilon}\,d\,L$

Table D.4: Expressions for the dimensionless hydrodynamic permeability, K_d.

Model/Array	Dimensionless permeability, $K_d = k/d^2$
Granular model:	$$\frac{\left(1 - (1-\epsilon)^{1/3}\right)\left(1 - (1-\epsilon)^{2/3}\right)^2}{25.4\,(1-\epsilon)^{2/3}}$$
Foam model (Crosnier et al. (2006)):	
Doubly staggered model	$$\frac{\epsilon^2}{36\,\psi^2\,(\psi-1)}$$
Singly staggered model	$$\frac{\epsilon^2}{24\,\psi^2\,(\psi-1)}$$
Non-staggered model	$$\frac{\epsilon^2}{12\,\psi^2\,(\psi-1)}$$
Fibre model:	$$\frac{(1 - \sqrt{1-\epsilon})^3}{13.5\sqrt{1-\epsilon}}$$

Table D.5: Expressions for the dimensionless hydrodynamic permeability, K_{ds}.

Model/Array	Dimensionless permeability, $K_{ds} = k/d_s^2$
Granular model:	$\dfrac{\left(1 - (1-\epsilon)^{1/3}\right)\left(1 - (1-\epsilon)^{2/3}\right)^2}{25.4\,(1-\epsilon)^{4/3}}$
Foam model (Crosnier et al. (2006)):	
Doubly staggered model	$\dfrac{\epsilon^2}{9\,\psi^2\,(\psi-1)^3}$
Singly staggered model	$\dfrac{\epsilon^2}{6\,\psi^2\,(\psi-1)^3}$
Non-staggered model	$\dfrac{\epsilon^2}{3\,\psi^2\,(\psi-1)^3}$
Fibre model:	$\dfrac{(1-\sqrt{1-\epsilon})^3}{13.5(1-\epsilon)^{3/2}}$

Table D.6: Expressions for the dimensionless hydrodynamic permeability, K_{dds}.

Model/Array	Dimensionless permeability, $K_{dds} = k/(d - d_s)^2$
Granular model:	$\dfrac{\left(1 - (1 - \epsilon)^{2/3}\right)^2}{25.4\,(1 - \epsilon)^{2/3}\left(1 - (1 - \epsilon)^{1/3}\right)}$
Foam model (Crosnier et al. (2006)):	
Doubly staggered model	$\dfrac{\epsilon^2}{9\,\psi^2\,(\psi - 1)(3 - \psi)^2}$
Singly staggered model	$\dfrac{\epsilon^2}{6\,\psi^2\,(\psi - 1)(3 - \psi)^2}$
Non-staggered model	$\dfrac{\epsilon^2}{3\,\psi^2\,(\psi - 1)(3 - \psi)^2}$
Fibre model:	$\dfrac{(1 - \sqrt{1 - \epsilon})}{13.5\sqrt{1 - \epsilon}}$

Table D.7: Expressions for the dimensionless drag factor, F_{0_d}.

Model/Array	Dimensionless drag factor, $F_{0_d} = f_{0_d} d^2$
Granular model:	$\dfrac{25.4 \, (1 - \epsilon)^{2/3}}{\left(1 - (1 - \epsilon)^{1/3}\right) \left(1 - (1 - \epsilon)^{2/3}\right)^2}$
Foam model (Crosnier et al. (2006)):	
Doubly staggered model	$\dfrac{36 \, \psi^2 \, (\psi - 1)}{\epsilon^2}$
Singly staggered model	$\dfrac{24 \, \psi^2 \, (\psi - 1)}{\epsilon^2}$
Non-staggered model	$\dfrac{12 \, \psi^2 \, (\psi - 1)}{\epsilon^2}$
Fibre model:	$\dfrac{13.5\sqrt{1 - \epsilon}}{(1 - \sqrt{1 - \epsilon})^3}$

Table D.8: Expressions for the dimensionless drag factor, $F_{0_{ds}}$.

Model/Array	Dimensionless drag factor, $F_{0_{ds}} = f_{0_{ds}}\, d_s^2$
Granular model:	$\dfrac{25.4\,(1-\epsilon)^{4/3}}{\left(1-(1-\epsilon)^{1/3}\right)\left(1-(1-\epsilon)^{2/3}\right)^2}$
Foam model (Crosnier et al. (2006)):	
Doubly staggered model	$\dfrac{9\,\psi^2\,(\psi-1)^3}{\epsilon^2}$
Singly staggered model	$\dfrac{6\,\psi^2\,(\psi-1)^3}{\epsilon^2}$
Non-staggered model	$\dfrac{3\,\psi^2\,(\psi-1)^3}{\epsilon^2}$
Fibre model:	$\dfrac{13.5(1-\epsilon)^{3/2}}{(1-\sqrt{1-\epsilon})^3}$

Table D.9: Expressions for the dimensionless drag factor, $F_{0_{dds}}$.

Model/Array	Dimensionless drag factor, $F_{0_{dds}} = f_{0_{dds}} (d - d_s)^2$
Granular model:	$\dfrac{25.4 \, (1 - \epsilon)^{2/3} \left(1 - (1 - \epsilon)^{1/3}\right)}{\left(1 - (1 - \epsilon)^{2/3}\right)^2}$
Foam model (Crosnier et al. (2006)):	
Doubly staggered model	$\dfrac{9 \, \psi^2 \, (\psi - 1)(3 - \psi)^2}{\epsilon^2}$
Singly staggered model	$\dfrac{6 \, \psi^2 \, (\psi - 1)(3 - \psi)^2}{\epsilon^2}$
Non-staggered model	$\dfrac{3 \, \psi^2 \, (\psi - 1)(3 - \psi)^2}{\epsilon^2}$
Fibre model:	$\dfrac{13.5\sqrt{1 - \epsilon}}{(1 - \sqrt{1 - \epsilon})}$

Table D.10: Expressions for the dimensionless drag factor, F_{∞_d}.

Model/Array	Dimensionless drag factor, $F_{\infty_d} \;=\; f_{\infty_d}\, d$
Granular model:	$\dfrac{\rho\, q\, (1-\epsilon)^{2/3}\, c_d}{2\,\mu\,\epsilon\,\left(1-(1-\epsilon)^{2/3}\right)^2}$

Foam model:
     Doubly staggered model
 	
     Singly staggered model
	$\dfrac{\rho\, q\, (\psi-1)(3-\psi)\,\psi^2\, c_d}{4\,\mu\,\epsilon^3}$
	
	 $\dfrac{\rho\, q\, (\psi-1)(3-\psi)\,\psi^2\, c_d}{8\,\mu\,\epsilon^3}$

Fibre model:	$\dfrac{\rho\, q\, \sqrt{1-\epsilon}\, c_d}{2\,\mu\,\epsilon(1-\sqrt{1-\epsilon})^2}$

299

Table D.11: Expressions for the dimensionless drag factor, $F_{\infty_{ds}}$.

Model/Array	Dimensionless drag factor, $F_{\infty_{ds}} = f_{\infty_{ds}} d_s$
Granular model:	$\dfrac{\rho\,q\,(1-\epsilon)\,c_d}{2\,\mu\,\epsilon\,(1-(1-\epsilon)^{2/3})^2}$
Foam model: Doubly staggered model	$\dfrac{\rho\,q\,(\psi-1)^2(3-\psi)\,\psi^2\,c_d}{8\,\mu\,\epsilon^3}$
Singly staggered model	$\dfrac{\rho\,q\,(\psi-1)^2(3-\psi)\,\psi^2\,c_d}{16\,\mu\,\epsilon^3}$
Fibre model:	$\dfrac{\rho\,q\,(1-\epsilon)\,c_d}{2\,\mu\,\epsilon(1-\sqrt{1-\epsilon})^2}$

Table D.12: Expressions for the dimensionless drag factor, $F_{\infty_{dds}}$.

Model/Array	Dimensionless drag factor, $F_{\infty_{dds}} \; = \; f_{\infty_{dds}} \, (d - d_s)$
Granular model:	$\dfrac{\rho \, q \, (1 - \epsilon)^{2/3}(1 - (1 - \epsilon)^{1/3}) \, c_d}{2 \, \mu \, \epsilon \, (1 - (1 - \epsilon)^{2/3})^2}$
Foam model: Doubly staggered model	$\dfrac{\rho \, q \, (\psi - 1)(3 - \psi)^2 \, \psi^2 \, c_d}{8 \, \mu \, \epsilon^3}$
Singly staggered model	$\dfrac{\rho \, q \, (\psi - 1)(3 - \psi)^2 \, \psi^2 \, c_d}{16 \, \mu \, \epsilon^3}$
Fibre model:	$\dfrac{\rho \, q \, \sqrt{1 - \epsilon} \, c_d}{2 \, \mu \, \epsilon(1 - \sqrt{1 - \epsilon})}$

Table D.13: Expressions for the streamwise pressure gradient, $-\mathrm{d}p/\mathrm{d}x$, as a function of Re_{Dh} and d predicted by the doubly staggered foam models.

Streamwise pressure gradient for the doubly staggered foam model:

Doubly staggered long duct foam model:

$$-\frac{\mathrm{d}p}{\mathrm{d}x} = \frac{36\,\psi^2(\psi-1)}{\epsilon^2 d^2}\,\mu\,q \;+\; \frac{(\psi-1)(3-\psi)^2\psi^2}{8\epsilon^3 d^2}\,c_d\,\mu\,q\,Re_{Dh}$$

Doubly staggered parallel plate short duct foam model:

$$-\frac{\mathrm{d}p}{\mathrm{d}x} = \frac{36\,\psi^2\,(\psi-1)}{\epsilon^2 d^2}\mu\,q\sqrt{1+\frac{0.0822\,(3-\psi)\,Re_{Dh}}{(\psi-1)}}$$
$$+\frac{(\psi-1)(3-\psi)^2\psi^2}{8\epsilon^3 d^2}\,c_d\,\mu\,q\,Re_{Dh}$$

Doubly staggered square short duct foam model:

$$-\frac{\mathrm{d}p}{\mathrm{d}x} = \frac{42.69\,\psi^2\,(\psi-1)}{\epsilon^2 d^2}\mu\,q\,\sqrt{1+\frac{0.0584\,(3-\psi)\,Re_{Dh}}{(\psi-1)}}$$
$$+\frac{(\psi-1)(3-\psi)^2\psi^2}{8\epsilon^3 d^2}\,c_d\,\mu\,q\,Re_{Dh}$$

Table D.14: Expressions for the streamwise pressure gradient, $-\mathrm{d}p/\mathrm{d}x$, as a function of Re_{Dh} and d_s predicted by the doubly staggered foam models.

Streamwise pressure gradient for the doubly staggered foam model:

Doubly staggered long duct foam model:

$$-\frac{\mathrm{d}p}{\mathrm{d}x} = \frac{9\,\psi^2(\psi-1)^3}{\epsilon^2 d_s^2}\,\mu\,q \;+\; \frac{(\psi-1)^3(3-\psi)^2\psi^2}{32\epsilon^3 d_s^2}\,c_d\,\mu\,q\,Re_{Dh}$$

Doubly staggered parallel plate short duct foam model:

$$-\frac{\mathrm{d}p}{\mathrm{d}x} = \frac{9\,\psi^2\,(\psi-1)^3}{\epsilon^2 d_s^2}\mu\,q\sqrt{1+\frac{0.0822\,(3-\psi)\,Re_{Dh}}{(\psi-1)}}$$
$$+\frac{(\psi-1)^3(3-\psi)^2\psi^2}{32\epsilon^3 d_s^2}\,c_d\,\mu\,q\,Re_{Dh}$$

Doubly staggered square short duct foam model:

$$-\frac{\mathrm{d}p}{\mathrm{d}x} = \frac{10.67\,\psi^2\,(\psi-1)^3}{\epsilon^2 d_s^2}\mu\,q\sqrt{1+\frac{0.0584\,(3-\psi)\,Re_{Dh}}{(\psi-1)}}+$$
$$+\frac{(\psi-1)^3(3-\psi)^2\psi^2}{32\epsilon^3 d_s^2}\,c_d\,\mu\,q\,Re_{Dh}$$

Table D.15: Expressions for the streamwise pressure gradient, $-\mathrm{d}p/\mathrm{d}x$, as a function of q and d predicted by the doubly staggered foam models.

Streamwise pressure gradient for the doubly staggered foam model:
Doubly staggered long duct foam model: $$-\frac{\mathrm{d}p}{\mathrm{d}x} = \frac{36\,\psi^2(\psi-1)}{\epsilon^2 d^2}\,\mu\,q \;+\; \frac{(\psi-1)(3-\psi)\psi^2}{4\epsilon^3 d}\,c_d\,\rho\,q^2$$
Doubly staggered parallel plate short duct foam model: $$-\frac{\mathrm{d}p}{\mathrm{d}x} = \frac{36\,\psi^2\,(\psi-1)}{\epsilon^2 d^2}\mu\,q\sqrt{1+\frac{0.16\,\rho\,q\,d}{\mu(\psi-1)}} \;+\; \frac{(\psi-1)(3-\psi)\psi^2}{4\epsilon^3 d}\,c_d\,\rho\,q^2$$
Doubly staggered square short duct foam model: $$-\frac{\mathrm{d}p}{\mathrm{d}x} = \frac{42.69\,\psi^2\,(\psi-1)}{\epsilon^2 d^2}\mu\,q\,\sqrt{1+\frac{0.12\,\rho\,q\,d}{\mu(\psi-1)}} \;+\; \frac{(\psi-1)(3-\psi)\psi^2}{4\epsilon^3 d}\,c_d\,\rho\,q^2$$

Table D.16: Expressions for the streamwise pressure gradient, $-\mathrm{d}p/\mathrm{d}x$, as a function of q and d_s predicted by the doubly staggered foam models.

Streamwise pressure gradient for the doubly staggered foam model:
Doubly staggered long duct foam model: $$-\frac{\mathrm{d}p}{\mathrm{d}x} = \frac{9\,\psi^2(\psi-1)^3}{\epsilon^2 d_s^2}\,\mu\,q \;+\; \frac{(\psi-1)^2(3-\psi)\psi^2}{8\epsilon^3 d_s}\,c_d\,\rho\,q^2$$
Doubly staggered parallel plate short duct foam model: $$-\frac{\mathrm{d}p}{\mathrm{d}x} = \frac{9\,\psi^2\,(\psi-1)^3}{\epsilon^2 d_s^2}\mu\,q\sqrt{1+\frac{0.33\,\rho\,q\,d_s}{\mu(\psi-1)^2}} \;+\; \frac{(\psi-1)^2(3-\psi)\psi^2}{8\epsilon^3 d_s}\,c_d\,\rho\,q^2$$
Doubly staggered square short duct foam model: $$-\frac{\mathrm{d}p}{\mathrm{d}x} = \frac{10.67\,\psi^2\,(\psi-1)^3}{\epsilon^2 d_s^2}\mu\,q\,\sqrt{1+\frac{0.23\,\rho\,q\,d_s}{\mu(\psi-1)^2}} \;+\; \frac{(\psi-1)^2(3-\psi)\psi^2}{8\epsilon^3 d_s}\,c_d\,\rho\,q^2$$

Table D.17: Expressions for the streamwise pressure gradient, $-\mathrm{d}p/\mathrm{d}x$, as a function of Re_{Dh} and d predicted by the singly staggered foam models.

Streamwise pressure gradient for the singly staggered foam model:

Singly staggered long duct foam model

$$-\frac{\mathrm{d}p}{\mathrm{d}x} = \frac{24\,\psi^2(\psi-1)}{\epsilon^2 d^2}\,\mu\,q \;+\; \frac{(\psi-1)(3-\psi)^2\psi^2}{16\,\epsilon^3 d^2}\,c_d\,\mu\,q\;Re_{Dh}$$

Singly staggered parallel plate short duct foam model:

$$-\frac{\mathrm{d}p}{\mathrm{d}x} = \frac{24\,\psi^2\,(\psi-1)}{\epsilon^2 d^2}\mu\,q\sqrt{1+\frac{0.0822\,(3-\psi)\,Re_{Dh}}{(\psi-1)}} \;+$$
$$+\;\frac{(\psi-1)(3-\psi)^2\psi^2}{16\,\epsilon^3 d^2}\,c_d\,\mu\,q\;Re_{Dh}$$

Singly staggered square short duct foam model:

$$-\frac{\mathrm{d}p}{\mathrm{d}x} = \frac{28.46\,\psi^2\,(\psi-1)}{\epsilon^2 d^2}\mu\,q\sqrt{1+\frac{0.0584\,(3-\psi)\,Re_{Dh}}{(\psi-1)}} \;+$$
$$+\;\frac{(\psi-1)(3-\psi)^2\psi^2}{16\,\epsilon^3 d^2}\,c_d\,\mu\,q\;Re_{Dh}$$

Table D.18: Expressions for the streamwise pressure gradient, $-\mathrm{d}p/\mathrm{d}x$, as a function of Re_{Dh} and d_s predicted by the singly staggered foam models.

Streamwise pressure gradient for the singly staggered foam model:

Singly staggered long duct foam model

$$-\frac{\mathrm{d}p}{\mathrm{d}x} = \frac{6\,\psi^2(\psi-1)^3}{\epsilon^2 d_s^2}\,\mu\,q \;+\; \frac{(\psi-1)^3(3-\psi)^2\psi^2}{64\,\epsilon^3 d_s^2}\,c_d\,\mu\,q\,Re_{Dh}$$

Singly staggered parallel plate short duct foam model:

$$-\frac{\mathrm{d}p}{\mathrm{d}x} = \frac{6\,\psi^2\,(\psi-1)^3}{\epsilon^2 d_s^2}\mu\,q\sqrt{1+\frac{0.0822\,(3-\psi)\,Re_{Dh}}{(\psi-1)}}$$
$$+\;\frac{(\psi-1)^3(3-\psi)^2\psi^2}{64\,\epsilon^3 d_s^2}\,c_d\,\mu\,q\,Re_{Dh}$$

Singly staggered square short duct foam model:

$$-\frac{\mathrm{d}p}{\mathrm{d}x} = \frac{7.12\,\psi^2\,(\psi-1)^3}{\epsilon^2 d_s^2}\mu\,q\sqrt{1+\frac{0.0584\,(3-\psi)\,Re_{Dh}}{(\psi-1)}}$$
$$+\;\frac{(\psi-1)^3(3-\psi)^2\psi^2}{64\,\epsilon^3 d_s^2}\,c_d\,\mu\,q\,Re_{Dh}$$

Table D.19: Expressions for the streamwise pressure gradient, $-\mathrm{d}p/\mathrm{d}x$, as a function of q and d predicted by the singly staggered foam models.

Streamwise pressure gradient for the singly staggered foam model:
Singly staggered long duct foam model $$-\frac{\mathrm{d}p}{\mathrm{d}x} = \frac{24\,\psi^2(\psi-1)}{\epsilon^2 d^2}\,\mu\,q \;+\; \frac{(\psi-1)(3-\psi)\psi^2}{8\,\epsilon^3 d}\,c_d\,\rho\,q^2$$
Singly staggered parallel plate short duct foam model: $$-\frac{\mathrm{d}p}{\mathrm{d}x} = \frac{24\,\psi^2\,(\psi-1)}{\epsilon^2 d^2}\mu\,q\,\sqrt{1+\frac{0.16\,\rho\,q\,d}{\mu(\psi-1)}} \;+\; \frac{(\psi-1)(3-\psi)\psi^2}{8\,\epsilon^3 d}\,c_d\,\rho\,q^2$$
Singly staggered square short duct foam model: $$-\frac{\mathrm{d}p}{\mathrm{d}x} = \frac{28.46\,\psi^2\,(\psi-1)}{\epsilon^2 d^2}\mu\,q\,\sqrt{1+\frac{0.12\,\rho\,q\,d}{\mu(\psi-1)}} \;+\; \frac{(\psi-1)(3-\psi)\psi^2}{8\,\epsilon^3 d}\,c_d\,\rho\,q^2$$

Table D.20: Expressions for the streamwise pressure gradient, $-\mathrm{d}p/\mathrm{d}x$, as a function of q and d_s predicted by the singly staggered foam models.

Streamwise pressure gradient for the singly staggered foam model:
Singly staggered long duct foam model $$-\frac{\mathrm{d}p}{\mathrm{d}x} = \frac{6\,\psi^2(\psi-1)^3}{\epsilon^2 d_s^2}\,\mu\,q \;+\; \frac{(\psi-1)^2(3-\psi)\psi^2}{16\,\epsilon^3 d_s}\,c_d\,\rho\,q^2$$
Singly staggered parallel plate short duct foam model: $$-\frac{\mathrm{d}p}{\mathrm{d}x} = \frac{6\,\psi^2\,(\psi-1)^3}{\epsilon^2 d_s^2}\mu\,q\,\sqrt{1+\frac{0.33\,\rho\,q\,d_s}{\mu(\psi-1)^2}} \;+\; \frac{(\psi-1)^2(3-\psi)\psi^2}{16\,\epsilon^3 d_s}\,c_d\,\rho\,q^2$$
Singly staggered square short duct foam model: $$-\frac{\mathrm{d}p}{\mathrm{d}x} = \frac{7.12\,\psi^2\,(\psi-1)^3}{\epsilon^2 d_s^2}\mu\,q\,\sqrt{1+\frac{0.23\,\rho\,q\,d_s}{\mu(\psi-1)^2}} \;+\; \frac{(\psi-1)^2(3-\psi)\psi^2}{16\,\epsilon^3 d_s}\,c_d\,\rho\,q^2$$

Appendix E

Alternative foam RUC models

The alternative doubly staggered foam RUC model, shown in Figure E.1, was introduced by Du Plessis (1992). In this model the fluid enters the RUC in the streamwise direction. At the end of the streamwise duct section, the streamwise flux is split equally into the two transverse channels after which the fluid exits the RUC again in the streamwise direction.
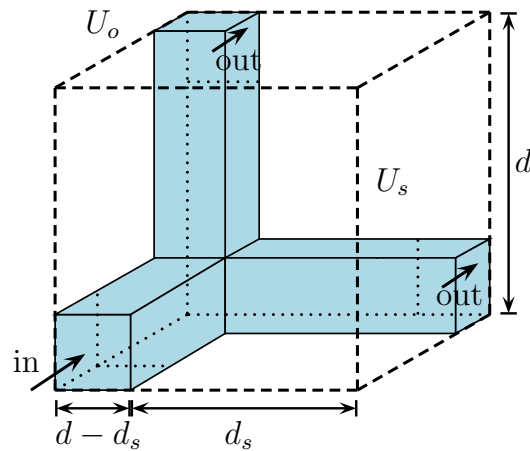
Figure E.1: Alternative doubly staggered foam RUC model.

In the alternative singly staggered model, shown in Figure E.2 (p 309), the fluid enters the RUC in the streamwise direction. At the end of the streamwise duct section the fluid can flow through either, but only one, of the two transverse duct sections, with the remaining duct section being stagnant. Both possibilities are shown in Figure E.2.
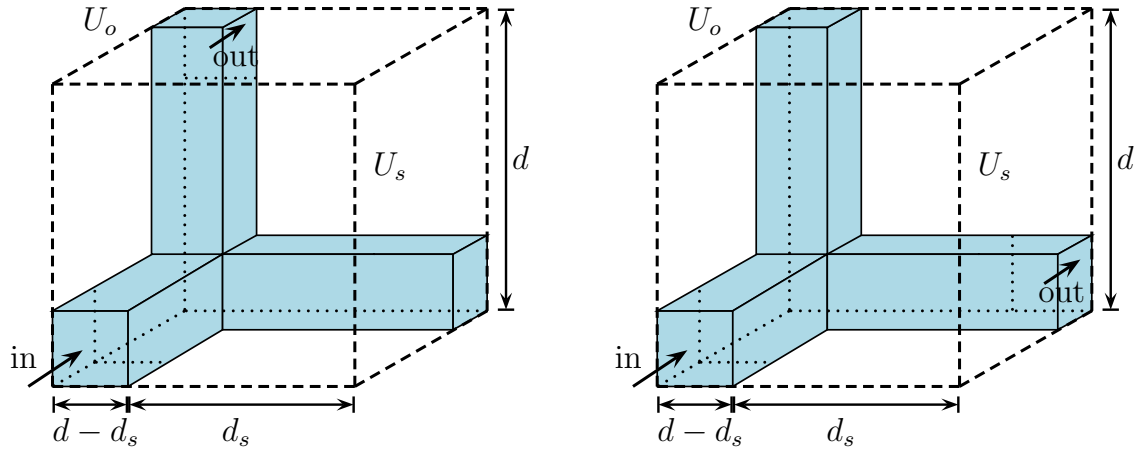
Figure E.2: Alternative singly staggered foam RUC models.

In the alternative non-staggered model, shown in Figure E.3 the fluid, after entering the RUC in the streamwise direction, continues to flow in the streamwise direction without being deviated into a transverse direction.
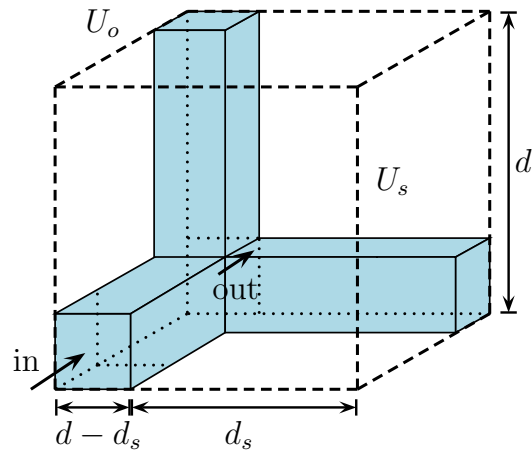

Figure E.3: Alternative non-staggered foam RUC model.

Appendix F

Weighted average applied to different arrays of the fibre RUC model
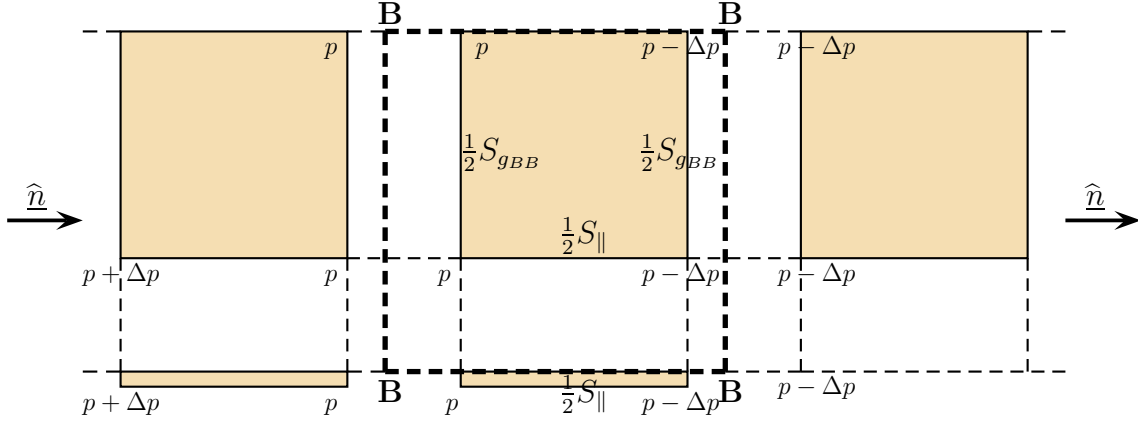
Lloyd (2003) showed for arrays of squares that the remaining surface integral of equation (4.13) may be expressed in terms of the gradient of the average pressure, as given by equation (4.14). In addition to the regular array, it will be illustrated that equation (4.14) is also applicable for the fully staggered array of the fibre RUC model.

Let Δp denote the change in pressure over a streamwise fluid volume and let δp be the change in pressure over a transverse volume in an RUC.

Weighted average applied to the regular array of the fibre RUC model

Consider Figure F.1 (p 311), which is a two-dimensional representation of a typical RUC with corner points BBBB associated with the regular array of the fibre RUC model. In Figure F.1 the arbitrary chosen initial pressure is $p + \Delta p$ and $\underline{n}$ denotes the normal vector directed into each solid in the RUC. The pressure drop over the surfaces are indicated. In the regular array there are no transverse channels, i.e. $U_\perp = 0$, and there is no pressure drop over the stagnant volumes and surfaces. The pressure gradient over the stagnant surfaces may accordingly be expressed as:

$$
\begin{aligned}
-\nabla \langle p \rangle &= \frac{d - d_s}{d} \frac{1}{U_o} \iint\limits_{S_{g_{BB}}} \underline{n}\, \overline{p}_w \, \mathrm{d}S \\
&= \frac{d - d_s}{d} \frac{1}{U_o} \left[(p) \frac{1}{2} S_{g_{BB}} - (p - \Delta p) \frac{1}{2} S_{g_{BB}} \right] \widehat{\underline{n}} \\
&= \frac{d - d_s}{d} \left[\frac{\frac{1}{2} S_{g_{BB}}}{U_o} (\Delta p) \right] \widehat{\underline{n}} \\
&= \frac{(\Delta p)}{d} \left(\frac{U_g}{U_o} \right) \widehat{\underline{n}} = \epsilon \frac{(\Delta p)}{d} \left(\frac{U_g}{U_f} \right) \widehat{\underline{n}} \quad \text{(F.1)}
\end{aligned}
$$

Figure F.1: Two-dimensional representation of a typical RUC with corner points BBBB associated with the regular array of the fibre RUC model.
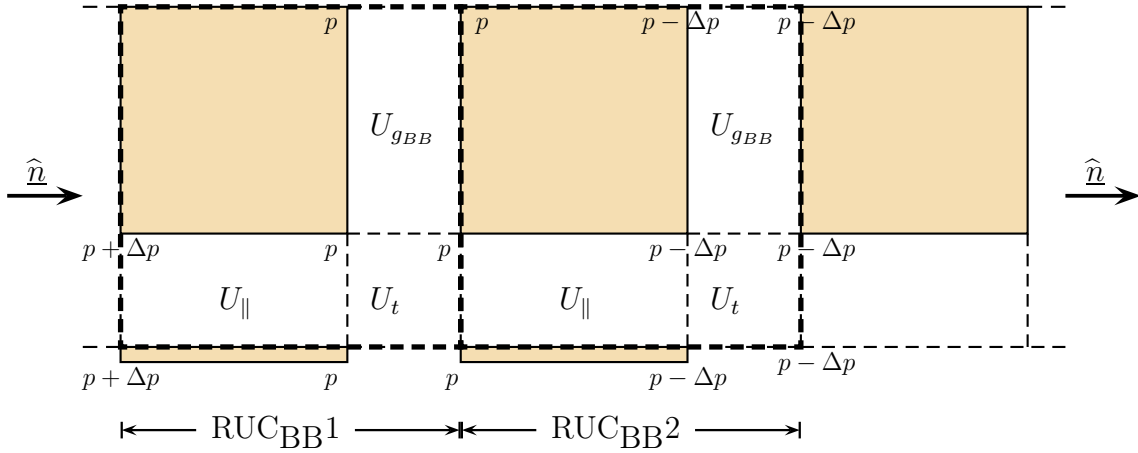
Figure F.2: Two-dimensional representation of the two types of RUCs associated with the regular array of the fibre RUC model.

Consider Figure F.2 in which two consecutive RUCs associated with the regular array are shown. The gradient of the average pressure over the streamwise displacement, d, (evaluated over two consecutive RUCs) leads to

$$
\begin{aligned}
-\nabla \langle p \rangle &= \frac{1}{U_o} \left[\frac{(p + \frac{\Delta p}{2})U_\| + (p)U_t + pU_g}{d} - \frac{\left[(p - \frac{\Delta p}{2})U_\| + (p - \Delta p)U_t \right]}{d} \right. \\
&\qquad\qquad\qquad\qquad\qquad\qquad\qquad \left. - \frac{(p - \Delta p)U_g}{d} \right] \widehat{n} \\
&= \frac{1}{U_o} \left[\frac{(\Delta p)U_\| + (\Delta p)U_t + (\Delta p)U_g}{d} \right] \widehat{n} \\
&= \frac{(\Delta p)}{d} \left[\frac{U_\| + U_t + U_g}{U_o} \right] \widehat{n} = \frac{(\Delta p)}{d} \left[\frac{U_f}{U_o} \right] \widehat{n} .
\end{aligned}
\tag{F.2}
$$

311

For the regular array $U_f = U_\parallel + U_t + U_g$, since $U_\perp = 0$. The transverse surfaces may thus be added to the surface integral of equation (F.1) without having an effect. It thus follows from equations (F.1) and (F.2) that

$$
\frac{d - d_s}{d} \frac{1}{U_o} \iint\limits_{S_{\perp_{BB}} + S_{g_{BB}}} n\,\overline{p}_w\,\mathrm{d}S = \epsilon \frac{(\Delta p)}{d} \left(\frac{U_g}{U_f} \right) \widehat{n}
$$

$$
= -\nabla \langle p \rangle \left(\frac{U_f - (U_\parallel + U_t)}{U_f} \right)
$$

$$
= \left(\frac{U_\parallel + U_t}{U_f} - 1 \right) \nabla \langle p \rangle . \tag{F.3}
$$

The result of equation (F.3) is the same as that of equation (4.14).

Weighted average applied to the fully staggered array of the fibre RUC model

Consider Figure F.3 (p 313) which is a two-dimensional representation of a typical RUC with corner points BBBB associated with the fully staggered array of the fibre RUC model. Let $p + \Delta p + \delta p$ be the arbitrarily chosen pressure at the upstream cross-section of the first solid shown in Figure F.3. The pressure drop over the different surfaces are indicated. The pressure gradient over the transverse surfaces, $S_{\perp_{BB}}$, of the RUC with corner points BBBB may accordingly be expressed as:

$$
\frac{d - d_s}{d} \frac{1}{U_o} \iint\limits_{S_{\perp_{BB}}} n\,\overline{p}_w\,dS = \frac{d - d_s}{d} \frac{1}{U_o} \left[\frac{\left((p + \delta p) + (p + \frac{\delta p}{2}) \right)}{2} \frac{1}{4} S_{\perp_{BB}}(2) \right.
$$

$$
\left. - \frac{\left((p + \frac{\delta p}{2} - \Delta p) + (p - \Delta p) \right)}{2} \frac{1}{4} S_{\perp_{BB}}(2) \right] \widehat{n}
$$

$$
= \frac{d - d_s}{d} \left[\frac{\frac{1}{2} S_\perp}{U_o} \left(\frac{\delta p}{2} + \Delta p \right) \right] \widehat{n}
$$

$$
= \frac{(\Delta p + \frac{\delta p}{2})}{d} \left(\frac{U_\perp}{U_o} \right) \widehat{n}
$$

$$
= \epsilon \frac{(\Delta p + \frac{\delta p}{2})}{d} \left(\frac{U_\perp}{U_f} \right) \widehat{n} \tag{F.4}
$$

Thus for this array the total streamwise pressure drop is Δp and the total transverse pressure drop is $\delta p / 2$.

Consider Figure F.4 (p 313) in which two consecutive RUCs with corner points BBBB associated with a fully staggered array are shown.
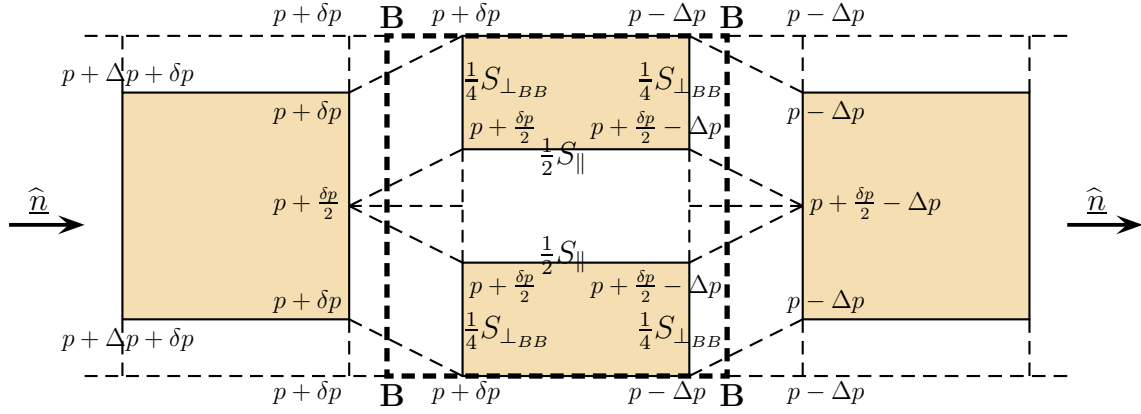
Figure F.3: Two-dimensional representation of a typical RUC with corner points BBBB associated with the fully staggered array of the fibre RUC model.
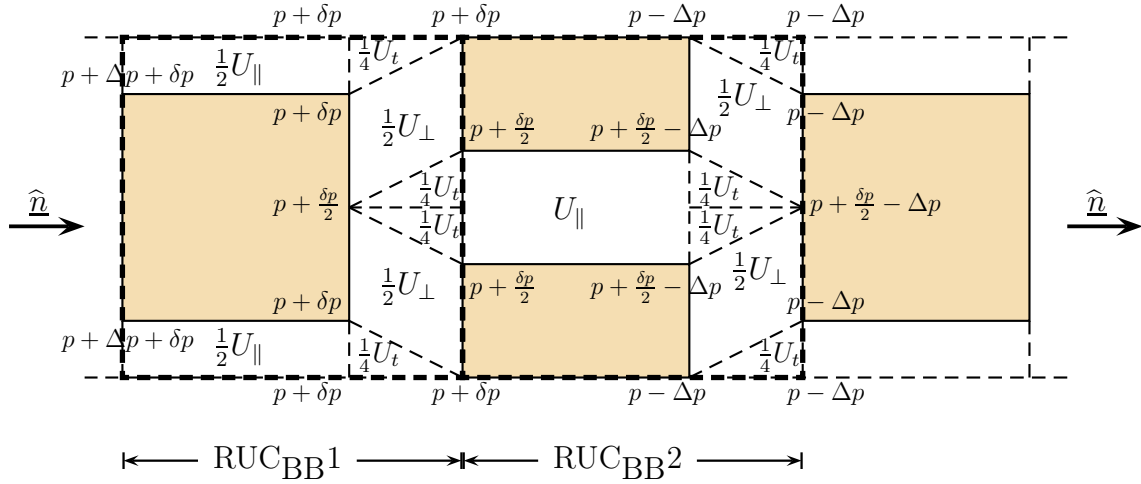
Figure F.4: Two-dimensional representation of two consecutive RUCs associated with the fully staggered array of the fibre RUC model.

The gradient of the average pressure may be determined by calculating the difference between the average pressure of the corresponding volumes of two consecutive RUCs over the streamwise displacement d, i.e.

$$
\begin{aligned}
-\nabla \langle p \rangle \;=\;& \frac{1}{U_o}\left[\frac{(p+\delta p+\frac{\Delta p}{2})\frac{1}{2}U_{\parallel}(2)+(p+\delta p)\frac{1}{4}U_t(2)+(p+\frac{3\delta p}{4})\frac{1}{2}U_{\perp}(2)}{d} +\right. \\
& \frac{(p+\frac{\delta p}{2})\frac{1}{4}U_t(2)}{d}-\frac{\left[(p+\frac{\delta p}{2}-\frac{\Delta p}{2})U_{\parallel}+(p+\frac{\delta p}{2}-\Delta p)\frac{1}{4}U_t(2)\right]}{d} \\
& \left.-\frac{\left[(p+\frac{\delta p}{4}-\Delta p)\frac{1}{2}U_{\perp}(2)+(p-\Delta p)\frac{1}{4}U_t(2)\right]}{d}\right]\,\widehat{n} \\
=\;& \frac{1}{U_o}\left[\frac{(\Delta p+\frac{\delta p}{2})U_{\parallel}+(\Delta p+\frac{\delta p}{2})U_t+(\Delta p+\frac{\delta p}{2})U_{\perp}}{d}\right]\,\widehat{n}
\end{aligned}
$$

313

Hence

$$
\begin{aligned}
-\nabla \langle p \rangle \;&=\; \frac{(\Delta p + \frac{\delta p}{2})}{d} \left[\frac{U_\parallel + U_t + U_\perp}{U_o} \right] \widehat{\underline{n}} \\
&=\; \frac{(\Delta p + \frac{\delta p}{2})}{d} \left[\frac{U_f}{U_o} \right] \widehat{\underline{n}} \\
&=\; \epsilon \frac{(\Delta p + \frac{\delta p}{2})}{d} \widehat{\underline{n}} \; .
\end{aligned}
\tag{F.5}
$$

For the fully staggered array $U_f = U_\parallel + U_t + U_\perp$, since $U_g = 0$. The stagnant surfaces may thus be added to the surface integral of equation (F.4) without having an effect. It then follows from equations (F.4) and (F.5) that

$$
\begin{aligned}
\frac{d - d_s}{d} \frac{1}{U_o} \iint\limits_{S_{\perp_{BB}} + S_{g_{BB}}} \underline{n}\,\overline{p}_w \, \mathrm{d}S \;&=\; \epsilon \frac{(\Delta p + \frac{\delta p}{2})}{d} \left(\frac{U_\perp}{U_f} \right) \widehat{\underline{n}} \\
&=\; -\nabla \langle p \rangle \left(\frac{U_f - (U_\parallel + U_t)}{U_f} \right) \\
&=\; \left(\frac{U_\parallel + U_t}{U_f} - 1 \right) \nabla \langle p \rangle \; .
\end{aligned}
\tag{F.6}
$$

The result of equation (F.6) is thus also the same as that of equation (4.14).

314

Appendix G

Alternative closure modelling procedure for the steady laminar limit of the inertial flow regime

In this appendix an alternative closure modelling procedure for the steady laminar limit of the inertial flow regime is presented. This procedure is based on the application of Bernoulli's equation. Although the closure modelling procedure involving the interstitial form drag coefficient is preferred in this study, the method based on Bernoulli's equation, which was used by Du Plessis (1994), Du Plessis (2002), Wilms (2006) and Woudberg (2006), will be presented here for completeness sake.

Terblanche (2006) found deviations between the application of Bernoulli's equation in the closure modelling procedure and that obtained from numerical simulations. He attributes the deviation to a loss in energy on the streamline along which Bernoulli's equation is applied due to a small frictional boundary layer that is still present. The upstream solid surface in Figure G.1, p 316 (i.e. the normal facing surface on which point A lies) as well as the corner point B are indicated as regions of high viscous dissipation. Certain assumptions made during the application of Bernoulli's equation that are not valid approximations are outlined. Those assumptions will be pointed out below. Terblanche (2006) then proposed an improved alternative method for the closure modelling procedure of the higher Reynolds number term. He still used Bernoulli's equation, but applied it to a streamline passing through regions with little or no viscous dissipation, i.e. the pressures were determined at points on the streamline further away from the solid. For the improved method, please refer to Terblanche (2006).

Owing to the definition of the stagnant fluid volumes in which the fluid remains stationary and interstitial recirculation which therefore do not occur in these volumes, it follows that the surface integral of equation (4.35) reduces to

$$-\nabla \langle p \rangle = \frac{1}{U_o} \iint_{S_\perp} \underline{n}\, p\, \mathrm{d}S \,. \tag{G.1}$$

315
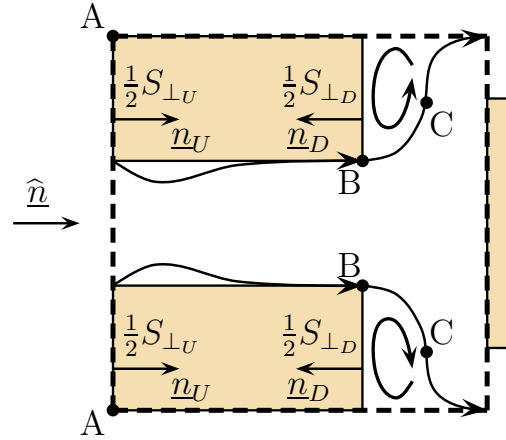
Figure G.1: Schematic illustration of the interstitial recirculation on the lee side of the
solids in an RUC associated with a fully staggered array.

The interstitial recirculation within the separation zone on the lee side of the solid cubes
is schematically illustrated in Figure G.1.

Let the total surface area of the upstream and downstream transverse surfaces be denoted
by $S_{\perp_U}$ and $S_{\perp_D}$, respectively. It then follows that

$$-\nabla \langle p \rangle \;=\; \frac{1}{U_o} \iint\limits_{S_{\perp_U}} \underline{n}\,p\,\mathrm{d}S \;+\; \frac{1}{U_o} \iint\limits_{S_{\perp_D}} \underline{n}\,p\,\mathrm{d}S \,. \tag{G.2}$$

Points A on $S_{\perp_U}$ in Figure G.1 represent stagnation points, points B on $S_{\perp_D}$ represent the
separation points of the dividing streamlines and points C denote the inflection points of
the dividing streamlines adjacent to the separation zones of interstitial recirculation. The
following assumption is made regarding the pressure on the upstream transverse surface:

Assumption G-1 : The pressure on the upstream transverse surface is uniform and
equal to the pressure at the stagnation point A.

Assumption G-1 was shown by Terblanche (2006) through numerical simulations not to
be valid in the steady laminar limit of the inertial flow regime since the mean pressure
on the upstream transverse surface deviates from the pressure at the stagnation point by
almost 20%. Regarding the pressure on the downstream transverse surface, the following
assumption is made:

Assumption G-2 : The pressure on the downstream transverse surface is uniform and
equal to the pressure at the inflection point C.

Assumption G-2 is a valid approximation according to Terblanche (2006).

Each of the two dividing streamlines along which Bernoulli's equation is to be applied
extends from point A and passes through points B and C. Let the pressure at the stagna-
tion points, A, and the inflection points, C, be denoted by p_C and p_A, respectively, and let
h_C and h_A respectively denote the height of points A and C of each dividing streamline.
Application of Bernoulli's equation along each dividing streamline ABC, leads to

$$\frac{p_A}{\rho} + \frac{v_A^2}{2} + gh_A = \frac{p_C}{\rho} + \frac{v_C^2}{2} + gh_C \, , \tag{G.3}$$

where v_A and v_C respectively denotes the magnitudes of the interstitial fluid velocities at
points A and C. Equation (G.3) is simplified with the following assumption:

Assumption G-3 : The difference in elevation between points A and C is negligible.

Based on Assumption G-3 and noting that $v_A = 0$ and $S_{\perp_U} = S_{\perp_D} = S_{face}$, the streamwise
pressure gradient simplifies to

$$-\nabla \langle p \rangle = \frac{1}{U_o} \iint\limits_{S_{face}} \frac{1}{2} \rho \, v_C^2 \, \mathrm{d}S \, \widehat{\underline{n}} \, . \tag{G.4}$$

Assumption G-4 allows for the quantification of the integral of equation (G.4):

Assumption G-4 : The partial occupation of the region of flow recirculation in the
transverse channel has a negligible effect on the ratio of the average
pore velocities.

Terblanche (2006) showed with the aid of numerical computations that Assumption G-4
leads to inaccurate results, since the magnitude of the velocity at the inflection point is
significantly smaller than the magnitude of the average velocity of the flow in the trans-
verse channel adjacent to the recirculation zone. Assumption G-4 is, however, justified
by the approximation that, at relatively high velocities the interstitial flow field approxi-
mates a uniform velocity profile (Du Plessis (1994)). This leads to $v_C = w_\perp = \beta \, w_\parallel$ and
the streamwise pressure gradient may be expressed as:

$$-\nabla \langle p \rangle = \frac{S_{face}}{2 \, U_o} \beta^2 \rho \, w_\parallel^2 \, \widehat{\underline{n}} \, . \tag{G.5}$$

Despite the inaccuracies pointed out by the numerical computations of Terblanche (2006),
equations (G.5) and (4.40) yield the same result for $c_d = \beta^2$.

Appendix H

Power addition technique of Churchill & Usagi (1972)

The power addition technique of Churchill & Usagi (1972), which is used several times in this dissertation, is briefly described below. For an extended discussion on this technique, the reader is referred to the work of De Wet (2010).

Consider the following two asymptotic conditions:

$$\mathcal{G} \;\to\; \mathcal{G}_0\{x\} = C_1\,x^\alpha \qquad \text{for} \qquad x \to 0 \tag{H.1}$$

$$\mathcal{G} \;\to\; \mathcal{G}_\infty\{x\} = C_2\,x^\nu \qquad \text{for} \qquad x \to \infty \tag{H.2}$$

Equation (H.1) represents the asymptotic behaviour of the functional dependency, $\mathcal{G}$, as the independent variable, x, approaches zero and equation (H.2) describes the asymptotic behaviour as the independent variable approaches infinity. A direct summation of equations (H.1) and (H.2) yields a single equation which holds over the entire range of the independent variable, i.e.

$$\mathcal{G}\{x\} \;=\; \mathcal{G}_0\{x\} \;+\; \mathcal{G}_\infty\{x\} \;=\; C_1\,x^\alpha \;+\; C_2\,x^\nu \;. \tag{H.3}$$

Equation (H.3) also provides values for the dependent variable, $\mathcal{G}$, at intermediate values of the independent variable. A shifting exponent, s, was introduced to improve equation (H.3) for cases in which the dependent variable does not correlate well with experimental values at intermediate values of the independent variable. The resulting expression is given by

$$\mathcal{G}^s\{x\} \;=\; \mathcal{G}_0^s\{x\} \;+\; \mathcal{G}_\infty^s\{x\} \;, \tag{H.4}$$

or

$$\mathcal{G}\{x\} \;=\; [\mathcal{G}_0^s\{x\} \;+\; \mathcal{G}_\infty^s\{x\}]^{1/s} \;. \tag{H.5}$$

318

The shifting exponent s does not influence the solutions in the two regimes of separate predominance. It only determines the rate at which the transition between the two processes takes place. The value of s can be adjusted to improve the predictive capabilities of equation (H.5) and hence its correspondence with experimental data. It is therefore an empirical parameter.

Appendix I

Relative percentage errors

The expressions used throughout this dissertation for the relative and absolute percentage errors are defined below.

The relative percentage error of a function, $\mathcal{G}_1$, measured with respect to another function $\mathcal{G}_2$, may be expressed as

$$\text{Relative percentage error} \;=\; 100 \times \frac{\mathcal{G}_2 - \mathcal{G}_1}{\mathcal{G}_2} \;, \tag{I.1}$$

whereas the absolute relative percentage error is given by

$$\text{Absolute relative percentage error} \;=\; 100 \times \frac{|\mathcal{G}_2 - \mathcal{G}_1|}{\mathcal{G}_2} \;. \tag{I.2}$$

Appendix J

Binomial series expansions

In this appendix the binomial series expansions are presented that are necessary to apply series truncation with throwback to the predictive equations of the granular RUC model in Chapter 5.

Since $0 \leq \epsilon \leq 1$ the infinite binomial series can be written as

$$(1 - \epsilon)^n = 1 - n\epsilon + \frac{n(n-1)}{2}\epsilon^2 - \frac{n(n-1)(n-2)}{6}\epsilon^3 + ... \qquad (J.1)$$

It then follows that

$$(1 - \epsilon)^{1/3} = 1 - \frac{\epsilon}{3} - \frac{\epsilon^2}{9} - \frac{5\epsilon^3}{81} - ... \qquad (J.2)$$

$$(1 - \epsilon)^{2/3} = 1 - \frac{2\epsilon}{3} - \frac{\epsilon^2}{9} - \frac{4\epsilon^3}{81} - ... \qquad (J.3)$$

$$(1 - \epsilon)^{4/3} = 1 - \frac{4\epsilon}{3} + \frac{2\epsilon^2}{9} + \frac{4\epsilon^3}{81} + ... \qquad (J.4)$$

$$(1 - \epsilon)^{-4/3} = 1 + \frac{4\epsilon}{3} + \frac{14\epsilon^2}{9} + \frac{140\epsilon^3}{81} + ... \qquad (J.5)$$

Consequently,

$$1 - (1 - \epsilon)^{1/3} = \frac{\epsilon}{3} + \frac{\epsilon^2}{9} + \frac{5\epsilon^3}{81} + ... = \frac{\epsilon}{3}\left[1 + \frac{\epsilon}{3} + \frac{5\epsilon^2}{27} + ...\right] \qquad (J.6)$$

$$1 - (1 - \epsilon)^{2/3} = \frac{2\epsilon}{3} + \frac{\epsilon^2}{9} + \frac{4\epsilon^3}{81} + ... = \frac{2\epsilon}{3}\left[1 + \frac{\epsilon}{6} + \frac{2\epsilon^2}{27} + ...\right] \qquad (J.7)$$

$$\left(1 - (1 - \epsilon)^{2/3}\right)^2 = \frac{4\epsilon^2}{9}\left[1 + \frac{\epsilon}{3} + \frac{19\epsilon^2}{108} + ...\right] \qquad (J.8)$$

$$\left(1 - (1 - \epsilon)^{1/3}\right) \left(1 - (1 - \epsilon)^{2/3}\right)^2 = \frac{4\epsilon^3}{27} \left[1 + \frac{2\epsilon}{3} + \frac{17\epsilon^2}{36} + ...\right] . \tag{J.9}$$

For the inverse it follows by long division that

$$\left(1 - (1 - \epsilon)^{2/3}\right)^{-2} = \frac{9}{4\epsilon^2} \left[1 - \frac{\epsilon}{3} - \frac{7\epsilon^2}{108} + ...\right] \tag{J.10}$$

$$\left[\left(1 - (1 - \epsilon)^{1/3}\right) \left(1 - (1 - \epsilon)^{2/3}\right)^2\right]^{-1} = \frac{27}{4\epsilon^3} \left[1 - \frac{2\epsilon}{3} - \frac{\epsilon^2}{36} - ...\right] . \tag{J.11}$$

Bibliography

Adler, P. M., Jacquin, C. G., & Quiblier, J. A. (1990). Flow in simulated porous media. *International Journal of Multiphase Flow*, *16*(4), 691–712.

Akaydin, H. D., Pierides, A., Weinbaum, S., & Andreopoulos, Y. (2011). Permeability of soft porous media under one-dimensional compaction. *Chemical Engineering Science*, *66*(1), 1–14.

Antohe, B. V., Lage, J. L., Price, D. C., & Weber, R. M. (1997). Experimental determination of permeability and inertia coefficients of mechanically compressed aluminum porous matrices. *Journal of Fluids Engineering*, *119*(2), 404–412.

Azzi, W., Roberts, W. L., & Rabiei, A. (2007). A study on pressure drop and heat transfer in open cell metal foams for jet engine applications. *Materials & Design*, *28*(2), 569–574.

Bachmat, Y. & Bear, J. (1986). Macroscopic modelling of transport phenomena in porous media. 1: The continuum approach. *Transport in Porous Media*, *1*(3), 213–240.

Bear, J. (1972). *Dynamics of fluids in porous media*. Dover Publications, Inc., Mineola, New York.

Bear, J. & Bachmat, Y. (1991). *Introduction to modeling of transport phenomena in porous media*. Kluwer Academic Publishers, Dordrecht, The Netherlands.

Bell, G. E. & Crank, J. (1974). Influence of imbedded particles on steady-state diffusion. *Journal of the Chemical Society, Faraday Transactions*, *70*, 1259–1273.

Bergelin, O. P., Brown, G. A., Hull, H. L., & Sullivan, F. W. (1950). Heat transfer and fluid friction during viscous flow across banks of tubes - III: A study of tube spacing and tube size. *ASME Journal of Heat Transfer*, 881–888.

Bhattacharya, A., Calmidi, V. V., & Mahajan, R. L. (2002). Thermophysical properties of high porosity metal foams. *International Journal of Heat and Mass Transfer*, *45*(5), 1017–1031.

Bird, R. B., Stewart, W. E., & Lightfoot, E. N. (2007). *Transport Phenomena*. Revised Second Edition, John Wiley & Sons, Inc., New York, United States of America.

Boomsma, K. & Poulikakos, D. (2002). The effects of compression and pore size variations on the liquid flow characteristics in metal foams. *Journal of Fluids Engineering*, *124*(1), 263–272.

Bourbie, T. & Zinszner, B. (1985). Hydraulic and acoustic properties as a function of porosity in Fontainebleau sandstone. *Journal of Geophysical Research*, *90*(B13), 11524–11532.

Brea, F. M., Edwards, M. F., & Wilkinson, W. L. (1976). The flow of non-Newtonian slurries through fixed and fluidised beds. *Chemical Engineering Science*, *31*(5), 329–336.

Buciuman, F. C. & Kraushaar-Czarnetzki, B. (2003). Ceramic foam monoliths as catalyst carriers. 1. Adjustment and description of the morphology. *Industrial & Engineering Chemistry Research*, *42*(9), 1863–1869.

Carman, P. C. (1937). Fluid flow through granular beds. *Transactions of the Institution of Chemical Engineers*, *15*, 150–166.

Chen, X. & Papathanasiou, T. D. (2006). On the variability of the Kozeny constant for saturated flow across unidirectional disordered fiber arrays. *Composites Part A: Applied Science and Manufacturing*, *37*(6), 836–846.

Christopher, R. H. & Middleman, S. (1965). Power-law flow through a packed tube. *Industrial & Engineering Chemistry Fundamentals*, *4*(4), 422–426.

Churchill, S. W. & Usagi, R. (1972). A general expression for the correlation of rates of transfer and other phenomena. *The American Institute of Chemical Engineers Journal*, *18*(6), 1121–1128.

Churchill, S. W. & Usagi, R. (1974). A standardized procedure for the production of correlations in the form of a common empirical equation. *Industrial & Engineering Chemistry Fundamentals*, *13*(1), 39–44.

Clennel, M. B. (1997). Tortuosity: a guide through the maze. *Geological Society, London, Special Publications*, *122*, 299–344.

Cloete, M. (2006). *Pore-scale modelling for fluid transport in 2D porous media*. MScEng thesis, Stellenbosch University, South Africa.

Collins, R. E. (1961). *Flow of fluids through porous materials*. Penn Well Books, Tulsa, Oklahoma.

Comiti, J. & Renaud, M. (1989). A new model for determining mean structure parameters of mixed beds from pressure drop measurements: application to beds packed with parallelepipedal particles. *Chemical Engineering Science*, *44*(7), 1539–1545.

Crank, J. (1975). *The mathematics of diffusion*. Second Edition, Clarendon Press, Oxford, United Kingdom.

Crosnier, S., Du Plessis, J. P., Riva, R., & Legrand, J. (2006). Modelling of gas flow through isotropic metallic foams. *Journal of Porous Media*, *9*(1), 35–54.

Currie, J. A. (1960). Gaseous diffusion in porous media. Part 2. - Dry granular materials. *British Journal of Applied Physics*, *11*, 318–324.

324

Dagan, G. (1989). *Flow and transport in porous formations.* Springer-Verlag, Heidelberg, Germany.

De Wet, P. D. (2010). *Powered addition as modelling technique for flow processes.* MSc thesis, Stellenbosch University, South Africa.

De Wet, P. D., Du Plessis, J. P., & Woudberg, S. (2011). Application of power addition as modelling technique for flow processes: Two case studies. *Chemical Enginering Science*, *66*(9), 1923–1931.

Depois, J.-F. & Mortensen, A. (2005). Permeability of open-pore microcellular materials. *Acta Materialia*, *53*(5), 1381–1388.

Diedericks, G. P. J. (1992). *Tracer dispersion in porous media.* MSc thesis, Stellenbosch University, South Africa.

Diedericks, G. P. J. (1999). *Pore-scale modelling of transport phenomena in homogeneous porous media.* PhD thesis, Stellenbosch University, South Africa.

Diedericks, G. P. J. & Du Plessis, J. P. (1995). On tortuosity and areosity tensors for porous media. *Transport in Porous Media*, *20*(5), 265–279.

Diedericks, G. P. J. & Du Plessis, J. P. (1996). Electrical conduction and formation factor in isotropic porous media. *Advances in Water Resources*, *19*(4), 225–239.

Diedericks, G. P. J. & Du Plessis, J. P. (1997). Modelling of flow through homogeneous foams. *Mathematical Engineering in Industry*, *6*(2), 133–154.

Diedericks, G. P. J., Du Plessis, J. P., Montillet, A., Comiti, J., & Legrand, J. (1998). Flow through a highly porous multifilament knit. *Chemical Engineering Communications*, *167*, 21–49.

Dietrich, B., Schabel, W., Kind, M., & Martin, H. (2009). Pressure drop measurements of ceramic sponges - Determining the hydraulic diameter. *Chemical Engineering Science*, *64*(16), 3633–3640.

Doyen, P. M. (1988). Permeability, conductivity and pore geometry of sandstone. *Journal of Geophysical Research*, *93*(B7), 7729–7740.

Drummond, J. E. & Tahir, M. I. (1984). Laminar viscous flow through regular arrays of parallel solid cylinders. *International Journal of Multiphase Flow*, *10*(5), 515–540.

Du Plessis, E. (2010). *Modelling of single phase diffusive transport in porous environments.* MSc thesis, Stellenbosch University, South Africa.

Du Plessis, E. & Woudberg, S. (2009). Modelling of diffusion in porous structures. *Proceedings of the Fifth International Conference on Computational and Experimental Methods in Multiphase and Complex Flow, Computational Methods in Multiphase Flow V (Editors: A.A. Mammoli and C.A. Brebbia), WIT Press, New Forest, United Kingdom, 15-17 June*, 399–408.

Du Plessis, E., Woudberg, S., & Du Plessis, J. P. (2010). Pore-scale modelling of diffusion in unconsolidated porous structures. *Chemical Engineering Science, 65*(8), 2541–2551.

Du Plessis, J. P. (1991). Saturated crossflow through a two-dimensional porous medium. *Advances in Water Resources, 14*(3), 131–137.

Du Plessis, J. P. (1992). Geometrical models for porous membrane morphologies. *Water Science & Technology, 25*(10), 363–372.

Du Plessis, J. P. (1994). Analytical quantification of coefficients in the Ergun equation for fluid friction in a packed bed. *Transport in Porous Media, 16*(2), 189–207.

Du Plessis, J. P. (1996). Power law flow in isotropic porous media. *Proceedings of the Seventh International Congress on Rheology (Editors: A. Aït-Kadi, J.M Dealy, D.F. James and M.C. Williams), Chemical Engineering Department, Laval University, Quebec, Canada, August 18-23*, 375–376.

Du Plessis, J. P. (1999). Introducing a percolation threshold in pore-scale modelling. *Physics and Chemistry of the Earth, Part A: Solid Earth and Geodesy, 24*(7), 617–620.

Du Plessis, J. P. (2002). *Modelling and industrial application of flow through two-dimensional porous media.* MScEng thesis, Stellenbosch University, South Africa.

Du Plessis, J. P. & Collins, M. R. (1992). A new definition for laminar flow entrance lengths of straight ducts. *N&O Joernaal, September*, 11–16.

Du Plessis, J. P. & Diedericks, G. P. J. (1997). *Fluid Transport in Porous Media, Advances in Fluid Mechanics*, chapter 2, (pp. 61–104). 13. Computational Mechanics Publications, Southampton, United Kingdom.

Du Plessis, J. P. & Masliyah, J. H. (1988). Mathematical modelling of flow through consolidated isotropic porous media. *Transport in Porous Media, 3*(2), 145–161.

Du Plessis, J. P. & Masliyah, J. H. (1991). Flow through isotropic granular porous media. *Transport in Porous Media, 6*(3), 207–221.

Du Plessis, J. P., Montillet, A., Comiti, J., & Legrand, J. (1994). Pressure drop prediction for flow through high porosity metallic foams. *Chemical Engineering Science, 49*(21), 3545–3553.

Du Plessis, J. P. & Roos, L. I. (1993). Permeability prediction for water seepage through low porosity granular porous media. *Water SA, 19*(2), 147–152.

Du Plessis, J. P. & Roos, L. I. (1994a). Improvement on prediction for water seepage through low porosity granular media. *Water SA, 20*(2), 175–178.

Du Plessis, J. P. & Roos, L. I. (1994b). Predicting the hydrodynamic permeability of sandstone with a pore-scale model. *Journal of Geophysical Research - Solid Earth, 99*(B10), 19771–19776.

Du Plessis, J. P. & Roos, L. I. (1995). Numerical analysis of near-wall channelling in a packed bed. *Engineering Computations*, *12*(4), 357–371.

Du Plessis, J. P. & Van der Westhuizen, J. (1993). Laminar crossflow through prismatic porous domains. *R&D Journal*, *9*(2), 18–24.

Du Plessis, J. P. & Woudberg, S. (2008). Pore-scale derivation of the Ergun equation to enhance its adaptability and generalization. *Chemical Engineering Science*, *63*(9), 2576–2586.

Du Plessis, J. P., Woudberg, S., & Coq, L. L. (2010). Modelling and analysis of permeability of anisotropic compressed non-woven filters. *Proceedings of the Third International Conference on Porous Media and its Applications in Science, Engineering and Industry (Editor: K Vafai), AIP conference proceedings, Montecatini, Italy, 20-25 June*, 272–277.

Dukhan, N. (2006). Correlations for the pressure drop for flow through metal foam. *Experiments in Fluids*, *41*(4), 665–672.

Dukhan, N. & Patel, P. (2008). Equivalent particle diameter and length scale for pressure drop in porous metals. *Experimental Thermal and Fluid Science*, *32*(5), 1059–1067.

Dullien, F. A. L. (1979). *Porous media; fluid transport and pore structure.* Academic Press, New York, United States of America.

Dybbs, A. & Edwards, R. V. (1984). *A new look at porous media fluid mechanics - Darcy to turbulent, Fundamentals of Transport Phenomena in Porous Media*, (pp. 201–256). Martinus Nijhoff Publishers, Boston, Massachusetts, United States of America.

Edouard, D., Lacroix, M., Pham Huu, C., & Luck, F. (2008). Pressure drop modeling on SOLID foam: State-of-the art correlation. *Chemical Engineering Journal*, *144*(2), 299–311.

Epstein, N. (1989). On tortuosity and the tortuosity factor in flow and diffusion through porous media. *Chemical Engineering Science*, *44*(3), 777–779.

Ergun, S. (1952). Fluid flow through packed columns. *Chemical Engineering Progress*, *48*(2), 89–94.

Farber, L., Tardos, G., & Michaels, J. N. (2003). Use of X-ray tomography to study the porosity and morphology of granules. *Powder Technology*, *132*(1), 57–63.

Firdaouss, M. & Du Plessis, J. P. (2004). On the prediction of Darcy permeability in nonisotropic periodic two-dimensional porous media. *Journal of Porous Media*, *7*(2), 119–131.

Firdaouss, M., Du Plessis, J. P., & Woudberg, S. (2009). Erratum: On the prediction of Darcy permeability in nonisotropic periodic two-dimensional porous media by Firdaouss M. and Du Plessis, J.P. (Journal of Porous Media, vol. 7, no. 2, 2004, pp. 119-131). *Journal of Porous Media*, *12*(2), 99.

327

Forchheimer, P. H. (1901). Wasserbeweguing durch boden. *Zeit. Ver. Deutsch Ing.*, *45*, 1782–1788.

Fourie, J. G. & Du Plessis, J. P. (2002). Pressure drop modelling in cellular metallic foams. *Chemical Engineering Science*, *57*(4), 2781–2789.

Fredrich, J. T., Greaves, K. H., & Martin, J. W. (1993). Pore geometry and transport properties of Fontainebleau sandstone. *International Journal of Rock Mechanics and Mining Sciences & Geomechanics Abstracts*, *30*(7), 691–697.

Garrouch, A. A. & Ali, L. (2001). Predicting the onset of inertial effects in sandstone rocks. *Transport in Porous Media*, *44*(3), 487–505.

Gebart, B. R. (1992). Permeability of unidirectional reinforcements for RTM. *Journal of Composite Materials*, *26*(8), 1100–1133.

Gerbaux, O., Buyens, F., Mourzenko, V. V., Memponteil, A., Vabre, A., Thovert, J. F., & Adler, P. M. (2010). Transport properties of real metallic foams. *Journal of Colloid and Interface Science*, *342*(1), 155–165.

Gerbaux, O., Vercueil, T., Memponteil, A., & Bador, B. (2009). Experimental characterization of single and two-phase flow through nickel foams. *Chemical Engineering Science*, *64*(19), 4186–4195.

Giani, L., Groppi, G., & Tronconi, E. (2005a). Heat transfer characterization of metallic foams. *Industrial & Engineering Chemistry Research*, *44*(24), 9078–9085.

Giani, L., Groppi, G., & Tronconi, E. (2005b). Mass-transfer characterization of metallic foams as supports for structured catalysts. *Industrial & Engineering Chemistry Research*, *44*(14), 4993–5002.

Gidaspow, D. (1994). *Multiphase flow and fluidization: Continuum and kinetic theory descriptions.* Academic Press, Inc., San Diego, California, United States of America.

Große, J., Dietrich, B., Martin, H., Kind, M., Vicente, J., & Hardy, E. H. (2008). Volume image analysis of ceramic sponges. *Chemical Engineering & Technology*, *31*(2), 307–314.

Halvorsen, B. M., Du Plessis, J. P., & Woudberg, S. (2006). The performance of drag models on flow behaviour in the CFD simulation of a fluidised bed. *Proceedings of the Sixth International Conference on Advances in Fluid Mechanics, Advances in Fluid Mechanics VI (Editors: Rahman, M. & Brebbia, C.A.), WIT Press, Skiathos, Greece, 8-10 May*, 3–12.

Happel, J. (1958). Viscous flow in multiparticle systems: Slow motion of fluids relative to beds of spherical particles. *American Institute of Chemical Engineers Journal*, *4*(2), 197–201.

Happel, J. (1959). Viscous flow relative to arrays of cylinders. *American Institute of Chemical Engineers Journal*, *5*(2), 174–177.

Happel, J. & Brenner, H. (1965). *Low Reynolds number hydrodynamics.* Prentice-Hall, Inc. United Kingdom.

Hasimoto, H. (1959). On the periodic fundamental solutions of the Stokes equations and their application to viscous flow past a cubic array of spheres. *Journal of Fluid Mechanics*, *5*, 317–328.

Helsør, T. & Svendsen, H. (2007). Experimental characterization of pressure drop in dry demisters at low and elevated pressures. *Chemical Engineering Research and Design*, *85*(3), 377–385.

Higdon, J. J. L. & Ford, G. D. (1996). Permeability of three-dimensional models of fibrous porous media. *Journal of Fluid Mechanics*, *308*, 341–361.

Hoogschagen, J. (1955). Diffusion in porous catalysts and adsorbents. *Industrial & Engineering Chemistry*, *47*(5), 906–912.

Hughes, W. F. (1979). *An introduction to viscous flow.* McGraw-Hill, New York, United States of America.

Huu, T. T., Lacroix, M., Huu, C. P., Schweich, D., & Edouard, D. (2009). Towards a more realistic modeling of solid foam: Use of the pentagonal dodecahedron geometry. *Chemical Engineering Science*, *64*(24), 5131–5142.

Hwang, J.-J., Hwang, G.-J., Yeh, R.-H., & Chao, C.-H. (2002). Measurement of interstitial convective heat transfer and frictional drag for flow across metal foams. *ASME Journal of Heat Transfer*, *124*(1), 120–129.

Incera Garrido, G., Patcas, F. C., Lang, S., & Kraushaar-Czarnetzki, B. (2008). Mass transfer and pressure drop in ceramic foams: A description for different pore sizes and porosities. *Chemical Engineering Science*, *63*(21), 5202–5217.

Innocentini, M. D. M., Salvini, V. R., Macedo, A., & Pandolfelli, V. C. (1999). Prediction of ceramic foams permeability using Ergun's equation. *Materials Research*, *2*(4), 283–289.

Innocentini, M. D. M., Salvini, V. R., Pandolfelli, V. C., & Coury, J. R. (1999a). Assessment of Forchheimer's equation to predict the permeability of ceramic foams. *Journal of the American Ceramic Society*, *82*(7), 1945–1948.

Innocentini, M. D. M., Salvini, V. R., Pandolfelli, V. C., & Coury, J. R. (1999b). The permeability of ceramic foams. *The American Ceramic Society Bulletin*, *78*(9), 78–84.

Jackson, G. W. & James, D. F. (1986). The permeability of fibrous porous media. *The Canadian Journal of Chemical Engineering*, *64*(3), 364–374.

Joy, A. S. (1953). Methods and techniques for the determination of specific surface by gas adsorption. *Vacuum*, *3*(3), 254–278.

Kaviany, M. (1995). *Principles of heat transfer in porous media, Second Edition.* Springer-Verlag, New York, United States of America.

Kemblowski, Z. & Michniewicz, M. (1979). A new look at the laminar flow of power law fluids through granular beds. *Rheologica Acta*, *18*(6), 572–739.

Kim, J.-H., Ochoa, J. A., & Whitaker, S. (1987). Diffusion in anisotropic porous media. *Transport in Porous Media*, *2*(4), 327–356.

Kirsch, A. A. & Fuchs, N. A. (1967). Studies on fibrous aerosol filters - II. Pressure drops in systems of parallel cylinders. *The Annals of Occupational Hygiene*, *10*(1), 23–30.

Krishnan, S., Murthy, J. Y., & Garimella, S. V. (2006). Direct simulation of transport in open-cell metal foam. *ASME Joural of Heat Transfer*, *128*(8), 793–799.

Kuwabara, S. (1959). The forces experienced by randomly distributed parallel circular cylinders or spheres in a viscous flow at small Reynolds numbers. *Journal of the Physical Society of Japan*, *14*(4), 527–532.

Lacroix, M., Nguyen, P., Schweich, D., Pham Huu, C., Savin-Poncet, S., & Edouard, D. (2007). Pressure drop measurements and modeling on SiC foams. *Chemical Engineering Science*, *62*(12), 3259–3267.

Lage, J. L., Antohe, B. V., & Nield, D. A. (1997). Two types of nonlinear pressure-drop versus flow-rate relation observed for saturated porous media. *ASME Journal of Fluids Engineering*, *119*(3), 700–706.

Le Coq, L. (2008). Influence on permeability of the structural parameters of heterogeneous porous media. *Environmental Technology*, *29*(2), 141–149.

Le Coq, L. (2010). *Personal Communication*.

Lee, Y., Jeong, J., Youn, I. J., & Lee, W. H. (1997). Modified liquid displacement method for determination of pore size distribution in porous membranes. *Journal of Membrane Science*, *130*(1-2), 149–156.

Liu, J. F., Wu, W. T., Chiu, W. C., & Hsieh, W. H. (2006). Measurement and correlation of friction characteristic of flow through foam matrixes. *Experimental Thermal and Fluid Science*, *30*(4), 329–336.

Lloyd, C. A. (2003). *Hydrodynamic permeability of staggered and non-staggered regular arrays of squares*. MScEng thesis, Stellenbosch University, South Africa.

Lloyd, C. A., Du Plessis, J. P., & Halvorsen, B. M. (2004). On closure modelling of volume averaged equations for flow through two-dimensional arrays of squares. *Proceedings of the Fifth International Conference on Advances in Fluid Mechanics, Advances in Fluid Mechanics V (Editors: Brebbia, C.A., Mendes, A.C. & Rahman, M.), WIT Press, Lisbon, Portugal, 22-24 March*, 85–93.

Lu, T. J., Stone, H. A., & Ashby, M. F. (1998). Heat transfer in open-cell metal foams. *Acta Meterialia*, *46*(10), 3619–3635.

Macdonald, I. F., El-Sayed, M. S., Mow, K., & Dullien, F. A. L. (1979). Flow through porous media - the Ergun equation revisited. *Industrial & Engineering Chemistry Fundamentals*, *18*(3), 199–208.

Mancin, S., Zilio, C., Cavallini, A., & Rossetto, L. (2010). Pressure drop during air flow in aluminum foams. *International Journal of Heat and Mass Transfer*, *53*(15-16), 3121–3130.

Massey, B. S. (1989). *Mechanics of fluids, Sixth Edition*. Van Nostrand Reinhold, Int., London, United Kingdom.

Mirbod, P., Andreopoulos, Y., & Weinbaum, S. (2009). On the generation of lift forces in random soft porous media. *Journal of Fluid Mechanics*, *619*, 147–166.

Mironer, A. (1979). *Engineering fluid mechanics*. McGraw-Hill, Inc., New York, United States of America.

Miwa, S. & Revankar, S. T. (2011). Hydrodynamic characterization of nickel metal foam, Part 2: Effects of pore structure and permeability. *Transport in Porous Media*, *89*(3), 323–336.

Molale, D. M. (2007). *A computational evaluation of flow through porous media*. MSc thesis, Stellenbosch University, South Africa.

Montillet, A., Comiti, J., & Legrand, J. (1992). Determination of structural parameters of metallic foams from permeametry measurements. *Journal of Materials Science*, *27*(16), 4460–4464.

Moreira, E. A. & Coury, J. R. (2004). The influence of structural parameters on the permeability of ceramic foams. *Brazilian Journal of Chemical Engineering*, *21*(1), 23–33.

Nabovati, A., Llewellin, E. W., & Sousa, A. C. M. (2009). A general model for the permeability of fibrous porous media based on fluid flow simulations using the lattice Boltzman method. *Composites Part A: Applied Science and Manufacturing*, *40*(6-7), 860–869.

Nakao, S.-I. (1994). Determination of pore size and pore size distribution 3. Filtration membranes. *Journal of Membrane Science*, *96*(1-2), 131–165.

Patankar, S. V. (1980). *Numerical heat transfer and fluid flow*. CRC Press, Boca Raton, United States of America.

Peak, J. W., Kang, B. H., Kim, S. Y., & Hyun, J. M. (2000). Effective thermal conductivity and permeability of aluminum foam materials. *International Journal of Thermophysics*, *21*(2), 453–464.

Pettijohn, F. J., Potter, P. E., & Siever, R. (1972). *Sand and sandstones, Second Edition*. Springer-Verlag, New York, United States of America.

Philipse, A. P. & Schram, H. L. (1991). Non-Darcian airflow through ceramic foams. *Journal of the American Ceramic Society*, *74*(4), 728–732.

Quintard, M. (1993). Diffusion in isotropic and anisotropic porous systems: Three-dimensional calculations. *Transport in Porous Media*, *11*(2), 187–199.

Rautenbach, C. (2009). *Modelling of flow through porous packing elements of a CO_2 absorption tower*. MSc thesis, Stellenbosch University, South Africa.

Richardson, J. T., Peng, Y., & Remue, D. (2000). Properties of ceramic foam catalyst supports: Pressure drop. *Applied Catalysis A: General*, *204*(1), 19–32.

Roberson, J. A. & Crowe, C. T. (1985). *Engineering fluid mechanics, Third Edition*. Houghton Mifflin, Massachusetts, United States of America.

Rohsenow, W. & Choi, H. Y. (1961). *Heat, mass and momentum transfer*. Prentice-Hall Inc., Englewood, New Jersey.

Roos, L. I. (1992). *Mathematical modelling of synthetic membrane morphology*. MSc thesis, Stellenbosch University, South Africa.

Rowe, P. N. (1961). Drag forces in a hydraulic model of a fluidised bed - Part II. *Chemical Engineering Research and Design*, *39*(a), 175–180.

Ryan, D., Carbonell, R. G., & Whitaker, S. (1981). A theory of diffusion and reaction in porous media. *American Institute of Chemical Engineers Symposium Series*, *77*(202), 46–62.

Sabiri, N.-E. & Comiti, J. (1995). Pressure drop in non-Newtonian purely viscous fluid flow through porous media. *Chemical Engineering Science*, *50*(7), 1193–1201.

Sadiq, T. A. K., Advani, S. G., & Parnas, R. S. (1995). Experimental investigation of transverse flow through aligned cylinders. *International journal of Multiphase Flow*, *21*(5), 755–774.

Sáez, A. E., Perfetti, J. C., & Rusinek, I. (1991). Prediction of effective diffusivities in porous media using spatially periodic models. *Transport in Porous Media*, *6*(2), 143–157.

Safinia, L., Mantalaris, A., & Bismarck, A. (2006). Nondestructive technique for the characterization of the pore size distribution of soft porous constructs for tissue engineering. *American Chemical Society*, *22*(7), 3235–3242.

Sakai, K. (1994). Determination of pore size and pore size distribution 2. Dialysis membranes. *Journal of Membrane Science*, *96*(1-2), 91–130.

Sangani, A. S. & Acrivos, A. (1982). Slow flow past periodic arrays of cylinders with application to heat transfer. *International Journal of Multiphase Flow*, *8*(3), 193–206.

Santamarina, J. C., Klein, K. A., Wang, Y. N., & Prencke, E. (2002). Specific surface: Determination and relevance. *Canadian Geotechnical Journal*, *39*(1), 233–241.

Scheidegger, A. E. (1957). *The physics of flow through porous media.* University of Toronto Press, Toronto, Canada.

Seguin, D., Montillet, A., & Comiti, J. (1998). Experimental characterisation of flow regimes in various porous media - I: Limit of laminar flow regime. *Chemical Engineering Science*, *53*(21), 3751–3761.

Seguin, D., Montillet, A., Comiti, J., & Huet, F. (1998). Experimental characterisation of flow regimes in various porous media - II: Transition to turbulent regime. *Chemical Engineering Science*, *53*(22), 3897–3909.

Shah, R. K. & London, A. L. (1978). *Laminar flow forced convection in ducts.* Advances in Heat Transfer, Supplement 1, Academic Press, London, United Kingdom.

Shaughnessy Jr., E. J., Katz, I. M., & Schaffer, J. P. (2005). *Introduction to fluid mechanics.* Oxford University Press, Inc., New York, United States of America.

Skartsis, L., Kardos, J. L., & Khomami, B. (1992). Resin flow through fiber beds during composite manufacturing processes. Part I: Review of newtonian flow through fiber beds. *American Institute of Chemical Engineers Journal*, *32*(4), 221–230.

Slattery, J. C. (1969). Single-phase flow through porous media. *American Institute of Chemical Engineers Journal*, *15*(6), 866–872.

Smit, G. J. F. (1997). *Mathematical modelling of non-Newtonian flow through isotropic porous media.* PhD thesis, Stellenbosch University, South Africa.

Smit, G. J. F. & Du Plessis, J. P. (1997). Pressure drop prediction of power law fluid through granular media. *Journal of Non-Newtonian Fluid Mechanics*, *72*(2-3), 319–323.

Smit, G. J. F. & Du Plessis, J. P. (1999). Modelling of non-Newtonian purely viscous flow through isotropic high porosity synthetic foams. *Chemical Engineering Science*, *54*(5), 645–654.

Smit, G. J. F. & Du Plessis, J. P. (2000). Modelling of non-Newtonian flow through isotropic porous media. *Mathematical Engineering in Industry*, *8*(1), 19–40.

Smit, G. J. F., Du Plessis, J. P., & Du Plessis Sr., J. P. (2007). Modelling of airflow through a stack in a timber-drying kiln. *Applied Mathematical Modelling*, *31*(2), 270–282.

Smit, G. J. F., Du Plessis, J. P., & Wilms, J. M. (2005). On the modeling of non-Newtonian purely viscous flow through high porosity synthetic foams. *Chemical Engineering Science*, *60*(10), 2815–2819.

Spielman, L. & Goren, S. L. (1968). Model for predicting pressure drop and filtration efficiency in fibrous media. *Environmental Science and Technology*, *2*(4), 279–287.

Stemmet, C. P., Van der Schaaf, J., Kuster, B. F. M., & Schouten, J. C. (2006). Solid foam packings for multiphase reactors: Modelling of liquid holdup and mass transfer. *Chemical Engineering Research and Design*, *84*(12), 1134–1141.

Taud, H., Martinez-Angeles, R., Parrot, J. F., & Hernandez-Escobedo, L. (2005). Porosity estimation method by X-ray computed tomography. *Journal of Petroleum Science and Engineering*, *47*(3-4), 209–217.

Terblanche, L. (2006). *The prediction of flow through two-dimensional porous media*. MSc thesis, Stellenbosch University, South Africa.

Topin, F., Bonnet, J.-P., Madani, B., & Tadrist, L. (2006). Experimental analysis of multiphase flow in metallic foam: Flow laws, heat transfer and convective boiling. *Advanced Engineering Materials*, *8*(9), 890–899.

Van der Westhuizen, J. & Du Plessis, J. P. (1994). Quantification of unidirectional fiber bed permeability. *Journal of Composite Materials*, *28*(7), 619–637.

Van der Westhuizen, J. & Du Plessis, J. P. (1996). An attempt to quantify fibre bed permeability utilizing the phase average Navier-Stokes equation. *Composites Part A: Applied Science and Manufacturing*, *27*(4), 263–269.

Wakao, N. & Smith, J. M. (1962). Diffusion in catalyst pellets. *Chemical Engineering Science*, *17*(11), 825–834.

Wang, D.-C. & Khalili, A. (2003). Flow visualization and quantitative measurements inside porous media by particle image velocimetry. *Proceedings of the International Society for Optics and Photonics (SPIE), Optical Technology and Image Processing for Fluids and Solids Diagnostics 5058 (Editors: Shen, G.X., Cha, S.S., Chiang F-P. & Mercer, C.R.)*, *5058*, 232–239.

Weissberg, H. L. (1963). Effective diffusion coefficient in porous media. *Journal of Applied Physics*, *34*(9), 2636–2639.

Welty, J. R. (1978). *Engineering heat transfer*. John Wiley & Sons Inc., New York, United States of America.

Welty, J. R., Wicks, C. E., & Wilson, R. E. (1969). *Fundamentals of momentum, heat and mass transfer*. John Wiley & Sons Inc., New York, United States of America.

Wen, C. Y. & Yu, Y. H. (1966). Mechanics of fluidization. *Chemical Engineering Progress Symposium Series*, *62*(62), 100–111.

Whitaker, S. (1968). *Introduction to fluid mechanics*. Prentice-Hall Inc., Englewood Cliffs, New Jersey.

Whitaker, S. (1969). Advances in theory of fluid motion in porous media. *Industrial & Engineering Chemistry*, *61*(12), 14–28.

Wilms, J. M. (2006). *On the hydrodynamic permeability of foamlike media*. MScEng thesis, Stellenbosch University, South Africa.

Winterberg, M. & Tsotsas, E. (2000). Impact of tube-to-paticle-diameter ratio on pressure drop in packed beds. *American Institute of Chemical Engineers Journal*, *46*(5), 1084–1088.

Woudberg, S. (2006). *Laminar flow through isotropic granular porous media.* MScEng thesis, Stellenbosch University, South Africa.

Woudberg, S. & Du Plessis, J. P. (2008). Predicting the permeability of very low porosity sandstones. *Transport in Porous Media, 73*(1), 39–55.

Woudberg, S., Du Plessis, J. P., & Smit, G. J. F. (2006). Non-Newtonian purely viscous flow through isotropic granular porous media. *Chemical Engineering Science, 61*(13), 4299–4308.

Xu, W., Zhang, H., Yang, Z., & Zhang, J. (2008). Numerical investigation on the flow characteristics and permeability of three-dimensional reticulated foam materials. *Chemical Engineering Journal, 140*(1-3), 562–569.

Zeng, Z. & Grigg, R. (2006). A criterion for non-Darcy flow in porous media. *Transport in Porous Media, 63*(1), 57–69.